Universitat Autònoma de Barcelona

# Dipole-induced water adsorption on surfaces

Juan José Segura Sugrañes

Tesi doctoral

Programa de doctorat en Química

Directors: Dr. Jordi Fraxedas Calduch

Dr. Albert Verdaguer Prats

Departament de Química

Facultat de Ciències

2012

**Agraıments:**

La tesi docotoral que aquí es presenta ha sigut realitzada dins el grup *Small Molecules on Surfaces*, que forma part del Centre d Investigació en Nanociència i Nanotecnologia (CIN2, però aviat canviarà de nom a ICN-2). Aquesta no hauria sigut possible sense el guiatge, les discusion científiques i els consells de certes persones, per tant, aquestes primeres pàgines vull dedicar-les a agraır a aquelles persones que han fet possible aquesta tesi.

En primer lloc vull agraır al meu director, el Dr. Jordi Fraxedas, i al meu co-director, el Dr. Albert Verdaguer l haver-me brindat l ocasió de passar aquests anys estudiant un tema tan apassionant. Heu sapigut trobar aquell punt d equilibri entre guiar el curs de la recerca que dirigiu i donar llibertat de decisió per desenvolupar els temes segons el criteri de l investigador. Gràcies per tot el que heu aportat al meu desenvolupament com a científic durant aquests anys.

Aquests anys d investigació tampoc haurien sigut possibles sense el finançament que he rebut per realitzar la meva tasca, per aquest motiu vull també agraır al CSIC i l ICN els respectius contractes amb els quals vaig començar la tesi i també els quatre anys de beca JAE PREDOC del CSIC amb els que he portat el gruix i finalització de la tesi.

Diferents persones han fet aportacions durant aquests anys de recerca sense les quals aquest treball no hauria sigut possible, i per tant vull agraır al Dr. Hernández i al Dr. Sacha les simulacions que van realitzar, a la Dra. Ocal i al seu doctorand en Luis Eduardo Garzón les probes complementàries de LFM, al Dr. Santiso per les difraccions de raigs-X, a la Dra. Paruch l haver-nos ajudat a entendre millor els ferroelèctrics i els materials PZT, i per haver-nos rebut a Suıssa amb tanta disposició per ajudar-nos. Al Dr. Catalán i la Dra. Domingo l accès al seu AFM, optimitzat per fer PFM, que tant important ha sigut per obtenir els resultats amb els PZT.

Molta gent m ha aportat les seves suggerències i idees durant aquests anys, i hem discutit sobre la millor manera d afrontar una complicació o d entendre un resultat, totes aquestes coses han anat encaixant dins aquesta tesi a mesura que s anava desenvolupant, per tot això vull agraır als meus companys de grup en Jorge, en Guillaume (o ja hauria dir el Dr. Sauthier?), la Mar i la nostra nouvinguda Laura i a la resta

de companys del CIN2, en Dani Ruiz, l Aitor, en Gustavo, la Miriam... l haver-me aportat idees i diferents punts de vista per estudiar els problemes d aquesta tesi.

Per acabar, però no pas menys important, vull agraır a totes aquelles persones que han format part del meu dia a dia enriquint-me com a persona i donant el toc humà que tant necessari és quan treballes amb números i molècules, per a ells, uns agraıments un xic especials: A l Albert Usagi Verdaguer les incontables hores parlant de ciència, de política, de cultura i de la vida, totes les partides jugades, i, en definitiva, tot el compartit durant aquests anys de tesi, molta sort!, al Jorge I m Mr. Wolf, and I solve problems Lobo i a la Neus Kellogg s Domingo pel seu bon humor, rialles i alegria, demostrant que per molt que es torcin les coses no costa res dur un somriure a la cara, i els viatges i sopars compartits, al Guillaume la classe Sauthier totes les bones estones i els invents amb tubs i vials, i la urbanització Bananarama. També a tots els companys que m han alegrat la tesi i han aguantat els meus constants shhhhhh! que estic fent SPFM! : L Elena, el Javi, el Pablo, la Bea, la Mireia, la Nuria, la Belen, el Joan, el Martí, la Lorena i tants altres, gràcies!.

Per últim, a la Miriam, amb qui ja he compartit 12 anys de ciència i de moments únics, i que espero que continuın sumant-ne més amb un post-doc. Gràcies per tot.

# Preface

Since I began working on my PhD thesis there has been a question appearing in my life that all my friends and family members have asked me sooner or later:

What do you work at, exactly?

During 5 years I have tried different ways to explain what I do to someone not familiar with Science: from telling them about really small record player needles able to see molecules, to water molecules running for the best place to stay while I watch them. Anyway, once I manage to somehow explain what I am working at, immediately the second and unavoidable question appears:

Why do you do that?

Why do I do that? We are scientist doing research, aren t we? We want to know more, that is it, right? Well, not exactly. People not familiar with Science do not want to hear you answering for the satisfaction of understanding Nature . What they know is that they are working hard for their money, and that a part of it is being used to pay you so you can do your research. They assume that you are using their money for something more than calming down your thirst for knowledge. In other words, they want to know the applications of your work. How do they benefit from your research. And looking at running water molecules with your small needle does not sound like for instance finding the cure for cancer, does it?

So, what brought me here, and why I think my field is just as amazing for me as it is useful for society?

I finished my degree in Chemistry at the UAB having spend some summers at the Organic Chemistry Department helping different PhD students do their lab work, so I decided to go for organic chemistry when I started doing research with a Master back in 2005. At that time my research line was synthesizing palladium complexes and characterizing them, as well as some palladium nanoparticles. One of the things I remember most from that year, are the nerves when a reaction was occurring. You studied and prepared it carefully, and after it took place, you had to characterize your product. If it was as it was expected to be, everything was OK and you moved further on. If not... well, a lot of thinking was going to come to undersand what

happened inside that Erlenmeyer. But during the moment when the product was being formed, when all the Science was taking place in that erlenmeyer, you couldn t know what was going on, you only could wait and hope it was working as expected. The funniest part of science was taking place when I was having my lunch.

I finished my Master, and looking to know about other fields in chemistry, I found myself ready for some new research. I met Dr. Jordi Fraxedas for the first time when he helped us to characterize our complexes and nanoparticules by XPS. The first thing that caught my attention was some really powerful tools he worked with I never listened about before: few amstrong sensitive tools. Wow. One day, as I was looking for a PhD project I got a phone call to have a meeting with Dr. Fraxedas, he explained to me that he had bought an AFM and was preparing all the necessary things to start working with it. He told me about the instrument and asked me if I may be interested in the field.

Curiousity is an intrinsic quality of human beings, specially in very young ones. When a kid sees something he does not know or he cannot reach, the image of him picking a stick and touching that thing with it comes to your mind. The kid uses the stick to interact with the object of his interest, to see how it reacts, what it does. The first thing I thought when Dr. Fraxedas told me what an AFM is able to do was something like  These people have a micron-stick so you can touch molecules and see what happens? are you kidding me?! . Even more, you could follow slow enough real time changes on a surface at molecular scale. With that instrument I was going to be able to see Science while it was taking place, I wouldn t miss the funny part anymore.

Shortly after I started working with Dr. Fraxedas, Dr. Albert Verdaguer joined the group after a postdoc in Berkeley with Dr. Salmeron doing research on water on surfaces at molecular level, mainly with AFM. I started working with him in this field, and I quickly realized how lucky I was to arrive short before him: immediatly he modified our AFM so it could scan without contacting the surface, enabling the sensing of surface charge in movement. Our AFM had now new features recently developed and rare to find in other laboratories.

What came after that is what you have now in your hands.

Well, that explains why I find nanoscience so interesting, but, what about its utility? Albert Einstein said once that Science is like having a clock and having the need to find out how it works without opening it. You can do whatever you want but not open it to watch what is inside. As long as Science could propose a model that explains perfectly all the behaviours of the clock, it would be sufficient, even if the model is wrong. AFM and the new instruments appearing the last decades are something close to getting tired of this old game and finally have the screwdrivers to open the clock and watch... and in some cases change the parts you don t like from it.

To think of its possibilities is like the presence of a spark inside a gunpowder barrel: the potential applications of nanoScience are at their best, begining to be conceived. Nanoscience and nanoenginyering will change the world in such a way that they will be part of our lifes in few decades: health, new material properties, energy efficiency, house caring, computers, enviromental control... the fields are as diverse as are the applications. Recently, I have seen videos of a nano-hand able to open and close depending on media conditions, and how it could be use to do non-invasive biopsies. Also a nano-robot self-propulsed inside hydrogen peroxide media, and how it moved a much bigger polymer. Every time I see this achievements, I realize how much nanoscience have to offer to the World.

So everytime that after explaining to someone what I work on, he/she does an odd face and asks me if working with AFM has any applications, I can put the best of my smiles and answer:

Take a sit, this will take a while .

# Synopsis

Water is present on almost any surface exposed to air. Both vapour and liquid water modify and determine the properties of molecules and materials (friction, adhesion, folding, reactivity...). There is still an important lack of knowledge about how water interacts with surfaces at the sub-micrometer level. Such interactions will determine the final macroscopic properties of surfaces and compounds. In addition to these facts, water also plays a central role in determining the structural conformation and the properties of biomolecules, such as proteins. During the last decade, much attention has been driven into achieving a deeper understanding in how water interacts with proteins. Nowadays, water is considered, not as the solvent media where proteins are placed, but as a proper part of the protein. Many theoretical studies have been done recently, but it is still necessary to extract more information with direct experiments. Scanning Probe Microscopy (SPM) has opened the door to powerful measures at the nanometer level that allow to follow processes and detect properties in scales not achieved until recently. Atomic Force Microscopy (AFM) is one member of the SPM family, and at the same time exhibits multiple working modes that turn it into a very versatile tool.

During this thesis work, I have studied the interaction of water with several surfaces, using different AFM operation modes. The study began by describing how water affects different crystal faces of several amino acid. Amino acids were chosen for their structural simplicity and their importance in the human-body biomolecules. The study revealed the importance that the amino acid dipoles play in their interaction with water. The structural changes on amino acid surfaces due to vapour and liquid water have been also studied. The electric field generated by some amino acid crystals has been studied as a possible factor of water freezing (as reported for some amino acids at the macroscopic level). I studied the effect of the natural electric field of several crystals on the water present in the media as a function of relative humidity and temperature.

The importance of dipole-dipole interactions in these processes drove me towards ferroelectric materials. In the last part of this thesis work, PZT2080 ferroelectric

thin films have been used because their dipoles can be oriented by means of AFM. I have used these surfaces to study the influence of their dipoles in the ordering of water.

## Objectives

This thesis work has a main objective to achieve a deeper understanding on the interaction of water molecules with surfaces relevant for life. Proteins are complex molecules, my intention was to begin with a more fundamental study, so the interaction of water with amino acids was chosen. The instrument used during the study was an AFM able to perform contact, AM-AFM and SPFM imaging; and also PFM writing and reading.

For these reasons, the main objectives of tmy study of water interaction with amino acids single crystal surfaces are:

- Crystalize and characterize several essential amino acids in the form of monocrystals.

- Find and describe the driving forces that turn an amino acids crystal surface hydrophilic or hydrophobic.

- Study and describe the structural changes that the hydrophilic surfaces undergo with the presence of water vapour.

- Study and describe the structural changes on the hydrophobic surfaces caused by the action of liquid water.

- Study the effectiveness of different amino acids single crystals to freeze water at the nm scale, relating it with the existence or not of an intrinsic electric field.

During the ongoing of this thesis work, the importance our interest was drove in the dipole−dipole interaction between water molecules and surfaces, for this reason two new objectives were added to the previous ones, involving the use of PZT2080 ferroelectrics:

- Optimize the experimental conditions to polarize a PZT2080 thin film for meanings of electrostatic interaction study.

- Describe the effect of a polarized PZT2080 surface on the nearby water molecules

as a function of relative humidity and temperature.

# Abbreviations

ABO3: Perovskite structure

AFM: Atomic Force Microscopy

AM: Amplitude Modulation

CPD: Contact Potential Difference

D: Debye, also Dextro form

$d_{xy}$: Piezoelectric coeficient

E: Electric field

EFM: Electric Force Microscopy

EUR: Euro

f: Frequency

F: Force

$F_{ES}$: Electrostatic Force

$F_f$: Friction Force

FM: Frequency Modulation

FFM: Friction Force Microscopy

IFAE: Institut de Física d Altes Energies

$k_B$: Boltzmann s constant

$k_c$: Force Constant

KPFM: Kelvin Probe Force Microscopy

LFM: Lateral Force Microscopy

MFM: Magnetic Force Microscopy

NBS: National Bureau of Standards

NSOM: Near-field scanning optical microscopy

p/l: Points per line

PFM: Piezoresponse Force Microscopy

PZT: Lead Zirconate Titanate

RH: Relative Humidity

RMS: Root Mean Square

S: Strain

SFM: Scanning Force Microscopy

SNOM: Near-field scanning optical microscopy

SPFM: Scanning Polarization Force Microscopy

SPM: Scanning Probe Microscopy

STM: Scanning Tunneling Microscopy

STO: $SrTiO_3$

UHV: Ultra High Vacuum

$V_{pp}$: Voltage peak-to-peak

: Dielectric constant

: Reference frequency

$\mu$: Dipolar moment

$\delta$: Charge density

# Contents

# Chapter 1

# INTRODUCTION

## 1.1 Introduction to SPM

### 1.1.1 Growing interest in Nanoscience

‘‘In the year 2000, when they look back at this age, they will wonder why it was not until the year 1960 that anybody began seriously to move in this direction .

Excerpt from **There s Plenty of Room at the Bottom.** 1959

‘‘With potential applications in virtually every existing industry and new applications yet to be discovered, nanoscale science and technology will no doubt emerge as one of the major drivers of economic growth in the first part of the new millennium .

Excerpt from **Small Wonders, Endless Frontiers.** 2002

According to the Massachusetts Institute of Technology (MIT), the definition of nanosciense is (see MIT webpage in references) *Nanoscience refers to the science and manipulation of chemical and biological structures with dimensions in the range from 1 to 100 nanometers. Nanoscience building blocks range from a few hundred atoms to millions of atoms. On this scale, new properties (electrical, mechanical, optical, chemical, and biological) that are fundamentally different from bulk or molecular properties can emerge. Nanoscience is about creating new chemical and biological nanostructures, uncovering and understanding their novel properties, and ultimately about learning how to organize these new nanostructures into larger and more complex functional structures and devices* And follows *Nanoscience is a new way of thinking about building up complex materials and devices by exquisite control of the*

*functionality of matter and its assembly at the nanometer-length scale. Nanoscience inherently bridges disciplinary boundaries. The "nano" length scale requires the involvement of chemical concepts at the atomic and molecular level. Devices and other functional structures engineered at the nano-scale often use light or electrical signals either to interact with the macroscopic world, or because the devices are designed to process information, with photons or electrons. The vision of nanoscience ultimately combines the science and engineering of man-made and biological entities, controlled at the nanometer scale, and assembled into complex, engineered structures that can interact with their surroundings at dimensions ranging from that of molecules to that of humans and beyond.*

Nanoscience and Nanotechnology have opened new doors to science and fantastic claims have been made about the smallest computers, medical breakthroughs, materials with new properties and a long, long list. Nanotechnology is expected to appear in products such as sport accessories, clothes that stay clean, self-cleaning cars, food, cosmetics, ambiental control... Interest in Nanoscience is a fact nowdays: governments are investing billions of dollars into nanoscience research. In 2006, the worldwide investments in nanotechnology research and development was estimated to be $12.4 billion. The American nanotechnology effort is called the National Nanotechnology Inititative (see National Nanotechnology Initiative webpage on references) and the European Union has identified nanotechnology as an important research area and dedicated 1300 million EUR on nanotechnology research in the period 2002 -2006 (see European Comission web page on references).

One of the first scientist to point out potential benefits of nanoscience and nanotechnology was Richard Feynman. In the now famous speech he gave in 1959 about the miniaturisation of devices, entitled *There's plenty of room at the bottom*, Feynman exposed what can be summarized as *Science doing the right thing in the wrong direction* (Feynman, 1959). At that time, science of the small worked in what is nowadays called the top-down direction , that is, miniaturisating structures more and more. In those years, electric motors of the size of your little finger nail were just proudly invented. What Feynman exposed was the feeling that science was working in the wrong direction and that in order to build a really small device one

should start working with even smallest parts and build up it with them, the so-called bottom-up direction . When science was working within the order of the millimeter Feynman started talking about angstrongs and microns and about using single atoms as data recording media.

Once this idea was conceived, the only limitation was purely instrumental and began to be solved with the invention of Scanning Probe Microscopy (SPM) techniques. Between 1965 and 1971 Russell Young and colleagues invented, at the National Bureau of Standards (NBS), the topografiner (Young, 1971), considered the first SPM instrument since it fulfills the four essential elements that distinguish scanning probe microscopes from other microscopes:

(1) A very sharp mechanical probe, the tip of which is maintained in close proximity to the sample surface.

(2) Detection of a surface property (in the topografiner what is used is the phenomenon known as field emission) that changes rapidly in the vicinity of the surface and therefore provides a very sensitive indicator of the tip-sample distance.

(3) Use of an electronic feedback system to control the tip-sample distance or to maintain a controlled low-force contact essential to prevent damage to the sharp tip and sample.

(4) The ability to position the tip with respect to the sample in three dimensions with sub-nanometer resolution, as for example through the use of piezoelectric devices.

The imaging capability of the topografiner was demonstrated on a 180 line/mm diffraction grating replica (Fig. 1.1). Young et al. estimated the resolution to be 3 nm perpendicular to the surface and 400 nm in the plane. The estimated ultimate resolution perpendicular to the surface was 0.3 nm (one atomic layer), limited by noise, and 20 nm in the lateral direction, limited by tip radius (Young, Ward and Scire, 1972).

SPM reached worldwide interest with the invention of the Scanning Tunneling Microscope (STM) in 1981 at IBM Zurich. Their inventors, Gerd Binnig and Heinrich Rohrer were awarded the Nobel Prize in Physics in 1986 *"for their design of the scanning tunneling microscope"*. (Binnig et al., *Phys. Rev. Lett.*, 1983 has

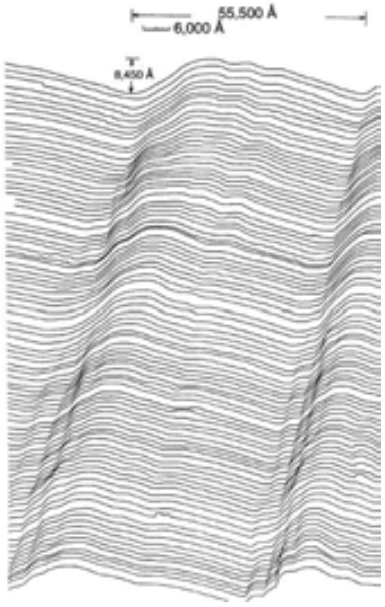


Figure 1.1: First Scanning Probe image: Topographic map of a 180-line-per-mm diffraction-grating replica, obtained with the Topografiner. Reproduced from Young, Ward and Scire, 1972.

around 1,300 citations, other related works are Binnig et al., *Appl. Phys. Lett.*, 1982; Becker et al., 1985; Binnig and Rohrer, 1986). This instrument uses the same principles as the topografiner, but is based on the tunnelling effect instead of field emission, achieving a much better resolution. The lateral and height resolution for an STM are typically 0.1 and 0.01 nm, respectively. With such resolutions, individual atoms are routinely imaged and manipulated (Chen, 1993; Bai, 2000). The principal drawback of STM is its limitation to conducting surfaces, mostly metals. Although the STM itself does not need vacuum to operate (it works in air as well as under liquids), ultrahigh vacuum (UHV) is required to avoid contamination of the samples from the surrounding medium.

Once the principles of SPM were published, much atention was driven into this new technique and a brand new way of doing Science was born: The Nanoscience.

### 1.1.2 Atomic Force Microscopy

Once the potential of STM was proved it was a matter of time for new variations of SPM instruments to appear. Just as the topografiner uses the field emission and the STM uses the tunneling effect other properties can be used to do the sensing of

the surface and obtain its topography as well as some other properties at the same time. Since the invention of the STM a large number of different SPM microscopies have been developed: Atomic Force Microscopy (AFM) (Binnig, Quate and Gerber, 1986), Electrostatic Force Microscopy (EFM) (Weaver and Abraham, 1991), Kelvin Prove Force Microscopy (KPFM) (Nonnenmacher, O Boyle and Wickramasinghe, 1991) , Magnetic Force Microscopy (MFM), (Hartmann, 1988) , Near-Field Scanning Optical Microscopy (NSOM) (Betzig et al. 1991) as well as techniques that were extended with the use of SPM techniques such as electrochemical STM (Itaya, 1998). They use contact repulsion, electrostatic interactions, contact potential difference, magnetic interactions and the properties of evanescent waves respectively as surface sensing property. The broad AFM techniques family will be explained in more detail in the following sections.

### Brief description and History

The AFM is a member of the SPM family and its roots lie on the STM. As STM, AFM can be operated under natural conditions and one of the main advantages of AFM respect to other SPM techniques consists in no need for the sample to be placed under destructive artificial conditions such as drying, coating with metal, vacuum or freezing. It is therefore a versatile and universal technique (Oncins, 2007).

Invented in 1986 by Binnig et al. (Binnig, Quate and Gerber, 1986), the first AFM worked in the now called Contact mode: a tip mounted onto the end of a flexible cantilever interacts interacts in contact with the surface of the sample (usually scanning it in a raster lines pattern) and reveals the sample topography. Due to the repulsive force acting upon the tip, a deflection of the flexible cantilever is produced, AFM reads (usually by means of a laser reflected on the backside of the cantilever and redirected to a photodiode (fig. 1.2) and corrects (by means of piezo systems) this deflection so to keep it constant by changing the relative z−position, and thus, extracting the topography. These changes on the deflection are proportional to the z−height variations of the topography and so the sample s topography is revealed (fig. 1.3).

When the tip scans over the surface, variations on its topography originate

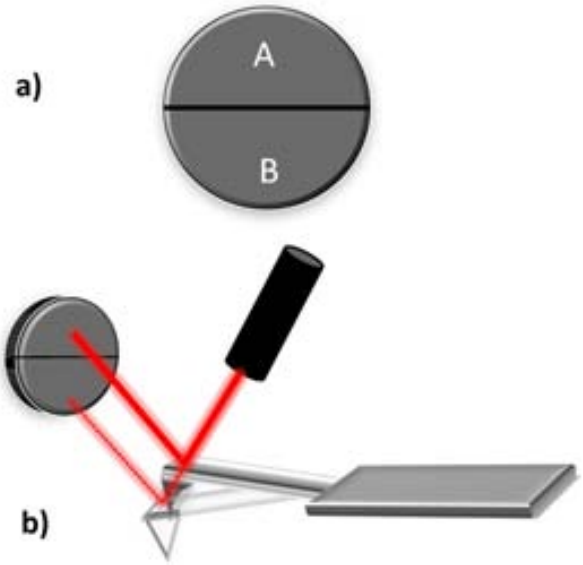


Figure 1.2: Two sectors photodiodes are used to read the cantilever s deflection. a) The signal measured on the B subsection is substracted from the signal measured on the A subsection (A-B) to obtain the cantilever s deflection. b) When the cantilever changes its deflection the reflected laser spot moves its position on the photodiode.

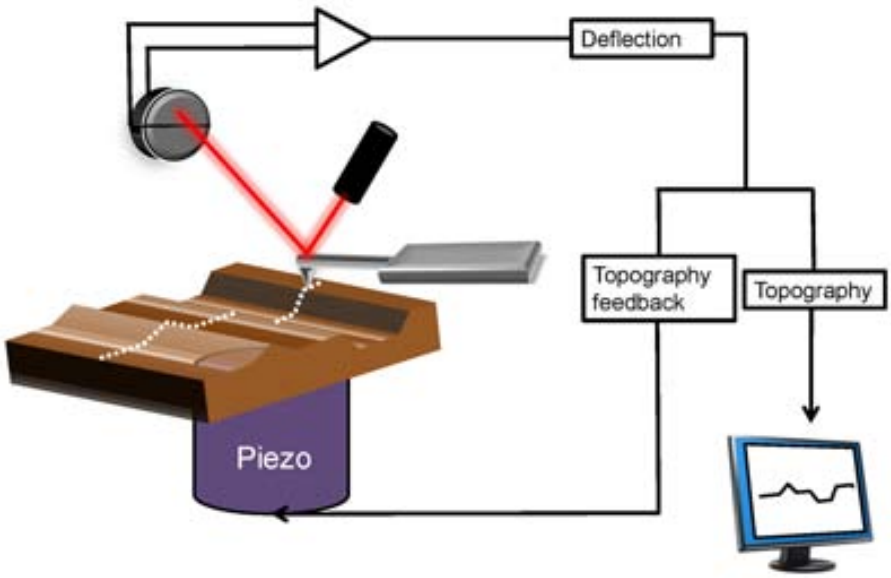


Figure 1.3: In the Contact mode, the AFM probe scans the surface in contact with it. Changes on surface topography produce changes on the cantilever s deflection. This is read and used to to readjust the z−value of the piezo and thus, reveals the sample topography.

changes on the deflection of the cantilever, small changes on the cantilever s deflection will produce measurable displacement of the laser spot on the photodiode, so the deflection can be measured with precison (also the cantilever s torsion can

be measured if the photodiode is a four−quadrant detector, see Lateral Force Microscopy). To keep the measurements stable, a feedback system is applied to a piezoelectric system, compensating these deflection variations by aproaching or retracting the tip along the z−direction to keep the cantilever s deflection constant to a desired value, called setpoint. This piezoelectric system is a common and important part of all SPM instruments, a brief description will be now provided.

**Piezoelectrics**

The piezoelectric scanner, sometimes called piezodrive or simply piezo is a central part of all the SPM instruments, and can move in a very precise way (sub Å precision) the sample and or the cantilever (see University of Leiden Web page at references). It is based on the piezoelectric effect, discovered by Pierre Curie and Jacques Curie about 100 years before the invention of the STM. They found that on certain materials, when a weight was applied to generate vertical tension, an electrical charge was detected by an electrometer. A few months later, Lippman predicted the existence of the inverse piezoelectric effect: by applying a voltage, a deformation should be observed. This deformation occurs in the three directions x, y and z, in the standard convention, these directions are labeled as 1, 2, and 3, respectively. The measure of the strain in a given direction (i.e. for z direction, the strain S would be $S_3$) is defined as the ratio between the elongation or contraction ($\delta$z) when applying a given voltage, and the initial length (z) in absence of this external voltage:

$$S_3 = \frac{\delta z}{z} \tag{1.1}$$

The piezoelectric coefficients are defined as the ratio between the strain component and the applied electrical field of the same (or another) component, for example, for the strain component at z, and the electric field also at component z:

$$d_{33} = \frac{S_3}{E_3} \tag{1.2}$$

Because strain is a dimensionless quantity, the piezoelectric coefficients have dimensions of meters/volt in SI units. Commercial piezoelectrics have d values of severeal Å V (as an example, EBL provides piezoceramic tubes with $d_{33}$ values

ranging from 2.20 Å V to 5.83 Å V at 293°K and different PZT with $d_{33}$ values ranging from 15 Å V to 65 Å V).

**AFM operational modes**

Nowadays, AFM can be used in different operational modes (García and Pérez, 2002; Jalili and Laxminarayana, 2004; NT MDT Web page) based on the same described principle: a sharp tip interacts locally with the sample s surface, producing the deflection or the relaxing of a flexible cantilever, and this is used to obtain information relative to the sample s surface. These different modes can read different sample s properties, and affect the sample in a wide range of grades. In this thesis I have used several of these AFM modes, they will be described next. At the end of the section a brief description of some AFM modes not used in the framework of the thesis will be provided.

#### 1.1.2.1 Contact mode

Contact mode (also called Constant Force mode) has been briefly described in the previous subsection and was the first and most basic AFM mode. As described, in this mode the tip scans the sample in contact with its surface (and never deattaching from it), the force that it exerts on the tip is repulsive with a mean value of the order of $10^{-9}$ N (this force is set by pushing the cantilever against the sample surface with a piezoelectric positioning element) and produces a deflection on the cantilever. This deflection is sensed (using a laser reflected on the back of the cantilever and directed to a photodetector) and is compared in a dc feedback amplifier; the piezoelectric system is adjuted so to keep the deflection constant to some desired value (called setpoint) (fig. 1.4).

As the probe scans the sample in raster lines (fig. 1.5), the voltage that the feedback amplifier applies to the piezoelectric is a measure of the height of features on the sample surface. It is displayed as a function of the lateral position of the sample, also controlled by piezoelectrics.

Working with AFM Contact mode have some intrinsic problems caused by excessive tracking forces applied by the probe to the sample (Normal force). Nowadays,

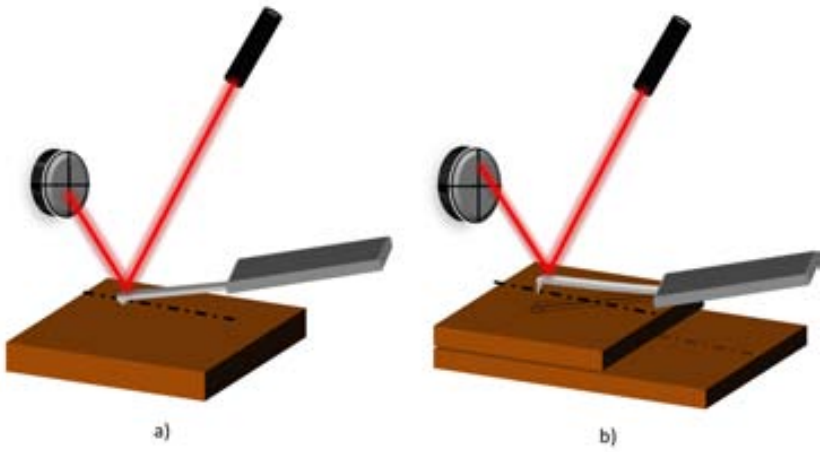


Figure 1.4: AFM Contact mode. a) The deflection of the cantilever is monitored reading the position of the reflected laser. b) Changes in surface topography (an increase in height due to a step in the figure) make the cantilever change its deflection and so the position of the reflected laser changes as well.

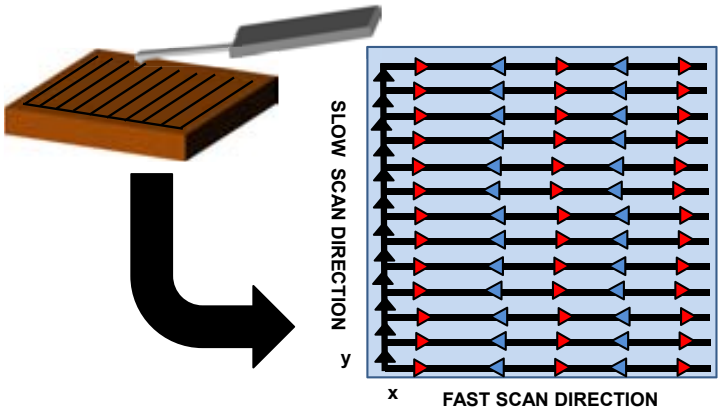


Figure 1.5: AFM images acquisition is performed in the form of raster lines scanned on the surface. Forward and backward directions compose the fast scan direction (in this work is arbitrary chosen as x direction). The slow scan direction is therefore the y direction. For every scanned line both forward (red triangles) and backward (blue triangles) data are acquired.

probes with force spring constant values ($k_c$) values ranging from 300 to 0.01 nN/nm are commercially available, so one may want to use cantilevers with low $k_c$ to image soft samples. When it comes to biological samples damage, the adverse effects can be reduced by minimizing tracking force of the probe on the sample, but there are practical limits to the magnitude of the force that can be controlled by the user during operation in ambient environments, as a consequence this mode is mainly adequate to scan hard materials as metals, oxides, minerals and certain polymeric

structures.

Water necks formation can be another problem when working in the AFM Contact mode: althought some instruments operate in UHV, the majority operate at ambient conditions. As will be explained in more detail in next section, under ambient conditions surfaces are covered by a layer of adsorbed molecules (mostly water but also hydrocarbons) which is $\sim$2.5 Å thick when Relative Humidity (RH) is around 30%-50% (Amrein and Muller, 1999). This water layer is also covering the AFM probe, and when the tip and the sample are close enough a water meniscus forms between them and the cantilever experiments a pulling force toward the sample surface. The magnitude of this force depends on the details of the probe geometry and the tip and sample nature, but is typically on the order of tens of nN (Eastman and Zhu, 1996). Due to this pulling force, soft samples may result damaged by the probe during the final part of the approach step. In those cases, the Contact mode can be performed inside liquid media neutralizing these forces and reducting other attractive forces like van der Waals interactions, performing in this way an approximation to the sample with no pulling forces. Technologically or biologically important processes at liquid solid interfaces are studied in this immersed Contact mode (Hemayet, Ying and Raymond, 2011). However, there are also some disadvantages involved with working in liquids such as sample damage on hydrated and vulnerable biological samples.

In addition, a large class of samples, including semiconductors and insulators, can trap electrostatic charge (partially dissipated and screened when working in liquid) (Marchi et al., 2008), this charge can contribute to additional substantial attractive forces between the probe and sample (Johnson and Lenhoff, 1996).

All of these forces combine to define a minimum normal force that can be controllably applied by the probe to the sample. Several normal force calibration techniques are available in the literature (Neumeister and Ducker, 1994; Sader et al., 1995; Ekwinska and Rymuza, 2009).

Also, the application of this normal force over a sample while the tip is performig raster lines in contact, originates a frictional force ($F_f$), these kind of frictional forces are more aggressive with the sample than the Normal force, and both of

them can damage the tip, affect the sample in several ways and distort the resulting data (Guilemany, 2001; Sundararajan and Bhushan, 2001; Chung, Lee and Kim, 2005). But far from being an undesirable side effect, frictional force turn out to be a remarkable source of information, as will be explained in the next.

#### 1.1.2.2 Lateral Force Microscopy

Lateral Force Microscopy (LFM), also called Friction Force Microscopy (FFM), is used to obtain the frictional properties of surfaces in the micro- to nanometric range (Socoliuc et al., 2006; Carpick, 2006; Park et al., 2006; Xie et al., 2008). This mode is used along with Contact mode during one scan to characterize your samples more completely, distinguishing areas with different friction coefficient and also to obtain edge−enhanced images of any surface.

The underlying mechanism of this mode is based on when the probe scans the sample in the described Contact mode a torsion of the cantilever parallel to the fast scan direction is produced along with the described deflection. With minor deflections, the angle of torsion is proportional to the lateral force, and related with the local friction coeficient in the nano range (Lin, 2011).

The required equipment is the same described for the Contact mode, but the photodetector must have four quadrants (fig. 1.6), so that the torsion of the cantilever can be sensed.

Friction force values are obtained performing what is called a friction loop (fig. 1.7): a single line is scanned from right to left (from now on called forward direction to avoid direction misspelling, which is arbitrary) and then from left to right (from now on, backward direction). The total friction energy dissipated during the scanning process is proportional to the area of the loop (fig. 1.7) and the average $F_f$ value in a certain scanned line is (Oncins, 2007):

$$F_f = \frac{F_f(forward) - F_f(backward)}{2} \tag{1.3}$$

If we define $\alpha$ as the angle formed by the surface and the cantilever normal (as shown in fig. 1.9), larger friction coefficients between the tip and the surface will have larger $F_f$ and will lead to larger $\alpha$ values, this way, two regions with identical

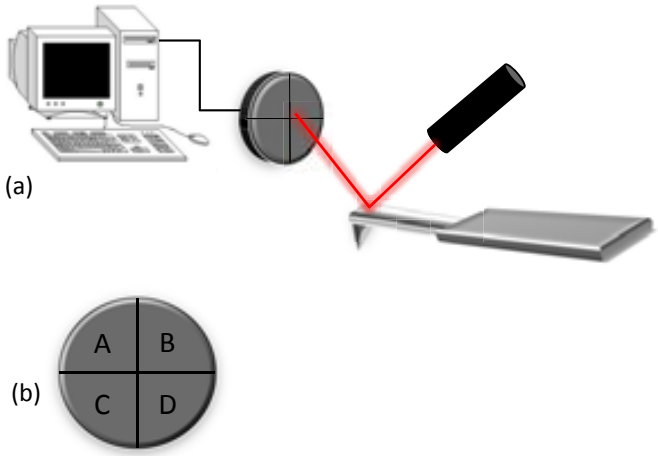


Figure 1.6: a) The four-sectors photodetector extracts the deflection information following the same principle than a two-sectors photodetector but can also obtain the torsion of the cantilever. b) Deflection information is obtained by the difference between the upper subsection (A+B) and the lower one (C+D). Torsion of the cantilever is obtained by the difference of the left subsection (A+C) and the right one (B+D).

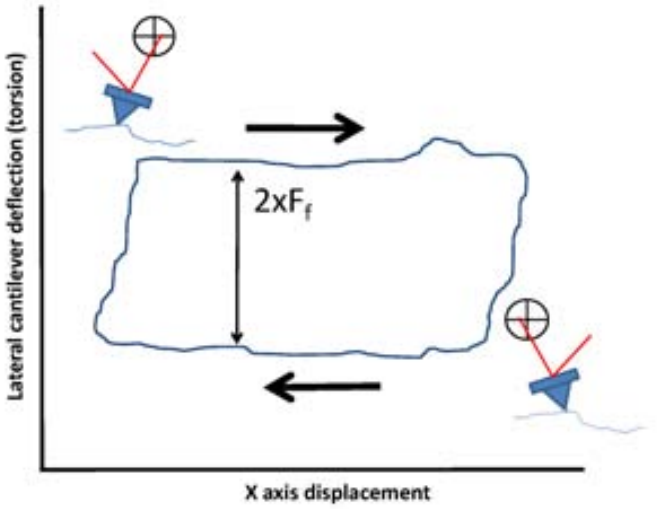


Figure 1.7: Cantilever's torsion vs. x displacement while a friction loop is obtained. The area of the loop is proportional to the total energy dissipated during the process and $F_f$ value in a certain position is proportional to the half width of the friction loop.

topography but different friction coefficient be sensed (Liley et al., 1998; Schonherr et al. 2000; Matsumoto et al., 2003; Okita and Miura, 2003)(fig. 1.8), this is not possible if working only in the Contact mode. But if the surface is not absolutely flat, such an interpretation is complicated.

If the friction coefficient has no dependency on the scanning direction and both

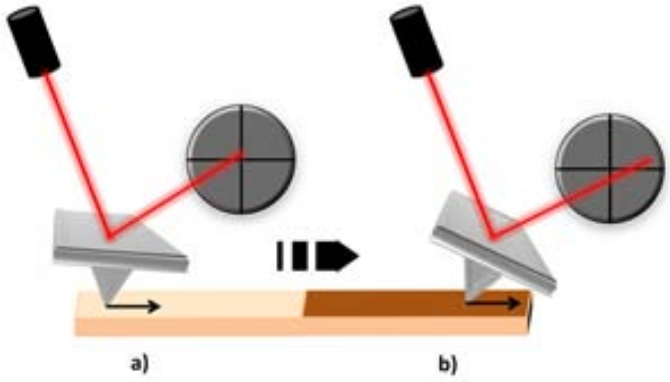


Figure 1.8: AFM frictional sensing of two domains with equal topography. a) When the tip scans over a zone with a low friction coeficient (light zone) its lateral torsion is small (i.e., (A+C)-(B+D) photodiode sectors is a small value). b) when the tip scans over a zone with a high friction coeficient (darker zone) its lateral torsion is more pronounced, (i.e., (A+C)-(B+D) is a larger value).

cantilever normal force and scan speed are kept constant, an inversion of the scan direction (from forward to backward) will lead to lateral forces of same absolute value but opposite sign (figs. 1.9 and 1.10).

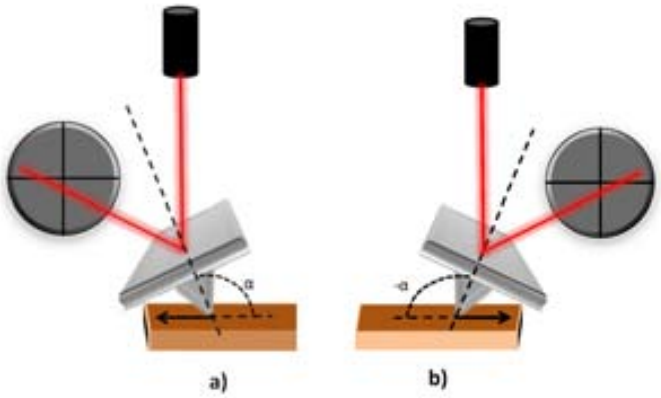


Figure 1.9: a) When surface friction coeficients are not direction dependent the probe senses the same friction coeficient on a given point both in the forward and backward directions. b) This originates torsions with the same absolute value but oposite sign. In other words, at a given point, a torsion of $\alpha$ degrees in the forward direction will have as response a torsion of $-\alpha$ degrees in the backward direction.

However, some surfaces exhibit friction coefficents which depend on the scan direction, in these cases, cantilever torsion asymmetry appears between forward and backward scanning (fig. 1.11).

Such asymmetric effect has been reported for organic ferroelectric crystals (Bluhm,

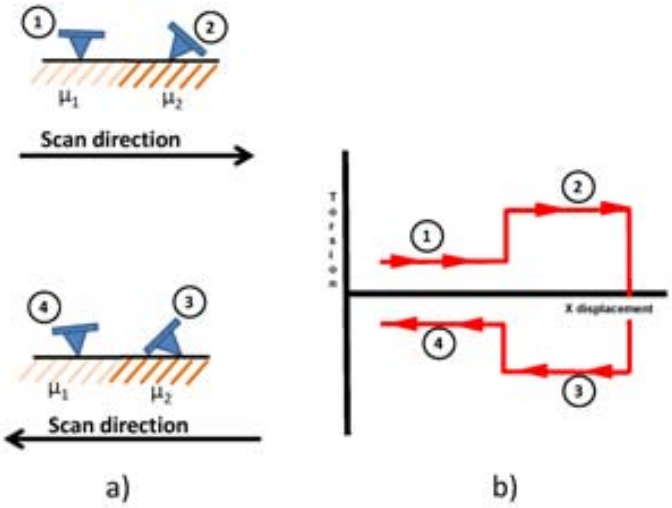


Figure 1.10: When the friction coefficients have no direction dependency, trace and retrace lines produce torsions of the same magnitude but opposite sign.

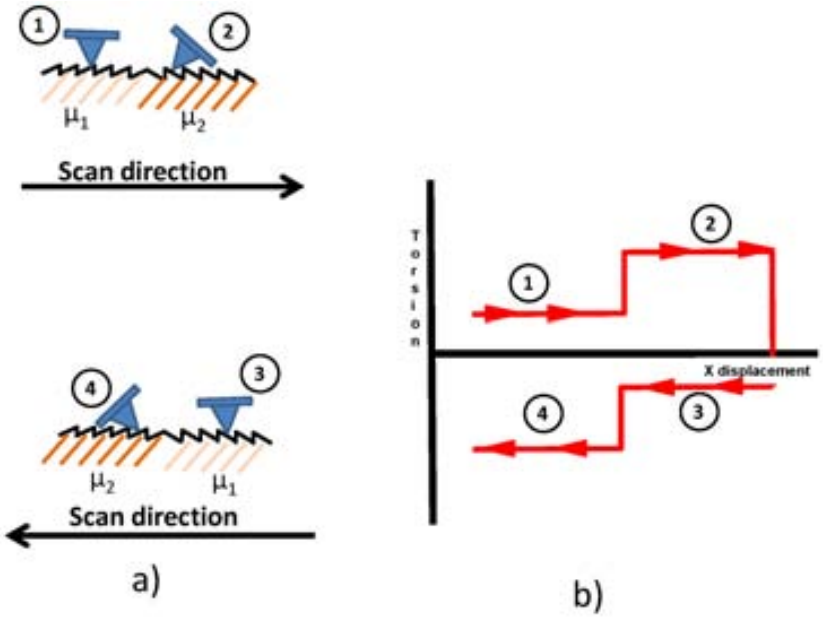


Figure 1.11: Effect of friction coeficient asymmetry on cantilever s torsion. $\mu_1$ represents a lower friction coeficient than $\mu_2$. a) When direction dependency exists the friction coeficients sensed by the probe in the forward and backward directions are not equal (this is represented as a sawed terrace) so cantilever absolute value of torsion is not the same for opposite scan directions at a given point. b) Following the previous example, a torsion in the forward direction of $\alpha$ degrees at a given point, will have as response a torsion in the backward direction of $-\beta$ degrees at the same point.

Schwarz and Wiesendanger, 1998), lipid monolayers on mica (Liley et al., 1998), alkanethiol SAMs domains on gold (Munuera, Barrena and Ocal, 2007), and for cleavage surfaces of alkaline earth sulfate crystals (Shindo et al., 1999). The origin

is an asymmetric tip−surface interaction potential (illustrated by a saw-tooth-like potential by Bluhm et al., 1998) ascribed either to domains with the same structure but opposite molecular tilt directions or to surfaces with a mirror plane surface structure.

LFM is a versatile tool that allows dilucidating the nature of different surface otherwise not differentiated by AFM Contact mode. Also, Lateral Force measuring easily provides the molecular and atomic resolution image of surfaces with more resolution degree than Contact mode.

#### 1.1.2.3 Amplitude Modulation Mode

Amplitude Modulation Mode (AM-AFM mode), also known as Tapping Mode (TappingMode is a registered trademark of Digital Instruments, Veeco Metrology Group) was a key advance in the AFM family. In this mode the cantilever is oscillating at or near its resonant frequency using a piezoelectric as the mechanical excitation source: the piezoelectric motion causes the cantilever to oscillate with a high amplitude (usually tens of nm) when the tip is not in contact with the surface (the so−called free amplitude). When the tip approaches the surface different long range attractive interactions arise, but the oscillation is high enough to overcome them, so the probe keeps oscillating, although with an amplitude slightly smaller than its free amplitude. Finally, the tip begins to slightly touch or tap the surface, and the amplitude of its oscillation is again reduced due to the interactions between probe and sample (Hoper et al., 1995; García and Pérez, 2002) (fig. 1.12). Once the tip is tapping on the surface, in the so−called semi−contact range, the system is ready to start the scanning ofthe sample.

During the scanning operation, the vertically oscillating tip alternately contacts the surface and lifts off at the resonant frequency of the cantilever (generally at a frequency between of 50 and 500 KHz). When changes on the surface topography reduces the distance between the cantilever and the surface, it has less room to oscillate and the amplitude of oscillation decreases, the opposite happens when the tip scans over a zone where the cantilever is farther from the surface, then the cantilever has more room to oscillate and the amplitude increases, approaching the maximum

free air amplitude (fig. 1.12). Using the signal coming from the photodetector, the system keeps the amplitude of the vibration constant to a desired setpoint (again by means of piezoelectric z−motion feedback) in order to keep the distance between the probe and the surface constant, and thus, topography is revealed (García and Pérez, 2002) (fig. 1.13).

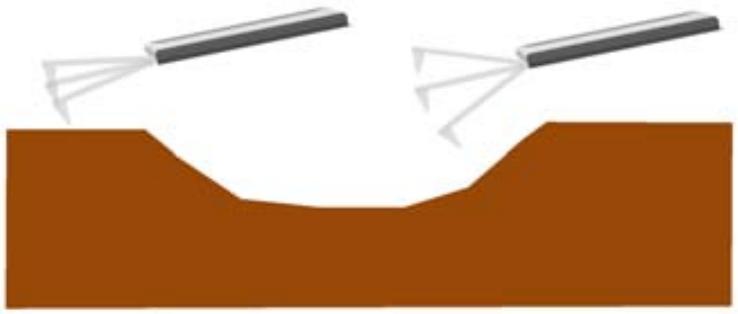

Figure 1.12: In AM-AFM Mode the amplitude of the oscillation changes when the cantilever has more (or less) room to oscillate. This is used to adjust the z−postion of the sample respect to the probe, extracting its topography.

The AM-AFM mode has poorer resolution than the Contact mode because the average distance between the tip and the sample is large (thus the interaction is weaker). Nevertheless, unlike Contact mode, sample degradation due to mechanical contact is strongly reduced, also surface material is not pulled sideways by shear forces (since the applied force is always vertical), minimazing in this way the lateral forces and being a suitable mode to image soft organic surfaces. Finally, water spreading is highly reduced because AM-AFM usually has sufficient oscillation amplitude to overcome the tip−sample adhesion forces.

Usually, AM-AFM probes $k_c$ may be in the range of 1-100 N/m (larger than those used for Contact mode). Alternatively, very soft cantilevers can be used to get good results in fluid, with $k_c$ typically around 0.1 N/m. The AM-AFM operation mode in fluid has the same described advantages for air or vacuum. However, imaging in a fluid medium tends to damp the cantilever s normal resonant frequency: when an appropriate frequency is selected (usually in the range of 5 to 40 KHz) the amplitude of the cantilever will decrease even more when the tip begins to tap the sample.

LFM imaging is not possible when working with the AM-AFM since no lateral

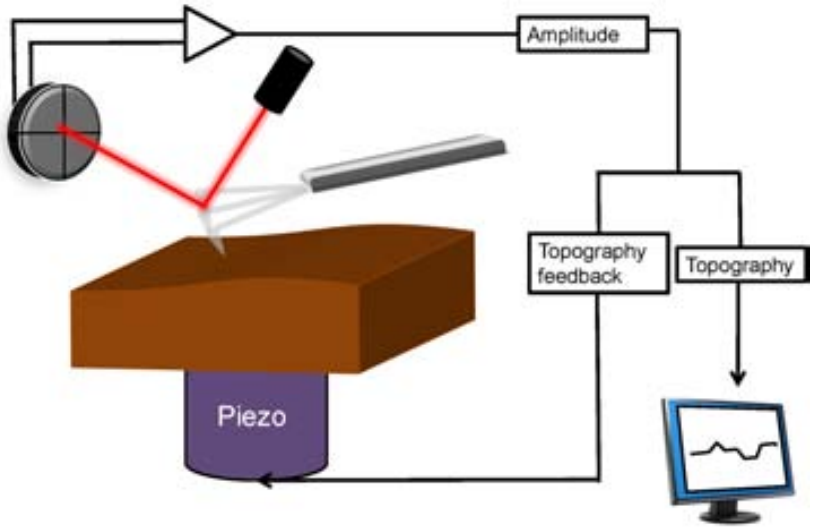


Figure 1.13: In AM-AFM Mode the tip scans the surface tapping it at a chosen amplitude. The system uses the cantilever s amplitude as the feedback signal and keeps it constant adjusting the relative z value of the tip respect to the sample.

forces are present in this mode, but due to probe−sample forces the ressonant frequency of the cantilever is shifted from the excitation signal and phase imaging is acquired in a single pass along with the topography. Phase imaging in the normal semi−contact AM-AFM is difficult to interpret but if the sample surface is not homogeneous, it must be phase shift when moving from a domain to another and the distribution of the phase shift over the sample surface reflects distribution of the sample material characteristics (fig. 1.14). Phase imaging gives valuable information for a wide range of applications, in some cases giving contrast where none was anticipated from the material properties. This mode is used, among others, for biological objects and specimens with magnetic and electric properties.

Finally, I would like to mention that our group, in collaboration with Dr. Santos from the Masdar Institute (Abu Dhabi) is studying the underlying reasons that make possible a real non−contact AM-AFM mode, with the oscillating probe scanning over the surface and never touching it. Although phase imaging in such mode is easily interpred as difference in the attractive and repulsive forces acting between the sample and the tip, topography data can lead to important deviations from real values, for this reason more research is being done in this field that should be soon published.

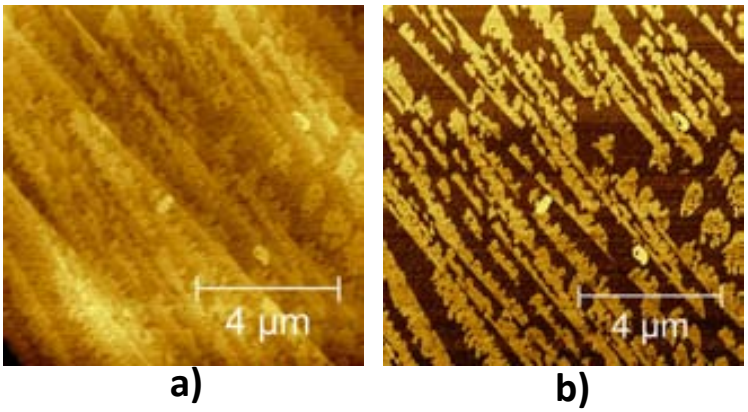


Figure 1.14: AM-AFM phase image displays differences in sample s inhomegenity. a) AM-AFM topography image of a calcite single crystal in contact with vapour water. b) AM-AFM phase image shows evident differences between wetted (dark) and no wetted regions (bright).

#### 1.1.2.4 Electrostatic Force Microscopy

Electrostatic Force Microscopy (EFM) maps vertical electric properties on a sample surface by measuring the electrostatic force between the surface and a grounded or dc biased AFM conductive probe. EFM images contain information about electric properties such as the surface potential of conducting materials, charge distributions of insulating materials, and electric domains of ferroelectric materials. The field due to trapped charges on or beneath the sample surface is often sufficiently large to generate contrast in an EFM image. Otherwise, a field can be induced by applying a dc voltage between the tip and the sample.

The classical EFM mode is the Non-Contact EFM, based on a two-pass technique. During the first pass, while the tip is grounded the cantilever performs a topographic adquisition of a scan line in the previously described AM mode; during the second pass (called lift mode) the cantilever is lifted few nm, piezodriven at resonant frequency and another scan line over the previously acquired line is obtained keeping constant the separation from the surface. Capacitive tip−sample electric force (or rather its derivative) leads to resonance frequency, amplitude and phase shifts. Both the amplitude and (or) the phase of oscillation deviations can be measured, and electric potential distribution over the sample surface is then imaged. Phase signal detection is preferred over the amplitude because the cantilever s phase response is less susceptible to height variations and it also is faster in response than

the amplitude response.

However, a single pass technique is also possible using attractive forces between the tip and the sample surface that are always present (like the van der Waals forces). The magnitude of these attractive forces changes according to the tip−sample distance, and therefore can be used to measure the surface topography in a real non−contact one−pass EFM technique where the obtained signal contains both information of surface topography and information of surface electrical property generated by the attractive and electrostatic forces, respectively. The key to successful EFM imaging in this one-pass mode lies in the isolation of the electrostatic interaction from the entire signal, which includes the use of lock-in systems and amplifiers (fig. 1.15). But it is important to remark that the use of van der Waals forces for real non−contact imaging is difficult and not always practical since this weak interaction implies a very close proximity of the tip to the surface (the force is about 1 nN at 10Å distance for a 500Å tip radius), which often results in instabilities (jump−to−contact). For this reason, the lift mode EFM is broadly used over this last one.

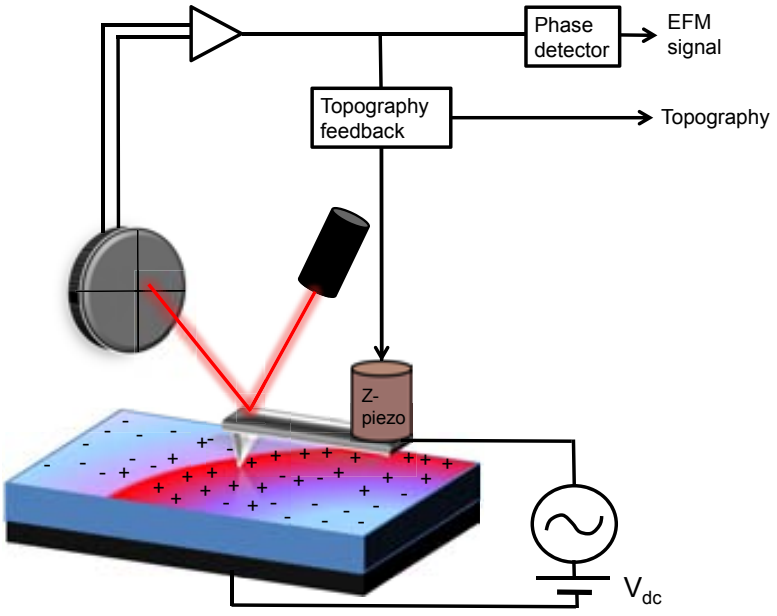


Figure 1.15: AFM EFM the non−contact one−pass mode, where topographic and electrostatic properties are obtained during the same sweep, using van der Waals and electrostatic interaction forces respectively.

#### 1.1.2.5 Kelvin Probe Force Microscopy Mode

Kelvin Probe Force Microscopy (KPFM) mode, but also known as Surface Potencial Microscopy, was proposed by Nonnenmacher in 1991 and introduced a new and powerful feature to the AFM family: measure contact potential difference CPD (also known as contact electromotive force, contact potential and Volta effect), the potential difference that exists across the space between two materials (in this case between the probe and the sample), obtaining information about charges and dipoles distribution at the surface.

The band gap between the vacuum and the Fermi levels, namely the work function ♯ , differs from one material to another. The difference between the work function of the tip and the sample is what we call the CPD:

$$CPD = \sharp_{sample} - \sharp_{tip} \tag{1.4}$$

The KPFM Mode can measure the CPD between the AFM tip and the sample using a two-steps mode similar to that of the EFM. In the first step a conductive tapping tip scans a line in AM-AFM Mode on the surface of the sample to obtain its topography, just the same than in EFM. During the lift mode the tip is lifted few tens of nm height from the sample surface to detect the electric surface potential ♯ . During this second pass the cantilever is no longer excited mechanically (like in EFM mode) but electrically by applying a voltage $V_{tip}$ containing dc and ac components:

$$V_{tip} = V_{dc} + V_{ac}\sin(\ \ t) \tag{1.5}$$

the induced electrostatic force $F_{ES}$ between the tip and the sample by the electric field is given by:

$$F_{ES} = \frac{1}{2}\frac{dC}{dz}[V_{tip} - \sharp\,]^2 \tag{1.6}$$

where C and z are the capacitance and distance between the tip and the sample, respectively. This equation assumes a parallel-plate capacitor geometry (other geometries can be also considered, although they require more complicate models). If voltage is divided in its dc and ac contributions:

$$F_{ES} = \frac{1}{2}\frac{dC}{dz}[(V_{dc} + V_{ac}\sin \quad t) - (\sharp_{\,sample} - \sharp_{\,tip})]^2 \tag{1.7}$$

If developed it leads to:

$$F_{ES} = F_{dc} + F_{\omega} + F_{2\omega} \tag{1.8}$$

where:

$$F_{dc} = \frac{1}{2}\frac{dC}{dz}[\frac{V_{dc} - (\sharp_{\,sample} - \sharp_{\,tip})^2}{2} + \frac{V_{ac}^2}{4}] \tag{1.9}$$

$$F_{\omega} = \frac{1}{2}\frac{dC}{dz}V_{ac} \;\; V_{dc} - (\sharp_{\,sample} - \sharp_{\,tip}) \;\; \sin( \;\; t) \tag{1.10}$$

$$F_{2\omega} = \frac{1}{2}\frac{dC}{dz}\frac{V_{ac}^2}{4}\cos(2 \;\; t) \tag{1.11}$$

Equation 1.10 is called the component signal and is the key function to understand KPFM. If $V_{dc}$ is equal to $\sharp_{\,sample} - \sharp_{\,tip}$, the value of component signal becomes zero. Therefore, we can obtain the intended potential by adjusting dc offset bias $V_{dc}$ to nul the component signal. If $\frac{dC}{dz}$ is kept constant by keeping constant the tip-sample separation, component is only sensitive to static charges and static dipoles (fig. 1.16).

#### 1.1.2.6 Scanning Polarization Force Microscopy Mode

Both EFM and KPFM are mostly used with the lift mode, due to jump-to-contact problems if van der Waals forces are used to perform non-contact imaging. Scanning Polarization Force Microscopy (SPFM) Mode is a variation of the KPFM Mode, its main feature is to scan samples in real non contact, avoiding the jump-to-contact problems.

Topographic images are obtained as well as contact potential and polarizability over the surface, it is highly indicated for the imaging of soft or weakly bound materials that could be easily damaged or removed by the tip, as well as for liquid adsorbates and liquid surfaces (materials that are extremely difficult to be imaged with modes based in contact, permanent or intermitent, without being perturbed).

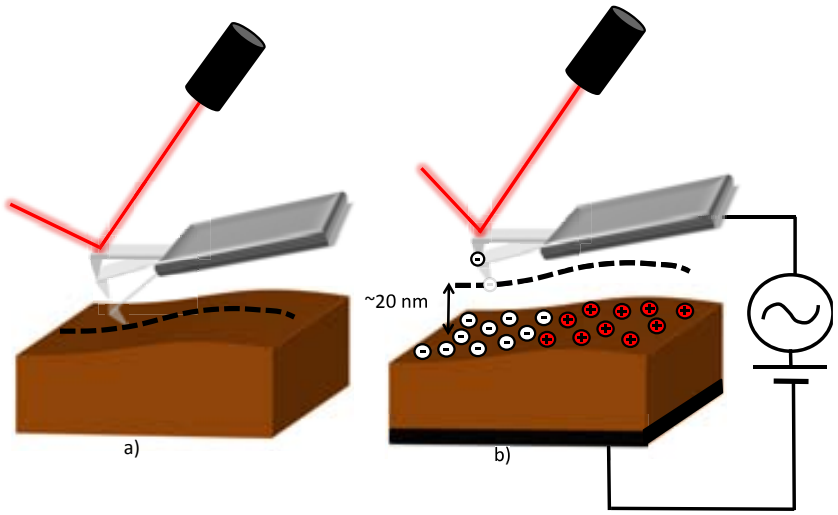


Figure 1.16: KPFM Mode is a two steps technique. a) the grounded conductive tip scans the surface in AM-AFM Mode to obtain its topography. b) The cantilever is lifted and a voltage is applied to the tip in order to sense the CPD as it scans the surface at a constant height.

It is very important to underline the possibilites that this operation mode offers. Not only the possibility of not disturb the sample while adquiring the images but also resolving the jump-to-contact problems generated when van der Waals forces are used to perform non−contact images. When using van der Waals interactions to perform non-contact images, water necks are easily formed between the AFM tip and surface when a layer of water is present on the surface (fig. 1.17). These jump-to-contact problem may lead to charge imbalance, to the breaking of the tip, to sample disturbing, to liquid spreading, local dissolving phenomena and electrochemical reactions.

Since electrostatic forces have a much longer range and magnitude than van der Waals forces, they can be easily used to perform noncontact imaging of both conducting and insulating materials. In SPFM a bias voltage (dc+ac) is applied to a conductive cantilever as in the KPFM mode. The electrostatic polarization induced by the tip on the sample surface generates a mutual attraction with an attractive force (polarization force) in the nN range, which bends the cantilever towards the sample. Because electrostatic forces are long range, they provide a means of imaging at a distance that is large enough (typically few tens of angstroms) to minimize perturbation even of a liquid surface (Xu and Salmeron, 2001) (fig. 1.18). The $\omega$

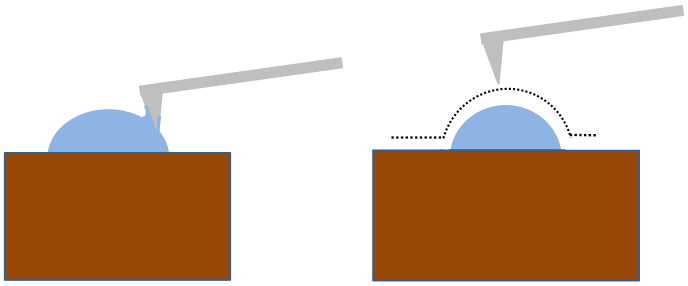

Figure 1.17: a) AFM scanning in Contact mode or AM mode disrupts water dropplets and water layers over the sample. Using van der Waals forces as feed back forms water necks that push the tip against the surface. b) Electrostatic forces are more effective to perform images without contacting the sample.

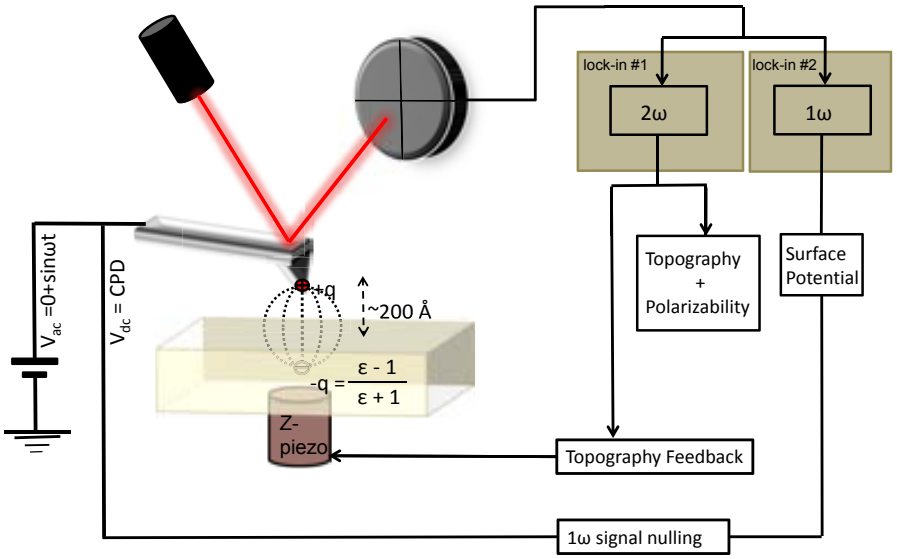


Figure 1.18: Schematic representation of the SPFM mode. The electrically biased AFM tip is attracted towards the surface of any dielectric material. The polarization force depends on the local dielectric properties of the surface. An ac signal is send at $\omega$ frequency, and signal is recorded at $\omega$ to obtain CPD information and $2\omega$ to obtain topograpy and polarizability.

component of the signal is recorded the same way as explained in KPFM mode to obtain CPD data by nulling it using a $V_{dc}$ (fig. 1.19).

Equation 1.11 is called the $2\omega$ component signal, being proportional to the z distance, in SPFM the $2\omega$ amplitude is used as the topography feedback. The $2\omega$ amplitude is kept constant by adjusting the z position of the tip with respect to the

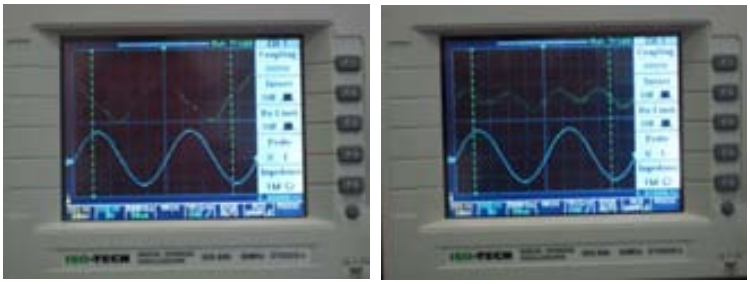


Figure 1.19: Oscilloscope reading (yellow) the deflection signal of the cantilever and (blue) the reference signal. a) when the KPFM mode is not connected, both and 2 frequencies are present in the cantilever. b) when the KPFM mode is connected, signal is nulled and only 2 signal is present.

sample by means of z-piezo motion. The resulting data is the topographic image (modulated by the local dielectric constant (x,y)).

The surface polarizability has differents contributions from (i) orbitals deformation, (ii) polar molecules orientation (they occur in the range of GHz) and (iii) ion mobility (they occur in the range of KHz). The KHz range can be easly achieved with conventional electronics. SPFM can sense ion solvation, mobility and exchange (Salmeron, 2001). Ionic difussion in liquid ranges from seconds to fractions of millisecond, so it is expected to substantially contribute to the polarization force at low ac frequencies as long as there is some degree of water over the sample to provide mobility.

When the tip has a positive potential with respect to that of the sample, negative ions will diffuse towards the surface region located under the tip. When the ac tip s voltage turns negative with respect to that of the sample, these negative ions will diffuse away from the spot under the tip and positive ones will replace them (fig. 1.20). This effect takes place over distances of a few tip radii or a few times the tip-surface distance, and can be quantitatively measured following the tip s deflection as the voltage switching takes place and the cantilever is repulsed from and attracted to the surface. When the tip is scanning the surface instead of being stationary, ion mobility comes along with topography.

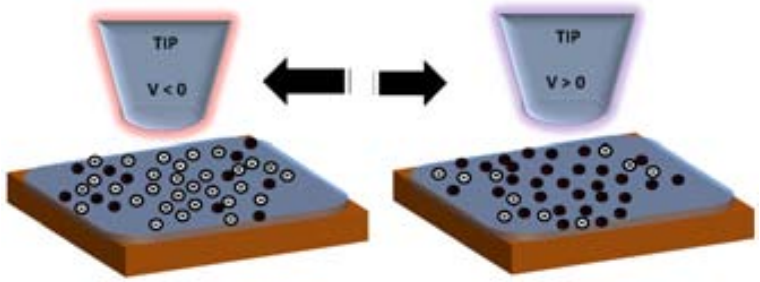


Figure 1.20: Repesentation of an ion mobility study. The tip s voltage changes between positive and negative values, and as long as this switching is slower than ions mobility they diffuse to creat an opposite charge on the sample hidratation layer.

#### 1.1.2.7 Piezoresponse Force Microscopy

Piezoresponse Force Microscopy (PFM) is used to map locally piezoelectric samples. The PFM technique is based on the converse piezoelectric effect and will be described in more detail in the introduction to the ferroelectric materials.

#### 1.1.2.8 Other AFM modes

The AFM techniques are not limited to these modes but other interesting and versatile variations are nowadays broadly used. Since they have not been used in this thesis work I will just tiptoe over them providing a list name and brief description for the reader s knowledge.

**Magnetic Force Microscopy (MFM):** MFM works in the previously explained lift mode (see EFM), performig first a topographic study of a scanning line and followed by a lift mode pass where a sharp magnetized tip detects the magnetic interactions between it and the sample. MFM is used to reconstruct the magnetic structure of the sample surface (Martin and Wickramasinghe, 1987).

**Frequency Modulation AFM (FM-AFM):** In FM-AFM the cantilever acts as the oscillator in an active feedback circuit, just the same as for AM-AFM, but instead of monitoring the cantilever s amplitude, its frequency is used (Albrecht et al., 1991; Durig, Zuger and Stalder, 1992; García and Pérez, 2002). FM-AFM is also able to work in liquid media (Higgins et al., 2005). With FM-AFM atomic resolution and identification (spectroscopic) have been achieved (Sugimoto et al., 2003).

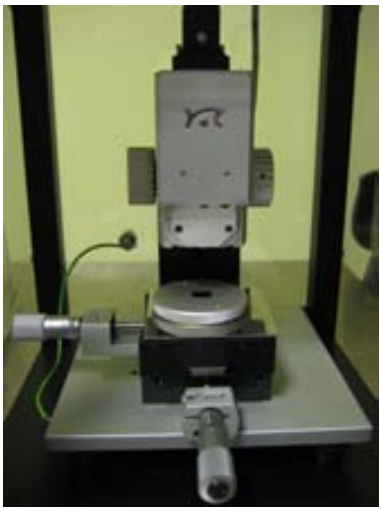

Figure 1.21: Nanite FM-AFM from Nanosurf A.G. installed in the group.

**NSOM:** As brief explanation for NSOM, it breaks the far field resolution limit using a very small light source as the imaging mechanism with a diameter much smaller than the wavelength of light and the probe, must be very close to the surface; much closer than the wavelength of the light. It can achieve resolutions better than the diffraction limit. This region is the Near-Field and hence the name of the technique.

## 1.2 Introduction to water and amino acids

### 1.2.1 Water: a simple structure with complex behaviours

Water is probably the most studied compound in history, still our knowledge to explain all its behaviours is poor. In the small size of water molecule often relies the wrong general opinion about its assumed simplicity, but the complexity of its behaviour and its singular capabilities is still far from being understood. The water molecule structure is made of two light hydrogen atoms and a relatively heavy oxygen atom ($H_2O$) and has the point group $C_{2v}$ having two mirror planes of symmetry and a 2-fold rotation axis (figure 1.22).

The near 16-fold mass difference between hydrogen and oxygen leads to its ease of rotation and the significant relative movements of the hydrogen nuclei. From the classical point of view water molecule is described as having four tetrahedrally ar-

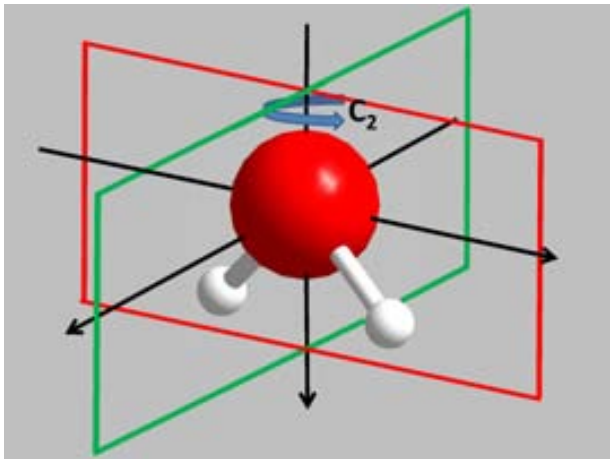


Figure 1.22: The water molecule has a $C_{2v}$ point group.

ranged $sp^3$-hybridized electron pairs, two of which are associated with the hydrogen atoms and the two remaining as lone pairs of the oxygen atom. If no distortion of the structure occurs, then the bond-bond, bond-lone pair and lone pair-lone pair angles would all be 109.47°. However such tetrahedral bonding patterns are mostly found in condensed phases such as hexagonal ice (fig. 1.24) but not in isolated gas molecules. The experimental values for gaseous water molecule are O-H length 0.95718 Å and H-O-H angle 104.474° (Hasted, 1972) but they depend on the vibrational state of the molecule, being able to reach values of H-O-H 180° during high order bend vibrations (Zobov et al., 2005). It turns then, difficult, to assign an $sp^3$ hybridization or not to water molecule, since it seems that this kind of approximation is not a solution to the Schrodinger-Pauli Hamiltonian and it is only valid for high ordered tetragonal water (i.e. ice).

**Isolated water gas molecule**

There is no full consensus about water hybridization. Ab initio calculations do not confirm the presence of the lone pair electrons for an isolated water molecule in those specific tetragonal directions (Ning et al., 2008) but it shows the negative charge being concentrated more evenly along the line between where these lone pairs would have been expected and lying closer to the center of the O-atom than the positive charge located on the hydrogen atoms. So, for isolated water molecules $sp^3$-hybridized lone pairs should be avoided (Liang, 1987; Martin, 1988) since a $sp^2$-

hybridized structure (plus a pz orbital) seems to rationalize the formation of (almost planar) trigonal hydrogen bonding that can be found around some restricted sites in the hydration of proteins and where the numbers of hydrogen bond donors and acceptors are unequal.

### Dimer formation

Due to the larger electronegativity of the oxygen atom with respect to that of the hydrogen atom, the electrons of their covalent bonding are attracted towards the former and this leaves a deficiency on the far side of the hydrogen atom and causing a molecular dipole. This dipole moment causes hydrogen atoms of water molecules being attracted to the oxygen atom of a nearby water molecule, the so-called hydrogen bonding. This force is strongest when the three atoms are in a straight line (represented as O-H$\cdots$O) and when the O atoms are separated by about 0.28 nm (fig. 1.23) so that water H-bonding is directional. The water hydrogen bond is never stronger than about a twentieth of the O-H covalent bond ($\sim$20 kJ mol for hydrogen bonding vs $\sim$460 kJ mol for the covalent O-H bond), it is thus a weak bond but still strong enough to be maintained during thermal fluctuations at or below ambient temperatures. Since hydrogen bonds are stronger when the three involved atoms (O-H$\cdots$O) form a line, they impose a certain linearity on the local structure, being ordered structures related with stronger bonds involved.

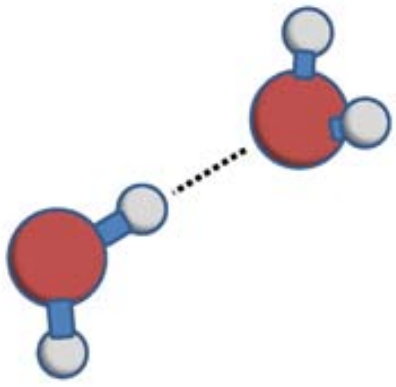

Figure 1.23: Water hydrogen bond is more stable when the atoms involved form a line. The water molecule that offers its hydrogen atom to the bond is called the donor molecule, while the other water molecule, is called the acceptor molecule.

**Solid water: Ice**

Each water molecule can form two hydrogen bonds involving its hydrogen atoms plus two further hydrogen bonds using its oxygen atom, having this way two hydrogen bond donors and two hydrogen bond acceptors. These four hydrogen bonds optimally arrange themselves tetrahedrally around each water molecule as found in ordinary ice (fig. 1.24).

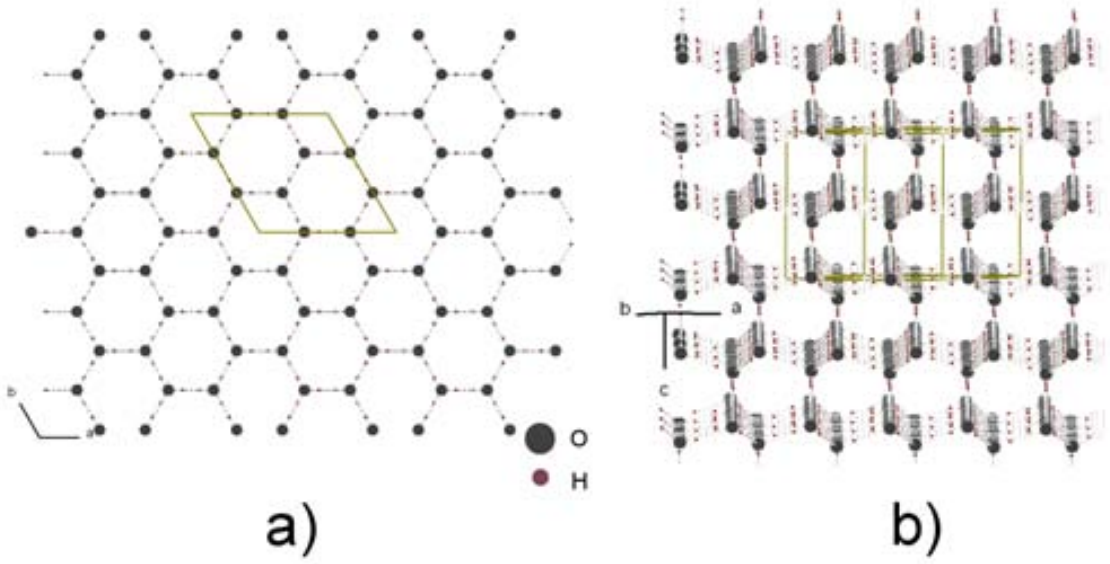


Figure 1.24: Natural ice is mostly found in the form of hexagonal ice. a) Top and b) layers.

Hexagonal ice (ice Ih, space group $P6_3/mmc$, fig. 1.24) (Petrenko and Whitworth, 2002) is the form of all natural snow and ice on Earth, as evidenced in the six-fold symmetry in common ice. Near the melting point the lattice parameters are $a = 0.4523$ nm and $c = 0.7367$ nm (Schulson, 1999). The crystals consist of sheets lying on top of each other (fig. 1.24b). The basic structure consists of a hexameric box where planes consist of chair-form hexamers (horizontal planes) or boat-form hexamers (vertical planes). In fig. 1.24 the hydrogen bonding is shown ordered whereas in reality it is random with ordered O-sublattice and disordered H-sublattice, as protons can move between (ice) water molecules at temperatures above about 130°K (Moon, Lee and Kang, 2008). Also, the H-O-H angles are about 106.6° (Petrenko and Whitworth, 2002) so the hydrogen bonds are not totally straight.

The basic principles that govern the arrangement of water atoms in ice are known as the ice rules or the BernalFowler rules. From the observations made by Pauling on the entropy and statisticals of hydrogen atoms configurations on ice (Pauling, 1935), these rules state that an ideal crystal is based on the following assumptions:

i) Each oxygen atom is covalently bonded to two hydrogen atoms at a distance of $\sim$0.95 Å.

ii) Each molecule is orientated so that its two hydrogen atoms face two, of the four, neighbouring oxygen atoms that surround in tetrahedral coordination.

iii) The orientation of adjacent molecules is such that only one hydrogen atom lies between each pair of oxygen atoms.

iv) Ice Ih can exist in any of a large number of configurations, each corresponding to a certain distribution of hydrogen atoms with respect to oxygen atoms.

The Bernal-Fowler rule allows the rotation of water molecules within the Ih ice lattice by hydrogen atoms jumping sites. This movement requires that all hydrogen atoms move simultaneously or the presence of point defects. The lattice energy, L, for Ih Ice is the difference between the energy of a motionless water molecule in the gas phase at 0°K and its energy in Ice Ih at 0°K. The lattice energy for Ice Ih is L=0.58 eV (Hobbs 1974). If this lattice energy is attributed to hydrogen bonding of water molecules, then the energy of the hydrogen bond will be half the value of the lattice energy (as each molecule contains two hydrogen atoms). Thus the energy of the hydrogen bond is 0.29 eV. The hydrogen bonding in the surface of hexagonal ice is predicted to be more ordered than that within the bulk structure (Pan et al., 2008) and ice nucleation occurs greatly enhanced, by a factor of $10^{10}$, at the air-water surface rather than within bulk water (Shaw, Durant and Mi, 2005). An extense bibliography about the ice growing mechanism exits (Beckman, Lacmann and Blerfreund, 1983; Nelson and Knight, 1998; Libbrecht, 2003; Libbrecht, 2004).

Not only hexagonal ice but other ice phases are possible. There are sixteen crystalline phases, all of them involve the water molecules being hydrogen bonded to four neighboring water molecules (Zheligovskaya and Malenkov, 2006) and three amorphous (non-crystalline) phases.

**Water in its liquid state**

Although in its liquid state 80% of the electrons are concerned with bonding, hydrogen atoms are constantly being tranferred between water molecules due to protonation/deprotonation processes and even at its slowest rate of exchange (pH=7) the average time for the atoms in an $H_2O$ molecule to stay together is only about a millisecond, this is however much longer than hydrogen bonding duration (few ps) (Loparo et al. 2004; Fecko et al. 2005) or molecular hydration duration (in the order of ps in protein solvation shell) (Ebbinghaus et al. 2007), so water is usually treated as a static structure when it comes about hydration processes and hydrogen bond formation/breaking.

Atomic distances and angles shown before are not maintained in liquid water, where both ab initio (O-H length 0.991Å, H-O-H angle 105.5°, Silvestrelli and Parrinello, 1999) (recent modeling gives values of 106.3°, Fanourgakis and Sotiris, 2006) and diffraction studies (O-H length 1.01 Å, O-D length 0.98 Å) (Soper and Benmore, 2008)(O-D length 0.970 Å, D-O-D angle 106°) (Ichikawa et al., 1991) show larger values as a consecuence of the weakening of the covalent bonding due to hydrogen bonding presence and reducing the repulsion between the electron orbitals. These values are far from being constant and polarization shifts, different hydrogen-bonded environments or bonding of the water molecules to solutes and ions will modify them. Commonly used molecular models for simulations (SPC/E, SPC, TIP3P/Fw, TIP4P...) use O-H lengths between 0.957 Å and 1.00 Å and H-O-H angles fom 104.52° to 109.5° (Guillot, 2002). Table 1.1 shows the parameters used from most common molecular models, being $q_1$ the hydrogen charge density, $q_2$ the oxygen charge density, ♯ is the angle formed by the three atoms of the molecule, $l_1$ is the length of the covalent bond and $\sigma$ and  are the Lennard-Jones parameters (the separation and depth of the potential energy minimum between two similar molecules). These parameters are shown in fig. 1.25.

If the water molecule could be entirely described using classical mechanics, then the theorem of equipartition of energy (a general formula that relates the temperature of a system with its average energies) could be used to predict that each degree of freedom would have an average energy in the amount of $(1/2)k_BT$ where $k_B$ is

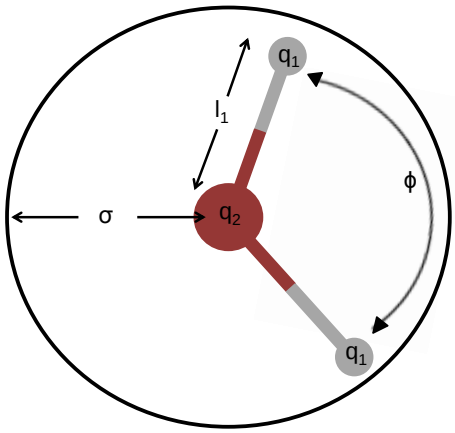


Figure 1.25: Parameters used in table 1.1 by molecular models.

| Model | Type | $\sigma$Å | $\varepsilon$ kJ/mol | $l_1$ Å | $q_1$ (e) | $q_2$ (e) | $\phi$ |
|---|---|---|---|---|---|---|---|
| SPC/E | planar | 3.166 | 0.650 | 1.0000 | +0.410 | -0.8200 | 109.47 |
| SPC | planar | 3.166 | 0.650 | 1.0000 | +0.4238 | -0.8476 | 109.47 |
| TIP3P/Fw | planar | 3.1506 | 0.6368 | 0.9600 | +0.4170 | -0.8340 | 104.5 |
| TIP4P | planar | 3.15365 | 0.6480 | 0.9572 | +0.5200 | -1.0400 | 104.52 |

Table 1.1: Parameters for some water molecular models.

Boltzmann constant and T is the temperature. For a water molecule in its ice form, it can only vibrate so it has only 3 degrees of freedom; while for a liquid water molecule, it can also move in space (translational motion) and rotate so it has 6 more degrees of freedom (Lianxi and Feng, 2008). So that the internal energy of a water molecule at room T is $\sim$1.8514x$10^{-20}$ J.

The same as for its ice form, there are also differences between bulk and surface water hydrogen bonding, and liquid water hydrogen bonds are more stable in the water surface than in the bulk (Gan et al., 2006) mainly due to lower anticooperativity (formation of two simultaneous donor or acceptor hydrogen bond) and compensation for the increased chemical potential on the loss of some bonding and also but in minor contribution due to the reduced competition from neighboring water molecules. The loss of hydrogen bonding of surface liquid water molecules also enhances their reactivity (Kuo, 2004) and the fact that hydrogen bonding is more stable makes surface be a greater ice nucleation (Shaw, Duranta and Mi, 2005). At 25°C water O$\cdots$O distance within 2-3 nm from the surface is about 6% larger than that of bulk water. Thermodynamics analysis shows that water structuring

is enhanced at the surface, having the same density than bulk water at under 4°C. Also the degree of structurating is less modified by temperature at the surface that in bulk water. Water-air surface studies reveal it to be about 1.7 nm thick at 22°C and more dense than the bulk liquid, behaving like water at a lower temperature (Greef and Frey, 2008) (fig. 1.26).

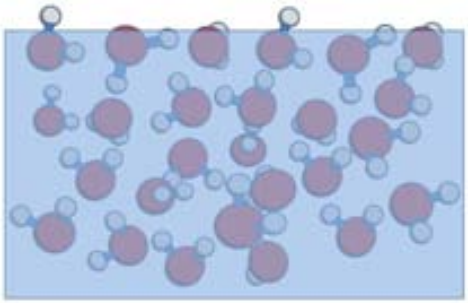

Figure 1.26: Water is more structured at the surface while bulk whater has greater disorder.

### 1.2.2 Water and surfaces

Any surface under ambient conditions is covered by a thin film of water. This film can be a fraction of a monolayer, many molecular layers or even a macroscopic film that can be seen with the naked eye. Unless in very high humidity conditions, where macroscopic films and droplets can form on surfaces, the thicknesses scale of water films are generally nanometers. Yet such a thin film can have strong effects on the chemical and physical properties of the substrate surface, so the study of the interaction of water with solid surfaces at ambient conditions is of paramount importance, since water−solid interfaces are involved in a myriad of relevant phenomena such as adhesion, friction, charge transport, dissolution, oxidation, chemical reactivity, etc. (Thiel and Madey, 1987; Israelachvili, 1991; Henderson, 2002; Finlayson-Pitts, 2003; Verdaguer et al., 2006; Hodgson and Haq, 2009).

The thickness of the film will depend not only on the ambient conditions but also on the wetting properties of the surface. The structure of the water molecules at the water-substrate interface determines their wetting properties and underlies the vast

array of phenomena known under the names of hydrophobicity (nonwetting) and hydrophilicity (wetting), which describe the interaction between objects in aqueous media. There are many fundamental questions on the nature of thin films of water that still need in-depth investigation. The thickness of water films and the structure of water molecules in the film, amorphous or ordered, are still unknown for many important surfaces. Both parameters will affect the thermodynamic properties of the surface and how the whole system interacts with the environment. Chemistry occurring in those water films can be very different from chemistry in bulk water and it is still not well understood. Interactions between surfaces change when water films are present: water films play a key role in friction and adhesion forces between surfaces. These phenomena are crucial in biology and in material sciences and most of them rely on the nanometer scale, a fact that might be surprising at first sight due to our macroscopic perception of our surroundings. However, such dimensions have been experimentally determined on surfaces of different materials with different affinity to water (Beaglehole and Christenson, 1992; Hu et al., 1995; Cantrell and Ewing, 2001; Goodman, Bernadrand and Grassian, 2001; Al-Abadleh and Grassian, 2003; Summer et al., 2004; Foster, DAgostino and Passno, 2005; Asay and Kim, 2005; Ewing, 2006; Fukuma et al. 2010; Xu et al. 2010). Several different techniques have been used to study such phenomena at nanometer scale: ellipsometry (Beaglehole and Christenson, 1992), infrared spectroscopy (Foster and Ewing, 2000), scanning probe microscopy (SPM) (Hu et al., 1995), and photoelectron spectroscopy (Bluhm et al., 2002), as well as simulated by computational methods (Engkvist and Stone, 2000).

The AFM is, due to its capability to work at ambient conditions, one of the most versatile tools to study water at the nanoscale and a large number of works are published studying the above mentioned processes at nanometric range: friction (Xu, Bluhm and Salmeron, 1998; Burton and Bhushan, 2005), hydrophobicity and hydrophilicity (Bhushan and Jung, 2006), ions mobility (Xu and Salmeron, 1998), adhesion (Xu and Siedlecki, 2007), oxidation processes (Avouris et al., 1998), reactivity (Lauritsen and Reichling, 2010) and dissolution (Dove and Platt, 1996) may serve as some examples.

It is important now to remark the importance of RH when it comes to the study of surfaces exposed to air, since it measures the amount of gas water present in the system. Many chemical and physical surface-water phenomena are RH depending and many are triggered when RH reaches values above ∼30%, related to the formation of the first water monolayer on many surfaces. As some case examples NaCl(001) surfaces have shown that the charge state is correlated with the ionic mobility, which is efficiently triggered above 35% (Verdaguer et al., 2008). Also SPM investigations on gold have shown that 0.2 nm high water islands grow from the steps at 35% RH, while full coverage is achieved at 65% RH (Gil et al., 2000).

Solvation forces (forces arising between solutes and near solvent molecule that modify the properties and structuration of the solvent and decay as one gets farther from the solute molecules), depend not only on the properties of the intervening medium but also on the chemical and physical properties of the surfaces, for example, whether they are hydrophilic or hydrophobic, whether amorphous or crystalline, smooth or rough, rigid or fluid-like or with dipole presence (Israelachvili, 1991). Such forces can be very strong at short range, and they are therefore particularly important for determining the magnitude of the adhesion between two surfafces or particles in contact (at their potential energy minimum).

### 1.2.3 Water contribution to protein structure stability

Blood, an aqueous-based solution, plays an essential role in the distribution of cells, proteins, nutrients, gases, and many other biological materials throughout organisms. Each of us has around 56 liters of the complex solution coursing through our arteries and veins. Blood may be separated into its two parts by centrifugation. The sediment is composed of three types of blood cells: erythrocytes, leukocytes, and platelets (thrombocytes). The supernatant, the liquid portion called blood plasma, is a solution consisting of approximately 90% water and 10% dissolved solutes such as plasma proteins, glucose, hormones, cholesterol, vitamins, inorganic ions, and many other biomolecules. Water plays many roles in cells and organisms and has great influence on the structure and behavior of biomolecules. The stabilization and packing of the proteins structures are a consequence of the hydration forces, water is

part of many hydrogen bond networks and plays an important role in screening electrostatic interactions. Water molecules can contribute favorably to protein complex formation (Li and Lazaridis, 2006) and plays a main role in protein folding thanks to its role in isolating hydrophobic attractions (Dill, 1990) that are responsible for the rapid gluing of hydrophobic residues. Also water is responsible for the affinity between specific interactions in proteins (Petrone and Garcia, 2004).

The hydration shell in the proximity of the protein surface is crucial for stabilizing folded proteins. It has been shown that water molecules can be structurally conserved in protein complexes, and that their residence time and diffusion characteristics are distinct from bulk and surface solvent (Bizarri and Cannistraro, 2002), fluctuations of the hydration water can slave the protein dynamics and thus affect its function (Ansari et al., 1992; Fenimore et al., 2002), yet the interplay between the protein and solvent complexity is an intriguing open question. Furthermore, water not only interacts with the protein surface, but it can directly interact with the protein backbone and side chains in the protein interior or even form clusters of two or more water molecules in hydrophobic cavities (Ernst et al., 1995). Buried water molecules have much longer mean residence time than water in the first hydration shell, and thus they constitute an integral part of the protein structure (Otting, Liepinsh and Wuthrich, 1991; Denisov and Halle, 1995; Garcia and Hummer, 2000). However, interior water molecules can escape to the bulk and be replaced by water from the hydration shell (Garcia and Hummer, 2000).

Recent simulations demonstrate the importance of water to improve protein structure prediction (Papoian et al, 2004) specially when it comes to large proteins where long-range interactions between polar or charged groups are mediated by water molecules. So the inclusion of water in simulated protein systems has improved folding predictions compared to *in vacuo* folding models, a molecular dynamics approach to study the importance of solvent in protein interactions (Hamelberg, Shen and McCammon, 2006; Samsonov, Teyra and Pisabarro, 2008). There are a variety of experimental and theoretical studies acknowledging the active role of solvent in protein stability and dynamics. Experimentally, x-ray, neutron diffraction (Savage and Wlodawer, 1986) , NMR (Otting, Liepinsh and Wuthrich, 1991; Ernst et al.,

1995), and femtosecond fluorescence (Pal, Peon and Zewail, 2002) measurements reveal the binding sites, structure, and dynamics of water.

The exact range of processes mediated by water is far from being understood, however, it is clear that protein hydration is very important for their three-dimensional structure and activity (Franks, 2002; Chaplin, 2006; Zhang et al., 2007). Indeed, proteins lack activity in the absence of hydrating water. The aqueous structuring around proteins is affected out to at least a nanometer from its surface or 2 nm between neighboring proteins, as shown by terahertz spectroscopy (Ebbinghaus et al., 2007). Some water molecules interact with the surface, reorienting both themselves and the surface groups whereas other water molecules link these to the bulk in an ordered manner whilst remaining in dynamically active (Zhong, Pal and Zewail, 2010). In solution proteins possess a conformational flexibility, which encompasses a wide range of hydration states, not seen in the crystal or in non-aqueous environments. Equilibrium between these states will depend on the activity of the water within its microenvironment; that is, the freedom that the water has to hydrate the protein. Thus, protein conformations demanding greater hydration are favored by more (re-)active water (for example, high density water containing many weak bent and/or broken hydrogen bonds) and drier conformations are relatively favored by lower activity water (for example, low-density water containing many strong intramolecular aqueous hydrogen bonds).

The interiors of folded proteins, or protein domains, are compact and well-packed (Richards, 1977; Richards and Lim, 1993; Valdez, 2001), but the packing of amino-acid residues is not perfect (i.e. proteins are compresible). Presence of internal cavities (Rashin et al., 1986) large enough to accomodate water molecules is usual, internal water can then act as a structure stabilizer (Takano et al., 1997) by maintaining good hydrogen bonds between the domains and filling sites of imperfect packing.

Water interacting with the amino acids of the protein surface contributes negatively to protein volume and compressibility. Difficulties in interpreting the precise changes in protein volume and compressibility induced by hydration at protein-water interfaces have led to empirical estimates of the intrinsic protein volume, that is, the

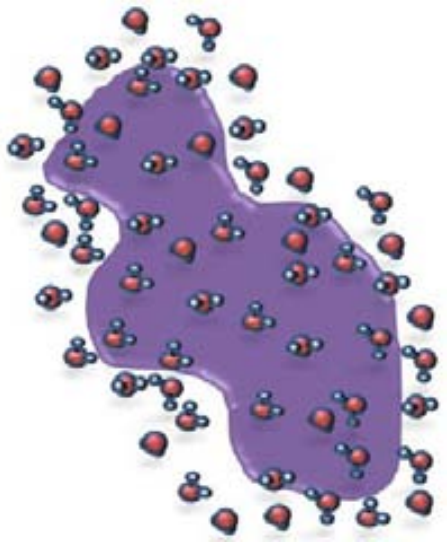

Figure 1.27: The first layer of water is of great importance in protein folding and activity.

volume that cannot be penetrated by the solvent (Paci and Velikson, 1997). There is no consensus on the exact value of the compressibility of the solvent-inaccessible protein core, or intrinsic protein compressibility, due to the diverse approaches used by different investigators (Ghekko and Noguchi, 1979; Gavish, Gratton and Hardy, 1983; Kharakoz and Sarvazyan, 1993; Chalikian et al., 1996).

Although many studies, both experimental and theoretical, have been performed to shed some light to the complex role of water on protein biochemistry (Colombo, Rau and Parsegian, 1992; Svergun et al., 1998; Lo Conte, Cothia, and Janin, 1999; Makarov, Pettitt and Feig, 2002; Milhaud, 2004; Lin, Balabin and Beratan, 2005; Garczarek and Gerwert, 2006; Ebbinghaus et al., 2007; Ball, 2008), an important lack of fundamental information about the interaction of water with the building blocks of proteins, amino acids, still exists, which can be in part overcome by investigating well characterized surfaces of amino acids crystals exposed to water.

### 1.2.4 Brief introduction to amino acids

Alpha amino acids are a family of organic molecules that share a common structure consisting of an amino group ($H_2N$-R) and a carboxylic acid group (R-COOH) both linked to the same carbon atom that also has an hydrogen atom and a radical R group (fig. 1.28a). It is this R group what differences one alpha amino

acid from another, giving each one its particular properties (solubility, hidrophobicity/hidrophilicity, particular reactivity...). Amino acids are usually found in solution or crystalline form as having both their carboxylic acid and amino group charged as ammonium group ($^{+}H_3N$-R) and carboxylate (R-$COO^{-}$) (fig. 1.28b). This structure is known as the zwitterionic form of the amino acid, and while the whole structure has no net charge, some parts have now punctual charge. The coexistence of the $NH_3^+$ and the $COO^-$ hydrophilic groups with a variable group R makes the hydration effects in amino acids a rather complex phenomenon that has received considerable interest in recent years, mainly from the theoretical point of view (Park, Ahn and Lee, 2003; Sagarik and Dokmaisrijan, 2005; Osted et al., 2006; Degtyarenko et al., 2008; Chowdhry et al., 2008).

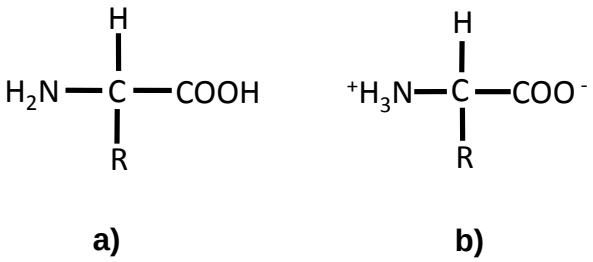


Figure 1.28: a) General amino acid formula b) Amino acid zwitterionic form.

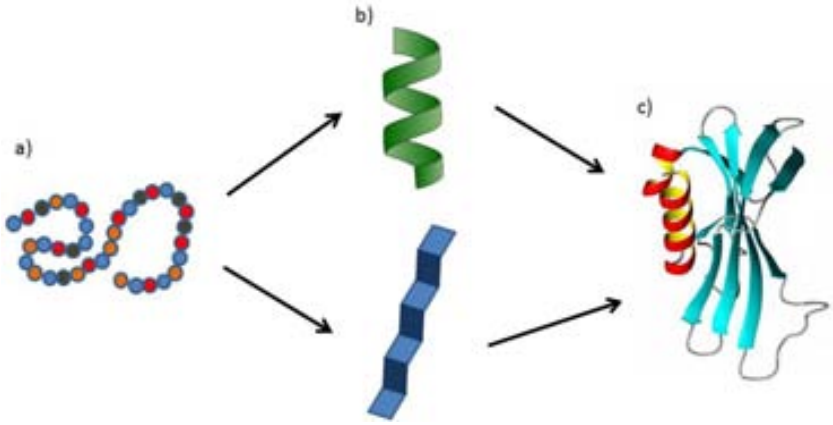


Figure 1.29: Amino acids are the building blocks of proteins. a) Amino acids form peptide chains via peptide bond (primary structure). b) These peptide chains organize themselves in the form of alpha helix or beta sheets (secondary structure). c) Alpha helix and beta sheets form new structures with particular conformation (tertiary structure). Proteins are formed by one or more tertiary strucutres.

A proper understanding of hydration effects in amino acids is still needed to understand water cluster formation around proteins, as well as their folding mechanisms and interaction sites nature. The hydrophilic or hydrophobic nature of a protein subsection depends on the amino acid peptide chain that originates it: the R groups that the amino acids expose, their total charge and relative orientation to the protein s surface, the near-by amino acids influence to the overall hydrophilicity/hydrophobicity of the subsection... many classifications of amino acids as a function of their affinity with water are available in the literature (as an example see Lienqueo, Mahn and Asenjo, 2002).

The exchange of water molecules close to amino acid residues has been related to the exposure of the amino acid groups to the bulk solvent (Bandyopadhyay et al., 2005; Bandyopadhyay, Chakraborty and Bagchi, 2005). The first hydration shell around protein surface amino acids is ordered; with high proton transfer rates and well resolved time-averaged hydration sites; surface water showing coherent hydrogen-bond patterns with large net dipole fields (Yokomizo et al., 2005; Yokomizo, Higo and Nakasako, 2005). The hydrogen bonds holding these water molecules to the protein are stronger with longer lifetimes than bulk water (Chakraborty, Sinha and Bandyopadhyay, 2007). This hydration shell is 10%-20% more dense than bulk water but not in a uniform way, a closer look to punctual water density shows zones with lower water density than that of bulk water, corresponding to non-polar exposed amino acid groups and other zones with higher water density corresponding either to surface conformation at depressions (Smith et al., 2002), exposed polar hydration sites (water molecules are held to other water molecules most strongly by the positively−charged basic amino acids) and also to electrostriction pressure (that is, local pressure increase due to the localized electric field) (Danielewicz-Ferchmin and Ferchmin, 2006). There are significant differences in the directional rates of water diffusion perpendicular and parallel to the protein surface that are maximal at about 6 Å but still determinable at 15 Å from the surface (Makarov et al., 2000; Makarov, Pettitt and Feig, 2002).

As said, bulk water affinity to amino acids is commonly related to the hydrophilicity or hydrophobicity of the R groups exposed by the amino acids. Thought this

may seem simple and obvious, it may be more hidden factors underlying this direct explanation. The works of Makarov et al., 2000 and Danielewicz-Ferchmin et al., 2006 indicate respectively (i) that the time that a water molecule remains close to a residue may significantly vary depending on the diffusing direction of this water molecule and (ii) that the presence of elecric fields may affect the density of water molecules lying close to a residue.

More research was done in these fields that led us to the work presented by Gavish et al. in 1992, where the importance of a net dipole moment in amino acid crystals was studied favouring factor for ice nucletaion at macroscopic scale. In this work the hydrophobic surface of several amino acids single crystals in a series of racemic and chiral-resolved hydrophobic $\alpha$-amino acids were used to freeze water vapor upon them, resulting in 4 to 5 temperature degrees more difficult to start the freezing on those crystals with not net dipole moment parallel to the studied surface, while easily water vapor freezing was observed when the crystal had a net dipole moment parallel to the studied face. The results were interpreted in terms of an electric field mechanism that helps to align the water molecules into ice−like clusters *en route* to crystallization. The study was performed by optical means but yet at this scale it seems to point out the importance on amino acids dipole direction and their capability to govern the water affinity with amino acid residues over the nature of the R group.

An analog study with these amino acids surfaces and the role of amino acid dipoles in water freezing, but at a smaller level, turns to be very interesting. Water vapor preferential binding points for different amino acids, the role of the amino acid dipole in water interaction with their surfaces, preferential ordering of water with positive or negative dipoles endings to start its freezing or amino acid diffusion in a water monolayer are just some of the questions that new SPM techniques allow us to study. AFM is specially adequate for these type of study due to the characteristics described in the previous chapter.

| Amino acid | Hydropathy index |
|---|---|
| Isoleucine | 4.5 |
| Valine | 4.2 |
| Leucine | 3.8 |
| Phenylalanine | 2.8 |
| Cysteine/cystine | 2.5 |
| Methionine | 1.9 |
| Alanine | 1.8 |
| Glycine | -0.4 |
| Threonine | -0.7 |
| Tryptophan | -0.9 |
| Serine | -0.8 |
| Tyrosine | -1.3 |
| Proline | -1.6 |
| Histidine | -3.2 |
| Glutamic acid | -3.5 |
| Glutamine | -3.5 |
| Aspartic acid | -3.5 |
| Asparagine | -3.5 |
| Lysine | -3.9 |
| Arginine | -4.5 |

Table 1.2: Amino acids sorted by their hydropathy index, one of the most used parameters to define amino acid hydrophobicity. The values are as they appear in the work of Kyte et al., 1982.

### 1.2.5 Molecular dipole moment

As previously said, there is a lack of fundamental study about amino acid-water interaction in its simplest level. Also some properties are not clearly defined, as the hydrophylic/hydrophobic degree of amino acids, with multiple variations depending on the parameter defined to measure it. For a wider explanation of hydrophylic/hydrophobic classification I cite the webpage of the The Rockefeller University (see Rockefeller University Webpage on bibliogarphy). As an example of a possible classification, I include the hydropathy index (a number representing the hydrophobic or hydrophilic properties of its sidechain)(table 1.2), but other parameters may as well be used.

But as previously mentioned, amino acids dipoles may greatly influence the hydrophobic character of the exposed surface. This will turn to be a very important point in this study, so a brief description of molecular dipole moments will be provided next.

#### 1.2.5.1 Introduction to molecular dipole

Most common and principal intramolecular force is covalent bond, a type of chemical bond in which there is mutual sharing of electrons between two non-metal atoms.

Bonds connecting atoms of different electronegativity are polar, with a higher density of bonding electrons around the more electronegative atom giving it a partial negative charge (designated as $\delta^-$). The less electronegative atom has some of its electron density taken away giving it a partial positive charge ($\delta^+$). Bond polarity is measured by its dipole moment ($\mu$), defined as the product of the magnitude of the charge ($q$) at either end of the dipole multiplied by the distance ($d$) that separates these charges.

$$\mu = q \cdot d \tag{1.12}$$

The Debye is the unit of dipole moment and has a value of $3\,336 \cdot 10^{-30}$ C·m. The dipole moment of a molecule (molecular dipole moment, m) is the resultant of all of the individual bond dipole moments of that molecule. Lone pairs contribute to the molecule s dipole moment even though they do not constitute a `bond . Clearly the nucleus `end of the lone pair is positive and the electron `end is negative so one might think of a `lone pair dipole contributing to the polarity of the molecule in analogy to a bond dipole. This behavior is demonstrated in the relative magnitudes and directions of the dipole moments in the molecules $PH_3$ (m=0.58 D), $NH_3$ (m=1.47 D), and $PF_3$ (m=1.03 D). Dipole moment plays a very important role in understanding the nature of chemical bonds and molecular interactions, defining the relative orientation of water molecules with each other. Molecules that possess a dipole moment are called polar molecules, water is polar and has a dipole moment of 1.85 D when in its isolated state. In liquid and ice water it increases up to ∼2.6 D due to the cooperativity effect.

As some examples table 1.3 shows the dipole moments of molecules, bonds and groups (in Debye units). Data compiled from Wesson (1948), Smyth (1955), Davies (1965) and Landolt-Bornstein (1982), (Israelachvili, 1991).

**Interactions: monopole-monopole**

Intermolecular forces are usually weaker than intramolecular forces and are longest-ranged when they are electrostatic. Interaction of charge monopoles is the longest-ranged electrostatic force.

| Molecule | Dipole moment (D) | Molecule | Dipole moment (D) |
|---|---|---|---|
| Alkanes | 0 | $H_2O$ | 1.85 |
| $C_6H_6$ (benzene) | 0 | $C_6H_{11}OH$ (cyclohexanol) | 1.7 |
| $CCl_4$ | 0 | $CH_3OH$,$C_2H_5OH$ | 1.7 |
| $CO_2$ | 0 | Hexanol, octanol | 1.7 |
| CO | 0.11 | $CH_3COOH$ (acetic acid) | 1.7 |
| $CHCl_3$(chloroform) | 1.06 | $C_2H_4O$ (ethylene oxide) | 1.9 |
| HCl | 1.08 | $CH_3COCH_3$ (acetone) | 2.9 |
| $NH_3$ | 1.47 | $HCONH_2$(formamide) | 3.7 |
| $SO_2$ | 1.62 | $C_6H_5OH$(phenol) | 1.5 |
| $CH_3Cl$ | 1.87 | $C_6H_5-NH_2$(anilina) | 1.5 |
| NaCl | 8.5 | $C_6H_5-Cl$(chlorobenzene) | 1.8 |
| CsCl | 10.4 | $C_6H_5-NO_2$(nitrobenzene) | 4.2 |
| Molecule | Bond moment | Molecule | Bond moment |
| $C-H^+$ | 0.4 | $C^+-N$ | 0.22 |
| $N-H^+$ | 1.31 | $C^+-O$ | 0.74 |
| $O-H^+$ | 1.51 | $C^+-Cl$ | 1.5-1.7 |
| $FH^+$ | 1.94 | $N^+-O$ | 0.3 |
| C−C | 0 | $C^+=O$ | 2.3-2.7 |
| C=C | 0 | $N^+=O$ | 2.0 |
| Molecule | Group moments | Molecule | Group moments |
| $C-^+OH$ | 1.65 | $C^+-NO_2$ | 3.1-3.8 |
| $C-^+NH_2$ | 1.2-1.5 | $C-^+COOH$ | 1.7 |
| $C-^+CH_3$ | 0.4 | $C-^+OCH_3$ | 1.3 |

Table 1.3: Dipole moments compilation.

Charge-Charge forces (found in ionic crystals) are in the form of:

$$F_{charge-charge} = \frac{q_1 q_2}{(4\pi \ _o) r^2} \tag{1.13}$$

For like charges (+,+) or (−,−), this Coulomb force is always repulsive. For unlike charges (+,−), it is always attractive.

**Interactions: dipole-monopole**

As previously said, an uncharged molecule can still have an electric dipole moment (water is a polar molecule) and thus have electrostatic interactions with charge monopoles. The force of this molecular dipole may be understood by decomposing the dipole into two equal but opposite charges and adding up the rest charge-charge monopole forces. Notice that *the Charge-Dipole forces depend on relative molecular orientation*, this means that the forces can be attractive or repulsive depending on whether like or unlike charges are closer together. On average, dipoles in a liquid orient themselves to form attractive interactions with their neighbors, but thermal motion makes some instantaneous repulsive configurations exist.

**Interactions: dipole-dipole**

Electrostatic interactions exist even between neutral polar molecules in the absence of charge monopoles in the form of dipole-dipole interactions. Again, this force

may be understood by decomposing each of the dipoles into two equal but opposite charges and adding up the resulting charge-charge forces.

Figure 1.30 shows two point dipoles of moments $\mu_1$ and $\mu_2$ at a distance r one from the other and with their relative orientation defined by $\theta_1$ , $\theta_2$ and $\sharp$ .

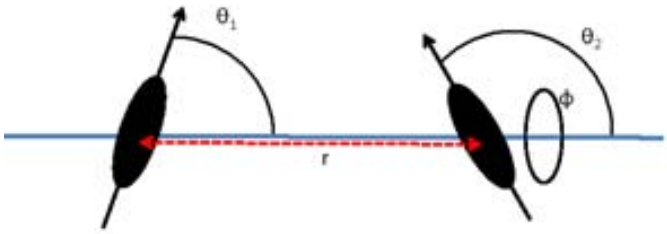


Figure 1.30: The interaction of two dipoles with moments $\mu_1$ and $\mu_2$ is determined by their separation r and their relative orientation defined by $\theta_1$ , $\theta_2$ and $\phi$

Their interaction energy is defined by equation 1.14

$$(r\ \theta_1\ \theta_2\ \sharp) = -\frac{\mu_1\mu_2}{4\pi\ _o\ _r r^3}[2\cos\theta_1\cos\theta_2 - \sin\theta_1\sin\theta_2\cos\sharp] \tag{1.14}$$

Thus dipole-dipole interactions are strongly angle dependent, and the maximum attraction occurs when the two dipoles are in line and pointing in the same direction.

$$(r\ \theta_1 = 0\ \theta_2 = 0\ \sharp) = -2\frac{\mu_1\mu_2}{4\pi\ _o\ _r r^3} \tag{1.15}$$

The relative strenght between two dipoles is of paramount importance for the study of water interaction with polar molecules. At what separation of two aligned dipoles of $\mu$ =1 D does the interaction energy equal kT at ambient temperature? According to equation 1.14, in the gas phase

$$r = (\frac{2(1 \times 3\ 336x10^{-30}C \cdot m)^2}{4\pi(8\ 85 \times 10^{-12}C^2J^{-1}m^{-1})(4\ 12 \times 10^{-21}J)})^{1/3} = 0\ 36nm \tag{1.16}$$

This distance equals the typical size of molecules, so the result means that dipole-dipole interaction fixes molecule alignment only between very polar molecules with high dipole moments in the gas phase at room T. Lesser interactions fail to force dipole alignment and individual dipoles are able to rotate.

In liquid solutions the strengh of interaction is diminished by the change screening of the dielectric constant. Dipole-dipole interactions are then diminished to

| Substance | Molecular Mass (g/mol) | Dipole moment (Debye) | Normal Boiling Point (K) |
|---|---|---|---|
| Propane | 44 | 0.1 | 231 |
| Dimethyl ether | 46 | 1.3 | 248 |
| Chloromethane | 50 | 2.0 | 249 |
| Acetaldehyde | 44 | 2.7 | 294 |
| Acetonitrile | 41 | 3.9 | 355 |

Table 1.4: Organic molecules with similar mass may have remarkable difference in their boiling points due to dipole moment difference.

the point where they are never strong enough to overcome thermal energy and the dipoles are relatively free to rotate with respect to each other (Strokes and Evans, 1997).

Even with such degree of relative rotation, some properties of polar molecules are strongly related with their dipole-dipole interaction, to underline the importance of dipole-dipole interactions role into material properties, table 1.4 demonstrates the effect of the dipole moment on the boiling point of several substances (source: University of Florida webpage).

#### 1.2.5.2 Molecular dipole in amino acids

As previously said, molecular dipoles are present in amino acids (if the R group is not polar, the dipole points from the amino group to the carboxylic group), specially when they are in their zwitterionic form and thus everytime a water molecule gets close to an amino acid molecule their dipole-dipole interaction comes into play.

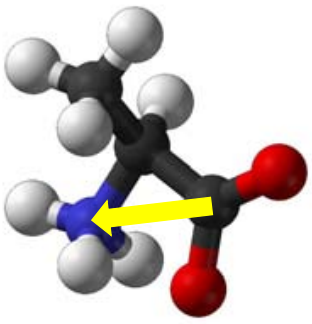

Figure 1.31: Amino acids in their zwitterionic form have a molecular dipole pointing from the carboxylate group to the ammonium group. The figure shows the amino acid L-alanine.

It is difficult to find in the literature experimental data with the values of zwitterionic amino acids dipoles in crystal form. Some values are available for amino acids in water, resumed in table 1.5 (Devoto, 1930; Devoto, 1931; Devoto, 1933;

| Amino Acid | $\mu(D)$ |
|---|---|
| $\alpha$-Alanine | 15.9 - 17.4 |
| L-Asparagine | 14.9 - 17.6 |
| L-Aspartic Acid | 17.4 |
| D-Glutamic Acid | 16.8 |
| L-Glutamine | 15.1 |
| Glycine | 15.7 - 17.0 |
| L-$\alpha$-Leucine | 16.5 |

Table 1.5: Dipole moments of some alpha amino acids in water solution. When two different values have been found for a same amino acid, both of them appear.

Wyman and McMeekin, 1933; Greenstein and Wyman, 1936). If compared to water (ranging from value of 1.5 D in isolated molecules to values of up to 3 D for liquid water), it can be seen that the moment values are much larger.

## 1.3 Introduction to ferroelectric materials

### 1.3.1 Interest in water dipole−dipole interaction

As explained in the previous section, amino acids dipoles seem to play a remarkable role in water-amino acid interaction and also affect some water constants, like water freezing point. More bibliographic search was done about the relation between surface dipoles and ice formation that led us to the interesting results obtained by Ehre et al. on 2010, *Water Freezes Differently on Positively and Negatively Charged Surfaces of Pyroelectric Materials*. In their work Ehre et al. studied how supercooled water freezes at different temperatures over a pyroelectric charged positively (favoured water freezing) or negatively charged (water freezing at lower temperatures).

Although good ice nucleators are often related with a good matching between the ice crystal and the nucleating surface lattice, both Gavish et al., 1992 and Ehre et al., 2010 works point at the importance of the electrostatic effect between water and the surface in order to favour their interaction and favour the freezing of water. This is easly understable since water molecules orient their oxygen atoms with their lone pair electrons pairs toward a positively charged surface, whereas water molecules orient their hydrogen atoms toward a negatively charged surface (Toney et al., 1994; Zhang et al., 2008), so different electrostatic interactions will greatly affect the initial configuration of water around the surface.

Because the electron pairs of oxygen are very different from those of the two

hydrogens, one should anticipate that the water molecules self-assemble and interact differently with the surfaces of opposite charge. But also, as Ehre et al. work points out, it still remains an open question how the different orientations of the water molecules surfaces may promote or suppress the formation of the cubic or hexagonal icelike nuclei. The potential importance in protein folding and ice freezing and at the same time the general lack of knowledge about the nature water-surface dipoles interaction led me to do some research on this field.

Ferroelectric thin films seemed to us a very reasonable sample to work with, since they are water-inert, easily cleaned and reusable, they provide flat study surfaces (rms of the order of few $nm^2$), their properties remain the same in a wide range of temperatures and they can be prepared epitaxially grown, with a controlled orientation of their surface dipoles. Not only this but their polarization can be locally modified with the use of an AFM.

### 1.3.2 Ferroelectricity and piezoelectricity

Ferroelectricity is a property of certain materials which possess a spontaneous electric polarization that can be reversed by the application of an external electric field.

The name refering an analogy with ferromagnetism, though it is somewhat misleading since it has no connection with iron (ferrum) at all. Ferroelectricity has also been called Seignette electricity, referring Seignette or Rochelle Salt (RS), the first material found to show ferroelectric properties in 1921. In the 1950 s, the

Figure 1.32: Rochelle salt crystal, the first ferroelectric material studied. Source: NASA

field of ferroelectricity took an important leap leading to the use of the well-known

barium titanate ($BaTiO_3$) based ceramics in capacitor applications and piezoelectric transducer devices. The development of new ferroelectric ceramics like lead titanate ($PbTiO_3$), lead zirconate titanate (PZT), lead lanthanum zirconate titanate (PLZT), and relaxor ferroelectrics like lead magnesium niobate (PMN) came afterwards (Kanzig, 1957; Panda, Janas and Safari, 1996).

Their use reaches a large variety of applications due to the unique dielectric (non conductive materials that develop an internal electric field if an external electric field is applied), piezoelectric (relation between a mechanical stress and an electrical voltage in solids) , pyroelectric (development of opposite electrical charges on different parts of a crystal that is subjected to temperature change) , and electro-optic properties of ferroelectric materials (Lines and Glass, 1979; Xu, 1991; Paruch, 2003). Until very recently, ferroelectrics have been used in the form of bulk ceramics and, where available, single crystals. These materials turned out as a robust and reliable solution for many applications, but producing thin layers (less than 10 mm) was not achieved until 1980 s, when new methods were developed to fabricate thin-films made of ferroelectrics (Paz de Araujo, 1996). These methods can be classified into three groups: (i) Physical vapour deposition (PVD), i.e. RF sputtering and pulsed laser deposition (Bruchhaus et al., 1999), (ii) Chemical vapour deposition (CVD), i.e. metal-organic chemical vapour deposition (Kijima, 1999) and (iii) Chemical solution deposition (CSD), i.e. sol-gel (Olding, Leclerc and Sayer, 1999).

### 1.3.3 Ferroelectric materials characteristics

At high temperature, ferroelectric materials generally exist in the form of a high symmetry paraelectric phase in which the unit cell is centrosymmetric and exhibits a simple dielectric response to fields (fig. 1.33). This phase follows a structural phase transition when temperature is cooled, breaking its symmetry into a lower symmetry phase and creating a permanent electric dipole moment at the so-called critical temperature $T_c$ (fig. 1.34)(Paruch, 2003).

When a ferroelectric material is in the ferroelectric phase, at least two states (with opposite polarization directions, fig. 1.34) are possible, energy equivalent in absence of electric fields and separated by an energy barrier $U_o$ (Nettleton, 1971). In

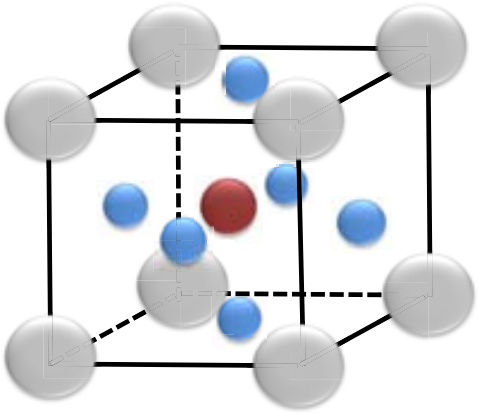

Figure 1.33: Ferroelectric $ABO_3$ (A represented as grey atoms, B as dark red atom and O as blue atoms) type unit cell. When temperature is higher than Tc, the high symmetry of the structure provides no dipole.

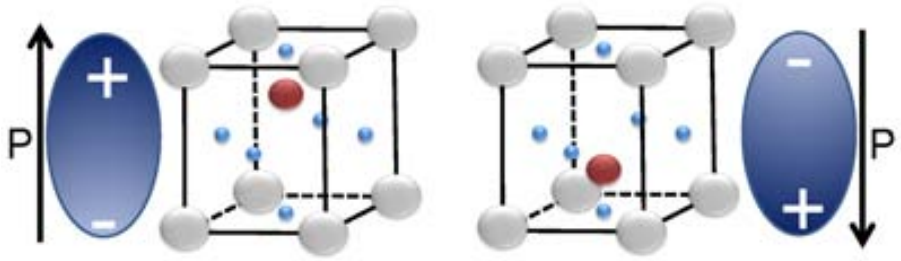


Figure 1.34: Diagram of the symmetry breaking of a ferroelectric $ABO_3$ type into two states. The two new states have a permanent and opposite dipole due to the displacement of the B atom respect to the center.

these states the center of gravity of negative charge in the unit cell is displaced with respect to that of the positive charge, resulting in a stable remanent polarization, P.

Regions with uniform polarization along a crystal are called ferroelectric domains, the application of an electric field decreases the necessary energy to change the polarization of one domain to another with parallel polarization respect the electric field and thus promotes the growth of these regions in the sample (Hippel, 1950).

### 1.3.4 Controlling polarization

Polarization study in ferroelectric samples is performed applying alternating electric fields at low frequencies, this leads to a characteristic polarization vs electric field

hysteresis loop (fig. 1.35). In these loops, as the electric field is increased the sample dipoles start aligning all in the same direction until a maximum saturation polarization ($P_s$) is reached. After that the electric field is decreased and when it reachs a value of E=0 the sample does not have the expected 0 net polarization but a remanent polarization ($P_r$). If the electric field continues decreasing to negative E values the polarization will eventually reach a value of 0, this is the coercive value of the electric field ($E_c$), from this point on the polarization will reach a negative maximum value of saturation and the electric field is again increased to close the loop.

### 1.3.5 PZT ferroelectrics

In tetragonal $PbZr_{0.2}\ Ti_{0.8}\ O_3$ (used in this thesis) the natural polarization is oriented along the c-axis of the material, pointing as a normal respect the (001) surface and thus providing an excellent surface both for AFM polarizing and reading.

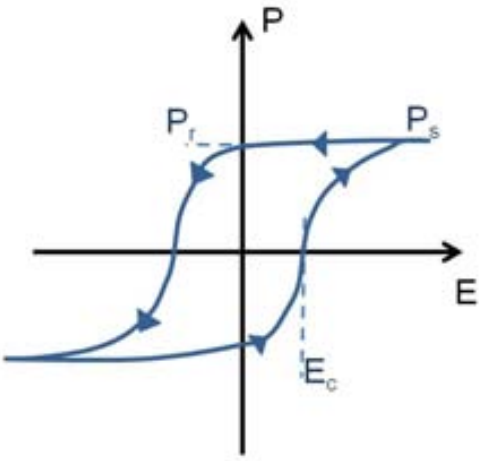


Figure 1.35: Polarization (P) vs Electric field (E) hysteresis loop.

Ferroelectric materials can be classified according to their structure, including: the corner sharing oxygen octahedra, compounds containing hydrogen bonded radicals, organic polymers and ceramic polymer composites. It is not my intention to show a detailed description of each one of those groups and subgroups, but a brief

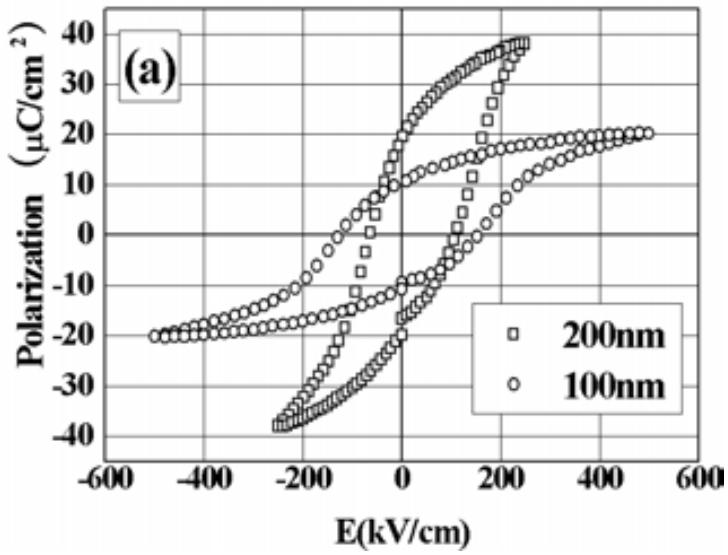


Figure 1.36: Hysteresis loop for ferroelectric PZT3565 obtained by Kim et al. The legend refers to the PZT thin film thickness.

description of used Lead Zirconate Titanate (PZT) ferroelectrics will be provided.

PZT ferroelectrics are corner sharing octahedra type (as perovskites, a family name of a group of materials and the mineral name of calcium titanate $CaTiO_3$ having the previously seen $ABO_3$ structure); a large class of ferroelectric crystals are made up of mixed oxides containing corner sharing octahedra of $O^{2-}$ ions schematically shown in fig. 1.33. Inside each octahedron there is a cation $B^{b+}$ where b varies from 3 to 6. The space between the octahedra are occupied by $A^{a+}$ ions where a varies from 1 to 3. In prototypic forms, the geometric centers of the $A^{a+}$, $B^{b+}$ and $O^{2-}$ ions coincide, giving rise to a non-polar lattice (fig. 1.37). When polarized, the A and B ions are displaced from their geometric centers with respect to the $O^{2-}$ ions, to give a net polarity to the lattice, as explained previously. These displacements occur due to the changes in the lattice structure when phase transitions take place as the temperature is changed. The formation of dipoles by the displacement of ions will not lead to spontaneous polarization if a compensation pattern of dipoles are formed which give zero net dipole moment.

Lead Zirconate Titanate [$Pb(Zr_xTi_{1-x})O_3$, PZT] is a binary solid solution of: $PbZrO_3$ an antiferroelectric (orthorhombic structure) and $PbTiO_3$ a ferroelectric (tetragonal perovskite structure). PZT has a perovskite type structure with the $Ti_4^+$

and $Zr_4^+$ ions occupying the B site at random. At high temperatures PZT has the cubic perovskite structure which is paraelectric but on cooling below the Curie point line, the structure follows a phase transition to a ferroelectric structure. It can be tetragonal or rhombohedral depending on the relation between Zr and Ti (Welberry et al, 2010). The former has the spontaneous polarization along the <100> set of directions, the latter has it along the <111> set of directions.

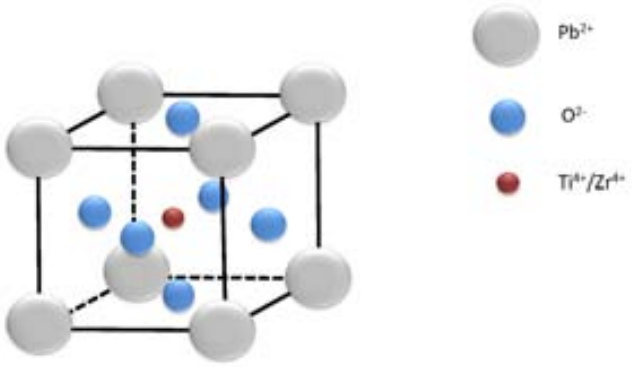


Figure 1.37: Crystal cell of Lead Titanate Zirconate (PZT) in its paraelectric high symetry form.

PZT materials are well known and characterized all over the literature, all their fases have been studied and very accurate graphs are available in order to know the phase of the sample depending on Zr/Ti composition and sample temperature (fig. 1.38)(Paruch, 2003).

Ferroelectric materials are as well piezoelectric, with a linear response of the tension under the influence of an applied electric field and a linear change in the remanent polarization P when subjected to stress S (Paruch, 2003). The piezoelectric response is direction dependent, determined by the coupling between the stress and the piezoelectric constant tensor, d.

$$\Delta P = d \cdot S \tag{1.17}$$

This effective change in the morphology induced by applied stress (i.e. by substrate-film strain) can be used to control the magnitude of the polarization in thin epitaxial ferroelectric films by using substrates with light lattice mismatch resulting in compresive or tensile stress applied to the film.

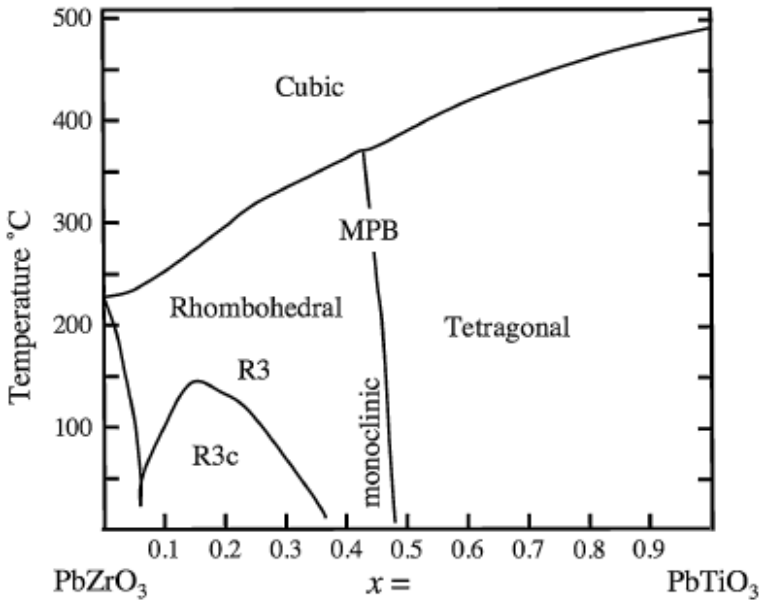


Figure 1.38: PZT phase diagram as appears in Welberry et al. The diagram shows the PZT fase for a given temperature and Zr/Ti relation. MPB stands for *morphotropic phase boundary* and separates the tetragonal and rhombohedral phases.

In the opposite way, the so-called inverse piezoelectric effect, when an electric field, E, is applied, a linear response in elastic strain, e (once again direction dependent) will be induced in these materials

$$\Delta e = d \cdot E \tag{1.18}$$

If the electric field is applied along the polarization direction (c-axis), we can multiply equation 1.18 by the thickness of the sample to obtain the more easily measurable thickness change in response to the applied voltage V in the direction of $d_{33}$ (equation 1.19).

$$\Delta thickness = d_{33} \cdot V \tag{1.19}$$

$d_{33}$ refers to the relative orientation between the stress and poling directions, being it two times smaller when they are perpendicular ($d_{31}$ model) than when they coincide ($d_{33}$ model) (Yu et al., 2001).

In order to control the polarization in PZT thin films, an electric field stronger than the coercitive field of the material must be applied. In a standard way the

tension is applied through the sample using two macroscopic electrodes in a capacitive structure. But the upper electrode can be replaced by a conductive AFM tip in contact with the PZT sample that is used as a force field local source while the conductive bottom part of the sample acts as the lower electrode (fig. 1.39).

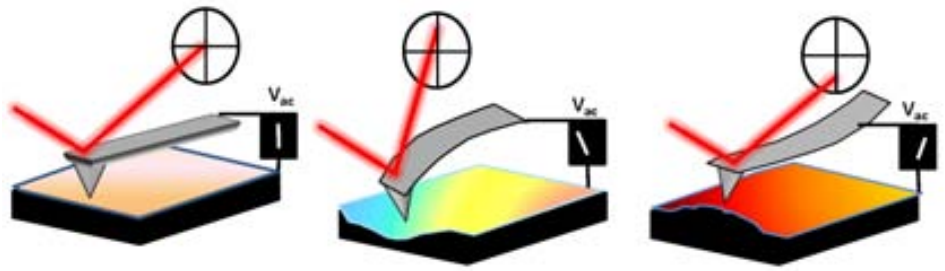


Figure 1.39: A conductive AFM tip in contact with the sample is used to control the ferroelectric polarization as top electrode while the conductive bottom part of the sample acts as the lower one. Short $\Delta V$ pulses or continuous $\Delta V$ while slow scanning are used for polarize a circular domain or a bigger zone respectively.

### Piezoresponse Force Microscopy

The inverse piezoelectric efect is used for Piezoresponse Force Microscopy (PFM) imaging of ferroelectric domains (Eng et al., 1999; Paruch, Tybell and Triscone, 2001; Terabe et al., 2003). Applying a small oscillating voltage (around 10 times lower than the voltages used for polarization switching) via the metallic AFM tip in contact with the film surface. The resulting electric field couples to $d_{33}$ in c-axis oriented films, exciting a local response in the film by the inverse piezoelectric effect. The sign (contraction vs elongation) of this piezoresponse depends on the orientation of the ferroelectric polarization in the underlying region with respect to sign of the applied voltage (fig. 1.40). PFM measures the sample mechanical response when an electrical voltage is applied to the surface with a conductive AFM probe. Two important signals are obtained during PFM acquisiton: amplitude and phase. In response to the electrical stimulus, the sample locally expands or contracts. When the tip is in contact with the surface and the local piezoelectric response is detected as the first harmonic component of the tip deflection, the phase , of the electromechanical response of the surface yields information on the polarization direction below the tip while in-plane domains are seen in the PFM amplitude

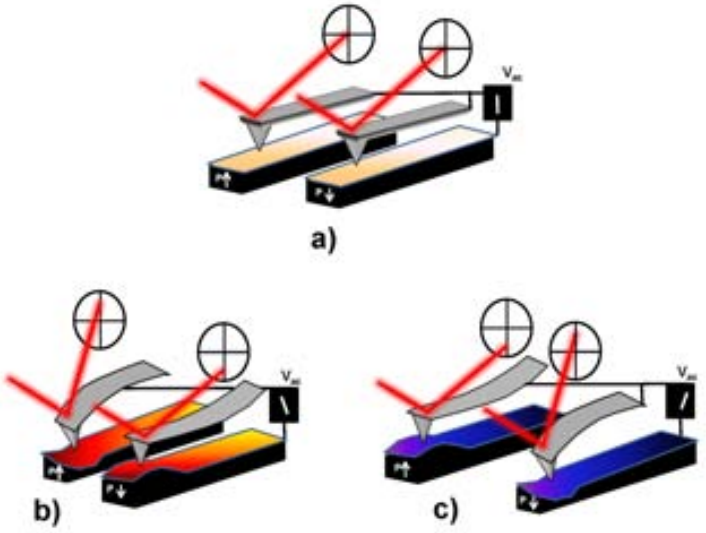


Figure 1.40: Sign dependence of the sample strain with domains (having vertical and opposite polarization). a) No voltage is applied. b) A positive voltage is applied. c) A negative voltage is applied.

image. For domains with polarization vectors oriented normal to the surface and pointing downward, the application of a positive tip bias results in the expansion of the sample, and surface oscillations are in phase with the tip voltage, =0°. For domains with polarization vectors oriented normal to the surface and pointing upwards, the response is opposite and =180°.

For a tip voltage of the order:

$$V_{tip} = V_{dc} + V_{ac}\cos(\quad t) \tag{1.20}$$

The relationship between the strain and the applied electric field for typical vertical PFM (in the $d_{33}$ component, since it couples directly into the vertical motion of the cantilever) is resulting in piezoelectric strain in the material that causes cantilever displacement:

$$z = z_{dc} + A(\quad V_{ac}\ V_{dc})\cos(\quad t + \quad) \tag{1.21}$$

For PZT materials with a thickness of $\sim$ 100 nm, $d_{33}$ ranges from 3 to 10 pm/V. A deeper understanding about the very complex interactions between the AFM tip and the substrate during domain writing and imaging is now achieved, both theoretically (Kalinin and Bonnell, 2001; Kalinin and Bonnell, 2001; Lambert, Guthmann

and Saint-Jean, 2003; Molotskii, 2003) and experimentally (Ganpule et al., 2002; Shvebelman, et al., 2002; Harnagea, et al., 2003).

PZT thin films provide multiple properties (smooth water innert surface, reusable, polarization reversability, precise control on the size of polarized zones, several months of polarization lasting...) that turn them a very interesting sample for the study of water-dipoles interaction. In addition, AFM is an ideal technique for both orientating the desired dipole configuration and also peform the study of water interaction with it (Hidaka et al., 1996; Tybell, Ahn and Triscone, 1998).

# Chapter 2

# INSTRUMENTAL SETUP

## 2.1 5500 Agilent microscope

Unless otherwise stated, all AFM experiments performed in this thesis have been obtained using a 5500 Agilent Technologies AFM (Agilent Technologies, Santa Clara, CA). In addition to the basic contact AFM and STM functions, this microscope is able to work in the AM−AFM mode. It also allows the user to control the voltage and current applied to the the sample or to the probe, so EFM imaging is also possible. The scanning operation is performed by the cantilever. Two AFM Agilent scanners have been used (see tables 2.1 and 2.2 for the specifications), both of them in the open loop mode. These multipurpose, top-down scanners are ideal for imaging in fluids, air and under controlled temperature and different environmental conditions. To deliver high-resolution imaging results, a balanced-pendulum design is utilized to eliminate artifacts in the image by keeping the relative position of the laser spot fixed in relation to the cantilever throughout the scan cycle. The cantilever holders assemblies of the scanner are completely interchangeable and are made from polyether ether ketone (PEEK) polymers, have low chemical reactivity, and can be used in a wide range of solvents. The scanning head is made of piezoelectric ceramics. The photodiode detector unit is placed in the rear part of the scanner module far from the sample conditions (fig. 2.1).

The microscope scanner head can be installed in an ambient chamber in order to control, for example, the RH. This was the main reason for the choice of this AFM, the electronics are kept outside of this chamber, not being exposed to conditions that could damage the system. The sample stages are loaded by magnetic

| | |
|---|---|
| Maximum range for imaging | 90$\mu$m ×90$\mu$m |
| Z Range | 8$\mu$m |
| Vertical noise | 0.5 Å RMS |

Table 2.1: Large Scanner specifications.

| | |
|---|---|
| Maximum range for imaging | 9$\mu$m ×9$\mu$m |
| Z Range | 2$\mu$m |
| Vertical noise | 0.2 Å RMS |

Table 2.2: Small Scanner specifications.

suspension, eliminating mechanical drift, a modular design allows the plates to be used in many options, such as open liquid cells, flow-through cells, salt-bridge cells (electrochemistry), live-cell imaging and glass microscope slides. The most used stage in this thesis work possess a thin glass in the center upon which the sample is usually positioned and provides some degree of electrical insulation, also, if voltage application is needed, it can be connected with the instrument or grounded using a metallic connector.

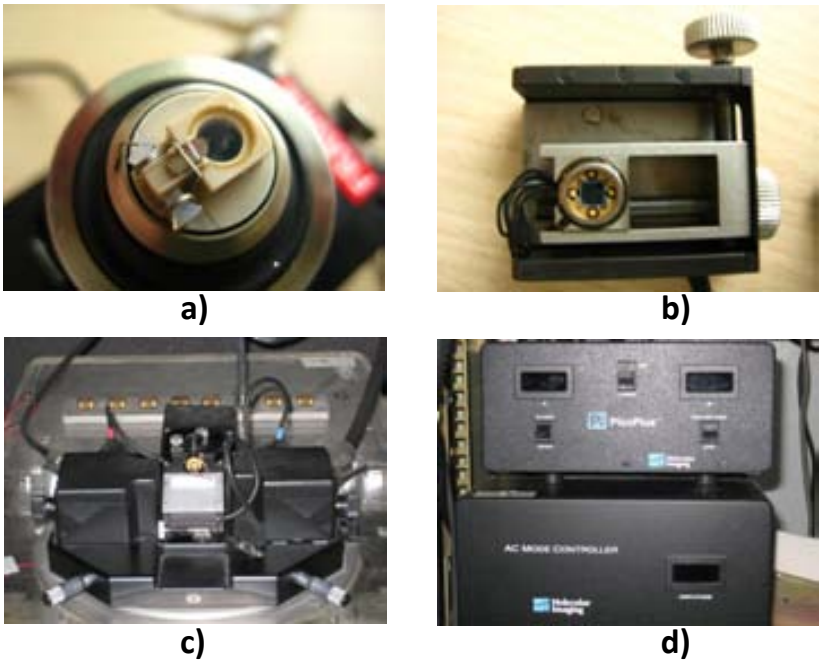


Figure 2.1: a) AFM scanner head with an AFM cantilever. b) Photodiode. c) Scanner and photodiode mounted on the glove box. d) Electronics.

**Optical systems**

A NAVITAR zoom lens system was used to locate the position of the tip over the sample in a macroscopic scale. It provides an optical magnification range of 2.1x - 13.5x to the camera. This is enhanced if the Molecular Imaging scanner is placed in the system (due to inner amplification lens), ranging from 3.8x to 24.3x. When more optical resolution was needed to study samples, an inverted optical microscope (external to the AFM system) was used, model Zeiss Axio Observer z1m with Epiplan-Neofluar 5x, 10x, 20x, 50x and 100x objectives.

## 2.2 Vibration isolating chamber

AFM experiments are very sensitive to any external source of vibrations, being the most common ones ambient noise and ground vibrations. In order to isolate the system from external sources of noise our group has designed and built a special chamber able to keep the AFM microscope and glove box isolated from these sources of noise.

The base structure is a robust aluminium structure (1.70 m $\times$ 0.90 m $\times$ 0.90 m) provided with vibration absorving material filled legs. The four walls (three walls and one door), the top and the base of the cage consist all of them of 1.5 cm thick wood conglomerate panels over the aluminium structure. The external face of these panels is fully covered by an isolating sound-reflecting sheet made of 5 mm thickness bituminous flexible and heavy compound, 10 Kg/m$^2$, it is provided with the desired physic characteristics to reduce surface vibrations (ref. LA-10, provider: Acustica Integral, fig. 2.2). The internal face of the panels is fully covered by an absorbing expanded polyurethane compound (thickness 25 mm, 30 Kg/m$^3$) with a special alveolar compression process to enhance its absorption level, with an average absorbing coefficient nrc = 0.77 (ref: Acusticell 25 mm, provider: Acustica Integral).

A flat 90 kg marble block is hanging inside the chamber by four strong springs ($k_c$ = 557.44 N/m, Gutekunst Federn). The glove box with the AFM microscope lies on the marble block. This block can hang freely or lay over a platform which one can retract or replace by a crank. When the system is lying over the platform,

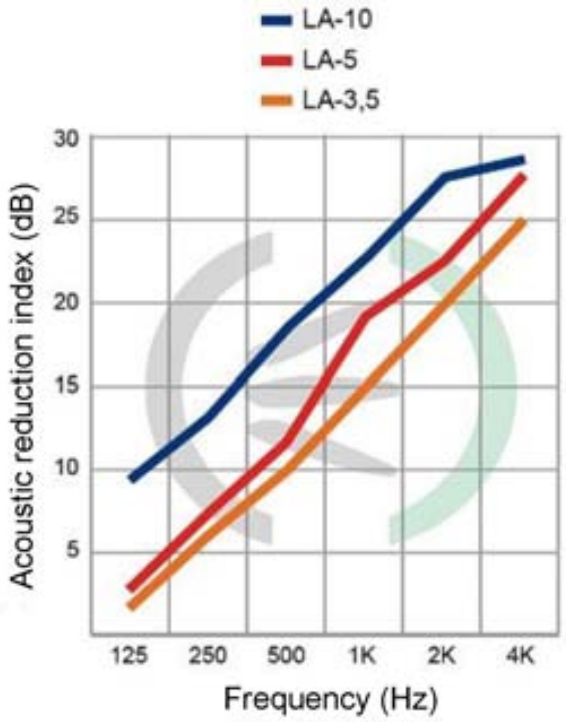


Figure 2.2: Acoustic reduction for several compounds, LA-10 was chosen due to its higher index. Source: Acustica Integeral.

stability to manipulate samples and AFM cantilevers is provided. When it is hanging stable (the system was designed to have the springs half elongated in their linear working range), the system becomes highly isolated from the surrounding noises and vibrations, . For an efective isolation, the frequency of the springs must be tens of thousands orders of magnitude lower than that of the AFM cantilever (usually few hundreds of KHz).

The frequency of a spring is:

$$f = \frac{1}{2 \cdot \pi}\sqrt{\frac{k_c}{m}} \tag{2.1}$$

where $m$ is the total mass of the hanging system. Thus, for a $k_c = 557.44$ N/m spring holding 25 Kg mass [$\sim$100 Kg (marble + AFM) system hanging from four springs] we have a resonance frequency of $\sim$0.7 Hz.

This system (fig. 2.3) is very effective in isolating the AFM microscope from most sources of external noise, achieving molecular resolution in spite of the non ideal laboratory conditions.

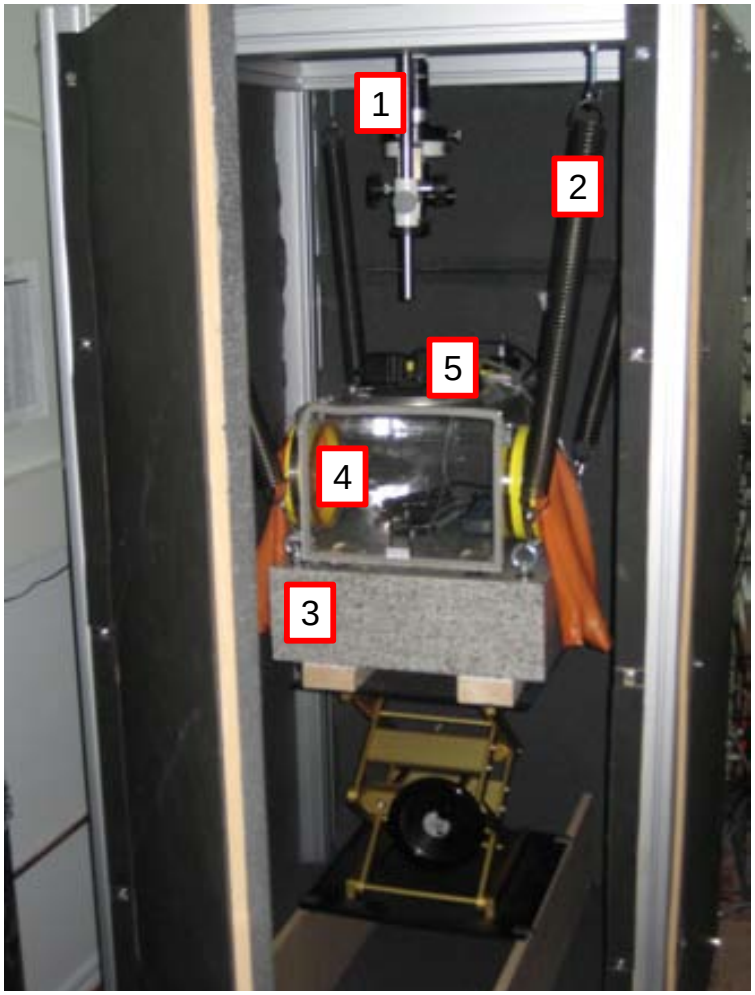


Figure 2.3: The AFM system used in this thesis was placed inside an isolating chamber. 1: Optic system. 2: Springs. 3: Marble bloc. 4: Glove box. 5: AFM scanner.

## 2.3 Sample stage temperature control

The decreasing of the sample s temperature was achieved using two different setups:

a) A commercial Agilent cooling stage connected to a Lake Shore Temperature Controller (model 331), provided with internal temperature measurement. From typical room temperatures of 25°C, it ranges down to $\sim$ -15°C and allows two different temperature variation modes, one for small and precise temperature changes and another one for more fast and broad changes.

b) A homemade temperature controller consisting on a Peltier system with a copper sample holder on the upper part and a copper block provided with a water circuit inside for heat dissipation purpouses in the lower part. The chosen Peltier

system was a TEC2−2.5 Thermoelectric Cooler Element, 2.5A (ThorLabs inc), its dimensions (1.6 cm x 1.6 cm) fit with the Agilent sample holder where it was attatched and its current and voltage range (up to 2.5 amps and 3.6 V) are easily achieved by common instruments. What is more important, it can be operated under high humidity conditions. The system was designed in our group as to match with our AFM model requirements and was fabricated by the IFAE mechanical workshop (fig. 2.4). Since no thermocouple was attached, calibrating curves were made prior to its use. The lowest achieved temperature was -18°C.


Figure 2.4: a) Top and b) side view of the self made cooling stage. The system was mounted in a commercial Agilent sample stage.

### Instrumental drawbacks when scannning at low temperature

When performing the low temperature experiments using a 5500 Agilent microscope at ambient RH, the most important drawback is the fact that water droplets condense all over the inner part of the scanner lens, becoming impossible to work due to laser path interruption by these water droplets. To solve this problem I installed a small tubbing circuit inside the scanner head in order to provide a low $N_2$ flux to remove all the humidity inside the scanner. With such modification, condensation was avoided but some degree of noise was added to the system due to the $N_2$ flux. After taking some images with the flux turned on and off several times, we concluded that this noise is far below our acceptable limits. Figure 2.5 shows the calculated RH on the sample holder for a given temperature and a given RH inside the glove

box. When the RH on the sample holder reaches 100%, water condenses on the sample holder. This is calculate using the ambient temperature, the RH inside the glove box and the temperature on the sample holder in order to obtain the RH on the sample holder and its temperature of condensation.

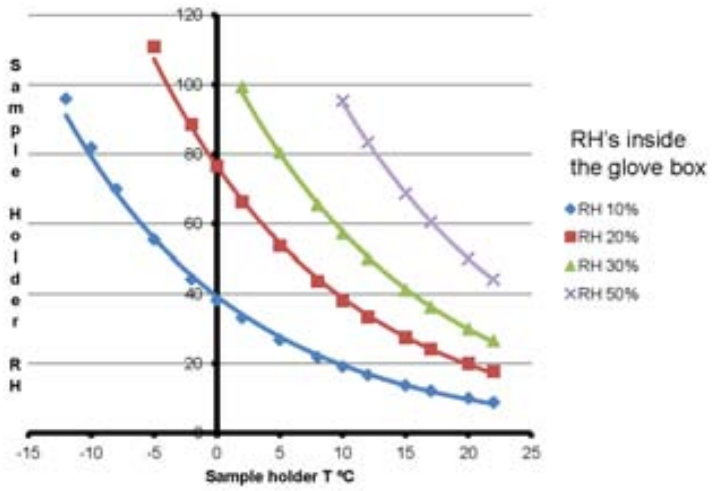


Figure 2.5: RHs on the peltier sample holder for a given temperature on it at several glove box humidities. The ambient temperature has been set at 22°C in these calculations.

Once the condensation problem was solved, I had to face the problem derived from the thermal gradient between the sample and the scanner, such a gradient induces melting of ice so its study becomes impossible. The ideal solution would consist of placing the whole AFM inside a thermalized chamber close to 0°C. Unfortunately, during this thesis work the construction and acquisition of such a chamber was not provided. I tried to thermalize the glove box placing a liquid $N_2$ container inside it with a small aperture, but the temperature decrease was not sufficient .

Since a gas $N_2$ flux was now reaching the scan, I decided to cool down the nitrogen flow that contacts the lens to cool down the whole scanner head. For this purpose the nitrogen is conducted through a copper circuit at about 0°C before reaching the scanner. With this method the temperature of the cantilever falled down to reasonable levels able to admit the growth of ice under it. At this point the ice formation is close to equilibrium and is still difficult to achieve, but once the ice is formed, it lasts long enough under the cantilever, being then possible to perform AFM scans over it (fig. 2.6).

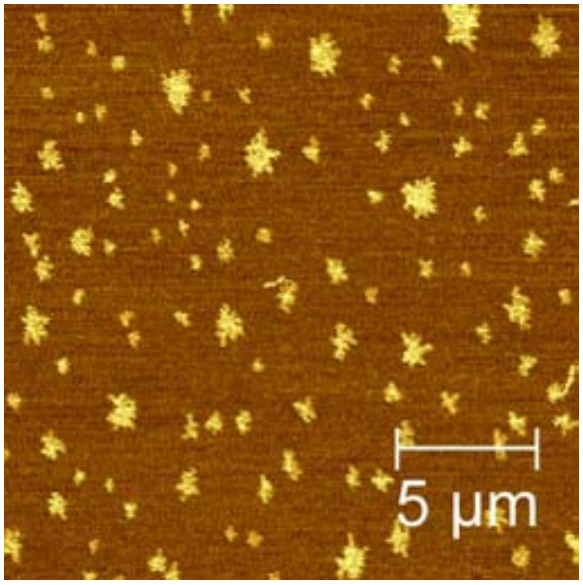


Figure 2.6: AM-AFM phase images of ice over mica. The ice was formed while scanning, an indication of the efectiveness of the system.

Drift is also a drawback, while scanning at low temperatures the center of the image has to be replaced during the experiment and the tip has to be withdrawn in order to correct of the contraction along the z-direction.

## 2.4 Humidity control system

Usually my experiments required the control of the RH inside the glove box, some times down to levels of RH $< 5\%$ and up to RH $> 90\%$ during the same experiment. The control of the RH was achieved using a glove box connected to a home-made humidity control system. This glove box must allow both insitu sample preparation and the performance of the AFM experiments, so that it must have space enough in order to allow sample manipulation and contain the AFM scanner (figs. 2.3 and 2.7).

The RH inside the glove box is adjusted to desired values using $N_2$ gas bubbled through Milli−Q water. A $N_2$ gas container is connected via teflon tubing to the AFM glove box (with eight inlet/outlet mm ports for gases or wires). The system provides a two ways path, controlled by three gas stopcocks that enable the nitrogen to flow freely or prior bubbling through MilliQ water before reaching the glove box

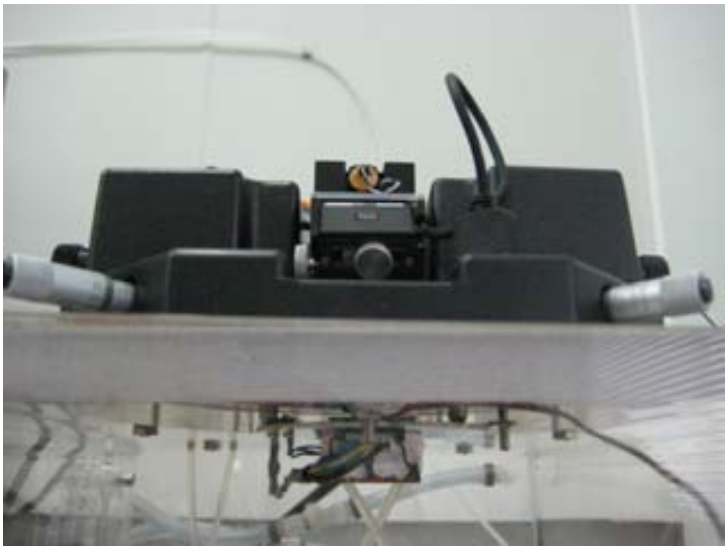

Figure 2.7: The scanner electronics (top part) is separated from the cantilever, sample and sample holder (lower part) by the glove box. While the sample stage and the cantilever are in the controlled humidity conditions the electronics remain outside the glove box. In the rear part the inlet of the $N_2$ gas can be seen.

(fig. 2.8). The relation between dry and wet nitrogen can be controlled and the relative humidity inside the glove box can be adjusted to a desirable value ranging from $\leq$ 5% to >95% (when values >70% are needed, the water container must be heated at 40°C). This system cannot reach high accuracy for small changes on the RH, and changes <3% are difficult. However, the efficiency of the system is satisfactory for my experimental purpouses. Also for RH higher than 90%, water droplets condense all over the inside of the glove box chamber and the teflon tubing. Only premier nitrogen (Carburos Metálicos, purity: 5.2, <2 ppm $H_2O$) and Milli-Q water (<18.2 M$\Omega$ cm at 35$^o$C and <4 ppb TOC) have been used in this system, minimizing the impurities that can reach the sample.

Humidity range inside the glove box was always checked in real time using a hygrometer (2080R from Digitron Instruments) with a nominal accuracy of 1.5%.

## 2.5 SPFM setup

Scanning Polarization Force Microscopy (see introduction chapter) is a technique not included in commercial instruments, so that some additional electronics are

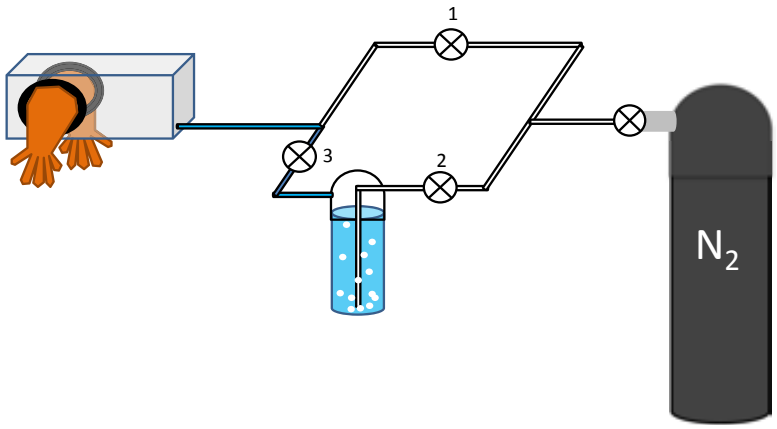


Figure 2.8: The humidity control system enables adjusting the RH value inside the glove box. To reach minimum values of RH (<5%), gas cockstop 1 must be fully open while gas cockstops 2 and 3 must be closed. In order to reach a certain value of RH, gas cockstops 2 and 3 must be fully open while gas cockstop 1 is adjusted to enable the desired amount of $N_2$ bubbling through the water. In order to reach high RH levels (>70%) the water bubbling system can be placed inside a hot water (40°C) bath.

required. In this section the exact setup of our SPFM system will be described.

**Required electronics:**

(i) A DS335 SRS function generator: it generates the reference synosoidal signal at a chosen amplitude and $\omega$ frequency (in these experiments typically 7 $V_{p-p}$ and 4 KHz) which is sent to the two lock-in amplifiers to be used as the reference signal, and also to the cantilever's tip as the ac excitation signal (in fig. 2.9 this instrument will appear labelled with as 1).

(ii) Two DSP (Digital Signal Processing) lock-in Amplifiers (SR830 SRS): they read and amplify the response of the cantilever tip to the excitation signal at a chosen frequency. As explained in the introduction chapter, two lock-in are needed to read both $\omega$ (lock-in amplifier ♯1) and $2\omega$ (lock-in amplifier ♯2) response. $\omega$ signal gives us the surface potential signal while $2\omega$ is used to get topographic signal along with the polarization (in fig. 2.9 lock-in amplifier ♯1 will appear labelled as 2 and lock-in amplifier ♯2 as 3).

(iii) A Mainframe (SIM900) to assemble RS SIM serie systems.

(iv) A summing amplifier (SIM980): A four-input, unity-gain amplifier for combining multiple analog signals from DC to 1MHz (in fig. 2.9 it will be labelled as

4).

(v) An analog PID (ProportionalIntegralDerivative) controller (SIM960): A feedback electronic system designed to maintain stability in systems requiring low noise and wide bandwidth (in fig. 2.9 it will be labelled as 5).

(vi) A Breakout Box model S/N 316-001163 from Molecular Imaging: a self-powered device used to test and rewire the signals coming from and going to the AFM head (in fig. 2.9 it will be labelled as 6).

**Electronics connection:**

Figure 2.9 shows a scheme of the electronics connections. This configuration was developed and tested for the first time by P. Ashby at the Lawrence Berkeley National Laboratory. The signals communicating the controller and the microscope (brown color in the diagram) are redirected to the breakout box to be modified in the following way: The deflection signal of the cantilever from the AFM head (red color) is used as the input signal for the two lock-in amplifiers while the ac signal coming from the function generator (dark blue color) is used as the reference ac signal. One lock-in amplifier (the lower one in the graphic) reads the amplitude of the second harmonic (2 ) of the deflection signal and sends it out (yellow color) to the breakout box, using it as the error signal for the AFM z−position feedback. It keeps the tip-sample distance constant by changing the piezo position. Topography information along with dielectric constant are obtained using this value.

The other lock-in amplifier (the upper one in the graphic) reads the amplitude first harmonic ( ) of the deflection signal (red color) and sends it (orange color) to the analog PID controller. The PID controller sends out a modified signal feedback (light blue color) to null the component. From this modified feedback signal, the Kelvin Probe signal is obtained and sent back as an external input to the AFM electronics to obtain a KPFM image. This signal is also the dc component that along with the ac reference signal (dark blue) will be added and sent to the the breakout box (purple color) as the excitement source for the cantilever.

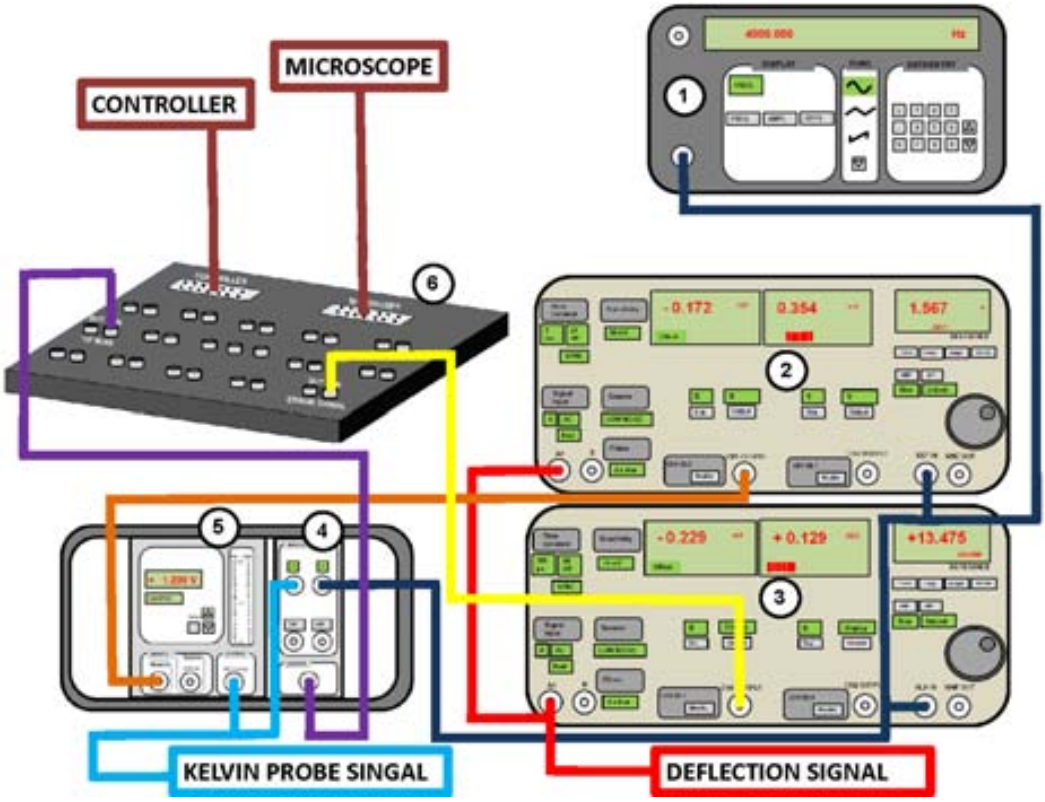


Figure 2.9: Diagram showing the connexions required for a SPFM experiment. The instruments required for this system have been descrived previously, and are: (1) function generator, (2) lock-in 1, (3) lock-in 2, (4) summing amplifier, (5) PID controller, (6) breakout box.

## 2.6 Probes

During this thesis experiments, different scanning parameters and probes have been used depending on the AFM working mode and the experimental requirements. The next tables show the information relative to the most important parameters used for each AFM mode and the cantilevers used in each one. Figure 2.11 shows some SEM images of a typical probe and tip (as the provider offers), all the probes used in this thesis had <10 nm radius (ultrasharp tips).

Table 2.3 shows the parameters used during the scanning operation for different AFM modes. Unless otherwise specified, when an AFM experiment has been performed, these parameters were used. All the scannings operations used 256 points/line.

Table 2.4 shows the parameters of the used cantilevers. All them were made out of $n^+-$silicon and with a resistivity of 0.01-0.02 $\Omega$·cm and a tip height of 10-15 $\mu$m.

| AFM mode | Free amplitude | Aproach speed | Stop setpoint | Scanning speed | Scan setpoint |
|---|---|---|---|---|---|
| Contact | - | 6 $\mu$m s | 0.3 V | 1.3 lines s | 0.5 V |
| AM | 2 V | 6 $\mu$m s | 90% free ampl. | 1.5 lines s | 1.4 V |
| SPFM | - | - | - | 0.7 lines s | - |
| EFM | 1 V | 6 $\mu$m s | 90% free ampl. | 1.2 lines s | 1.5 V |
| Contact molecular resolution | - | 6 $\mu$m s | 0.3 V | 20 lines s | 0.4 V |
| PFM writing | - | 6 $\mu$m s | 0.3 V | 1 line s | 0.7 V |
| PFM reading | - | - | - | 1.5 line s | 0.7 V |

Table 2.3: Operational parameters for different AFM modes.

| Ref. | AFM Mode | Thickness/Length/ Width ($\mu$m) | Resonance Frequency | Force Constant | Coating |
|---|---|---|---|---|---|
| PPP-CONT | Contact | 2.0±1/450±10/50±7.5 | 6-21 kHz | 0.02- 0.77 N m | none |
| PPP-NCHR | Tapping | 4.0±1/125±10/30±7.5 | 204-497 kHz | 10- 130 N m | Al-coating |
| PPP-CONTPt | SPFM PFM | 2.0±1/450±10/50±7.5 | 6-21 kHz | 0.02- 0.77 N/m | Pt/Ir-coating |
| PPP-EFM | EFM PFM | 3.0±1/225±10/28±7.5 | 45-115 kHz | 0.5- 9.5 N/m | Pt/Ir-coating |
| PPP-CONTR | Molecular resolution | 2.0±1/450±10/50±7.5<br>2.0±1/450±10/50±7.5 | 6 - 21 kHz<br>6 - 21 kHz | 0.02-0.77 N/m<br>0.02-0.77 N/m | Al-coating<br>Al-coating |

Table 2.4: Cantilevers parameters.

(Provider: NanoandMore Gmbh).

### Photodiode sensitivity and cantilever s $k_c$

Several force curves were peformed on clean $SiO_2$ (duration: 3 s. Num. of points: 2000) to calculate the photodiode sensitivity. Only the trace signal (red line in fig. 2.12) was used. We found sensitivities around 15 mV/nm four our probes.

To extract a cantilver s $k_c$ I assumed a linear relation between $k_c$ and frequency, then it becomes easy to extract $k_c$ from the real f: using the range of frequencies and the range of $k_c$ given by the provider, we obtained the real $k_c$ by linear extrapolation (see fig. 2.13).

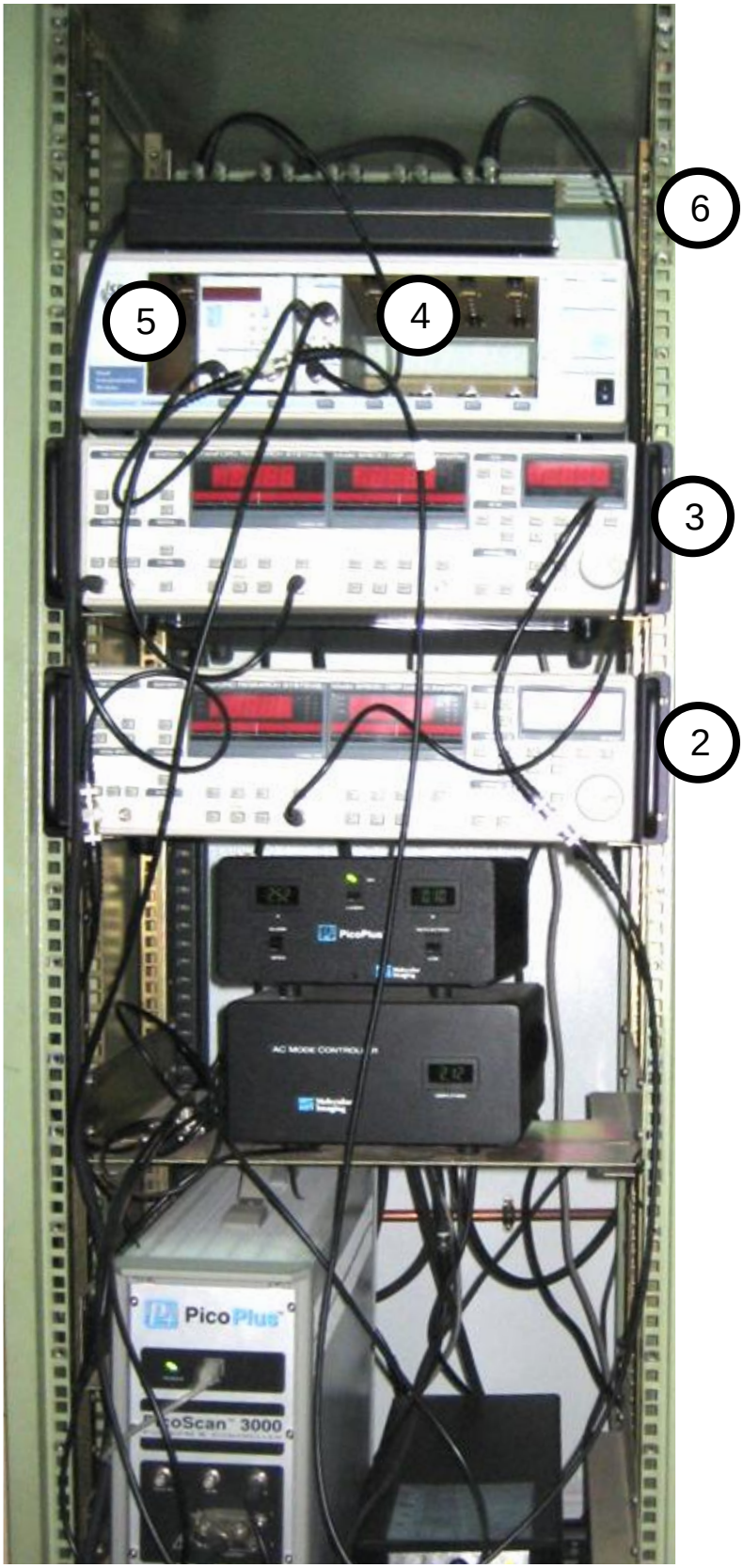


Figure 2.10: SPFM setup used in this thesis work. Labelled with numbers are the equivalent instruments displayed in figure 2.9. In the lower part of the image the controllers for the AFM microscope and the AM-mode can be seen.

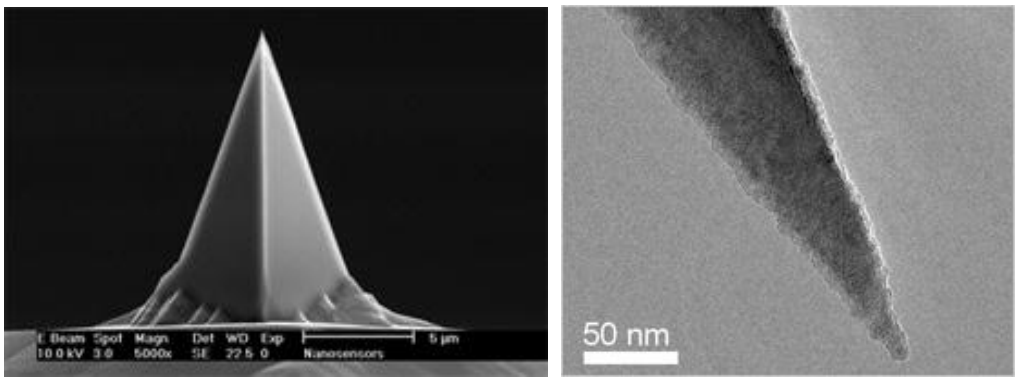


Figure 2.11: a) AFM tip SEM image and b) magnification of a PPP−NCH tip. Source: Nano and More.

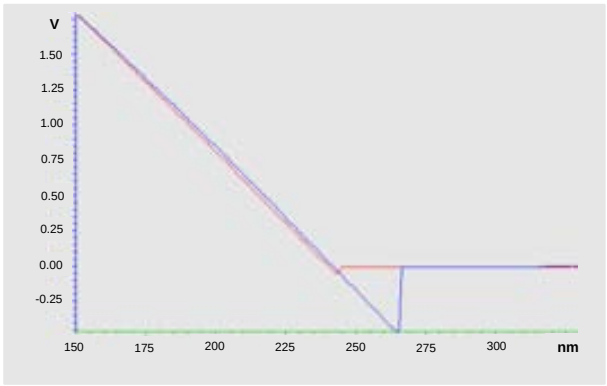


Figure 2.12: Approach (red) and retract (blue) signals in a force curve using a PPP-CONT cantilever on clean Au.

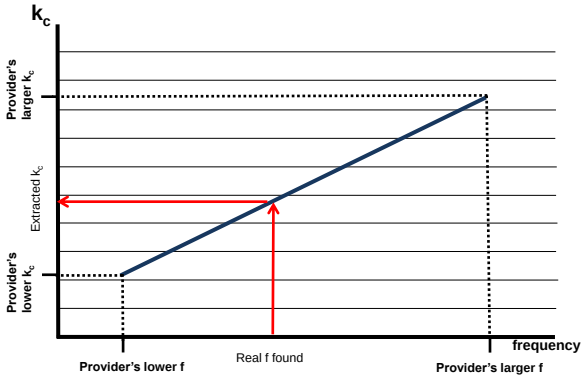


Figure 2.13: Using a linear relation between frequency and $k_c$ it is possible to extract a close value of the real cantilever s $k_c$ from the measured f.

# Chapter 3

# EXPERIMENTAL

## 3.1 Amino acid crystallization

Two different methods were used to perform amino acid crystalization from the as-received powder:

a) Precipitation through slow acetone diffusion into an amino acid water solution.

b) Precipitation by slow oversaturation triggered by a negative temperature ramp.

**Precipitation through slow acetone diffusion:**

Precipitation of a solute by slow co-solvent diffusion has the following requirements: (i) the solute must be soluble in a solvent A, (ii) the solute must be not soluble in a volatile solvent B and (iii) solvents A and B must be miscible.

The operation is carried out as follows: a container with a solution of the solute in solvent A is placed inside a sealed chamber together with a separated container with pure solvent B, and the system is left unperturbed for several hours/days. The volatile solvent B slowly diffuses inside the A solvent solution and triggers the slow precipitation of the solute. If the process takes place slow enough, the precipitation will take place in the form of single crystals (fig. 3.1).

In this thesis work all amino acids crystals obtained by this method used water as solvent A and acetone as the volatile solvent B. The exact process was performed as follows.

(i) All the necessary laboratory apparatusses were carefully cleaned to avoid any contamination of the final solution. Sequential cleaning with water-soap solution,

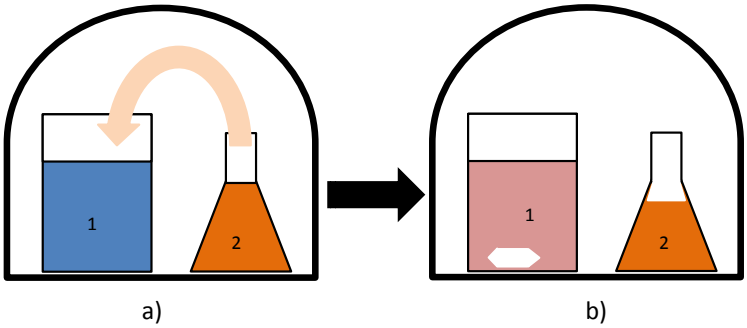


Figure 3.1: Amino acid precipitation. a) two glass beakers are placed in a sealed container, glass beaker number 1 contains the water solution of the amino acid and Erlenmeyer number 2 contains a volatile solvent where the amino acid is not soluble. b) Through slow difusion, the volatile solvent mixes with water and the amino acid precipittes in the form of single crystals.

tap water, acetone immersion under ultrasounds and Milli-Q water immersion under ultrasounds were employed to clean all the required laboratory material.

(ii) Amino acids, as well as water and acetone, must be of high purity (HPLC grade acetone, Milli-Q water and highest purity commercial amino acids were used).

(iii) A slightly undersaturated amino acid water solucion is prepared, the slight undersaturation ensures that small temperature changes (as the decrease of temperature during the night) in the system will not trigger the precipitation too soon. The solution is filtered to a glass beaker to remove any non-desirable nucleating agents.

(iv) The glass beaker containing the filtered amino acid solution, and an Erlenmeyer (the smaller aperture of an Erlenmeyer respect to that of a glass beaker is desirable) containing the acetone were placed inside a sealed chamber.

(v) The system was left in the dark, avoiding exposure to light and at ambient temperature. When the crystals were formed, they were removed and placed in a proper container.

**Precipitation through slow oversaturation under temperature decreasing:**

The second crystallization method is based on the dependence of the solubility with the temperature: solubility is proportional to temperature. Thus cooling of a warm saturated solution triggers the precipitation of its solute. Amino acids single crystals obtained by this method in this thesis work were prepared as follows:

(i) All the necessary laboratory apparatuses were carefully cleaned to avoid any

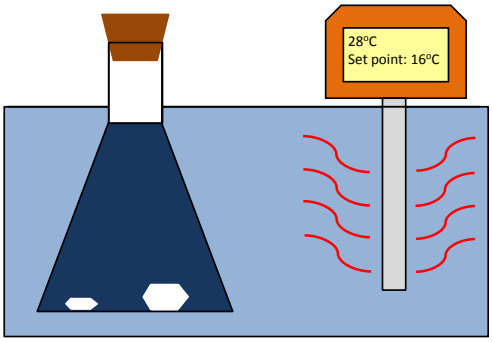


Figure 3.2: Amino acid precipitation. A warm saturated water solution of the amino acid is placed in a temperature controlled bath and then is slowly cooled, triggering precipitation from the now oversaturated solution.

contamination of the final solution, as explained in the previous method.

(ii) Amino acids, as well as water, must be of high purity.

(iii) A warm (∼45°C) saturated solution of the amino acid is prepared and filtered to an erlenmeyer immersed into a temperature-controlled bath set slightly over the solution temperature (to avoid sudden precipitation by negative temperature gradient).

(iv) The Erlenmeyer is sealed. The bath temperature is then slowly cooled down (in this thesis I used a slope of -0.05°C/h) to ambient temperature. If the precipitation rate is slow enough, crystals are formed. The water bath temperature was controlled using a LAUDA Ecoline Staredition E 3xx. This programmable system allows very precise temperature control with slow and accurate temperature variations. It also provides internal temperature measurement, fast heating, homogeneous temperature all over the water bath and allows readjusting of the conditions while the process is running.

Both described methods need to prepare an initial amino acid solution in water. As already mentioned, solutions must be of high purity, so only Milli-Q water (<18.2 MΩ·cm at 25°C and <4 ppb TOC) must be used and it must contain no buffer compounds that could be incorporated in the crystal structure as impurities. These two methods have provided large single crystals (with no inner deffects and dimensions ranging from 5 mm to 2 cm) for: L-alanine, D-alanine, L-valine, D-valine, DL-valine, L-leucine and DL-leucine. However, DL-alanine crystallizes in the form of sharp long

| Amino Acid | Purity | Molecular Weight | Melting Point | Solubility |
|---|---|---|---|---|
| L-Alanine | ≥99.5% | 89.09 g/mol | Decomposes: 210°C | 166.5 g/L $H_2O$ (25°C)<br>sparingly soluble in ethanol |
| D-Alanine | ≥99% | 89.09 g/mol | Decomposes: 210°C | soluble in cold water<br>cold water |
| L-Valine | ≥99.5% | 117.15 g/mol | 315°C | Partially: cold water<br>Very slightly: methanol, acetone |
| D-Valine | ≥99% | 117.15 g/mol | 302-303°C<br>decomposes at 230°C | 56 g/l in water (20°C) |
| L-Leucine | ≥99.5% | 131.17 g/mol | Sublimes: 144°C | Soluble: cold water. |

Table 3.1: Amino Acids physical and chemical properties, source: Material Safety Data Sheet.

needles. I did not succeed in the crystallization of DL-tryptophan in any of the described methods. All the amino acids were received as high purity crystalline white powder from Fluka. In our opinion the second method is desirable over the first one due to no extra chemicals contacting the amino acid solution. However, it may have some drawbacks like the possibility of growing some undesirable fungus-like organisms into the solution. This can be avoided purging the erlenmeyer with nitrogen gas.

Fresh surfaces were generated either by cleavage using a razor blade (with those crystals presenting a 3D structure) or by exfoliation with a sticky tape (with those crystals presenting a 2D structure of layers bonded between them by weak forces).

## 3.2 PZT samples

The PZT ferroelectric films used in this thesis work were purchased from Phasis, Switzerland and are epitaxially grown using off-axis RF magnetron sputtering on STO and Nb-STO substrates. All the samples have a 10 x 10 $mm^2$ area. The compound is tetragonal and ferroelectric at room T with a $T_c$ of ∼735 K, the bulk material possess an in-plane lattice parameter of 3.95 Å, and a c-axis length of 4.15 Å, although these values may differ due to substrate induced strain (Haeni et al., 2004). The remanent polarization (see introduction) is ∼40 $\mu C$ $cm^2$ and is directed along de c-axis (again this value may differ due to substrate induced strain). Ferroelectric films were therefore grown on (001) single crystal $SrTiO_3$ substrates (some of them doped with Nb), whose in-plane lattice parameter of 3.905 Å minimizes mismatch

| Type | Substrate 10 × 10 mm$^2$ | ferroelectric thickness (nm) |
|---|---|---|
| PZT2080 | 1.0 at% Nb-$SrTiO_3$ (conducting) | 50 |
| PZT2080 | 1.0 at% Nb-$SrTiO_3$ (conducting) | 100 |
| PZT2080 | 1.0 at% $SrTiO_3$ (insulating) | 50 |
| PZT2080 | 1.0 at% $SrTiO_3$ (insulating) | 100 |

Table 3.2: PZT films used in this thesis work. Provider: Phasis.

and therefore strain. In the PZT films used in the present study, strain relaxation was not studied.

The films present an extremely high degree of structural quality including surfaces with very low corrugation and also good ferroelectric properties. Such films are ideal for nanoscopic investigations of ferrolectric domains, i.e. using AFM it is possible to read and write ferroelectric regions with inverted polarization. Table 3.2 shows the description of the four used samples. Two insulating (STO) and two conducting (Nb-STO) substrates were chosen, having each one of them a sample with a thickness of 50 nm and another one of thickness 100 nm. No thinner films were chosen to ensure a certain degree of total dipole moment once the samples are polarized (the polarization value is proportional to the thickness of the film). Since the polarization is directed along the c-axis of the material, the piezoelectric coupling between the AFM tip and the thin film during the local switching and imaging of ferroelectric domains in this system is therefore maximized. In order to maximize the charge dissipation, the sample with 100nm thickness and Nb doped STO substrate was wired with a conductive string from its top down to the metallic sample holder (fig. 3.3). This operation was performed using an instrument specially designed for this function.

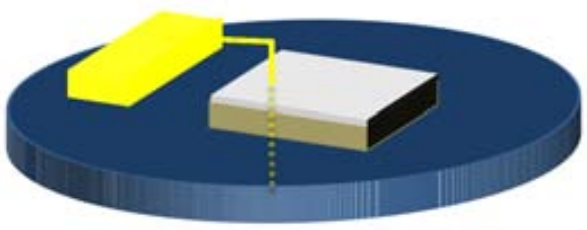

Figure 3.3: The PZT2080 100 nm Nb−doped sample was wired from its top to the sample holder using a conductive gold wire.

Characterization of the samples was provided by AFM topographical scans, revealing uniform surfaces with root-mean-square roughness of 0.24 nm ± 0.09 nm measured over several 5x5 $\mu$m areas as shown in figure 3.4. The maximum heights are of the order of 1.8 nm, ∼50 times lower than the film thickness. High crystalline quality and smooth surfaces are advantageous for effective writing and imaging of ferroelectric domains, as will be shown in the following chapters, since the presence of morphological defects could perturb the interaction between the AFM tip and the sample (Paruch, 2004).

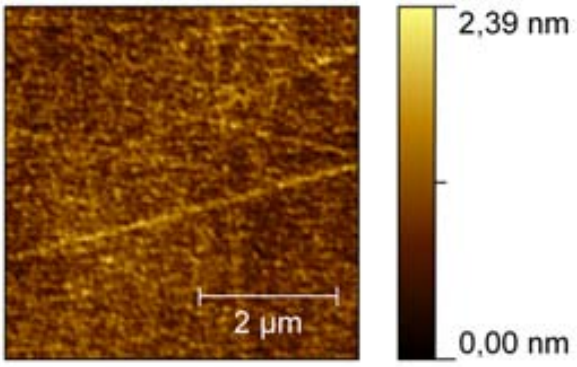


Figure 3.4: PZT2080 AFM contact topography image.

### PZT setup

Before performing the polarizing (or writing) operation, the samples must be carefully cleaned by passing an ultraclean cotton soaked in isopropyl alcohol followed by the same operation with Milli-Q water. Even after performing the cleaning process described above some non-desirable micro-sized particles may still be found on the surface, so before polarization I performed two 30 $\mu$m x 30 $\mu$m sweeps in the contact mode at 256 points line and 0.5 lines s, in order to remove such particles.

The AFM cantilevers used to polarize and read the samples were both PPP-CONTPt and PPP-EFM cantilevers (table 2.4). Several experimental values were used depending on the experiment, and they will appear in the corresponding experiment. The scanner appearing on table 2.1 has been used to perform both the writing and reading operations when working with the Agilent system. The sample is attached to the sample holder using conductive adhesive tape (both copper and

carbon tape has been used in this thesis work) and the sample holder was grounded during experiments.

Figure 3.5 shows the electrical connection to operate in the piezoresponse mode. The signals comunicating the controller and the microscope (brown color in the diagram) are redirected to the breakout box to by modified in the following way: the deflection signal of the cantilever (red color) is used as the input signal for the lock-in amplifier, while the ac signal coming from the function generator (dark blue color) with a frequency equal to that of the cantilever in contact with the sample was used as the reference signal (this frequency is not the free amplitude frequency of the cantilever, and for EFM is ∼300 KHz). The lock-in amplifier reads the first harmonic ( ) of the deflection signal (red color) and extracts the amplitude R (light blue color) and phase $\theta$ (green color) that are sent to the electronics to obtain amplitude and phase PFM images. The reference signal (dark blue) is also sent to the cantilever as the excitation signal.

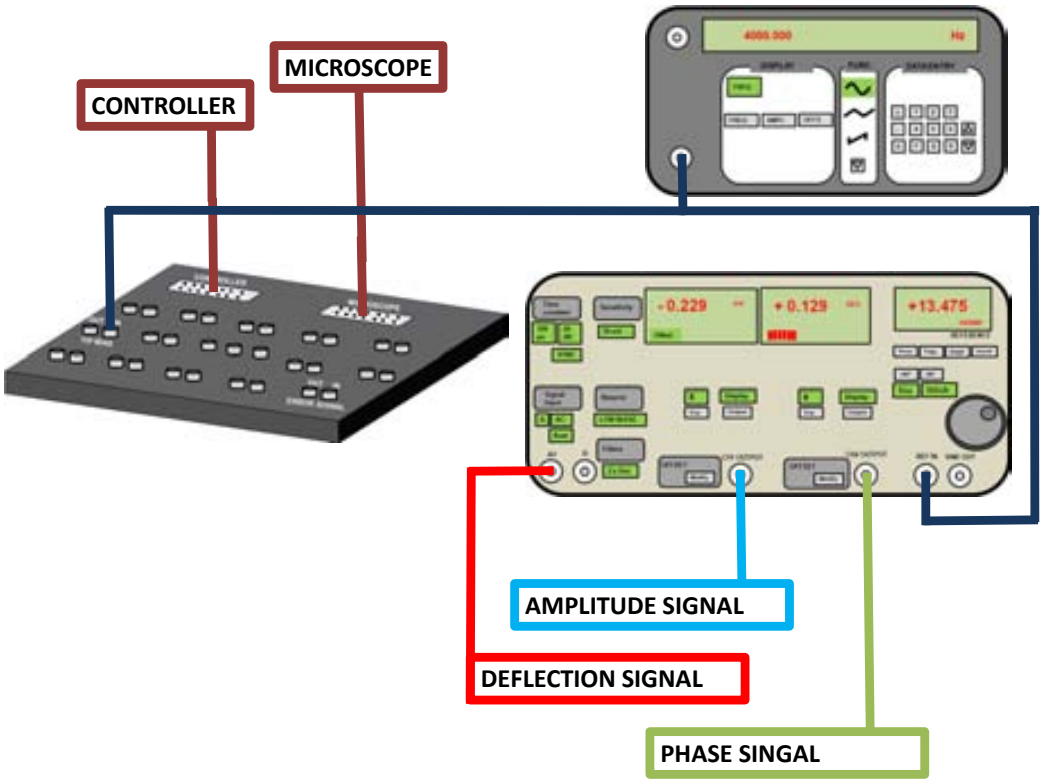


Figure 3.5: Diagram showing the connexions required for a piezoresponse experiment.

# Chapter 4

# AMINO ACIDS: RESULTS AND DISCUSSION

### Alanine

S-2-Aminopropanoic acid and abbreviated as alanine, Ala or A (for an insight about amino acid nomenclature see IUPAC-IUB, 1984), is an $\alpha$-amino acid with chemical formula $CH_3CH(NH_2)COOH$. It is one of the 22 proteinogenic amino acids, i.e., the ones that can be found in proteins. L-Alanine is second only to leucine in rate of occurrence, accounting for 7.8% of the primary structure in a sample of 1,150 proteins (Doolitle, 1989) (fig. 4.1). Alanine is classified in literature as a nonpolar and relatively soluble amino acid (Kyte et al., 1982; Rockefeller University Webpage) and is one of the simplest amino acids.

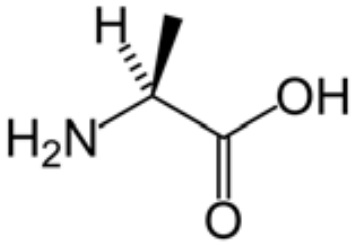


Figure 4.1: Scheme of the L-alanine molecule.

Alanine (as commonly happens for other amino acids) is found in its zwitterionic form with the carboxylic and amino groups deprotonated and protonated, respectively, when building single crystals (fig. 4.2), as described in the introduction chapter. This provides a large permanent dipole to the molecule between the

carboxylate group and the amino group, with an average value of 15.1 D. The competition between such dipole and the apolar methyl side group makes the affinity of water to alanine a rather complex problem.

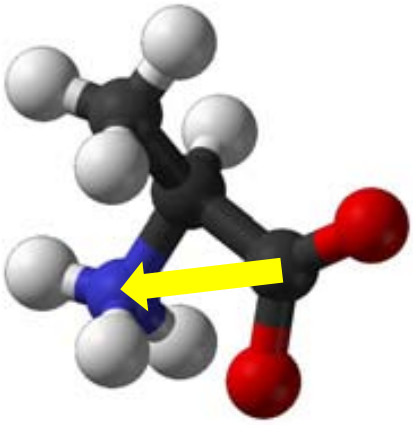

Figure 4.2: 3D model of L-alanine in its zwitterionic form showing the resulting dipole represented by a yellow arrow.

## 4.1 L-Alanine

The crystal structure of L-alanine is orthorhombic, with space group $P2_12_12_1$, with four molecules per unit cell and cell parameters $a$=0.6032 nm, $b$=1.2343 nm and $c$=0.5784 nm (Lehmann et al., 1972). Figure 4.3 shows projections of the (011) and (120) crystal planes of L-alanine, the planes studied in this work.

It has been argued (Gavish et al., 1992) that the (120) plane of L-alanine is hydrophobic and that this hydrophobic character is due to the presence of exposed methyl groups pointing out of this crystal face. However, a quick inspection of the crystal structure along the $c$-axis (bottom right in fig. 4.3) reveals that only one molecule out of every four has its methyl group pointing outward on this surface, and that carboxylate and amino groups are also clearly exposed. Thus, the experimental evidence of the low affinity to water that exhibits this surface is in contrast with the molecular distribution of its non-polar group and hence the interest in this apparent contradiction. Likewise, both polar and nonpolar groups are present at the hydrophilic (011) surface (see bottom left in fig. 4.3).

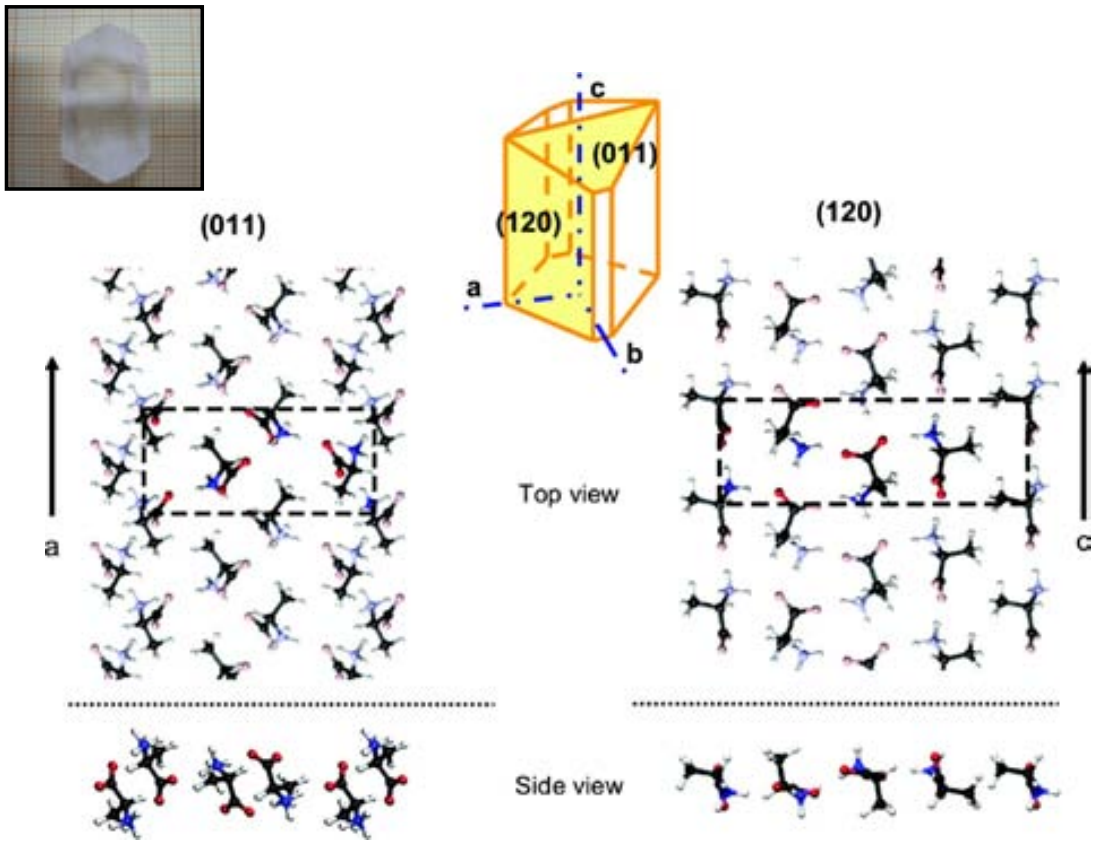


Figure 4.3: Top left: Up to 2 cm lenght L-Alanine crystals were obtained from their high purity powder. (Left) Top and side view of the (011) crystal face projected across (top) and along (below) the a-axis. Carbon, oxygen, nitrogen, and hydrogen atoms are represented by black, red, blue, and white spheres, respectively. (Right) Top and side view of the (120) crystal face projected across (top) and along (below) the c-axis.

In conclusion, the prediction of the hydrophobic/hydrophilic character from the ideal molecular structure alone may lead, in certain cases to erroneous conclusions, so that other criteria are needed. For this reason the first objective of this thesis was to study the affinity to water of both (120) and (011) L-alanine crystal planes by means of AFM experiments.

Using both of the previously described methods of crystallization, L-alanine single crystals with long dimensions spanning from 5 mm to 2 cm are obtained (fig. 4.3), largely enough for AFM experiments. Fresh L-alanine crystals were obtained by cleavege.

### 4.1.1 Affinity of water to L-alanine (120)

L-Alanine (120) plane was studied prior to (011) face because being described as hydrophobic we expected it to undergo minor changes under the action of humidity. The adopted methodology was:

(i) place the amino acid crystal inside the glove box, where RH can be adjusted and AFM experiments can be performed,

(ii) cleave a new fresh (120) surface under low RH conditions,

(iii) immediatelly perform AFM scanning to obtain topography, and

(iv) perform a series of AFM topography images while rising the RH inside the chamber to see how the crystal plane evolves as a function of the presence of water.

Step (iii) implies chosing one of the AFM operation modes. I decided to use AM-AFM mode due to the following reasons: in spite that the contact mode would achieve a better z-resolution, when performing an AFM study as a function of humidity it is desirable to avoid the contact between the tip and the sample as much as possible because it distorts the real ongoing of the process due to water spreading on the scanned zone and also to an incresing of the real RH value around the tip (wich is hydrophilic) to values larger than the monitored inside the glove box by the hygrometer (fig. 4.4), aminoacids' surface can also be damaged by the normal load exerted on the tip (it varies with the typical force range of 0.1-100 nN for routine measurements. For a nominal contact area tip/surface of several squared nanometers, this load corresponds to local pressure ranging from several MPas to tens GPas). For these reasons the use of the AFM Contact mode was avoided despite its better lateral resolution.

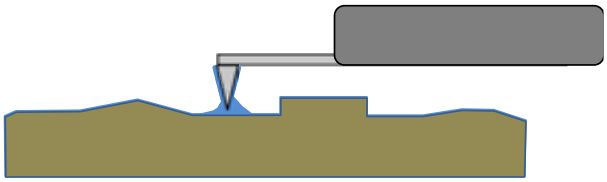

Figure 4.4: Hydrophylic $Si_3N_4$ tips can increase the real water density under its zone of influence.

Real non−contact Scanning Polarization Force Microscopy would be the best choice. Despite its poorer lateral and z−resolution the fact that this operational

mode would not interfere with the suface and the water layer over it ensures a real non invasive experiment. Unfortunately amino acids are not suitable samples for SPFM experiments since they are good insulators and showed highly polar nature that requires values of compensation voltage higher than those acquired with our instrumentatice, limited to ±10 V for the kelvin probe value. Only surfaces with a high density of defects (i.e. steps) can be compensated below 10 V. Thus, SPFM was discarded.

AM-AFM does not present the water spreading problem that contact mode implies, and the water meniscus problem can be partially avoided if large amplitudes are used so the breaking of the water neck avoids the creation of a permanent over-concentrated water zone under the tip. It provides a more than acceptable resolution and is unaffected by the sample s dielectric constant. For the exposed reasons the AFM measures in this set of expermiments were performed using the AM-AFM mode.

However, the AM-AFM mode on amino acids is not free from some minor drawbacks. Ideally, the amino acids crystal surface must be cleaved at very low RH ( 5%) to avoid the effects of exposure to water. All amino acids studied by AFM in this thesis work exhibit repulsive electrostatic interactions against the AFM cantilevers when they are cleaved at low RH. Approaching the tip in these circumstances is difficult due to deflection jumping, and the scanning must be performed exerting high forces that reduce the oscillation to very low values in order to overcome the electrostatic repulsion. Imaging in this situation gives topography data good enough for a qualitative study but complicated for extracting accurate quantitave values. Tips of different nature and different coatings (as $Si_3N_4$, Au or Ir-Pt) and different cantilever s physical constants did not show any improve respect to the usual AM cantilevers.

This problem can be solved either by (i) maintaining the crystal during several minutes at low humidity (indicated for hydrohpilic surfaces) or (ii) by increasing the RH up to ∼30% (in good agreement with the first water monolayer formation (Gil et al., 2000; Verdaguer et al., 2008)). Unfortunately, both solutions involve a certain degree of interaction between water and the crystal surface, this is not desirable

but no other solution was found to solve the problem without involving the action of water. The chosen procedure was to obtain the first images at low RH (even if the quality of the image in this circumstances is good only for qualitative analysis) and then keep scanning while rising the RH slowly until the undesired interaction disapears.

The L-alanine single crystals were placed inside the glove box along with all cleaving material required. RH was lowered until $\leq 5\%$ was reached and a fresh (120) face was obtained as previously described.

Surface topography images were adquired in the AM−AFM mode, showing a planar structure composed by micrometer-sized terraces limited by straight parallel monomolecular steps following the [001] direction (crystal c-axis) (fig. 4.5) as determined by X-ray diffraction.

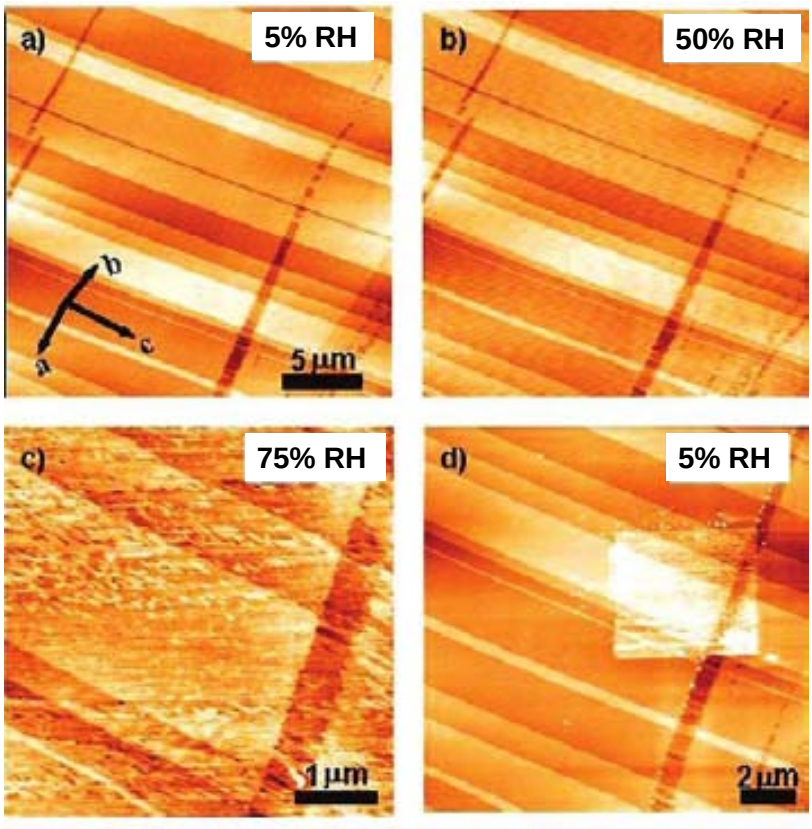


Figure 4.5: Topographic AM-AFM images of a (120) surface of a L-alanine single crystal. The images were acquired on freshly cleaved surfaces inside a glove box at room temperature and at the relative humidities: a) 5%, b) 50%, c) 75%, and d) 5% after exposure to 75%. Cleavage was performed at RH <5%.

Terrace limiting steps following the [001] direction (fig. 4.5) is in good agreement with the crystal structure (fig. 4.6). The resulting steps directions are related with the energy to form them (and also with the direction of the applied energy respect with the crystal structure). In this case, producing a step in the [001] involves the breking of less hydrogen bonds than producing a step with the same lenght in another direction. Also, optimal energy transfer is also achieved by [001] direction avoiding saw-like step formation.

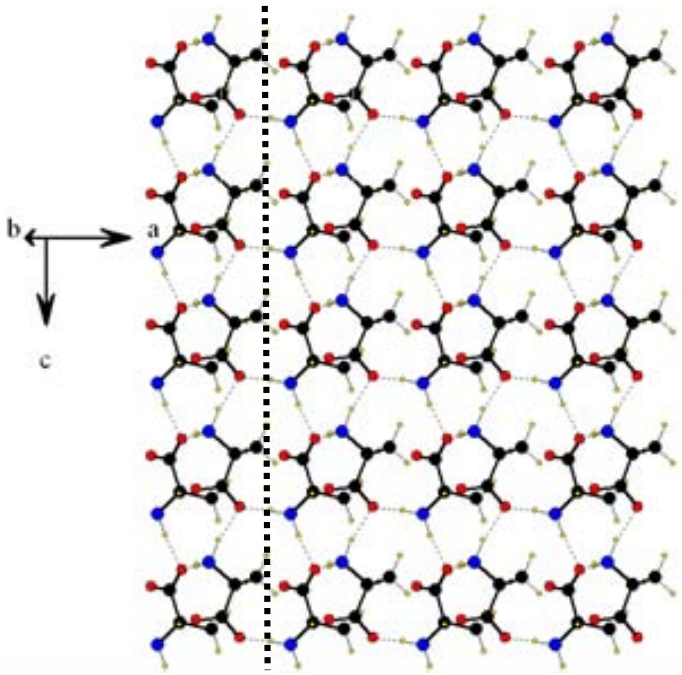


Figure 4.6: Upper view of the L-alanine (120) plane. To produce a step following the [001] direction requires less energy than the other directions.

Both mono and multimolecular steps were formed, as can be extracted from step s height with values of ∼0.5 nm and multiples of it, which is in good agreement with the theorical (XRD using $CuK_\alpha$, $\lambda$=0.15405 nm $2\theta$ =20.62°, Guo et al. 2004) 0.43 nm of an L-alanine (120) monostep. The initial step s height was measured for several crystals, and averaged obtaining a value of 5.02 Å±0.52Å per step.

Once (120) plane topography was characterized at low humidity, RH was slowly increased to study the surface evolution with the increasing presence of water vapor. Once the RH started to increase, the image adquisition took place always on the

same region. This experiment was repeated several times on different crystals to ensure its reproducibility. No topographic changes were observed up to values of RH = 50%, being L-alanine (120) plane unnafected by the action of water vapor. Again steps heights were averaged at RH between 30% and 50% obtaining a result of 5.35 Å±0.56Å. As can be seen in fig. 4.5b, L-alanine (120) plane does not develop any topographic changes and the steps height remains almost the same as for lower humidities. Leaving the system in these conditions for few hours shows no changes in topography features.

Further RH increasing up to values of 75% leads to important morphological changes. (120) terraces appear now remarkably covered by displaced material in a random-like distribution, although the original step structure can still be observed (fig. 4.5c). This distortion of the surface with the increasing RH may be the natural behaviour of the sample or maybe a side effect of the influence of the scanning tip. In order to determine its origin, relative humidity was decreased again down to values of 5%, and then a larger area was scanned (fig. 4.5d). The image evidences that only the square area corresponding to the region where the tip had been performing the scanning under high humidity conditions was affected, while the rest of the surface remained unperturbed. This indicates that distortions of the (120) plane at high RH are just a side effect of the tip due to its hydrophilic nature, increasing the real RH value under its area of influence. Topography degradation induced by the tip is possibly due to the formation of a tip-sample liquid water neck, even working with AM-AFM mode, for large enough humidity (Sacha, Verdaguer and Salmeron, 2006). Negligible affinity of the L-alanine (120) surface to water vapor even at elevated RH s is observed when there are no external influences: RH values as high as 85% do not affect the L-alanine (120) plane topography, concluding that it is highly hydrophobic even at nanometric level.

Macroscopically, contact-angle measurements were carried out in several single crystals. They lead to non-conclusive results as the values obtained for the (120) surface were rather small (30°), well below the accepted values for hydrophobic surfaces. The reason for these low values lies in the stepped nature of the cleaved surfaces. As AFM phase images on (120) plane show (fig. 4.5), water presence takes

place on the steps, being less hydrophobic than the terraces. Increasing the number of hydrophilic asperities on a surface causes water dropplets to extend over the it (Burton and Bhushan, 2005). I conclude that the influence of the hydrophylic steps distorts all the contact angle measures.

### 4.1.2 Affinity of water to L-alanine (011)

The affinity of the L-alanine (011) surface to water was studied using the same procedure as for the (120) plane. AM-AFM images on freshly cleaved surfaces at low humidity show terraces with triangular steps (fig. 4.7a) and a preferential step direction along the [100] direction (crystal a-axis), as determined by X-ray diffraction.

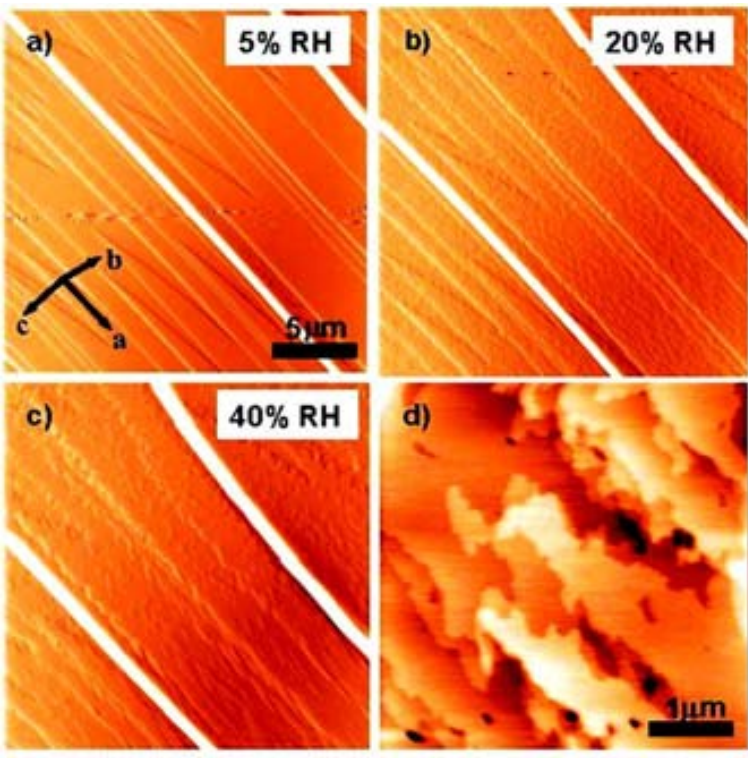


Figure 4.7: AM-AFM deflection images of a (011) surface of a L-alanine single crystal. The images were acquired on freshly cleaved surfaces in a glovebox at room temperature and at the relative humidities: a) 5%, b) 20%, and c) 40%. A topography image zoom taken at 40% RH is shown in d).

Cleavage induces the formation of triangular V-shaped terraces, with extremely long step edges (several tens of micrometers) forming acute angles between 5° and

30°, corresponding to the direction of the crack propagation (Engelhardt, Dabringhaus and Wandelt, 2000). The measured step height is again ∼0.5 nm, corresponding to the distance between two adjacent (011) planes (L-alanine molecules possess a standing up configuration within the surface and the separation between adjacent molecular planes is 0.52 nm, see fig. 4.8). Several single crystals were cleaved to ensure the reproducibility of the initial situation. The averaged height of these steps was 5.2 Å±0.4Å.

Contrary to what is observed in the (120) plane, irreversible roughening of the terraces is observed at the lowest achieved RH s. In fact, roughening is already observed at the first image taken after cleavage at RH 5%, a clear proof of the high affinity to water and an opposite response to the one of (120) plane. Unfortunately I was not able to take any image before this initial attack of the water takes place on the surface, and even at the minimum RH values that the system can provide the surface was perturbed yet at the first image, highlighting the velocity at what this effect takes place. An AM-AFM study at high vacuum may be required to achieve a non-affected surface. Not having access to that kind of measures at the moment when this thesis was performed, I continued the experiments from this initial roughness.

If humidity is slowly increased to RH 10% surface roughness evolution is immediately observed indicating the proclivity of water to induce surface modifications. Conversely to what is expected from an interaction activated at defects, both step edges and terraces are equally perturbed for a wide range of humidities, pointing to a mechanism involving incorporation of water to the crystal surface.

Slowly RH increasing shows dramatic changes and already at RH 20% terraces and steps appear strongly perturbed (fig. 4.7b). When 40% RH is reached, steps are hardly recognizable (fig. 4.7c). A detail of a terrace (fig. 4.7d) shows the strong perturbation caused by water. For larger RH values the influence of the tip becomes then more relevant, however, important perturbation induced by the sweeping action of the tip is discarded since surface roughening is observed as well in regions of the surface that have been not previously scanned. Figure 4.9a shows the first topography image of a region which possess an inner smaller region scanned previ-

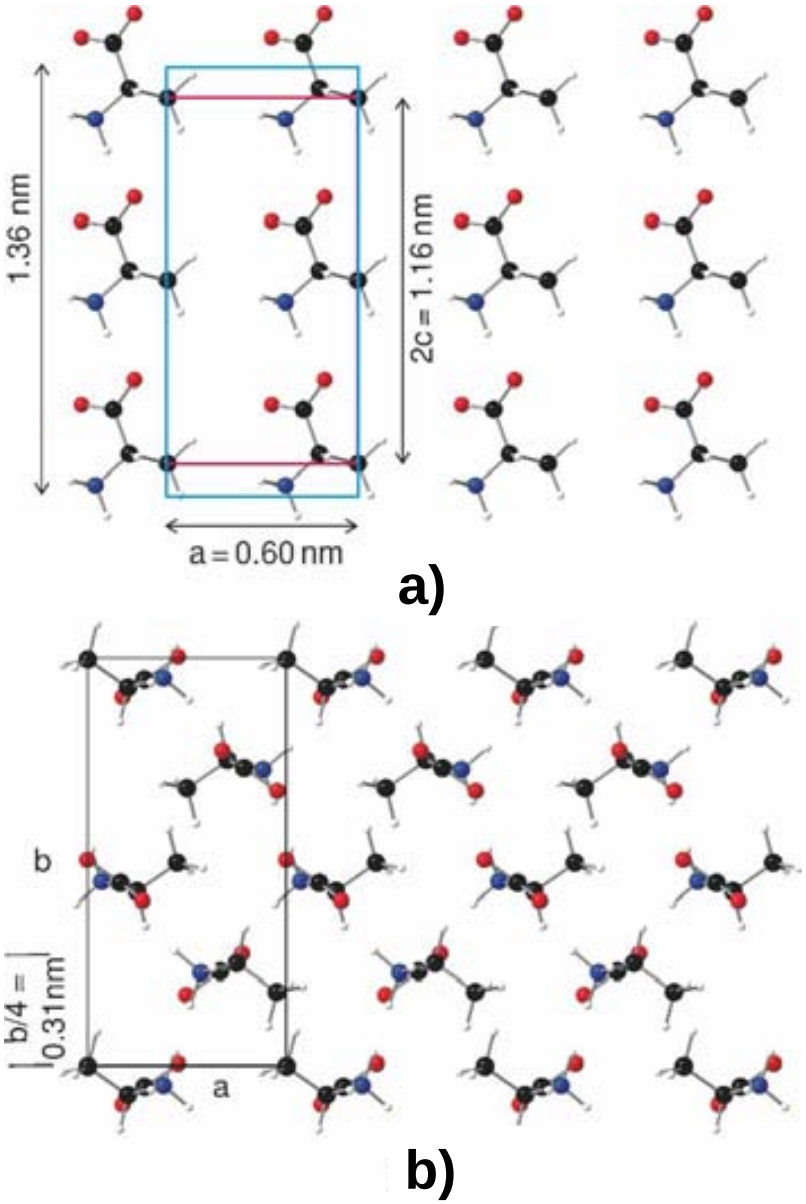


Figure 4.8: a) Top and b) side views of the (011) crystal face of L-alanine projected across and along the a-axis, respectively. Carbon, oxygen, nitrogen, and hydrogen atoms are represented by black, red, blue, and white spheres, respectively. The surface unit cell, in blue in (a), is 0.60 x 1.36 $nm^2$.

ously for several times. As can be observed, both regions present similar features, a clear indication of the minor effect of the tip. However, the phase image (fig. 4.9b) shows some indication of the inner scanned zone (scanned at RH 23%), probably due to a relative effect of water spreading due to water necks breakings. Consequently to what is observed at the topography images, this surface degradation process is

mainly induced by water action rather than the tip influence.

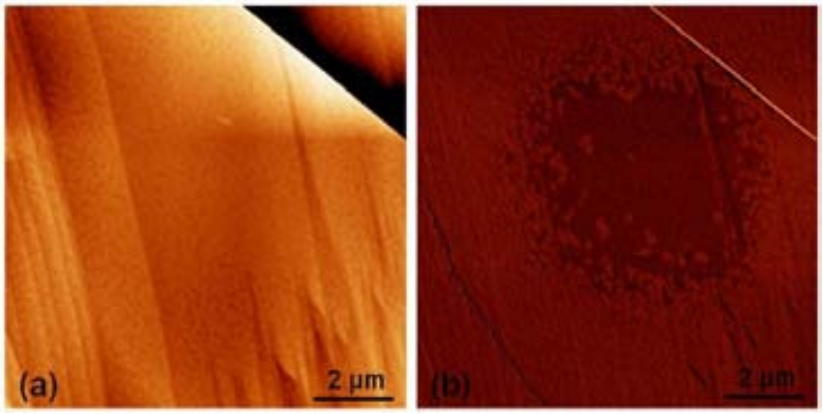


Figure 4.9: AM-AFM topography a) and phase b) images of (011) surface scanned several times at RH 23%. The phase image shows the scanned region. The topography image indicates high affinity of the (011) plane to water even at zones where the tip effect is not present.

### 4.1.3 Comparison of L-alanine hydrophobic/hydrophilic behaviour

When describing the crystal structures of (120) and (011) L-alanine planes I have underlined the generally accepted explanation of (120) hydrophobicity being a consequence of the methyl group exposed by one of each four molecules out of its surface. It is at least questionable the fact that a ratio of 1 of each 4 molecules exposing a non-polar group is enough to overcome the effect of the remaing 3 molecules exposing polar groups in a more or less open way. This explanation makes difficult to predict if an amino acid crystal plane would be hydrophilic or hydrophobic when exposed to air. A detailed study at this point could give a clear answer able to unravel the prediction about the hydrophilicity or hydrophobicity of other amino acids crystal planes.

The first step we considered was to perform some computer simulations of water distribution near a (120) and a (011) L-alanine crystal plane. We were specially interested in observing the distribution of water molecules near each molecule exposed to the surface, and check the relative importance of the methyl group to confere the hydrophobic character all over the (120) plane. The here shown computer simulations were performed by Dr. E. Hernández at the ICMAB.

**Computational details**

The Molecular Dynamics simulations were performed using the CHARMM (MacKerell et al., 1998) parametrization to model the alanine and water molecules, as well as their mutual interaction. For a detailed description of this model, the reader should consult the original reference, but briefly, the CHARMM model includes harmonic springs to describe all pairs of covalently bonded atoms within a molecule; it also uses harmonic potentials to account for bond angles; dihedral angles are also described. Partial charges on the atoms are used to reproduce the dipole of the alanine and water molecules (average water dipole 2.6 D, average alanine dipole 15.1 D). Lennard-Jones-type potentials are used to describe the dispersion-type forces arising between pairs of atoms.

MD simulations have been carried out employing the DL-POLY (Smith and Forester, 1996) package. In this package, the electrostatic interactions are accounted for with the Ewald summation method. Simulations have been conducted within the microcanonical (constant number of particles, constant volume, and constant energy) ensemble, using a time step of 1 fs, which is sufficiently short to result in good energy conservation during the length of our simulations. Initial velocities were chosen randomly from the Maxwell-Boltzmann distribution at room temperature, and the system was allowed to equilibrate at this temperature at the start of each simulation. In the case of the (120) surface, we simulated a L-alanine slab consisting of an 8 x 3 surface supercell, having dimensions of 4.63 x 5.18 $nm^2$; for the case of the (011) surface, we employed an 8 x 4 supercell, with dimensions of 4.83 x 5.4 $nm^2$. The (120) slab contained a total of 1152 alanine molecules, while the (011) slab consisted of 1024. The total number of water molecules in the simulation box varied between a minimum of 7500 up to a maximum of 8800. The dimension of the simulation box perpendicular to the crystal slab was chosen so as to tune the conditions to ambient temperature and pressure (300 K, 1 atm) during an equilibration period previous to the production runs. We used values of 15.18 and 15.07 nm for the (120) and (011) surfaces, respectively. Initial configurations for the simulations were generated by placing a slab (exposing the desired surfaces) cut out of the perfect alanine crystal in the middle of the simulation box and placing the appropriate

number of water molecules at random positions above and below the slab. We then simulated the combined system for several picoseconds while constraining the alanine molecules in their equilibrium positions, so as to allow the water molecules to equilibrate. Subsequently, all restraints were lifted, and the whole system was allowed to equilibrate for a subsequent period of time, previous to the production runs. For convenience of analysis and visualization, in some cases (as discussed in the text), we imposed restraints on the mobility of the alanine molecules, although the conclusions from these simulation work are extracted from simulations in which no constraints were imposed.

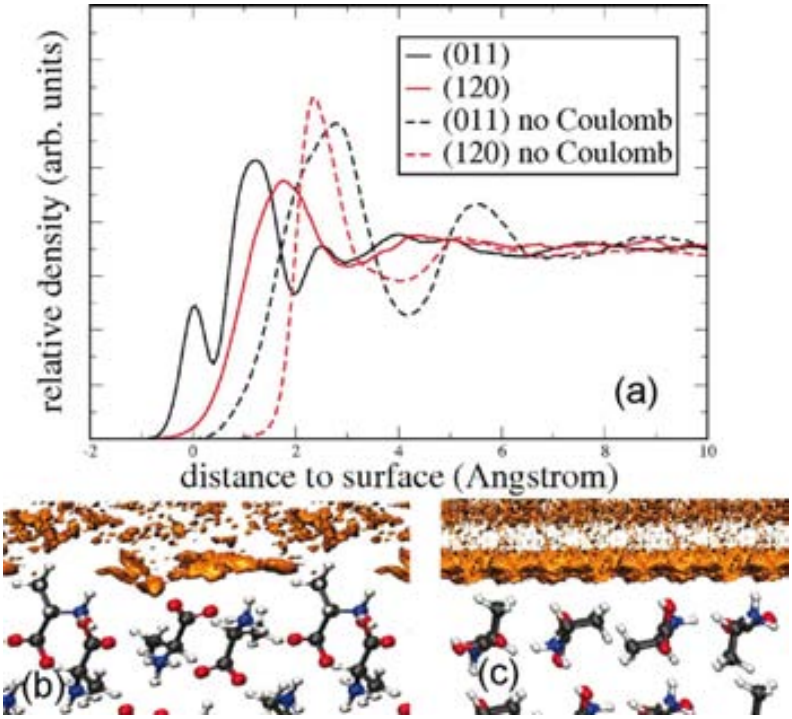


Figure 4.10: Distribution of water molecules on L-alanine surfaces. (a) Probability density of water molecules above surfaces (011) (black) and (120) (red) of alanine, obtained from MD simulations. Continuous lines show water probability densities calculated with water/alanine charges switched on and including the dynamics of the alanine molecules, while the dashed lines are the resulting densities obtained without water/alanine electrostatic interactions and fixing the alanine molecules at perfect crystal positions. The lower panels show the spatial distribution of the nearest water molecules on l-alanine crystal surfaces; (b) (011) surface viewed along the a-axis; note that during the MD simulations the (011) surface reconstructs slightly (compare with fig. 4.3 left); (c) (120) surface viewed along the c-axis. No appreciable reconstruction is observed in this case.

In fig. 4.10a, I plot the density profile (integrated over planes parallel to the surface) of water molecules as a function of the height above the surface, for both

the (011) and (120) surfaces, as well as the spatial distribution of this density. The probability densities have been calculated with the positions of the center of mass of the water molecules. The distance origin is somewhat arbitrary, given that the topographies of the two surfaces are different. A common origin for the various curves is set by overlapping the distribution of atoms belonging to the surface alanine molecules and setting the zero mark at the point where these distributions fall down to zero. The peaks appearing in fig. 4.10a measure approximate distances to the plane of outermost atoms of the alanine crystal surface. The fact that in some cases the distributions take finite values at negative height is indicative of a degree of penetration of the water molecules into the alanine crystal surfaces, due to the rugosity of the latter.

As it can be seen in the figure, the density profiles of water on both surfaces at distances smaller than 8 Å are markedly different, with water molecules getting much closer to the outer alanine molecules in the case of the (011) surface than in the (120). In fact, in the case of the (011) surface, there is a first peak centered at zero, which reveals the presence of water molecules in close contact to the surface. This peak corresponds to hydrogen bond formation between water molecules and surface carboxyl groups mediated by a proton from the water molecule participating in the bond, as well as between the amino groups and water molecules, mediated by a proton from the amino group. No similar peak is found for the (120) surface, where the distribution has a first peak at a position of 1.8 Å from the surface. Although there is also some degree of hydrogen bond formation between water and alanine groups on this surface, it does not happen to the extent it does on the (011) surface. These different patterns confirm the relative hydrophilic/hydrophobic character of the (011) and (120) surfaces, respectively. The positions of the distribution peaks shown in fig. 4.10a correspond to typical hydrogen bond distances that are established between water and alanine molecules at the surface. These results are in line with the accepted view that water molecules move away from extended hydrophobic surfaces forming a depleted density region near such a surface (Stillinger, 1973; Lum, Chandler and Weeks, 1999; Chandler, 2005; Jensen, Mouritsen and Peters, 2004; Poynor et al., 2006; Mezger et al., 2006).

To uncover the reasons behind these different patterns, we have repeated the same simulations, but turning off the electrostatic interactions between the alanine and water molecules, by setting the partial charges on alanine constituent atoms to zero. Since neglecting the contribution of the electrostatic interactions would significantly change the structure of the alanine crystal, in these simulations, we have frozen the alanine molecules at their perfect crystal positions and only considered the dynamics of the water molecules.

The resulting densities from this second set of simulations are shown in fig. 4.10a as dashed lines. As can be seen by comparing the distributions obtained with and without electrostatic interactions, these play a crucial role in determining the distribution of water molecules on the (011) surface but are of lesser importance in the case of the (120) surface. Indeed, without electrostatic interactions, the density profile of water on alanine (011) changes dramatically, losing all of the structure present when alanine atomic charges are considered. In particular, the short distance peak disappears, and the density takes its first maximum at roughly the same position as in the case of the (120) surface (also without Coulomb interactions). In contrast, in the case of the latter surface, the exclusion of the electrostatic interactions does not change quite so radically the form of the water density profile; it only results in an approximately rigid shift toward longer distances and a slight narrowing of the features already present in the distribution when alanine charges are turned on. The overall effect of the electrostatic interactions in this case is to bind the water molecules slightly more strongly to the (120) surface, but the actual shape of the distribution is determined by the dispersion-type interactions, the only ones present between substrate and water when alanine charges are not included.

The results are in line with recent MD simulations of bulk water in contact with extended hydrophobic and hydrophilic crystalline surfaces of n-alkane $C_{36}H_{74}$ and n-alcohol $C_{35}H_{71}OH$, respectively (Jensen, Mouritsen and Peters, 2004), and with neutron reflectivity experiments conducted on self-assembled monolayers in water (Maccarini et al., 2007). However, a notable difference between previous results and those reported here is that hitherto either the substrate (Jensen, Mouritsen and Peters, 2004) or the solvent (Maccarini et al., 2007) were changed (from polar to

nonpolar) to observe a change in the hydrophilic/hydrophobic character. Here, in contrast, it is the same material that is displaying two markedly different behaviors. Since one normally associates hydrophobicity with nonpolar materials, and at the same time expects polar ones to be hydrophilic, it remains to be explained how can a polar material such as the L-alanine molecular crystal display both characters, depending on the exposed surface.

Fig. 4.10 is in line with the view that corrugated surfaces have a tendency to be more hydrophilic than flat or featureless ones. The presence of asperities in the former allows water molecules to arrange themselves in such a way as to minimize the disruption to the hydrogen bond network in water close to the surface; the impossibility to do this in the proximity of featureless surfaces leads, in contrast, to dewetting (Lum, Chandler and Weeks, 1999; Chandler, 2005). Indeed, fig. 4.10b shows that the (011) surface is more highly corrugated than the (120) one. This, in turn, leads to a more irregular pattern in the distribution of water molecules in the proximity of the (011) surface, with some regions having water molecules going into cavities or voids in the surface. In contrast, the distribution of water molecules in the proximity of the (120) surface is comparatively featureless (see fig. 4.10c), with no close contacts between alanine and water molecules. The presence of an increased water density (with respect to the liquid bulk) close to the (120) surface that can be seen in fig. 4.10a is not incompatible with the hydrophobic character of the surface (Chandler, 2005; Mittal and Hummer, 2008). It is interesting to remark that no influence of the hydrophobic methyl group is observed in the structure of water molecules surrounding it.

At first sight, it is natural to assume that the contrast in the observed behaviour of water on the (011) and (120) surfaces is due to the different disposition of the polar groups of the alanine moieties in each of these surfaces. Such arguments, however, do not lead to a clear criterion for determining the hydrophobic/hydrophilic character of a given surface. Indeed, they may even lead to error; noticing the presence of methyl chemical groups in the (011) surface (see fig. 4.10b), one may easily conclude that this surface should be hydrophobic when in fact it is not. A much more revealing observation is obtained by focusing not on the disposition of the different chemical

groups on the exposed surfaces but rather on the orientation of the molecular dipoles.

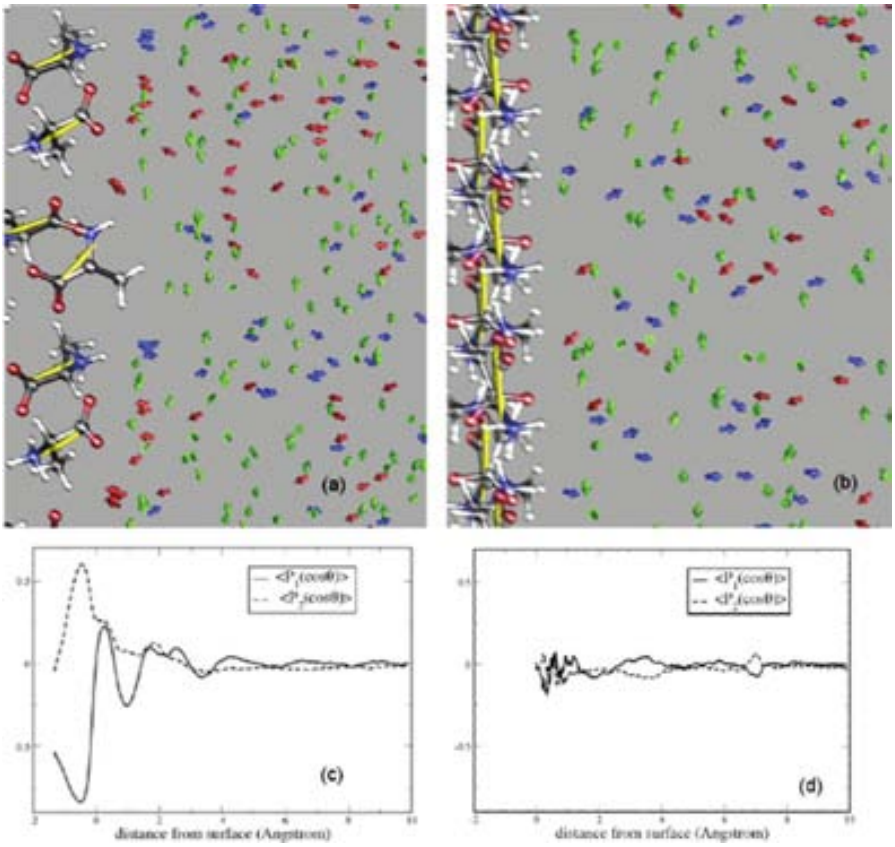


Figure 4.11: Distribution of molecular dipoles at L-alanine/water interfaces. Instantaneous configurations of the dipoles of water molecules resulting from simulations of the (011) (a) and (120) (b) surfaces exposed to water. Alanine molecular dipoles are shown in yellow, superimposed on the corresponding molecules. The average value of the alanine dipole obtained in our simulations is 15.1 D. Water molecular dipoles are shown in a color code, where blue indicates dipoles pointing away from the interface ($\cos\theta \geq$ -0.5, where $\theta$ is the angle between the molecular dipole and the outward pointing surface normal), red indicates dipoles pointing toward the interface ($\cos\theta \leq$ -0.5), and green indicates dipoles lying roughly parallel to the surface (-0.25 $\leq \cos\theta \geq$ 0.25). In order to highlight the orientation of the water molecular dipoles, the water molecules themselves are not shown. The average value of water molecular dipoles obtained in our simulations is 2.6 D. (c,d) Functions $P_1(\cos\theta)$ and $P2(\cos\theta)$ calculated as a function of distance along the surface normal, for the (011) and (120) surfaces, respectively.

In fig. 4.11, I display two snapshots obtained from simulations of the (011) (left) and (120) (right) surfaces exposed to bulk water. The first striking observation to be extracted is the different disposition of the alanine dipoles (shown as yellow arrows) seen in both surfaces. While in the case of the (011) surface the alanine dipoles are arranged in such a way as to form angles of roughly 45° and 135° with the surface normal, in the (120) surface, they are contained within the plane of the surface. The second key observation is that the orientation of the alanine dipoles in the two

surfaces induces a radically different distribution of dipole orientations in the nearby water molecules. On the (011) surface, water molecules close to the surface orient themselves with their dipoles either pointing out (blue color) or in (red), depending on whether the dipole of the nearest alanine molecule is pointing out of or into the crystal, as this optimizes the dipole-dipole interaction energy; green arrows are for water molecules with dipoles oriented roughly parallel to the surface. This can be clearly seen in fig. 4.11a, where there is a predominance of red (blue) arrows at the points where the surface alanine dipoles are pointing in (out) from the surface, with only a minority of green arrows. In the case of the (120) surface (see fig. 4.11b), the situation is different: no clear preference for any given orientation of the water dipoles can be discerned, and all orientations can be observed. Although panels a and b of fig. 4.11 show instantaneous configurations of the water dipoles in the proximity of the (011) and (120) surfaces, the differences revealed by these images are actually maintained in average over time, as shown in panels c and d. There, I plot two functions, $P_1(\cos\theta)$ and $P_2(\cos\theta)$, where $P_1$ and $P_2$ are the first -and second- order Legendre polynomials, defined as

$$P_1(x) = x \tag{4.1}$$

and

$$P_2(x) = 1\ \ 2(3x^2 - 1) \tag{4.2}$$

$\theta$ is the angle formed by the dipole of a water molecule with the outward pointing surface normal, and the angular brackets indicate an average over water molecules and over configurations produced during the simulation. $P_1$ provides information about the average orientation of the water dipoles, while $P_2$ allows one to distinguish between two possible cases leading to the same value of $P_1$, namely, the case of anisotropic orientation of dipoles ($P_1 = 0$, $P_2 = 0$) and the case of orthogonal orientation to the surface normal ($P_1 = 0$, $P_2 = -1/2$).

It is apparent that the arrangement and orientation of water molecules is significantly different in both cases. Considering first the (011) surface, we see that $P_1$ takes negative values at short distances, consistent with the fact that the nearest water molecules have their dipoles oriented antiparallel (red) to the surface nor-

mal. As the distance to the surface is increased, there is some oscillation from negative to positive values, reflecting local domains of slight predominance of antiparallel/parallel orientation of the water dipoles to the surface normal, decaying to zero further away from the surface. The decay of $P_1$ to zero, and that of $P_2$, is indicative of a transition from highly oriented dipolar arrangements close to the surface toward a situation of randomly oriented dipoles as we move into the liquid bulk. In contrast, the values of $P_1$ and $P_2$ on the (120) surface are always close to zero, regardless of the distance to the surface; clearly, in this case, interaction with the surface is not strong enough to induce any favored orientation of the water molecular dipoles.

Thus, it can be seen that the orientation of the alanine molecular dipoles is the key to the hydrophobic/hydrophilic nature of the alanine crystal surfaces. In the introduction chapter I defined the interaction energy (see eq. 1.14). When two dipoles, separated by a distance r are in a colinear orientation, their interaction is twice as favorable as when they are in an antiparallel orientation at the same distance. It can be seen in eq. 1.15, where if the angles are changed in the following way: $\theta_1 = 90$, $\theta_2 = 0$, $\sharp = 180$ (that is, the dipoles are antiparallel), the energy becomes half the value. The most favorable orientation that the water molecules can adopt above the (120) alanine surface is such that their molecular dipole is oriented antiparallel to that of the nearest alanine surface molecule. Since on this surface the alanine molecules are placed such that their dipoles are contained in the plane of the surface, the nearby water molecules cannot orient themselves in a more favorable way than this. However, in the case of the (011) surface, it is possible for the water molecules to orient themselves such that their dipoles are nearly colinear with that of the nearest alanine surface molecule, leading to a more strongly favorable interaction.

Taking these considerations into account, it is now easy to explain the observations reported in fig. 4.10 concerning the effects on the distribution of water molecules when switching off the electrostatic interactions between alanine and water molecules, where it was seen that the electrostatic interactions had a much more noticeable effect in the case of the (011) surface and a very small one for the (120)

surface. Analyzing our simulation trajectories, we find that water molecules tend to form hydrogen bonds with the (011) surface more readily than they do in the case of the (120) surface. This is consistent with the hydrophilic character of the first surface and the hydrophobic one of the latter.

### 4.1.4 Surface dynamics of L-alanine (011) surface

Once the underlying origin of the hydrophilicity difference between L-alanine (120) and (011) planes was understood, I took a closer look at the interactions between the highly hydrophilic (011) plane and water. Experiments were performed under controlled ambient conditions (room temperature and variable RH), by employing different scanning probe microscopies in a combined manner.

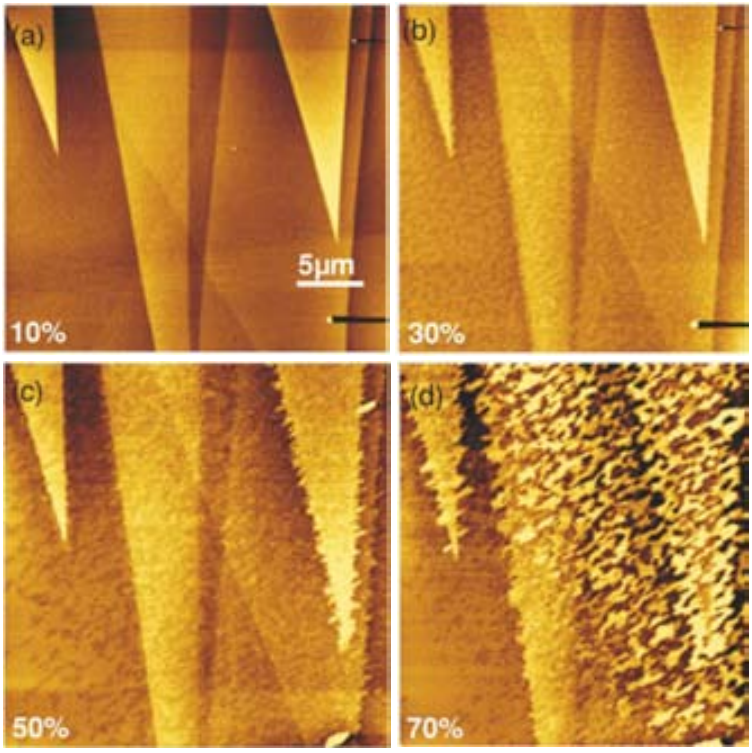


Figure 4.12: Topographic AFM images of a (011) surface of a L-alanine single crystal. The images were acquired on freshly cleaved surfaces in the AM mode in a glovebox at room temperature and at the RHs: (a) 10%, (b) 30%, (c) 50%, and (d) 70%. Cleavage was performed at RH 5%. The scale is 30 $\mu$m x 30 $\mu$m.

Fig. 4.12 shows again AM-AFM images of L-alanine (011) surface plane evolution with humidity. As mentioned, the formation of triangular V-shaped terraces, with extremely long step edges (several tens of micrometers) forming acute angles between

5° and 30° can be observed. Similar structures have been reported for cleavage surfaces of different single crystals such as $CaF_2$ (Engelhardt, Dabringhaus and Wandelt, 2000), $BaF_2$ (Cardellach et al., 2010), and monoclinic L-arginine phosphate monohydrate (Geng et al., 2005). The measured step height is again close to 0.52 nm, the corresponding distance between two adjacent (011) planes.

Fig. 4.13 shows, at larger magnification, the change from the initial state of the (011) plane at low humidity to the same zone at 43%.

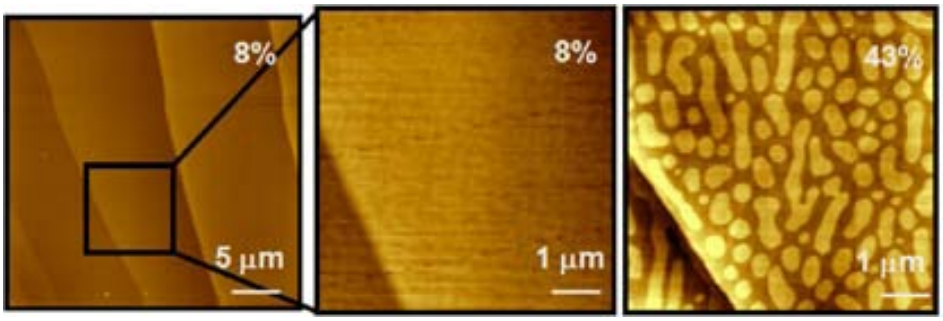


Figure 4.13: Initial state of (011) L-alanine at 8% (left). Magnification zoom of a step of the previous region (center). Same image at 36 % (right).

Fig. 4.14 shows the evolution of another (011) surface after being exposed to ∼25 and ∼40% RH. The initial scenario consisting of flat regions (terraces) separated by steps has evolved as to reveal two important points that will be addressed in detail next: (i) each region exhibits now two well differentiated levels (we call them terraces and islands ). The measured islands heights are ∼0.35 nm (fig. 4.15), clearly smaller than the distance between adjacent (011) molecular planes (∼0.5 nm), a clear indication of the restructuration of the surface induced by water. (ii) The islands size is much larger for the higher RH, suggesting a coarsening process in which both increasing humidity and elapsed time play a joint role. Provided below ∼20% only small changes in islands evolution are observed after several hours, I illustrate the coarsening process for a given humidity as a function of time with data obtained at ∼40% (fig. 4.14b). At this RH the effects induced by water are quite evident in a reasonable time scale (few hours) (fig. 4.16). Quick inspection of the images clearly reveals that larger islands grow at the expense of smaller ones, a well-known phenomenon termed (2D) Ostwald ripening (Krichevsky and Stavans, 1995;

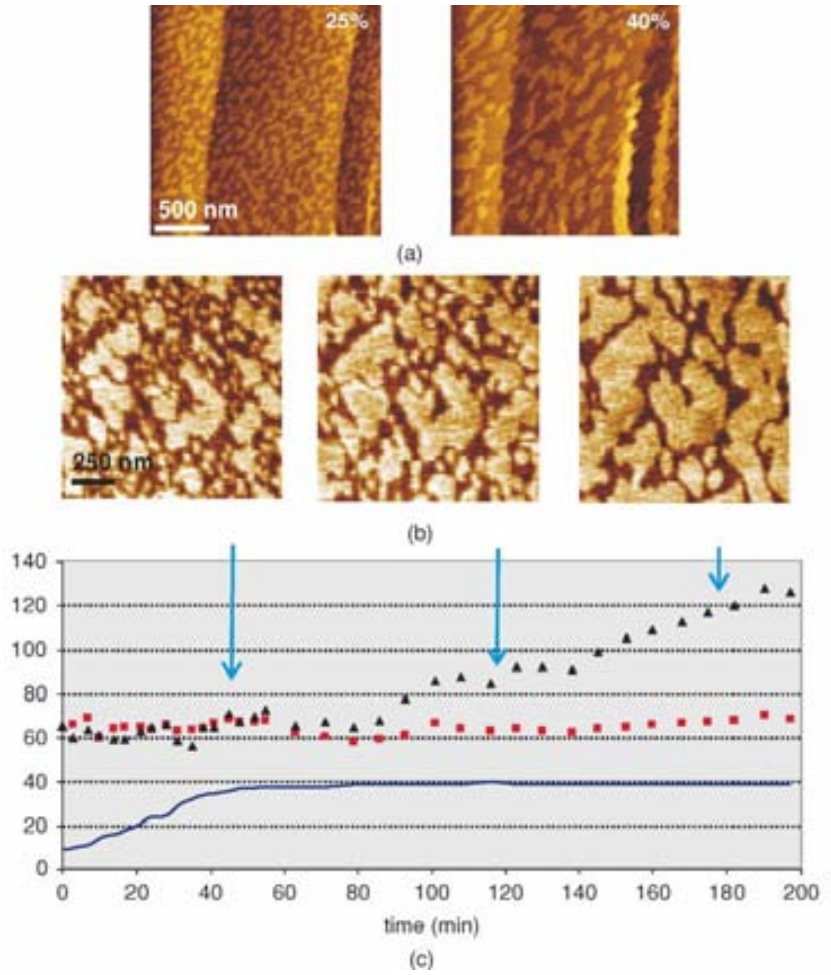


Figure 4.14: (a) Topographic AFM images of a (011) surface of a L-alanine single crystal. The images were acquired on freshly cleaved surfaces in the AM-AFM mode in a glovebox at room temperature and at RHs: (left) ∼25% and (right) ∼40%. Cleavage was performed at RH <5%. (b) Time evolution of images evidencing Ostwald ripening taken at RH ∼40%. (c) Time evolution of the area fraction (in %, red squares), the area to perimeter ratio (black triangles), and RH (blue continuous line). The time where the images from (b) were taken is indicated by blue arrows.

Semin et al., 1996; Basagaoglu et al., 2004). This process takes place because atoms (or molecules) exposed at the surface of a particle are energetically less stable than the ones in the interior, so in Ostwald ripening processes smaller particles follow a process of solvation in which their molecules deattach from the surface of the smaller particles and aggregate into the larger ones.

Due to the difficulty of tracking individual islands as they evolve, I instead compare the total area covered by islands and the corresponding area to perimeter ratio, as shown in fig. 4.14c. In order to understand the role and influence of RH in the process, the recorded glovebox humidity is also shown (continuous blue

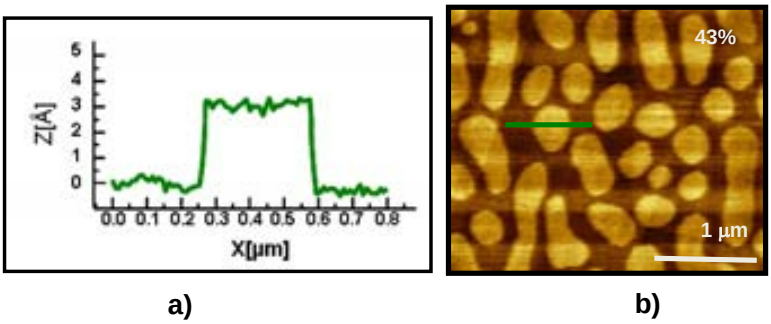


Figure 4.15: (a) The height of the islands appearing on (011) L-alanine is less than the 0.52 nm interplane distance. (b) Topography image corresponding to the zone where the profile has been obtained.

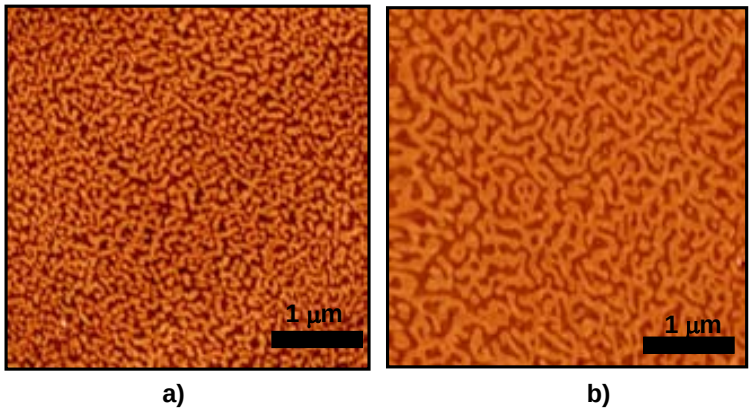


Figure 4.16: t=0 (a) and t=1 h. (b) of the coarsening process of the islands at RH 30%.

line). It displays a slow increase up to a constant value kept at 40%. This RH value can be regarded as a threshold dividing the plot into two clearly differentiated regions. The area to perimeter ratio is constant only below the stabilization of RH and it increases almost monotonically from there on. This first result indicates that below the threshold the small islands formed at the beginning are essentially stable but above it the islands coalescence building larger islands. On the other hand, the covered area remains quite constant (slightly above 50% of the total explored surface) over the entire experiment and basically equal to the area of the islands formed from cleavage to acquisition of the first image at the lower RH. This second result supports the existence of a process where water strongly interacts, likely incorporated into the surface at low humidity. Surface diffusion seems to be relatively moderate until

an increase in humidity provides an extra mobility to the surface species triggering the Ostwald ripening process. As it will be discussed later on, this threshold RH seems to have a crucial role leading to an unexpected increase in friction asymmetry, supporting the interpretation of an increase in mobility. Observation by AFM of Ostwald ripening induced on a surface by adsorbed water films has been already reported for salt nanocrystals deposited on silicon oxide substrates (Arima et al., 2009) and for boric acid surfaces (Cleaver and Wong, 2004).

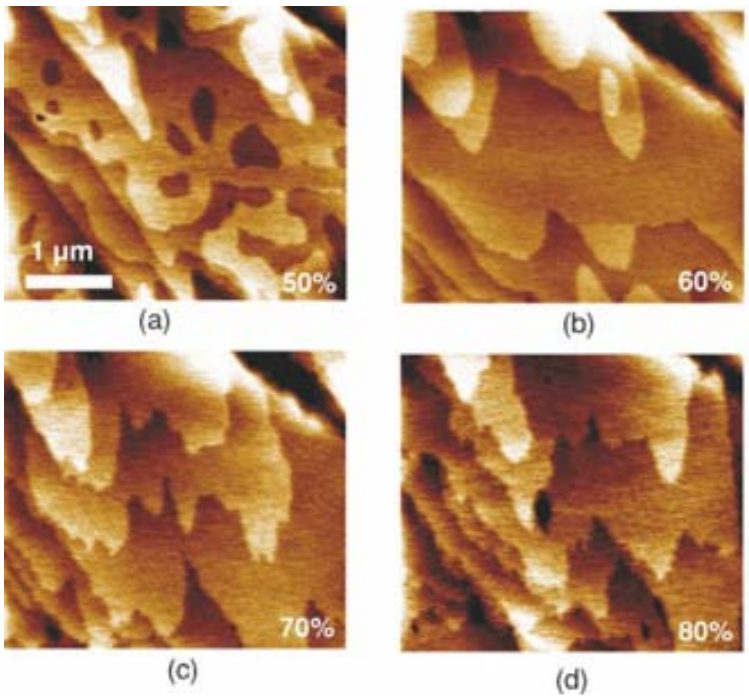


Figure 4.17: Topographic SFM images of a (011) surface of a L-alanine single crystal. The images were acquired on freshly cleaved surfaces in the AM-AFM operation mode in a glovebox at room temperature and at RHs: (a) 50%, (b) 60%, (c) 70%, and (d) 80%. Cleavage was performed at RH 5%.

As already seen (fig. 4.12d), for RH well above 40% surface disruption becomes evident. This is exemplified in fig. 4.17, where the evolution from 50% up to 80% is shown. Already at 50% the species mobility is so high that Ostwald ripening leads to the formation of large terraces with rounded edges and embedded voids, reminiscent of pre-existing islands and the empty space between them. As humidity keeps rising, an enhanced molecular diffusion permits minimizing the surface area by filling the holes (surface healing), reducing hills (i.e., species diffusion is no longer strictly 2D), and smoothing the terraces edges in a way that the surface

topography becomes hardly distinguishable from the original surface. A change in mass transport mechanism from 2D to 3D is evident when even higher humidity is reached (between 70% and 80%). The step edges start to roughen and eventually new holes appear at the terraces. Conversely to the mechanism commented above for low RH, under severe humidity conditions a true roughening occurs and the surface becomes dissolved. This process is surely enhanced by the influence of the tip, but real time visualization of surface diffusion evidences that dissolution takes place with no correlation with the scanning direction.

### 4.1.5 Water-mediated friction asymmetry on L-alanine (011)

From the physical properties point of view, the tribological response of organic surfaces under diverse humidity conditions becomes an obvious subject of interest by itself. A powerful tool to understand different dissipation mechanisms at surfaces is the Scanning Force Microscope in its Lateral Force imaging mode (LFM) (also known as friction force microscopy, FFM) (Carpick and Salmeron, 1997; Salmeron et al., 2001), see the introduction chapter for a more detailed description.

In particular, surface characteristics influencing the frictional properties can help visualizing regions of different nature (chemical composition, structural order), well designed and sensitive FFM measurements can provide structural information such as molecular tilt angles and/or tilt angle azimuths. This would be, for instance, the case of observing friction anisotropy or friction asymmetry (see introduction), both of them related to the dependence of friction with the sliding direction.

The term friction anisotropy in general refers to the variation of friction with the relative orientation angle between sliding surfaces and is commonly correlated with surface crystallographic orientations with respect to the sliding direction (azimuth dependence). A nonisotropic structure or surface packing would, for instance, produce such an effect (Liley et al., 1998; Hisada and Knobler, 2002; Park et al., 2005; Munuera, Barrena, and Ocal, 2007). On the other hand, friction asymmetry refers to a change in friction, for the same surface symmetry relationship, when the sliding direction is changed by 180°. This effect can be observed, for instance, if a molecular tilt out of the surface plane exists, being the sliding direction parallel or

antiparallel to the tilt angle direction depending on the scan direction (Liley et al., 1998).

FFM has been successfully employed in organic self-assembled monolayers (SAMs) not only to discriminate between ordered configurations presenting different friction coefficients (Barrena, Ocal and Salmeron, 2000) or different packing (Munuera, Barrena, and Ocal, 2007) but also to decipher between equivalent structural domains as well as to identify highly dissipative transient molecular configurations during phase transitions (Munuera and Ocal, 2006).

All water-induced processes described above (water incorporation, species diffusion, Ostwald ripening, and roughening) involve molecular displacements and rearrangements where a large number of degrees of freedom significantly contribute to energy dissipation. Because lateral force imaging is especially useful to get insight on the dissipation mechanisms occurring at surfaces, in the following text I describe results obtained by this technique.

Fig. 4.18a shows topography (left) and forward lateral force (right) images taken in contact mode at room temperature and 40% RH. The topographic image shows the already described two-level distribution and the lateral force image reveals clear contrast between them, with the islands exhibiting a higher (brighter in color scale) forward lateral force. Note that lateral force signals are measured as a result of the cantilever torsion, hence having an opposite sign for reversed scan directions, i.e., larger lateral forces are visualized as bright colors in the forward scans but as dark colors in the backward path. Consequently, opposite image contrast must be recorded if surface regions of different friction coexist, as for the case of chemically differentiated regions. In fig. 4.18b simultaneous topography (top left), forward (middle left) and backward (bottom left) lateral force images taken at room temperature and 40% RH are shown. Taking the terrace level as *in situ* reference in the corresponding topographic profile, the islands height is 0.35 nm. Interestingly, lateral force imaging reveals that the islands appear brighter than the terrace in both scan directions. This result means that the lateral force is asymmetric, i.e., the cantilever absolute lateral torsion changes within each region when the sliding direction is reversed (180°). On the other hand, the same difference in cantilever

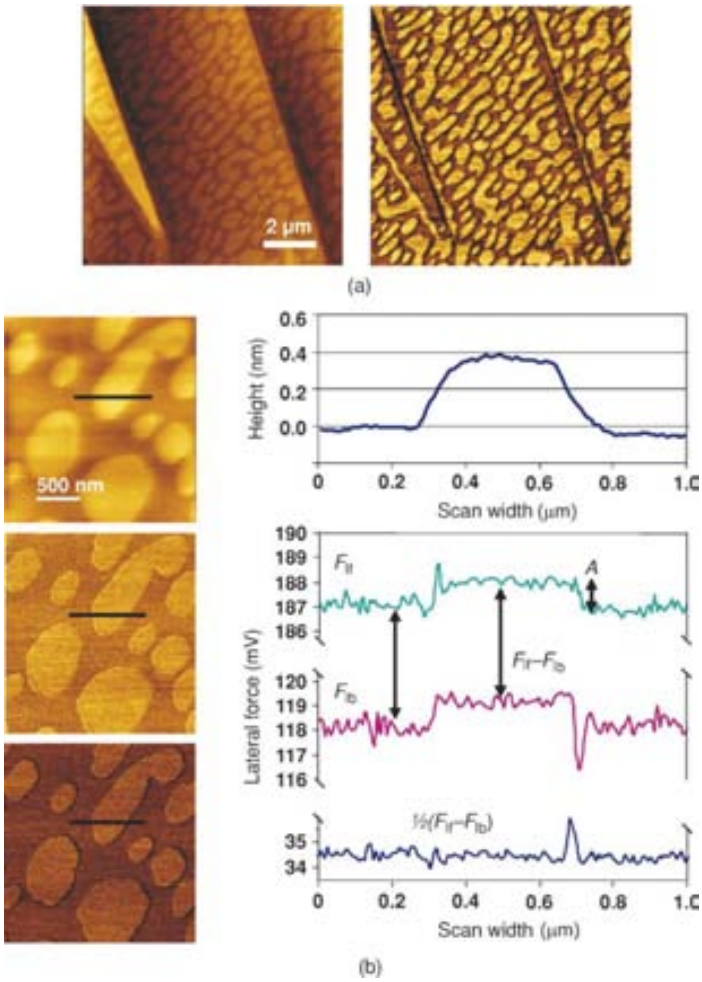


Figure 4.18: a) Topography (left) and lateral force (right) images taken in contact mode at room temperature and 40% RH. Scale is 11 $\mu$m x 11 $\mu$m. b) Topography (top left), forward scan lateral force (middle left), and backward scan lateral force (bottom left) images taken at room temperature and 40% RH. The corresponding cross section profiles are shown to the right. A stands for the friction asymmetry while $F_{lf}$ and $F_{lb}$ represent the lateral force signals along the forward and backward scan directions, respectively. The total friction is calculated as $1/2(F_{lf} - F_{lb})$.

torsion magnitude (A in the profiles) between islands and terrace is measured. More specifically, friction calculated as $1/2(F_{lf} - F_{lb})$ (bottom of line profiles) reveals that an equal value (same friction coefficient) is obtained on islands and terrace, as otherwise characteristic of areas of homogeneous surface properties and, in particular, same chemical composition. Note that this effect is observed, except at the islands boundaries where cantilever torsion is influenced by the topographic change, independently of the area of the islands, discarding size effects.

As previously said in the LFM introduction, similar asymmetric effect has been

reported for organic ferroelectric crystals (Bluhm, Schwarz and Wiesendanger, 1998), lipid monolayers on mica (Liley et al., 1998), alkanethiol SAMs domains on gold (Munuera, Barrena and Ocal, 2007), and for cleavage surfaces of alkaline earth sulfate crystals (Shindo et al., 1999). The origin is an asymmetric tip-surface interaction potential (illustrated by a saw-tooth-like potential by Bluhm et al., 1998) ascribed either to domains with the same structure but opposite molecular tilt directions or to surfaces with a mirror plane surface structure.

Islands and terraces of fig. 4.18 can be visualized as such surface domains and in the following I will focus on the origin of their asymmetry in terms of friction. In order to exclude electrostatic interaction as the origin of the frictional asymmetry (asymmetric contact potential difference), SPFM combined with KPFM measurements are presented (fig. 4.19).

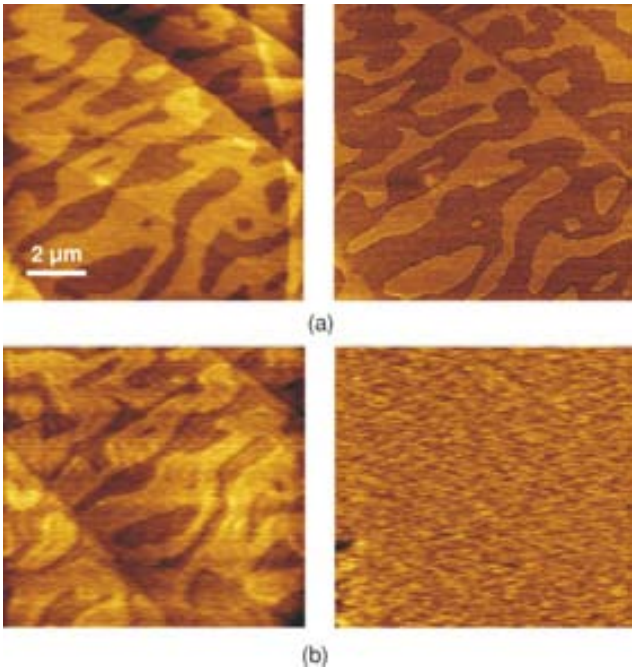


Figure 4.19: a) Topography (left) and lateral force (right) contact mode images and b) SPFM (left) and KPFM (right) images of (011) surfaces of L-alanine taken at 50% RH.

Fig. 4.19a shows contact mode topographic (left) and lateral force (right) images of a (011) surface taken at 50% RH where the two regions corresponding to terraces and islands can be identified and 4.19b shows SPFM (left) and KPFM (right) images of the same region. SPFM topographic images show the same topography features

and same height values (within experimental error) as observed in contact mode, indicating that no dielectric differences exist between islands and terraces. Similarly, a featureless KPFM image implies the existence of a unique surface contact potential in both regions, supporting once more their same chemical nature.

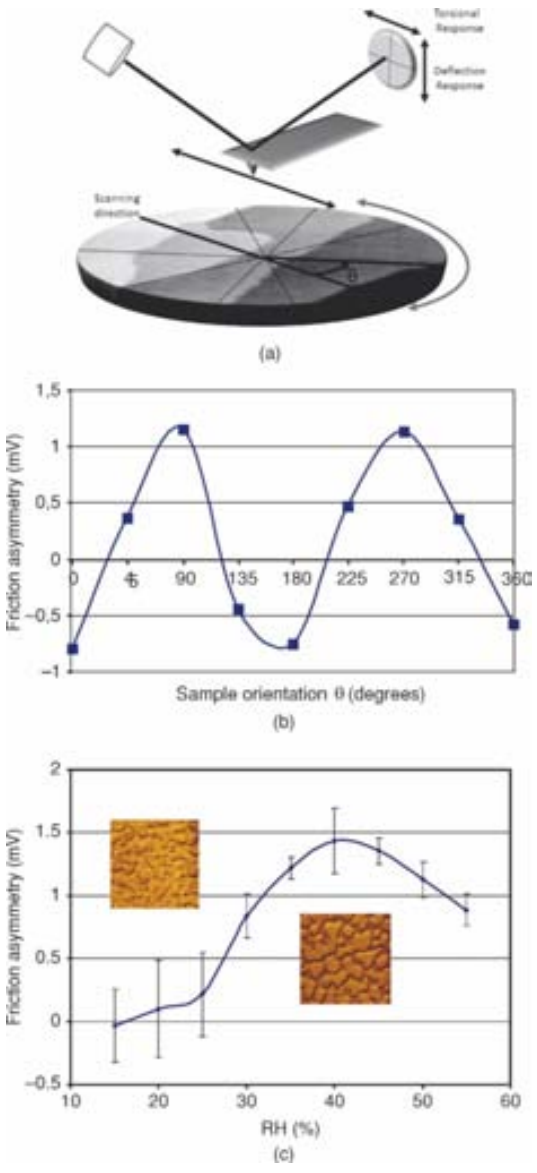


Figure 4.20: a) Scheme showing the cantilever scanning direction and sample orientation ($\theta$) with regard to the torsional and deflection responses in the four-sectors detector. b) Friction asymmetry as a function of $\theta$ with respect to the forward scan direction. c) Friction asymmetry as a function of RH. Selected lateral force images corresponding to $\sim$ 20 and 40% RH are displayed. The lines in b) and c) are guides to the eye.

In fig. 4.20b the friction asymmetry is represented as a function of the sample orientation $\theta$ while keeping the scan direction fixed (see fig. 4.20a). The 180° periodicity reveals that both friction asymmetry and anisotropy simultaneously exist. The analysis as a function of RH is also presented in fig. 4.20c. It turns out that the observed friction asymmetry is dependent on RH with a maximum at $\sim 40\%$, in agreement with the triggering value of enhanced surface species mobility (fig. 4.14), and falls back to the lowest detectable value after removal of water vapor. This fact points to a possible reversible incorporation of water within the surface as discussed below. Altogether, the above results indicate that ascribing friction asymmetry to an asymmetric (180° rotated) molecular structure of islands and terraces is adequate and this can be best explored with high resolution LFM.

High resolution images follow the same principles than Contact AFM but working at such small scale needs some special considerations. As the scanned area is really small (typically few hundreds of $nm^2$) the stress that the tip induces on the surface would be much greater than normal contact imaging (with typically hundreds of $\mu m^2$) since it remains on the same zone continually. This can easly lead to serious disturbing on the sample surface. To minimize this effect high velocity scan rate is used, increasing it as the size of the image decreases. This decreases the amount of time the tip is located over a single molecule. However, some sample distortion is always present when performing this kind of images on aminoacids.

Figure 4.21 shows a molecular resolution image of a surface obtained after exposure to 40% RH over an area including part of one terrace and part of one island. Resolution is high enough to show molecular order in both regions, with $\sim 1.6$ nm separated rows running along a common crystallographic direction. Even though the observation of a unique 2D order supports our interpretation, regretfully, resolution does not reach the level needed to distinguish molecular positions within the surface unit cell.

Summarizing, as the product of watersurface interaction, 0.35 nm high islands develop on the surface terraces at moderate RH. Both, islands and terraces, have the same chemical composition, exhibit rectangular 2D order with the large dimension equal to 1.6 nm and a high friction asymmetry with no differences in dipole

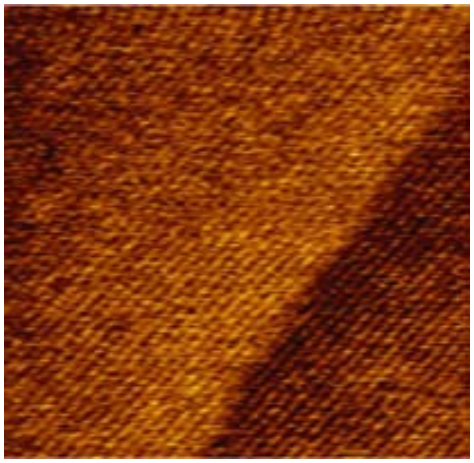

Figure 4.21: High resolution topographic image (100 nm x 100 nm) of a terrace and an island, took in contact mode after exposure to the sample to 40% RH.

orientation. These two levels must be mirrorlike symmetric and should have a lower molecular density than the (011) initial surface. This scenario is compatible with a 2D surface ordering in which the molecular species at the exposed surface are ordered in a lying flat arrangement with Pm rectangular symmetry in which water molecules are importantly involved.

In pure single component surfaces, usually dense molecular packing sterically prevents many of the possible modes of energy dissipation such as rotational motions or molecular bending, otherwise more probable at open molecular structures. On the other hand, it is known that 2D arrangements different than those corresponding to ideal (bulk terminated) surface planes, known as reconstructions, can be stabilized at surfaces. The reasons for the appearance of such surface reconstructions are diverse but strong interaction with gas or liquid molecules are usual triggers of surface species reordering. Eventually, the final surface is that minimizing the surface energy for specific environmental conditions. One way or the other, a reduction of molecular density at surfaces may certainly result in an enhancement of possible dissipation routes as observed here. Instead of hypothesizing a completely new 2D molecular structure as responsible for the results reported here, I evaluate the viability of specific packings already existing in L-alanine crystal planes with the aim of searching for possible structural models.

The stripelike structure observed in figure 4.21 reminds that observed for the

(120) plane. High resolution images taken on (120) cleavage surfaces (fig. 4.22) reveal parallel molecular chains running along the crystallographic c-axis with a well resolved periodicity of 1.7 nm, i.e., the expected surface unit cell for the ideal (120) surface and coinciding with previous LFM results (Guo, H. M. et al., 2004).

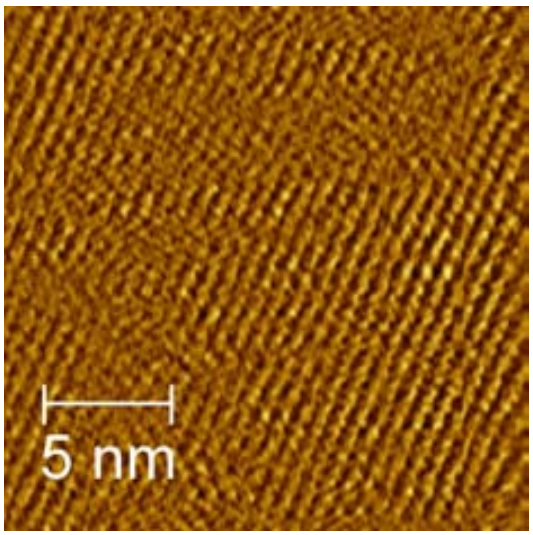


Figure 4.22: High resolution topographic image (20 nm x 20 nm) of a L-alanine (120) plane.

Though this periodicity agrees reasonably with the in-plane separation between rows in figure 4.21, the inter-plane separation is 0.43 nm, clearly larger than the measured islands height. Moreover, a molecular density of 4 molecules $nm^{-2}$ is too close to that of the (011) to justify the observed two levels landscape. A more appropriate molecular packing, able to match with the surface symmetry of the initial (011) surface, and consisting of a planar arrangement of molecules, is presented in figure 4.23.

This structure corresponds to the (040) crystal plane with a surface unit cell of 0.603 nm x 0.578 nm, along the a- and c-crystallographic axis, respectively, i.e., it perfectly matches with the (011) plane in one direction. The reduced unit cell of the (011) plane (fig. 4.8a) has been drawn in figure 4.23a to illustrate that the uniaxial mismatch between both planes is adequate so that two lying molecules in an arrangement as that of the (040) plane would perfectly match on the fourfold positions (labelled 1, 2 in figure 4.8a) of the underlying (011)-terminated crystal.

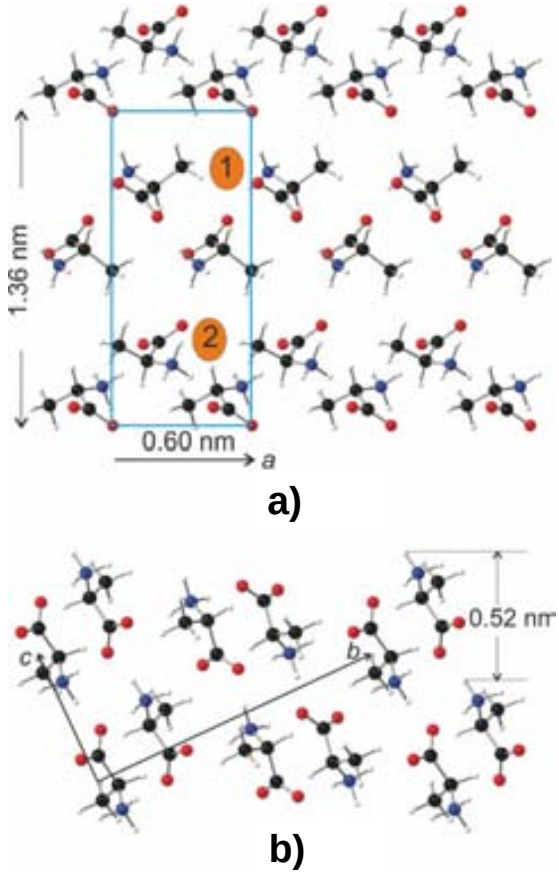


Figure 4.23: (a) Top and (b) side views of the (040) crystal face of L-alanine projected along the b- and c-axis, respectively. Carbon, oxygen, nitrogen, and hydrogen atoms are represented by black, red, blue, and white spheres, respectively. The surface unit cell, a x 2c = 0.60 x 1.16 $nm^2$ (red), is compared to that from (011) shown in fig. 4.8, 0.60 x 1.36 $nm^2$ (blue).

With a density of $\sim$ 2.9 molecules $nm^{-2}$, this packing is consistent with the formation of two levels out of one initial much denser (011) surface ($\sim$ 4.9 molecules $nm^{-2}$). In terms of friction, such an open 2D structure with a large area per molecule (34.8 $Å^2$ *vs* 20.5 $Å^2$) would favor molecular motions responsible for large dissipation processes. The friction asymmetry between islands and terraces may be explained via the uniaxial mismatch and the unique molecular orientation within the surface plane, which makes equally probable the formation of 180° rotated domains. Finally, a good estimation for the expected thickness of this planar arrangement is the distance between adjacent (040) planes, which is $b/4$ - 0.31 nm (fig. 4.23b), very close to the observed islands height. In addition, a lying down surface molecular distribution supports a hydrophobic character since the molecular dipoles lie nearly parallel to

the surface, as explained for the L-alanine (120) case.

How credible is the water-mediated formation of a surface as the model proposed here? The high affinity to water exhibited by the (011) surface, which is experimentally observed at low RH values and has been interpreted in the previous section in terms of nearly collinear alanine−dipole water−dipole interactions, may lead to the dissociation of the L-alanine intermolecular bonds. In crystals, L-alanine molecules are bound together through N-H$\cdots$O hydrogen bonds between the ammonium and carboxylic groups of nearest molecules. Water molecules may break such bonds and solvate the individual molecules through N-H$\cdots$O and O$\cdots$H-O hydrogen bonds. The solvated zwitterionic form of L-alanine can differ significantly from the crystalline phase but has been found to be stable (Degtyarenko et al., 2008).

However, the solvated system cannot stand the whole set of molecules at the same terrace level and some are liberated to the surface. They would diffuse and nucleate in islands adopting a lying down configuration to optimize van der Waals interactions and growing by Ostwald ripening to reduce surface energy. On the other hand, molecular removal would cause a relaxation of the now less dense terrace level in such a way that the remaining molecules are able to bend and eventually, for a low enough density, arrange in a lying down configuration as well. If approximately one out of two L-alanine molecules is displaced during solvation, islands will cover 50% of the terraces (or a bit more if water is incorporated), in good agreement with figure 4.14c. For energetic reasons, both levels must be equivalent domains. Their expected tension-free hydrated structure is presumably uniaxially strained to match the underlying (011) lattice, providing an appropriate 180° surface asymmetry. At this stage, with the molecular dipoles parallel to the surface in both levels, the strength of the dipolar interactions is reduced and the initial hydrophilic character turns into hydrophobic. *In this case, hydrophobicity is induced by water.*

D-Alanine crystals were studied following the same procedures described for L-alanine and the same results were obtained.

## 4.2 L-Valine

The next essential amino acid in complexity after alanine is valine. Valine (2-amino-3-methyl butanoic acid, abbreviated as Val or V) is a non-polar essential amino acid that has a non-reactive hydrophobic isopropyl group as side chain. Valine was also studied by the large difference in the T of ice crystallization between its pure and racemic crystals (Gavish et al. 1992), this behaviour catch along with being the next amino acid after alanine in R group complexity, drove great interest in studying its intereactions with water vapour molecules.

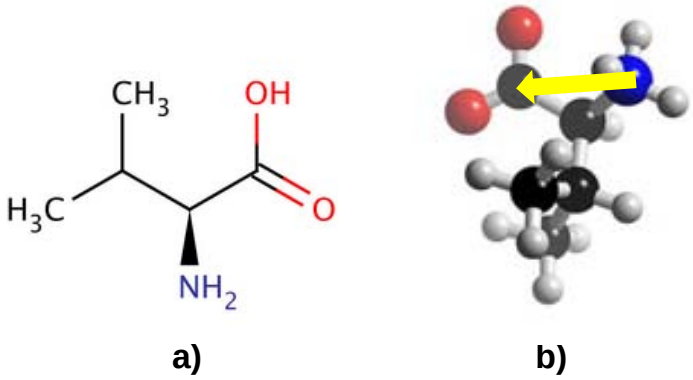


Figure 4.24: a) L-Valine molecule. b) 3D L-valine model in its zwitterionic form. The molecular dipolar moment is represented as a yellow arrow.

It is considered as a hydrophobic amino acid but it exhibits a relatively good solubility in water (8.85 g in 100 g of $H_2O$ at 25°C) due to its zwitterionic form (Karplus, 1997). The crystals of L−valine form flat flakes that can be easily exfoliated using adhesive tape as explained, exposing fresh (001) surfaces. These crystals are formed by molecular bilayers (fig. 4.25).

To my knowledge valine is the smallest biorelated molecule building a lamellar−like structure. In the case of the closely related alanine molecule, where the isopropyl group is substituted by a methyl group, bilayers are not formed, as explained in the alanine chapter. The intrabilayer interactions are of electrostatic origin (hydrogen−bonding) due to the zwitterionic charge distribution while interbilayer interactions are of van der Waals type involving methyl groups. The weak interbilayer interaction is the cause of the ease to exfoliate the crystals. The crystallographic data, P21, $a = 0.971$ nm, $b = 0.527$ nm, $c = 1.206$ nm, $\beta = 90.8°$ have been

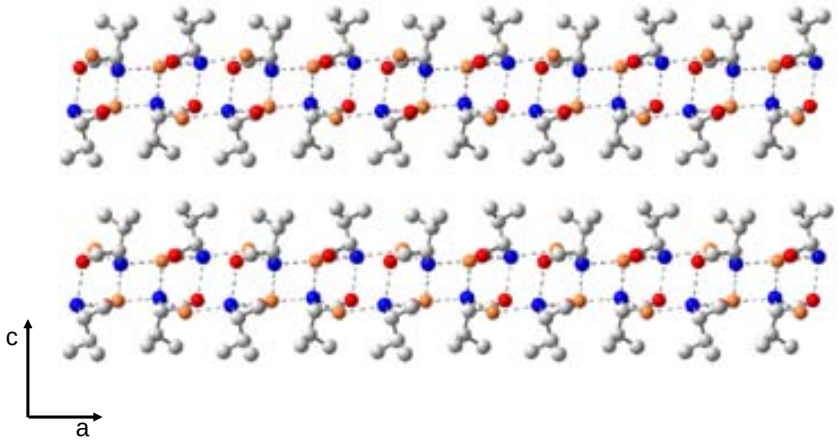


Figure 4.25: L-Valine grows through the c−axis in the form of bilayers.

taken from Torii and Iitaka, 1970.

Prior molecular-resolution AFM studies of cleaved L-valine surfaces measured in air have shown that the (001) surface corresponds to the truncated bulk structure, indicating negligible surface relaxation or reconstruction within the experimental accuracy (Manne et al., 1993; Wang et al., 2002). Since the water−induced pattern dimensions that I observe are of the order of few microns, I have concentrated on lower resolution images. I have also acquired high-resolution images with the smaller scanner (see tables 2.2 and 2.3 for the experimental conditions) and obtained the expected surface lattice parameters (fig. 4.26).

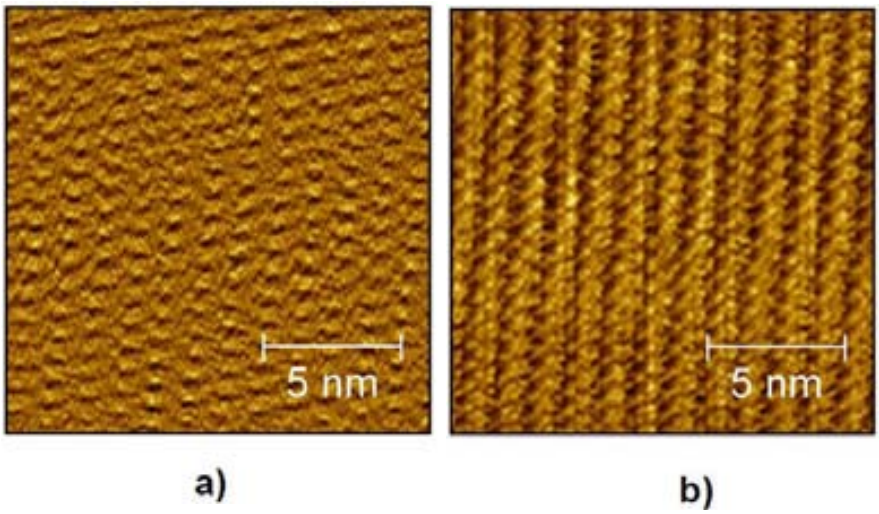


Figure 4.26: L-Valine a) deflection and b) friction images with molecular resolution.

Freshly cleaved (001) surfaces show large micron-sized terraces separated by irregular steps (fig. 4.27).

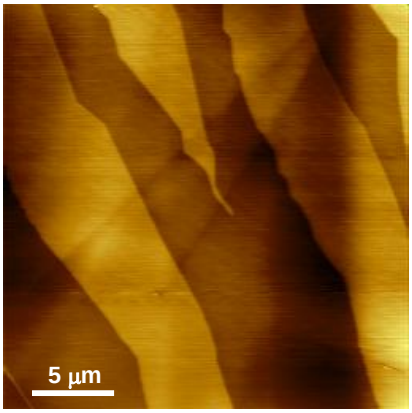


Figure 4.27: L-Valine (001) crystal plane at ambient conditions after fresh cleaving.

The step heights are integer numbers of the distance between two adjacent bilayers (1.25±0.07 nm). As shown in figure 4.25, the layered structure exposes hydrophobic methyl groups while steps expose the hydrophilic $COO^-$ and $NH_3^+$ groups (fig. 4.28).

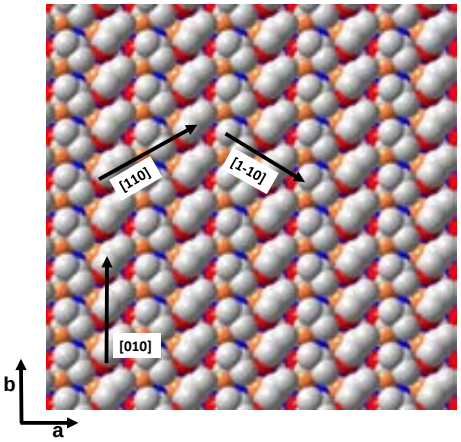


Figure 4.28: L-Valine (001) top view.

This exposed surface is extremely stable with the rising of the RH, and at values as hight as 85% no topography changes are observed when scanning over it with the AM mode. If the crystal is immersed in Milli-Q water for a few seconds and then

dried with nitrogen remarkable features appear on the surface as shown in figure 4.29.

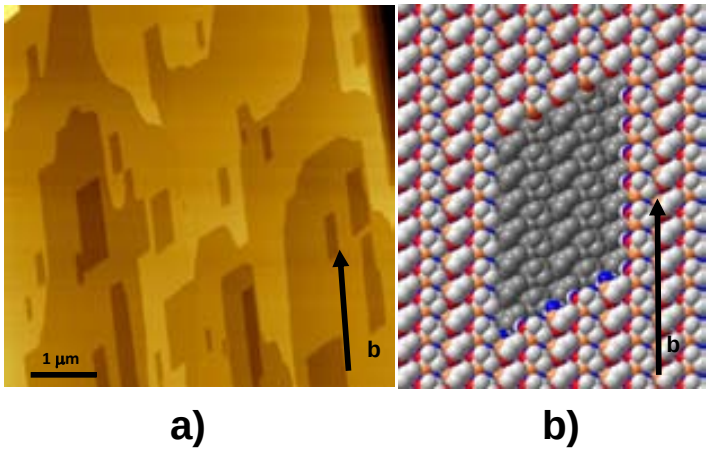


Figure 4.29: a) AFM topography image taken at ambient conditions after immersion of a L-valine crystal exposing (001) surface in Milli-Q water and drying with nitrogen. b) The corresponding crystal structure of the (001) surface is represented in the space-filling mode.

Such features consist of regular parallelepipeds, whose sides are steps one bilayer high. Figure 4.29 shows an AFM image of a (001) face of L-valine. Note that the steps are aligned along two well-defined crystallographic directions, namely [010] and [110], which form angles of 60° and 120° between them. We observe that all patterns show longer sides along the [010] direction and are formed with steps along the [110] direction but not along the [1-10] direction.

The fact that only [010] and [110] directions are observed suggests that water must be more reactive on [1-10] steps. In addition, the elongation of the patterns along the [010] indicates that water is less reactive on [010] steps than on [110] steps. The difference observed for [110] and [1-10] steps is surprising at first sight since they are structurally equivalent. Thus, in principle, water should etch both [110] and [1-10] steps identically and as a consequence pseudo-hexagonal patterns should appear, contrary to what is experimentally observed. In order to exclude any artifacts induced by the preparation of the sample I have performed the following test experiment: taking a L-valine single crystal, and arbitrarily assigning one of its surfaces as the (001) plane and the opposite one as the (00-1) plane, new crystal faces of both planes were obtained and the effect of liquid water on them was studied.

Figure 4.30 shows AFM images after immersion of both surfaces under the same conditions.

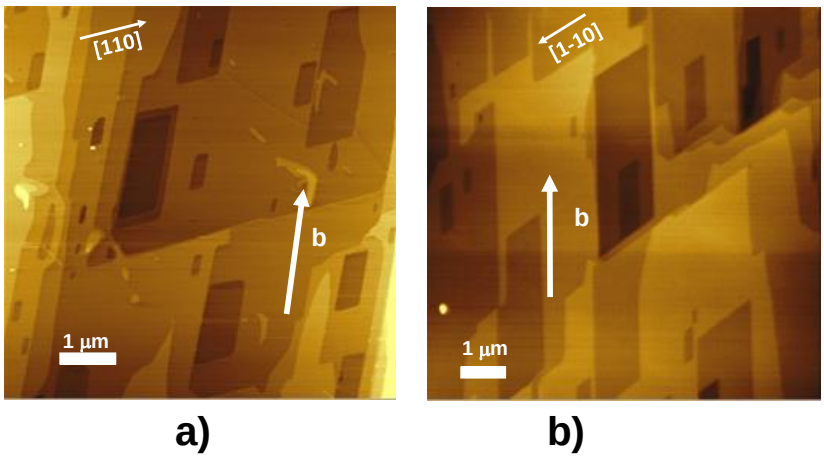


Figure 4.30: AFM images comparing patterns created on the two faces obtained from a cleavage of a crystal: L-valine a) (001) and b) (00-1).

From the images it becomes evident that etching generates the same surfaces, the only difference is that the steps run along the two opposite step directions, [110] and [1-10], as indicated in figure 4.30. That means water is able to differentiate the layers building the bilayer even if they are structurally equivalent. This cannot be understood solely from geometrical arguments because of translational symmetry. However, the water molecules close to a step are also close to the hydrophobic surface and it is well known that a depletion layer is built between water and hydrophobic surfaces. This depletion layer, $\leq$0.3 nm thick, has been measured and simulated for hydrophobic methyl terminated self-assembled monolayers (Jensen, Mouritsen and Peters, 2004; Chandler, 2005; Mezger et al., 2010; Chattopadhyay, 2010). I expect a similar behavior on the L-valine terraces where it should play a relevant role, since the depletion layer is of the order of the separation between two adjacent bilayers.

### Simulations results

As for the L-alanine case (see previous section) here I assumed that the interaction of water with valine crystals will be also dominated by Coulombic interactions and decided to test if the dipole model can explain the observed structure of the patterns on L-valine. Dr. Sacha (from UAM at the time where the simulations were

performed) performed the potential localization on the L-valine structure. In figure 4.31 I show the structure of a hexagonal pattern on a (001) L-valine surface with the three principal steps directions, namely [010], [110] and [1-10].

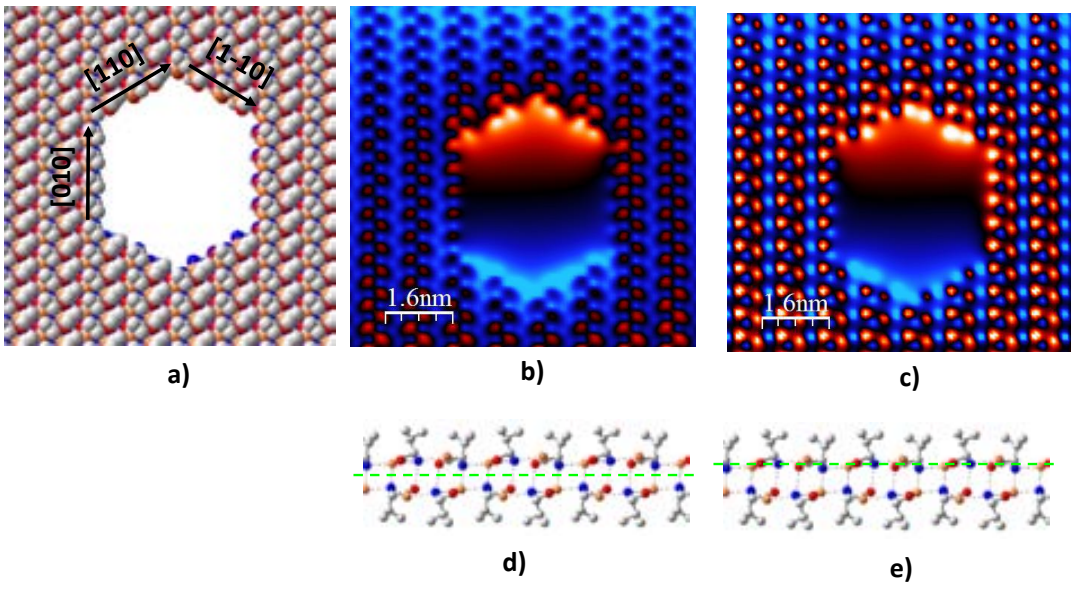


Figure 4.31: a) Hexagonal etched pattern on a L-valine (001) surface taking into account equal dissolution rates for the three steps. b) and c) show 2D cuts of a three dimensional plot of the potential created by all the charges of the structure shown in a) where positive potential is shown in blue and negative potential in red. +1e and -1e charges have been considered at the position of the N and single bounded O atoms, respectively. The green dashed lines show the cuts performed d) at the center of the bilayer and e) at the level of the O and N atoms of the upper layer.

This is the pattern that would be expected on AFM images if water would etch equally all possible steps. In figure 4.31b I plot a representation of the potential generated by the charges (+1e charge located at $NH_3^+$ and -1e located at the single-bonded oxygen of $COO^-$) for the hexagonal step structure shown in figure 4.31a. Positive potential is shown in blue and negative potential in red. The three dimensional representation of the potential has been cut for a 2D view at the center of the bilayer as shown in the lower part of the figure. Dipoles along the [010] direction are parallel to the step, as it can be observed by the alternate positive (blue) and negative (red) maximum along the step. For [110] and [1-10] steps dipoles are more perpendicular to the step edge, positive or negative depending on which group is exposed. Water will preferably etch [110] and [1-10] steps rather than [010] following the collinear vs. parallel argument discussed above and as a consequence the

patterns should be elongated along the b direction, as experimentally observed in the AFM images. However, the plot shown in figure 4.31b cannot explain why [110] steps are dominant over [1-10] steps. As mentioned above water does not interact equally with the upper and the lower part of the bilayer due to the presence of hydrophobic groups at the terrace inside the patterns. Thus, what determines the etching is the interaction of water with the upper molecules of the bilayer. In figure 4.31c I show the same representation as in figure 4.31b but cut at 2Å above the center, just at the level of the hydrophilic groups. In this plot charges along [110] show again alternation of blue and red spots thus creating dipoles approximately parallel to the step edge. Conversely, along [1-10] steps dipoles are clearly perpendicular to the step edge. Thus, water will etch preferentially [1-10] steps and as a result [110] steps will be dominant, as experimentally observed.

## 4.3 D-Valine

D-Valine crystalizes, like its mirror image amino acid L−valine, in the form of flat, fish scale like crystals easily exfoliated by means of adhesive tape. Just as described for the L-valine crystals, the intrabilayer interactions are of electrostatic origin (hydrogen bonding) due to the zwitterionic charge distribution while interbilayer interactions are of van der Waals type involving methyl groups. The weak interbilayer interaction is the cause of the ease to exfoliate the crystals. The crystallographic data, D-valine, P21, $a = 0.967$ nm, $b = 0.527$ nm, $c = 1.204$ nm, $\beta = 90.75°$ has been taken from Wang et al., 2003. Prior molecular-resolution AFM studies of cleaved D-valine surfaces measured in air have shown that the (001) surface corresponds to the truncated bulk structure, indicating negligible surface relaxation or reconstruction within the experimental accuracy (Manne et al., 1993; Wang et al., 2002). Again, I have focus the study in a lower scale than the water−induced pattern dimensions that are observed.

Freshly cleaved (001) surfaces show large micron-sized terraces separated by irregular steps just like the ones observed for L-valine (fig. 4.32) and steps heights of 1.22±0.16 nm.

The crystal surface is equivalent to that of L-valine: A layered structure ex-

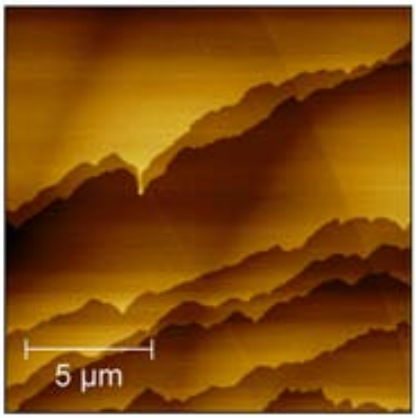


Figure 4.32: D-Valine (001) plane topography image (contact mode) after cleaving at ambient conditions.

posoing the hydrophobic methyl groups in the outter parts of the bilayer, with the hydrophilic $COO^-$ and $NH_3{}^+$ groups in the inner part and also exposed at the setps. The exposed surface is again extremely stable against water vapor and at values as hight as 85% no topography changes are observed, but liquid water affects drammatically the crystal surface and if immersed in Milli-Q water for a few seconds and then dried with nitrogen, windows appear on the surface as shown in figure 4.33.

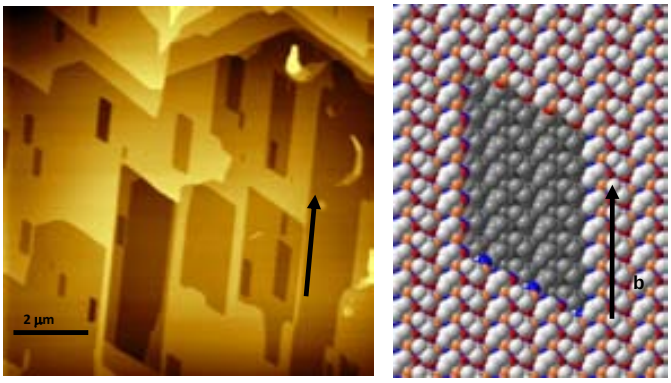


Figure 4.33: a) AFM topography image taken at ambient conditions after immersion of a D-valine crystal exposing (001) surface in Milli-Q water and drying with nitrogen. b) The corresponding crystal structure of the (001) surface is represented in the space-filling mode.

As for the L-valine case, regular parallelepipeds appear whose sides are steps of one bilayer high. Figure 4.33 shows an AFM image of a (001) face of L-valine. Note

that the steps are aligned along two well-defined crystallographic directions, namely [010] and [110], which form angles of 60° and 120° between them. Again, we observe that all these patterns show longer sides along the [010] direction and are formed with steps along the [110] direction but not along the [1-10] direction. In the case of D-valine, the etching patterns are the specular images of those observed on L-valine crystals (fig. 4.29). The same procedure than that of L-valine was performed to exclude any artifacts induced by the preparation of the sample and topography images was adquired over (001) and (00-1) planes. Again no difference between both planes was observed on the adquisition of surface images. The shape and nature of D-valine features formed by the action of liquid water are explained by the same reasons as for the case of L-valine and I refer the reader to the previous section for simulations images and description.

From both studies we observe that (i) all the patterns show longer sides along the [010] direction and present steps along the [110] direction but not along the [1-10] direction and (ii) As a side result from this study, water etching previous AFM imaging has proved to be an effective tool to resolve chirality between L- and D-valine crystals and a single topography image can tell us what amino acid is forming the crystal. Stereoselective etching of $\alpha$-amino acid crystals has been already reported using water dissolutions including additives, a method that has been successfully applied to the direct assignment of their absolute molecular configurations (Shimon, Lahav and Leiserowitz, 1985; Weissbuch, Leiserowitz and Lahav, 2008) but as far as I know, no previous selective water etching on amino acids has been reported.

### Partial etching of valine crystals

When etching is only partially achieved, the patterns show all possible step directions, which can be taken as a snapshot of the evolving etching process. In order to produce incomplete etching of the surface I have wiped it with a wet ultra clean cotton (using Milli-Q water) and then dried it immediately with nitrogen. Although the surface becomes also etched by water and well defined patterns appear on the surface, there is a marked difference with the samples prepared by immersion. The most common patterns observed exhibit a trapezoidal shape formed by steps in both

the [110] and the [1-10] directions, as shown in figure 4.34.

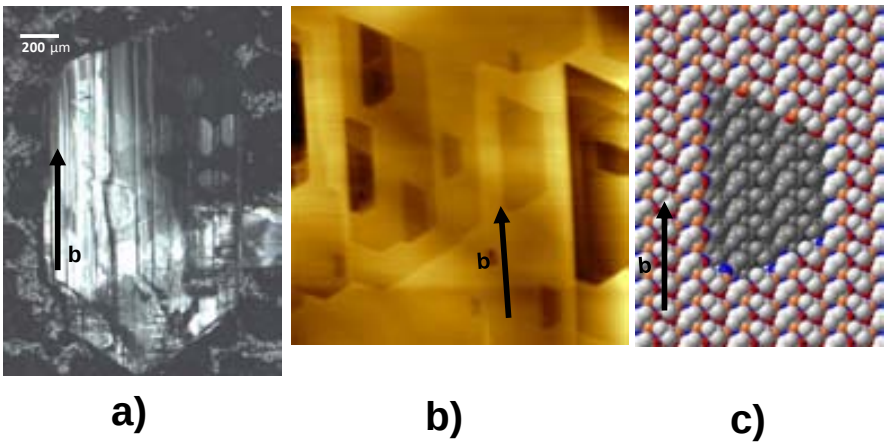


Figure 4.34: a) Optical microscope image of a D-valine crystal. The crystal is polar along b due to the orientation of the valine molecules in the structure. The orientation of the valine dipoles was established by Kelvin Probe Force Microscopy. b) Trapezoidal patterns obtained by wetting the surface using a soaked cotton. c) Simulated structure of the trapezoidal patterns. The upper straight step corresponds to a [110] step exposing $COO^-$ groups equivalent to the structure obtained by immersion of the crystal. The lower steps correspond to [110] and [1-10] steps exposing $NH_3^+$ groups. For immersed crystals only [110] steps were obtained.

Note that the trapezoidal patterns always show one of the edges with only one direction, [110], the direction observed in the immersed samples, and the other edge with both [110] and [1-10] directions. By inspection of the structures of L- and D-valine patterns discussed in the main text it becomes evident that the two steps located at the top and bottom sides of the windows do not have the same structure (it can be clearly seen in figure 4.31c). The step formed at the lower edge of the pattern is exposing $NH_3^+$ groups (positive dipoles) while the step at the higher edge is exposing $COO^-$ groups (negative dipoles). In order to identify the chemical nature of the terminations I have used Kelvin Probe Force Microscopy (KPFM) to determine the orientation of the surface dipoles on each edge of the crystal I took a thick valine crystal flake, cut it in two pieces and glue them standing up on a metal substrate, each of them exposing one of the two different edges along the b direction (fig. 4.35).

I approached a conductive AFM tip to each edge and performed KPFM measurements. I observed that one edge needs a positive voltage to null while the other needs a negative voltage, meaning this that positive dipoles or charges are

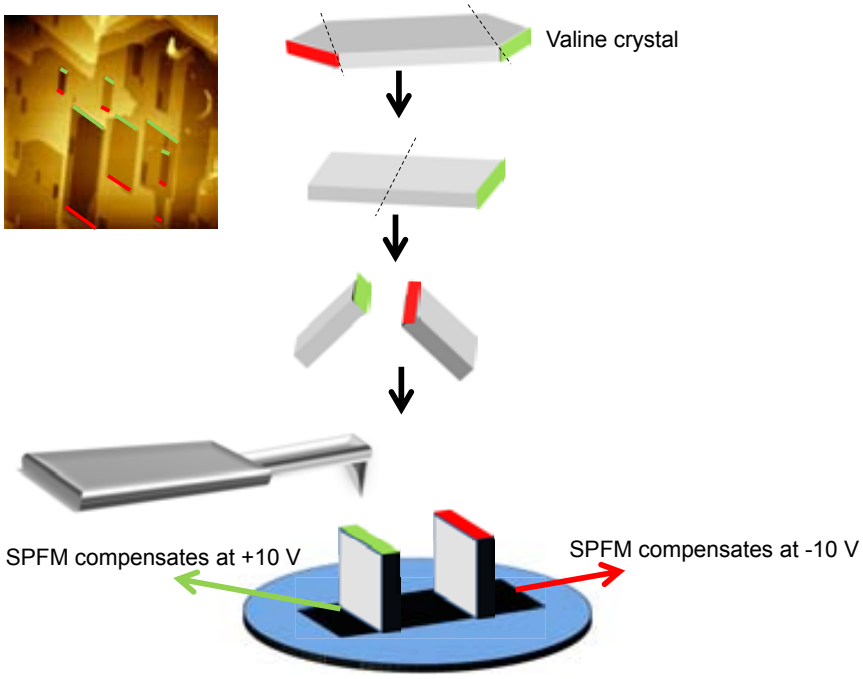


Figure 4.35: Schematic diagram showing the procedure to assign the termination of a valine crystal.

present on the first edge and negative charges or dipoles on the second one. Thus we were able to identify the positive edge as the edge that exposes $NH_3^+$ groups and the negative as the edge that exposes $COO^-$ groups. Using this analysis the structure of the steps showed in figure 4.34 was determined. The side of the patterns that only shows [110] steps correspond to steps exposing $COO^-$ groups and the side showing [110] and [1-10] steps correspond to steps exposing $NH_3^+$ groups. This study demonstrates that while in their final state windows will show only the [110] direction in their upper and lower steps, the kinetics of their formation can start by both [1-10] or [110] step formation for the $NH_3^+$ while for the $COO^-$ side only [110] starts the formation of the step. It is difficult to assign a reason for this difference, no steric influence seems play a greater role on the first respect to that of the latter. The number of hydrogen bonds is the same for [1-10] molecules in both steps and the difference of strenght of those hydrogen bonds formed between water and $NH_3^+$ groups and water and $COO^-$ groups cannot explain either this difference. In figure 4.31b it can be seen that dipoles exposed out of [110] and [1-10] steps are greater in those steps $NH_3^+$-terminated, this can be the underlying reason for the

initial aparition of the two directions, but the greater weight of the upper part of the bilayer respect to the lower one would drive the etching process to form the [110] direction. Anyway, I propose this reason as a tentative one, as no other reason seems to explain this difference.

## 4.4 DL-Valine crystals

D- and L-valine crystals have a global dipole in their monocrystals, DL-Valine crystals, in the other hand, have all their dipoles perfectly compensated at a one by one ratio, so the monocrystal has a net dipole of 0. For this reason I decided to study them and compare their behaviour with water with that of their enantiomerically pure crystals by means of dipoles distrubution. Racemic DL-valine crystals were formed as described in the setup chapter. Like its pure D- and L- crystals, DL-Valine form flat flakes that can be easily exfoliated using adhesive tape exposing fresh (001) surfaces and is formed by molecular bilayers (fig. 4.36). Just like the previous cases, the intrabilayer interactions are of electrostatic origin (hydrogen-bonding) due to the zwitterionic charge distribution while interbilayer interactions are of van der Waals type involving methyl groups.

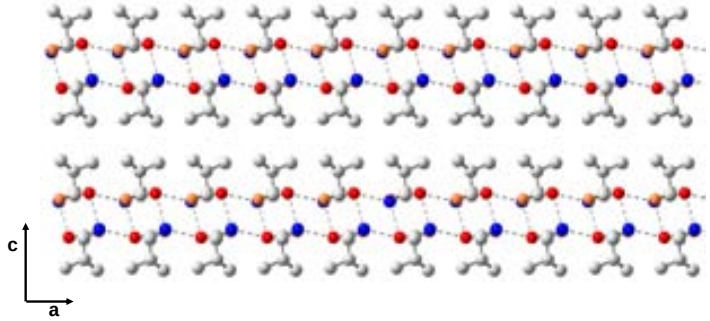


Figure 4.36: DL-Valine grows through the c−axis in the form of bilayers.

The crystallographic data, P-1, a = 0.522 nm, b = 0.541 nm, c = 1.084 nm, $\alpha = 90.89°$, $\beta = 92.34°$, $\gamma = 110.02°$, have been taken from Dalhus and Gorbitz, 1996 and step heights are integer numbers of the distance between two adjacent bilayers. As shown in figure 4.36 the layered structure exposes hydrophobic methyl groups while steps expose the hydrophilic $COO^-$ and $NH_3^+$ groups (fig. 4.37), but

DL-valine crystals have a different bilayer structure than the one depicted at figure 4.25. Again the bilayer exposes the hydrophobic methyl groups at the terraces but in this case each part of the bilayer is formed by either L- or D-valine molecules.

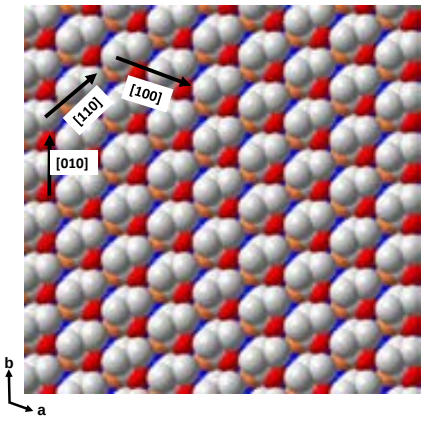


Figure 4.37: DL-Valine (001) top view.

Prior molecular-resolution AFM studies of cleaved DL-valine surfaces measured in air have shown that the (001) surface corresponds to the truncated bulk structure, indicating negligible surface relaxation or reconstruction within the experimental accuracy (Manne et al., 1993; Wang et al., 2002). Like in the case of L-valine and D-valine, I have also acquired high-resolution images with the small scanner (see tables 2.2 and 2.3 for the experimental conditions) and obtained the expected surface lattice parameters (fig. 4.38).

Freshly cleaved (001) surfaces show large micron-sized terraces separated by irregular steps (fig. 4.39).

Monosteps heights were the expected from the crystall cell and the surface turned once again extremely stable with the rising RH, not undergoing any topographic change at values as hight as 85% when scanning over it with the AM-AFM mode. The crystal was then immersed in Milli-Q water for a few seconds and then dried with nitrogen, and as it happens for its enantiomeriaclly pure crystals, window-like features appear on the surface, as shown in figure 4.40.

AFM images of the DL-valine (001) surface after being etched by water show parallelepiped structures as the patterns observed for enantiomeric pure L- and D-

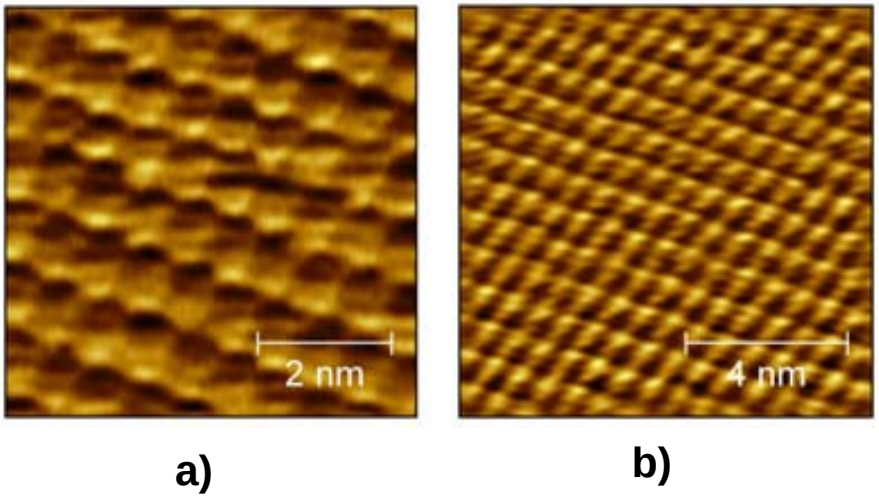


Figure 4.38: DL-Valine a) topography and b) friction images with molecular resolution.

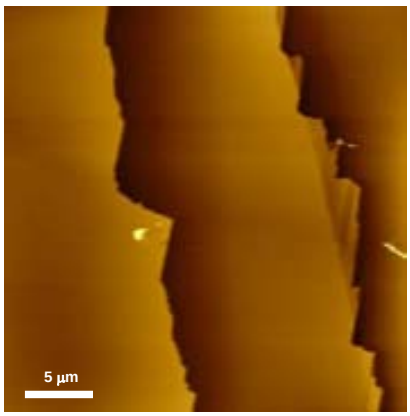


Figure 4.39: DL-Valine (001) crystal plane at ambient conditions after fresh cleaving.

valine crystals, but this time with a similar length on both sides of the parallelepiped. As depicted from figure 4.41 the two specular images can be obtained on DL-valine crystals depending on the orientation, but for a given orientation only one chirality is observed.

Thus, in opposition to D- and L-valine crystals, for DL-valine crystals the choice of the orientation is not arbitrary since the (001) face exposes L-valine molecules while the (00-1) face exposes D-valine molecules. As for pure enantiomeric crystals three different steps corresponding to well defined crystallographic directions [100], [010] and [110] can be formed on a DL-valine (001) surface. The steps directions on

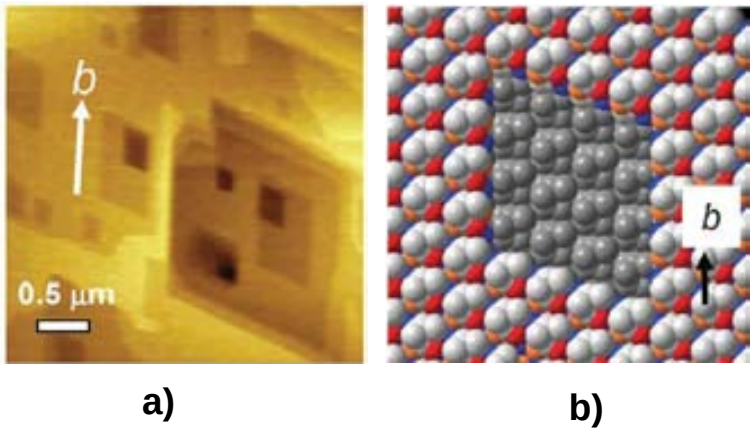


Figure 4.40: a) AFM topography image taken at ambient conditions after immersion of a DL-valine crystal exposing (001) surface in Milli-Q water and drying with nitrogen. b) The corresponding crystal structure of the (001) surface is represented in the space-filling mode.

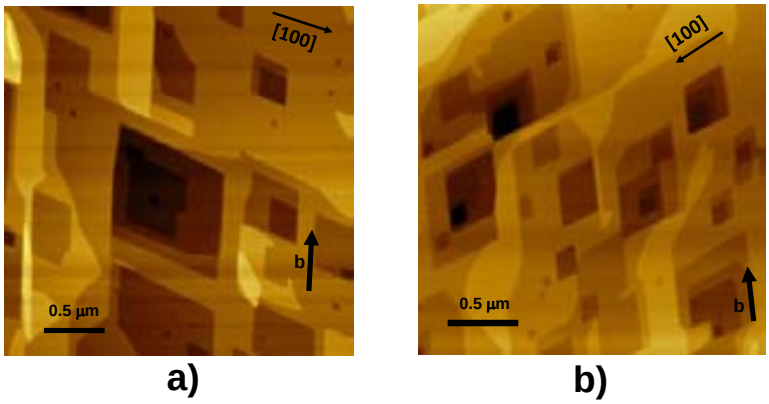


Figure 4.41: AFM images comparing patterns created on the two planes of DL-Valine: a) (001) and b) (00-1).

the AFM images were determined from comparison of X-ray diffraction measurements (pole figures) performed on the crystals with the known crystal structure. I conclude that the patterns in DL-valine are formed only by steps running along both [100] and [010] directions. Such patterns do not show a marked elongated aspect encountered in the enantiomeric counterparts indicating no strong preferential water etching on any of the two directions.

### Simulation results

We can apply the same simulation model used for L-valine to DL-valine to explain the etch patterns observed by AFM. In figure 4.42 I plot the structure of an hexag-

onal pattern with all the possible steps at the (001) face and the potentials of the positive and negative charges cut at the middle of the bilayer. The potential plot shows that dipoles are oriented parallel to both [100] and [010] steps and perpendicular to [110]. Thus, water will preferentially etch [110] steps and to a lesser extent [100] and [010] steps. No clear predilection for either [100] or [010] steps is observed from the dipoles configuration. Thus, patterns should be formed by steps along [100] and [010] steps with no preferential elongation in any of both directions, as shown in figures 4.40 and 4.41. We cannot exclude a certain degree of stacking disorder in the DL-valine crystals, as suggested by S. Grayer Wolf et al. (Grayer et al., 1990), although the good agreement between experiment and theory suggests that its presence would have a negligible influence.

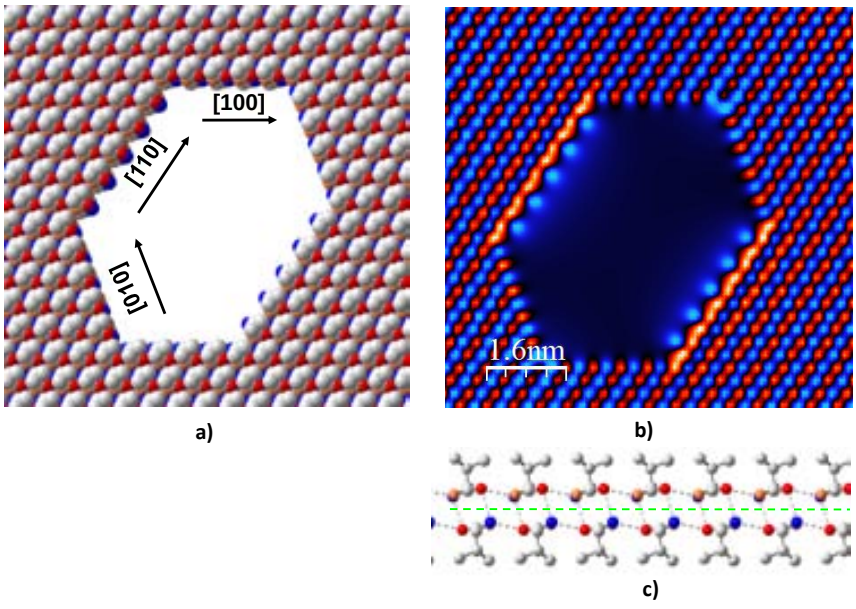


Figure 4.42: a) Hexagonal etch pattern on a DL-valine (001) surface where equal dissolution rate for each of the three possible steps has been assumed. b) 2D cut of a three dimensional plot of the potential created by all the charges of the structure shown in a). c) The cut was performed at the middle of the bilayer as shown by the green dashed line in the bilayer structure shown below the potential plot.

## 4.5 Water adsorption and ice formation on valine crystals

Once the interaction of vapor water with valine crystals and their etching with liquid water was studied at the submicrometer level, the next step in my study was to study the anchoring of condensed water and the ice crystallization on these surfaces at the same scale. The study was done using the same AFM modes than those used in the previous sections. Also SPFM analysis was carried on samples this time, as previously said, it is difficult to apply this technique on amino acid crystals, and it is important to remark that it took many tryings to achieve each successful SPFM experiment, because initial suitable regions may turn into not adequate due to thermal changes on sample s thickness, water condensation on surface and top and material displacement. However, we had a special interest in achieving complete experiments because while SPFM allows the imaging of liquids films and droplets on surfaces, simultaneous KPFM can give information on the structure of the water films. As described by Gavish et al. in their 1992 work, the presence of electric fields in D- and L-valine macroscopic cracks (and windows in the submicrometer level) is supposed to trigger the formation of ice on these features sooner than those of DL-valine due to its absence of electric field.

D-, L- and DL-valine crystals were prepared as described in the setup section and before experiments took place, valine crystals were cleaved to obtain fresh (001) planes and the obtained surfaces were etched with water by short immersion of the crystal inside Milli−Q water and quicly dried off by wipping of the surface with a strong $N_2$ flux. Using such procedures, the described regular etch figures are obtained as explained in the previous sections, made of steps following well-defined crystallographic directions. Such windows offer an ideal surface to study fundamental aspects of step influence on water adsorption and ice formation for valine crystals using AFM. For a detailed description of the system and its instrumental drawbacks I refer the reader to the setup chapter, but briefly explained, the samples were attached to a cooling peltier system adapted to the AFM that allows to decrease the temperature to values down to $-20°C$ as measured from a termopar included inside

the peltier system. They were attached to the sample using copper tape to assure the best thermal conductivity between the sample and the cooling system. However, a difference of some degrees between the temperature of the upper copper piece of the system and that of the sample is expected. With this system only the sample is cooled down, the rest of the system (including the tip and the end of the scanner that are very close to the sample) are kept at room temperature.

**Water adsorption above the dew point:**

At room conditions KPFM taken on the surface revealed two very different contrasts. The observed contrast depends on the sample (fig. 4.43 1b and 4.43 2b) and even on regions of the sample (fig. 4.43 3c).

In figure 4.43 3b a KPFM image shows a huge contrast between the right and the left part of the image of the order of 1V. In the dark part of the image the steps appear brighter as observed in some experiments in the whole surface as shown in figure 4.43 1b. In the bright part steps show a dark sharp contrast. In addition very bright features ($\sim$150 mV above the terraces) with irregular shapes can be observed sometimes on the terraces of the bright part (fig. 4.43 2b). This is the most common contrasts observed at ambient conditions (T=22°C, RH between 40% and 50%)while the contrast observed in figure 4.43 1b is rare to find. The AFM tip used to obtain simultaneous SPFM and KPFM images can be also used to perform contact images of the sample taking into account that after a contact image water on the surface is being strongly perturbed due to the formation of water meniscus between the water condensed on the tip and water at the surface. Using the contact mode I observed that there was no evident relationship between the separations of the different regions of the KPFM contrast and the topographic features on the surface (fig. 4.43 3a). This indicates differences in the chemical nature of the surface and to be more precise on the molecules adsorbed on it, mainly water and dissolved valine molecules. Due to the preparation method of the sample, the surface will have plenty of valine molecules detached from the surface during the etching induced by water that forms the windows structures. Some of these molecules go to the solution but some of them can remain on the surface. In addition, the drying procedure by

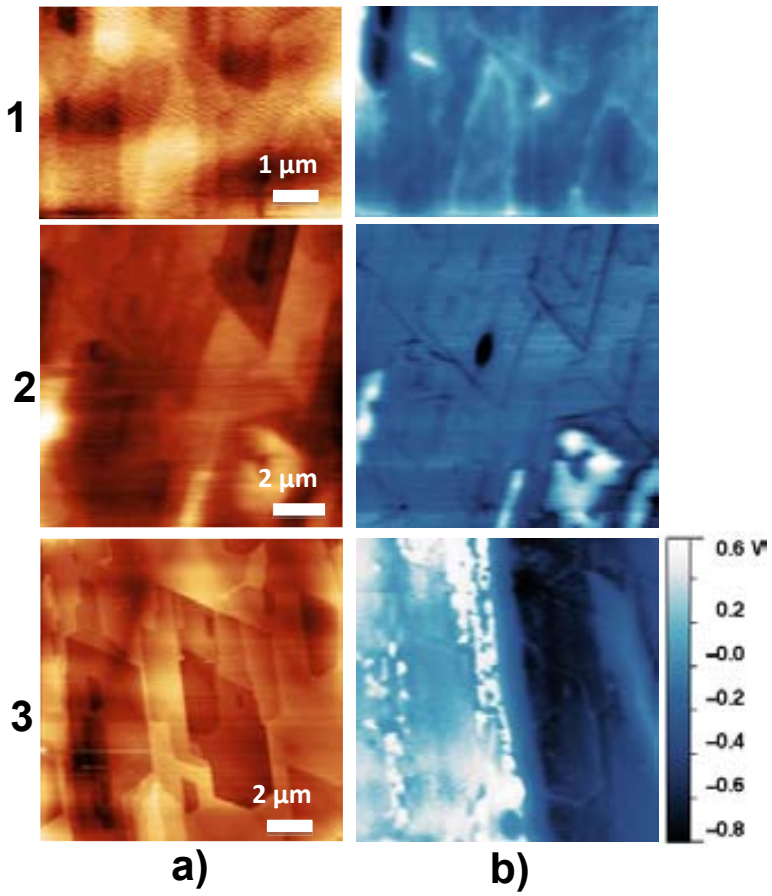


Figure 4.43: D-Valine AFM images. 1a) SPFM image. 1b) KPFM image adquired along with 1a. The edges of the windows appear with a positive contrast respect to that of the terraces. 2a) SPFM image. 2b) KPFM image adquired along with 2a. The windows' edges appear now darker than the terraces. Also some bright spots appear, they correspond to liquid bulk water with dissolved material. 3a) Contact topography image. 3b) KPFM image corresponding to 3a) showing at the same time all the previous explained situations.

blowing with nitrogen, does not assure that all water on the surface is removed. So we expect to have on the surface regions with different amount of water and valine molecules. My perception is that the differences between the bright and dark regions shown in KPFM images correspond to wet and dry regions with different quantity of water and dissolved valine molecules. To corroborate this assumption, samples were kept for a few hours in low humidity conditions (RH5%) and warmed up to 110°C degrees for 10 minutes. Images showed only regions with steps slightly brighter similar to what's shown in figure 4.43 1a and to the region with dark contrast in figure 4.43 2c. As mentioned above in addition to the difference in step contrast for the wet and dry regions on the wet regions bright irregular features are observed

in the KPFM images that correspond also to bright protrusions observed in the SPFM images (see figure 4.43 2b). The bright white features evolve on the surface indicating some degree of diffusion although no clear relationship between the RH in the chamber and the diffusion of the features was observed for a range from 20% to 80% RH. On figure 4.44 two examples of diffusion, growing and reduction of the bright features observed in KPFM images are shown. A contact image of the same region is also shown for a clear identification of the step structure of the surface.

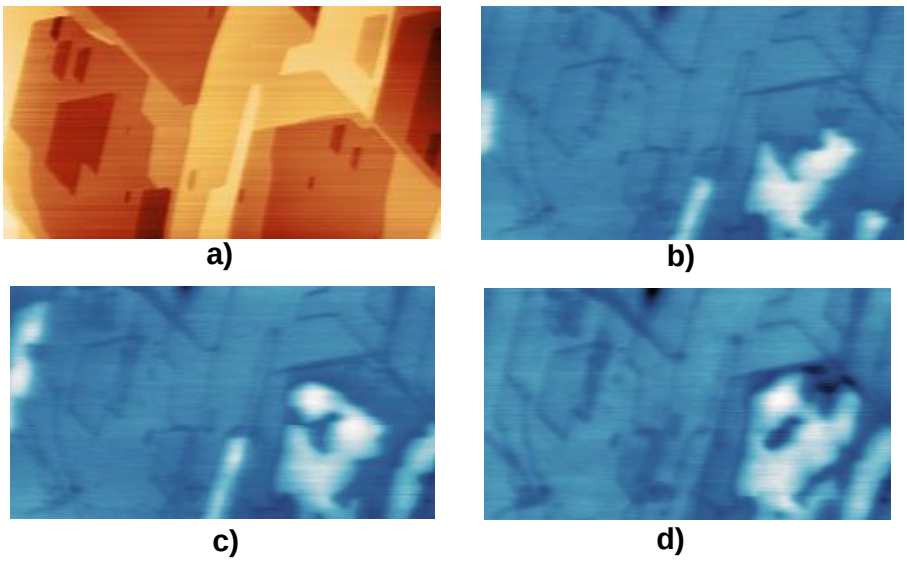


Figure 4.44: a) Contact image. b), c) and d) KPFM images showing the evolution of the bright feature. Bright features can decrease or decrease in size, but always following crystallographic directions.

It can be seen in the bottom corner of the figure 4.44b the growing of a bright feature at 12% RH. The evolution of the bright contrast follows the step structure of the surface filling the terraces and avoiding trespassing over a step. In the final image dark spots not filled correspond exactly to the positions of the small windows in the lower terrace observed in the contact image. The presence of the step acts as a barrier for the diffusion of the white features. This can be observed in figure 4.45 in wich most of the surface is covered by the white features but it still reveals the steps structure of the surface.

All these observations suggests that those brightest features are solvated valine molecules with a limited movement on the terraces independent of humidity due

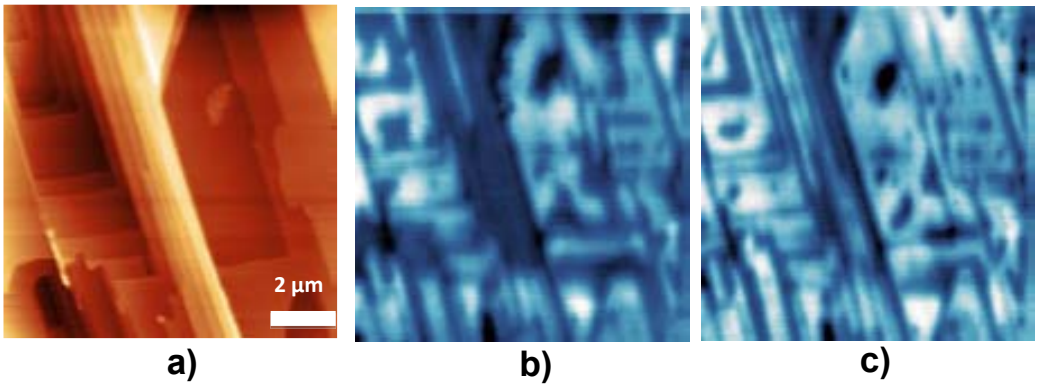


Figure 4.45: a) Topography and b), c) KPFM images. The bright features that grow and diffuse through valine surfaces follow always the step structure.

to the hydrophobic character of the surface. The molecules would be basically interacting with the surface through the isopropyl groups and linked to each other through H-bonds between them and water molecules forming what can be described as a partial monolayer on top of the bilayer. The features appear as very tall structures (17 nm height) on SPFM images, much higher than a monolayer. However in SPFM images relative heights are dramatically affected by differences in dielectric constant on different areas of the sample (Sacha et al., 2009) and similar behavior in SPFM images has been related to ionic diffusion on alkali halide surfaces (Verdaguer et al., 2005). In that case no ions are expected on the sample but the mobility of the valine molecules on the surface with a large dipole is expected to induce the same kind of contrast. This seems to be corroborated by the displacement of material from left to right observed in the contact image (fig. 4.45a), taken after the SPFM image that clearly indicates that on the left part of the surface imaged there is some loose material that is dragged by the tip. Figure 4.46 shows a representation of all the described situations.

In addition to SPFM + KPFM, AM-AFM has been used to investigate the absorption of water at the terraces and steps with humidity. The mode was set up to a real non contact mode in which water films adsorbed on the surface and on the tip never directly contact (Santos et al., 2011). In such mode water films on the surface are not perturbed and the true height of the films can be measured. Measurements have been performed on many samples at different humidity conditions and no well-

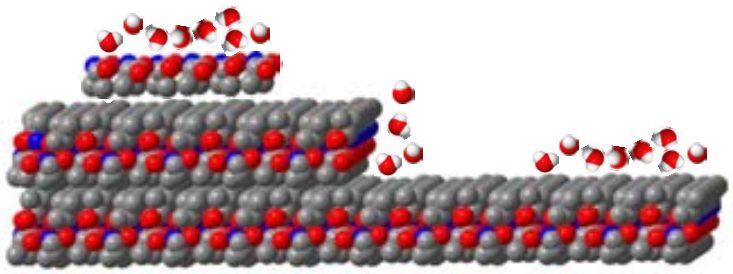

Figure 4.46: Theoretical model of the three observed KPFM images on valine. When water is solvating valine molecules (left part) bright features moving along the crystallographic directions appear. When water is not dissolving valine molecules the dark features can be observed on both steps (center and taking place usually) or as dark round spots on terraces (right, less usual).

defined water patches have been observed, contrary to what has been reported on hydrophilic surfaces (Cardellach et al., 2010). This is not surprising taking into account the hydrophobic nature of the terraces. However, something similar to the watermarks observed by KPFM in the darker contrast regions was observed.

Two interesting things must be remarked. In many images although the water films are not observed on the topographic images they can be clearly identified in the phase (fig. 4.47 1b). They appear as darker regions and mainly linked to windows, totally filling some windows and making rounded patches on terraces. In a few experiments, water patches are visible and a ribbon of some kind of layer is observed along some steps that clearly resembles the initial formation of water films on the surface that even can fill some of the windows (fig. 4.47 2b). By comparing such structures to KPFM images obtained on wet areas we can relate the presence of water to darker contrast on the KPFM images as observed in figure 4.47 3b. In that case darker contrast is observed in some windows, forming ribbons along some steps and rounded or irregular patches on the terraces that are not related to any topographic feature. The contrast is similar to the contrast observed between terraces and steps (of about 45 mV), which must be the first places to wet since they are the only hydrophilic spots of the surface.

### Water absorption below the dew point

The absorption of liquid water on the surface of valine has been studied by i) increasing the humidity in the glove box while scanning and by ii) reducing the temperature

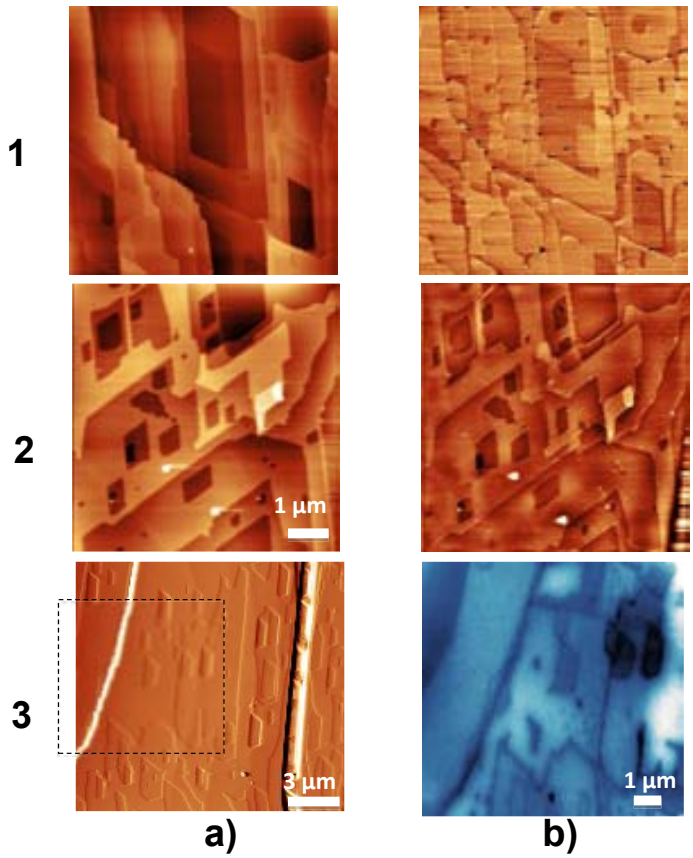


Figure 4.47: Real non contact AM-AFM images. 1a) Topography and b) Phase images on D-valine. 2a) Topography and b) Phase images of valine windows partially filled. 3a) contact and b) KPFM images on D-valine, water covering the sample appears with a dark contrast.

of the sample (but keeping it above 0°C). Using the second procedure allows us to reach the dew point on the sample while avoiding condensation of water on other parts of the chamber. Major changes on the surface can be observed by AM−AFM when the dew point is reached. At these conditions bright dots start to appear at the steps and increase in number as the temperature is further decreased but seem to keep its size constant. Such bright dots appear mainly at the corners of the windows and at irregular steps with a high density of kink sites (fig. 4.48).

Since only the steps are hydrophilic we expect water to adsorb mainly along them. Depending on the free amplitude and the set point chosen for imaging, those bright spots can show an important phase contrast (from positive to negative if the phase was set to a value of 0 far from the surface) that has been already related to the change from a repulsive to an attractive mode of the tip−sample interaction when going from a dry to a wet sample when scanning (Santos et al., 2011). Such

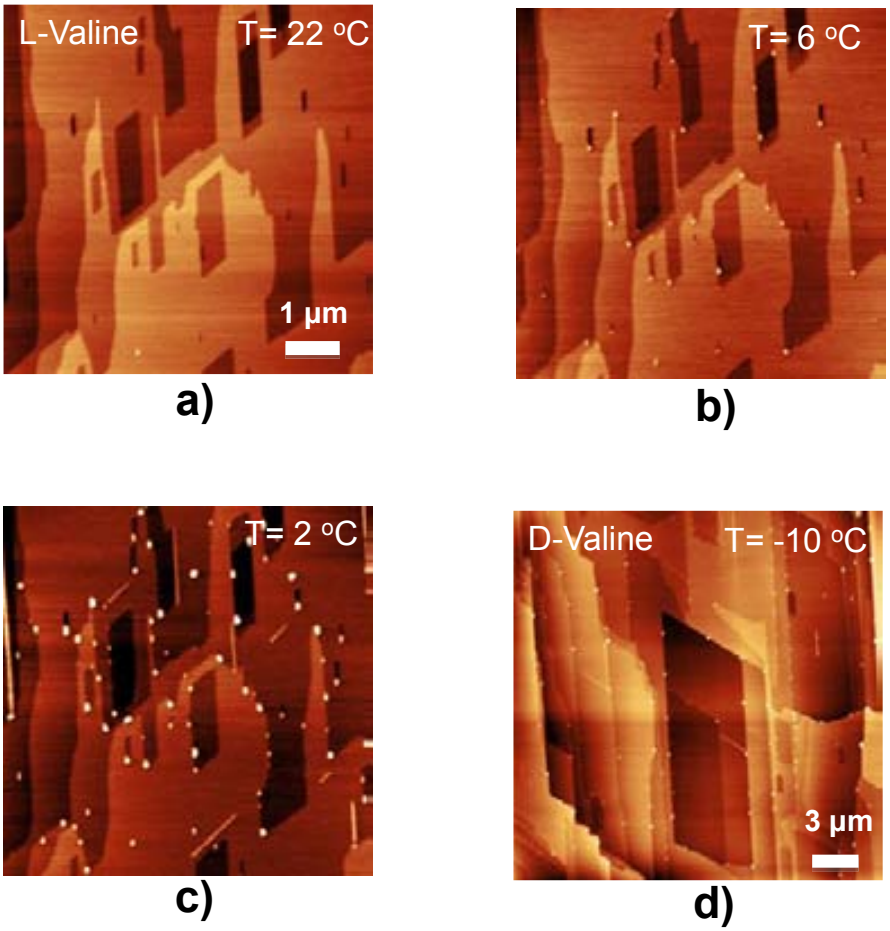


Figure 4.48: AM-AFM topography images. a), b) and c) L-valine at different temperatures and RH = 30%. d) D-valine at RH = 27%.

spots can be observed sometimes on a freshly prepared surface, probably induced by the preparation of the surface. Since the dry procedure by blowing nitrogen is not perfect some water droplets can be left on the surface especially at the steps as already observed on HOPG following a similar dry procedure (Hu et al., J.; 1996). For the same reason, in many cases the spots are observed distributed regularly along the steps, at the same separation between them. This observation on HOPG was attributed to the drying process of the water on the surface HOPG although it has been also observed by trapping water using graphene sheets (Cao et al., 2011).

As previously described, water etches valine steps very easily so it is not easy to determine if the bright spots correspond to water droplets or valine molecules detached from the surface due to water action. Although no changes on the steps

morfology are observed at the magnification used in my AFM images, we must remember that the bright dots are solvated valine molecules. This is corroborated by the moving patterns of the droplets induced by the AFM tips. In figure 4.48c and d we can observe bright lines appearing at the topography when scanning. Such bright lines correspond to the multiple collisions experimented by the tip with bright spots when the collision displaces the tip over the surface.

The manipulation of particles of nanometric dimension on a surface using AM-AFM have been experimentally and theoretically studied (Rao, Gnecco, Marchetto, et al., 2009 and Rao, Wille, Gnecco, et al., 2009). According to these studies for an AFM system that scans using a raster scan path, as in this case, the particles should be deflected in a direction defined by the geometries of the tip, the particles and the spacing between consecutive scan lines. The deflection angle of spherical particles varies from 90° for infinitely close scan (spacing between scan lines decreasing down to 0 and becoming 0 when the spacing between scan lines equals the radius of the particles. In my observations only two well defined angles are observed that correspond to the directions of the windows (fig. 4.48c). The scattering directions are independent of the scan angle, that suggests that the movement of the particle on the surface is determined by the interaction between the surface and the particle. The friction experimented by the particle when moving on the surface is thus anisotropic and forces the particle to move only on the [010] and [110] directions for the range of energies that the tip is transferring to the particle in my experimental conditions. It s interesting to remark that on D-valine the wires also follow the windows directions (fig. 4.48d) and thus they move at 90 degrees from what s observed in L-Valine clearly indicating a structural cause of the movement observed. The limited movement of the droplets suggest some kind of structural matching between the surface of the valine terraces and the surface of the droplets. This is probably due to a coating of the water droplets by a monolayer of valine molecules that would expose the hydrophobic radicals at the surface and the hydrophilic $COO^-$ and $NH_4{}^+$ groups into the water creating an hydropobic $CH_3-$terminated interface of the droplets that would adapt to the $CH_3-$terminated valine surface. The two surfaces in contact probably will have matching structures that would facilitate the

movement of the droplets in some directions and hinderer the movement in others.

If the temperature of the sample is decreased several degrees below the dew point, micron wide water droplets can be observed through the optical microscope acoplated to the AFM system and imaging becomes unstable due the amount of water adsorbed on the surface. A quick dry of the sample (increase the temperature and reduce RH in the glove box) reveals the modifications induced by the water droplets on the surface (fig. 4.49). Using the large scan (see table 2.1) AFM imaging micron wide hillocks can be identified at the positions where water droplets were observed by the optical microscope. Such hillocks are formed by a rounded pyramid-

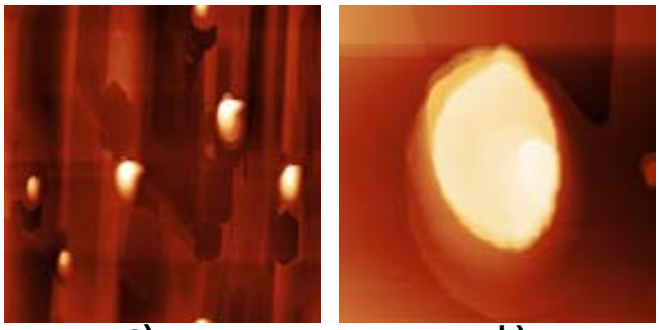


Figure 4.49: AM-AFM topography images of micron sized hillocks originated by water condensation over valine. a) 90x90 $\mu$m b) 10x10 $\mu$m.

like structure of monosteps formed by the process of crystallization of a saturaded solution once dryed as already reported on ionic inorganic crystals (Garcia-Manyes et al., 2004), the areas of the surface where the material was dissolved appear as large flat terraces. All these observations make evident that exposing valine crystals to temperatures below the dew point induce water adsorption, especially at the steps that dissolves molecules of the surface thus no pure water is present at the surface but a saturated solution of valine molecules.

### Ice on valine

If the temparute is lowered enough under low relative humidity conditions it is possible to induce ice formation on the surface avoiding the condensation of macroscopic quantities of liquid water (see table 2.5) that would strongly modify the surface as

described above. The formation of ice could be observed on the metallic sample holder and on sample regions far from the tip by naked eye but no macroscopic ice on the region close to the tip was observed, not even by the optical system integrated to the AFM. The origin of this behaviour has been explained in the SetUp chapter. Despite that, AFM images on the region show features not observed on AFM images taken above 0°C that clearly indicates the formation of ice on the surface even if not macroscopic ice is observed in the optical microscope images. In figure 4.50 we can see some of the features regularly observed on L and D-valine surfaces exposed to temperatures well below 0°C.

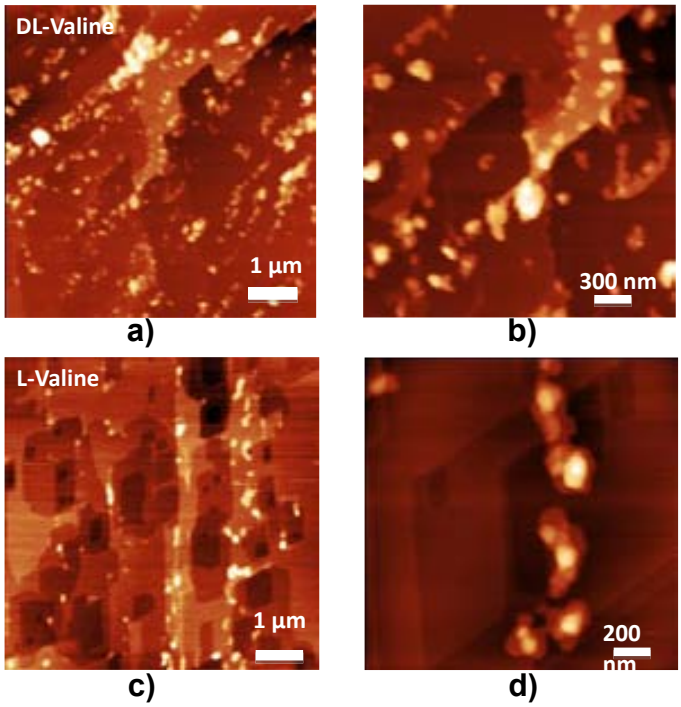


Figure 4.50: AM−AFM topography image of ice nucleation on valine crystals. a) DL−valine (a zoom section is showed in b)) and c) L−valine (a zoom section is showed in d)).

They look like a complex of multilayered structure showing flat terraces and steps of rounded edges plus more irregular features on the top of them. It clearly resembles the crystallization of a solved valine crystal but with step hundreds of Å higher than the expected bilayer height. That suggests that we are observing a structure formed by solid water trapped between two valine monolayers. That will be in line with the model presented in the previous section where the results

suggested that water adsorbed on the surface below the dew point is formed by a solution of valine molecules probably coating the water droplets. The fact that the observed features are not pure ice is also verified by increasing temperature and registering the evolution of the features. They diminish when the temperature is increased up to room temperature (25°C) but some material can still be observed on the surface corresponding to the valine molecules. The structures observed in many cases follow the directions of the crystal due to the needed matching between the valine molecules in the interface between the terraces and the solution surface as already observed in the movement of water droplets in the previous section.

In oposition to the observations reported by Gavish et al. in 1992 and although many ice crystals can be observed on steps and several expermients were repeated for D−, L− and DL−valine, no relationship between the ice formations and the bilayer steps were observed, which seems to indicate that the electric field created by the dipoles of the monosteps plays a minor role in establishing the ice nucleation regions. However, it seems to be important in surface cracks formed from windows made of several bilayers (fig. 4.51).

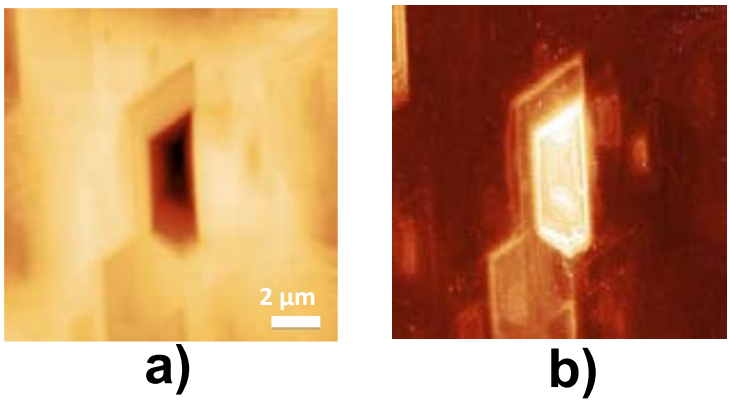


Figure 4.51: L-Valine AM-AFM images of ice formation on multisteps a) topography and b) phase.

In those cracks it is usual to observe ice accumulated at the steps, in figure 4.51b we can observe ice accumulation at the steps specially at the steps in the [110] and [1-10] directions that correspond to the steps where the dipoles are normal to the surface and according to the explanation of Gavish et al., electric fields would

facilitate ice nucleation. One interesting remark is that we can observe a phase shift from negative at the terraces far from the crack to positive on the crack that would correspond to an attractive mode at the terraces changes to a repulsive mode on the crack. Such change has been observed when scanning from a wet to a dry region. In that case that would indicate that while on the terraces we have some liquid water films (as it can be distinguished in the image), in the crack we have water in a solid like nature, i.e. water on the cracks is forced to freeze while water on terraces keep its liquid nature at the range of temperatures we have on the surface.

## 4.6 Etching of L-leucine.

L-Leucine (2-Amino-4-methylpentanoic acid, abbreviated as Leu or L) crystals, grow following a similar procedure as for the valine crystals, they also expose (001) surfaces when cleaved (Coll et al., 1986 for the crystallographic structure). L-Leucine surface after immersion in Milli-Q water shows a similar etching pattern as for L-valine, as shown in figure 4.53.

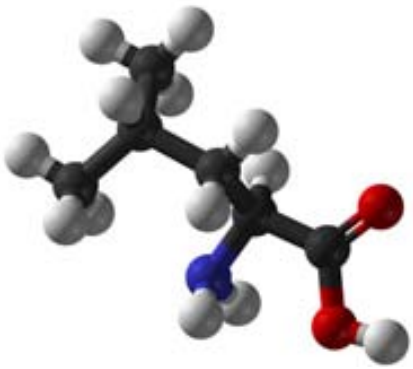

Figure 4.52: L-Leucine 3D model.

The analysis described for L-valine is also valid for L-leucine. The dipoles of L-leucine follow the same distribution of those of L-valine, and the exposed hydrophobic groups on the terrace along with the polar $COO^-$ and $NH_3^+$ groups exposed on the steps produce the same kind of crystal surface studied for valine.

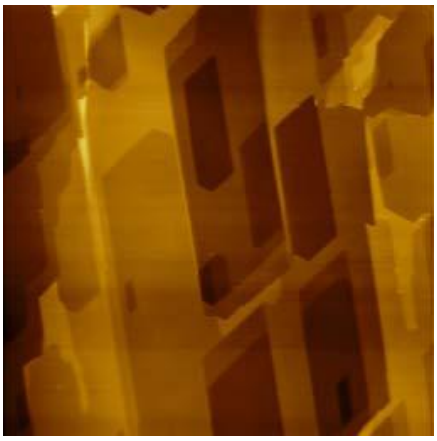

Figure 4.53: Topography AFM image of a freshly cleaved (001) L-leucine surface after immersion in Milli-Q water taken at ambient conditions. The scale is 10 $\mu$m x 10 $\mu$m.

# Chapter 5

# FERROELECTRICS: RESULTS AND DISCUSSION

## 5.1 Previous considerations

As described in the previous chapter, amino acids are always affected by water in a minor or major degree: when water starts condensing from vapor to liquid, it always modifies the surface and dissolves amino acids molecules. Amino acids however, pointed out the critical importance of surface dipoles on the wetting of a surface. I decided to study this phenomena on other surfaces. Ferroelectric materials turned out to be a good choice due to their stability in a wide range of temperatures, not being modified by water action (both vapor and liquid) and their hability to allow the re-orientation of their dipoles by means of AFM techniques (for a description of ferroelectric materials and their properties, I refer the reader to the introduction chapter).

Thin film PZT2080 ferroelectrics were adquiered from Phasis (see the SetUp chapter for their description) with different thickness (50 nm and 100 nm) and with both conductive and insulating substrates. These kind of samples are easy to clean (see expermiental chapter) and once their dipoles are re-oriented by means of AFM, the polarization stays stable for several days (they are described to be stable for months, but none of these experiments kept studying one same polarized zone for more than some days), and the samples can be used for years. Four different samples were acquired, all of them PZT2080: two with 50 nm PZT thickness and two more with 100 nm PZT thickness, each one was deposited over an insulating

STO substrate or on a conductive STO substrate Nb doped to have all the possible combinations.

### Initial state of the samples

To ensure that the cleaning process of the samples (see SetUp chapter) did not affect their topography, the study started by checking their roughness after the cleaning process, obtaining values $< 0.5$ nm in all cases by contact AFM (fig. 5.1).

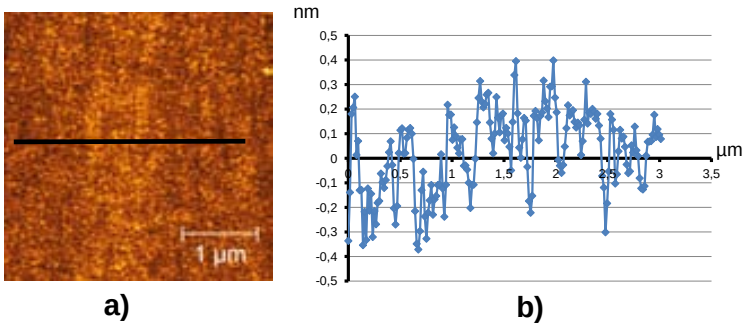


Figure 5.1: a) AFM contact mode PZT2080 thin film topography image, b) marked cross section.

After inspection, the study continued by checking the effect of the polarization process on the PZT topography. For this reason I scanned in contact mode (using a conductive PPP-CONTPt tip) the topography of the samples and immediately polarize over them with the maximum voltage that the system can provide (+10 V). The experiment was repeated with negative potentials (−10 V) in a different area. No difference on topography was observed prior and after polarization. One example is shown in figure 5.2.

### Natural domains of the samples

Once the cleaning and polarization processes were proved to be non-affecting the topography of the samples, PFM readings were performed using a PPP-EFM tip (see table 2.4) to obtain the initial distribution of domains. Two different domains were expected, with dipoles pointing outside and inside the surface, respectively. To perform the PFM reading it is necessary to find the resonance frequency of the tip in contact with the PZT surface when the cantilever is under an ac current (this ac voltage makes the PZT crystal cells expand and contract, and this is readed by the

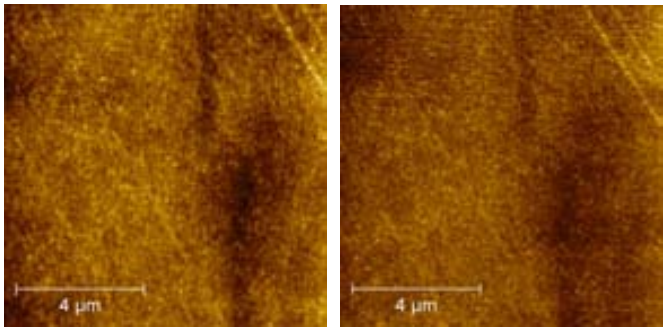


Figure 5.2: AFM contact images of the same are a) before (with a RMS roughness of 0.282 nm) and b) after (with a RMS roughness of 0.247 nm) polarization with a −10 V voltage.

probe in contact with the sample, acquiring both the amplitude of the oscillation and the phase respect to the reference ac signal). I used a 500 mV excitation ac current and the main ressonant peak (named contact ressonant frequency) in these conditions was found to be around 300 KHz with the PZT samples (much larger than the 60 KHz usually found for these tips in air free amplitude). Then, contact images of the sample were acquired with the 500 mV ac current on the tip and the sample s response was read at the contact ressonance; the amplitude and phase of the ferroelectric response were obtained (figs. 5.3, 5.4 and 5.5), with the domains (phase signal) and boundaries (amplitude signal) of the samples displayed. In phase images, the different domains show a 180° contrast due to the 180 degrees interaction diference from the dipoles, while in amplitude the domain boundaries are highlighted, where the response of the positive dipoles and the negative dipoles is measured simoultaneously and is therefore close to 0 (amplitude is not equal in both domains due to non symmetric response of the crystall cell to deformation).

As can be seen in figures 5.3, 5.4 and 5.5, the natural domains distribution can be very different between samples. This is a consequence of several factors as can be the thickness of the PZT film and the nature of the substrate, but even equal substrates and film thickness can derive into different domains because the process of the thin film formation is highly sensitive to small changes in the experimental conditions.

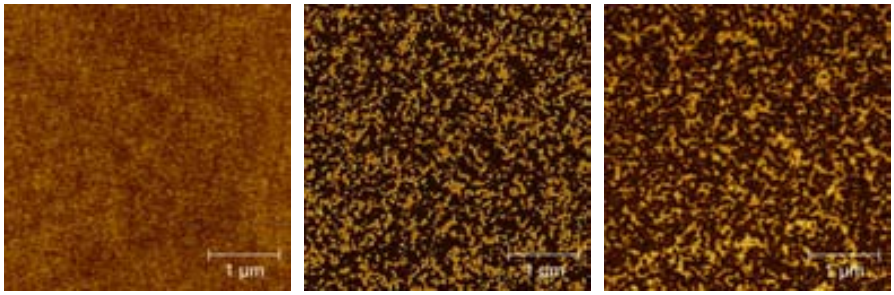


Figure 5.3: a) 4 $\mu$m x 4 $\mu$m contact topography image of a PZT2080 100 nm thick on a NbSTO substrate. b) Phase PFM image showing the two possible orientations (bright and dark regions). c) Amplitude PFM image.

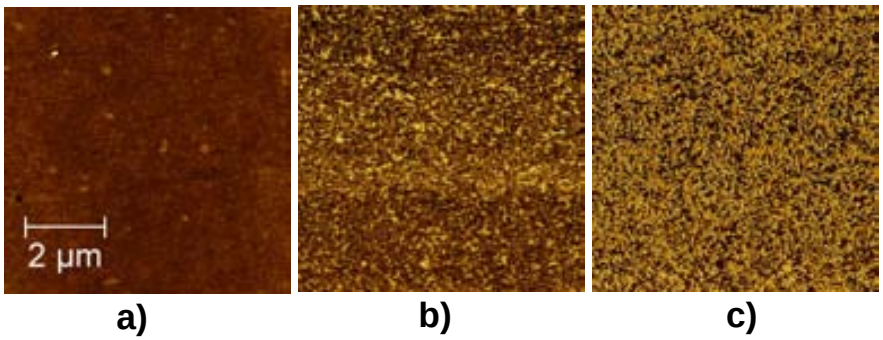


Figure 5.4: a) 7 $\mu$m x 7 $\mu$m contact topography image of a PZT2080 100 nm thick on STO substrate. b) Phase PFM image showing the two possible orientations. c) Amplitude PFM image.

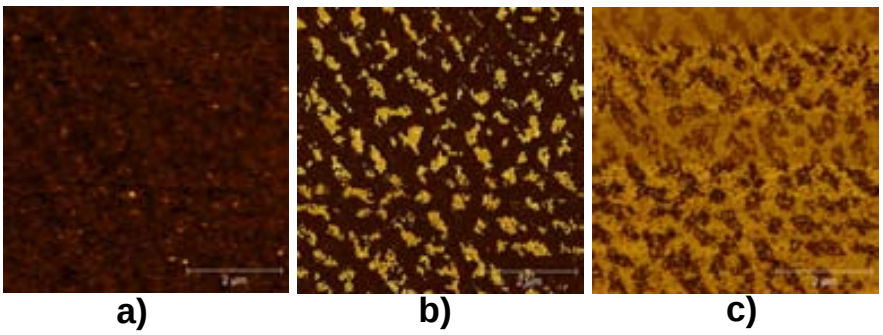


Figure 5.5: a) 6 $\mu$m x 6 $\mu$m contact topography image of a PZT2080 50 nm thick on a NbSTO substrate. b) Phase PFM image showing the two possible orientations. c) Amplitude PFM image.

### Polarizability of the samples

The re-orientation of the sample s dipoles by means of AFM was performed on the four samples. A positive potential (+10 V) and a negative potential (−10 V)

polarization were used on each sample using PPP-CONTPt tips. Each process was performed as follows: (i) an initial topographic square image was acquired in the contact mode, (ii) PFM was performed to acquire both the amplitude and the phase images on the unpolarized sample, (iii) the polarization took place in an inner, smaller area inside the previously scanned zone, (iv) a second topography image was acquired to check if the polarization process led to changes on the surface, (v) PFM was performed again to acquire both the amplitude and the phase images of the polarized zone.

If both the polarization and the PFM reading are correctly done, the second PFM reading must show only one squared domain on the polarized zone. The described operation was repeated twice for each one of the four samples (once with positive voltages and another one with negatives voltages). Not all the samples lead to good results, those samples with isolating substrates didn t show changes in their domains with respect to what was seen in the PFM signal prior to the polarization process. On the other hand, those samples with conductive substrates presented good polarization response (fig. 5.6, for the PFM signal prior to the polarization see fig. 5.3).

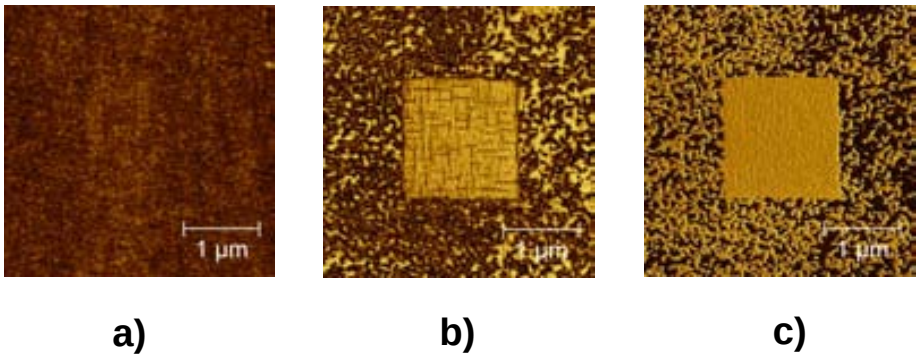


Figure 5.6: a) Contact mode topography image of a 100 nm thick PZT2080 film grown on a Nb−doped STO substrate. When the sample is polarized using −10 V we obtain: b) amplitude PFM image showing the polarized zone, c) phase PFM image showing the polarized zone.

A second instrument (Cypher from Asylum Research, located at the Université de Genève, Switzerland) able to reach values as high as 100 V was used to polarize the insulating samples, not obtaining any change in the initial domains configuration. From this point on, only Nb-doped STO substrates were used, and the 100 nm thick

thin film was better connected by passing a conductive wire through it from its surface to its metallic sample holder to improve its conductivity and enhance the charge dissipation.

## 5.2 Polarization and charge dissipation

The polarization of a ferroelectric thin film is a complex process: if the applied tip potential is not large enough, the polarization will take place partially or even will not take place at all. But the solution to this problem is not as easy as just apply large voltages, specially if you want to study electrostatic interactions involving the polarized surface, because charges can be trapped inside the sample after the polarization process (even when using good conductive substrates and low voltages, fig. 5.7) and if too large voltages are used, an excess of injected charge would lead to non desirable effects like the screening of the dipoles by the trapped charge or the polarization reversal due to charge injection (Abplanalp and Gunter, 2001; Morita and Cho, 2004; Buhlmann, 2005). The trapping of the charges inside polarized PZT films is a critical point of this study, because negative potentials on the tip will orient the surface dipoles pointing with their positive ends out of the surface while the KPFM imaging (as will be shown in this chapter) reveals negative electrostatic CPD transferred. This originates competitive contributions in the overall electrostatic affect that will effect the final response of the approaching water molecules and the way that they will orient themselves when attaching to the surface.

The effects that control the trapping of the charges and the discharging time of the samples are a function (among others) of the applied voltage, the geometry and nature of the tip, the force applied over the sample during the polarization process, the scanning speed during the polarization, the sample thickness and topography, the relative humidity etc. all this makes very difficult to predict how a ferroelectric sample will behave when it comes to charge injection. For this reason I decided to start a charge trapping and dissipation study with my samples and tips rather than using other existing studies with different ferrolectrics.

The 50 nm thick PZT2080 film with Nb−doped substrate was tested. A 10 $\mu$m x 10 $\mu$m square was polarized with the parameters shown in the table 5.1. The low

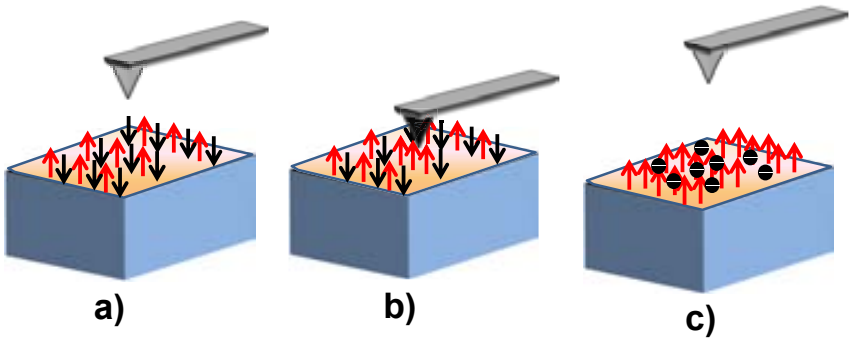


Figure 5.7: During a polarization process dipoles are re-aligned and charge is trapped inside the ferroelectric. a) The initial state of the ferroelectric shows both up and down dipoles. b) The tip is performing the polarization of the sample with negative voltage. c) The dipoles of the ferroelectrics are now all aligned pointing their positive end up, while negative charges are trapped on the sample.

| | |
|---|---|
| Cantilever ref. | PPP-CONTPt |
| Approaching speed | 6 $\mu$m/s |
| Stop setpoint | 0.3 V |
| Num. of lines | 512 |
| Points/line | 512 |
| Scanning speed | 0.2 lines/s |
| Setpoint while scanning | 0.5 V |
| Voltage | -10 V |
| Num. of sweeps | 3 |

Table 5.1: Operational parameters to maximize the charge injection.

scan speed and the 512 points per line value ensure that large amounts of charge would be trapped inside the PZT.

The amount of trapped charge and its dissipation was monitorized by reading the KPFM signal, method previously used to study the discharging of other surfaces, like graphene (Verdaguer et al., 2009), able to measure both trapped charges and permanent dipoles. Changing from the contact mode (used during the polarization) to the SPFM mode (necessary to obtain the KPFM signal) takes several minutes for this reason the first minutes are lost. Anyway a clear exponential process can be observed (figure 5.8a). Repeating the experiment produces always an exponential decay, with time constants depending on the relative humidity or the tip's geometry, which is of paramount importance and varies for every experiment (Bühlmann, 2005).

Trapped charges inside the PZT thin films can remain for long times on the

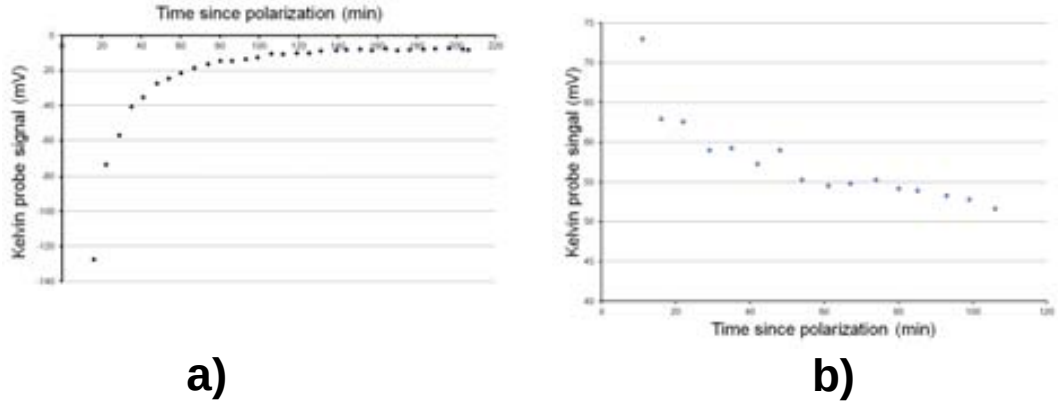


Figure 5.8: Charge dissipation after polarizing at a) −10 V and b) +10 V. KPFM signal has been used to monitorize the dissipation of the trapped charges.

sample, and after leaving the process of dissipation taking place overnight, KPFM imaging still showed a main influence of the trapped charges. The most important point to highlight is that after several hours, the influence of the trapped charges is still overscreening the influence of the re-oriented dipoles, obtaining negative values of CPD when in the absence of injected charge positive CPD are expected.

The discharging was also studied for positive voltages, the 50 nm thick PZT2080 with Nb doped substrate was polarized in a 10 $\mu$m x 10 $\mu$m square region with the parameters shown at table 5.1 but applying this time +10 V. Again, an exponential decay can be observed (figure 5.8b). The same as for the polarization with negative potentials, the effect of the injected charges is overscreening the dipoles signal, and KPFM shows always positive values on the polarized region.

### Optimization of the polarization process

The injection of charges during polarization is an unavoidable result of the polarization process. To study the effect of the dipoles in water interaction it was very important that the electrostatic influence of the dipoles of the PZT was greater than that of the trapped charges, so the study continued by optimizing the polarizing process to ensure a complete re-orientation of the dipoles while transferring the minimum charge to the sample. Between the two conductive substrate samples, I decided to continue my study with the 100 nm thickness, due to (i) higher thin film

thickness produces larger total dipolar moment (as long as all the dipoles ranging from the surface to the bottom of the film are co−linear they will increase the total dipolar moment) and (ii) the 100 nm thickness film was wired through it with a conductive wire to ensure a better conductivity.

The first step of the optimization process was to find the scanning speed value able to polarize the sample using the minimum time. Although some works (Paruch, 2004) recommend really slow velocities ($\sim$ 0.2 Hz) when polarizing, these works studied the ferroelectric polarization just by means of PFM analysis, not being the trapped charges an interfering problem. But much higher velocities can be applied when polarizing, obtaing polarizations near the 100% of effectiveness. The optimization tests were performed in the sample using a MFP-3D Asylum Research AFM, optimized for performing PFM operations. The sample shown that polarization velocities as high as 1 Hz are able to completely polarize a 1 $\mu$m x 1 $\mu$m PZT area when +10 V or −10 V are applied. In addition, a single pass is enough to polarize the scanned area, thus decreasing the number of scans over the zone will minimize the amount of injected charge (fig. 5.9).

The second step of the optimization refers to the applied voltage during the polarization. As explained above, the injected charges are of the opposite sign than the permanent dipole orientation, i.e., when the PZT dipoles are oriented pointing their positive end upwards, negative charges are being injected, while when PZT dipoles are oriented pointing their negative end upwards, positive charges are being injected. While injecting less quantity of charges, low potentials will not have enough strength to change the orientation of the dipoles, so the minimum potential, scanning at 1 Hz and in a single scanned area able to re-orient the sample dipoles must be found for the sample. The two permanent electrostatic forces appearing are opossite, each one canceling the other, so it is expected that at some point, the injected charge will perfectly nullify the oriented dipoles making the scanned surface appear in the KPFM image as not having any CPD difference with the rest of the sample. If charge injection goes on from this point, the permanent signal of the scanned zone will be of opposite nature to that we intended to achieve. Since PZT ferroelectrics do not have an equal response to positive and negative voltages (it has been reported that

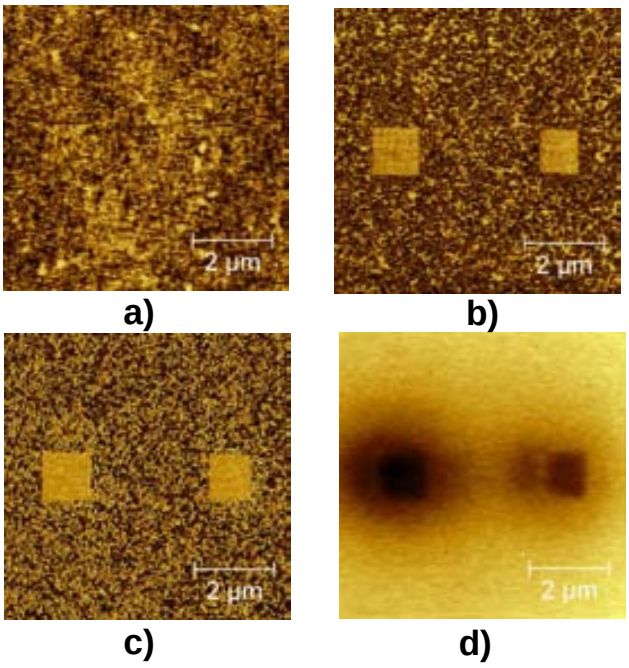


Figure 5.9: Effect of the scan speed on the injected charge. a) topography, b) Amplitude PFM, c) Phase PFM and d) KPFM images of two polarized zones with a voltage of −8 V. The left polarization was adquiered at 1 Hz and 256 points/line, while the right one was acquired at 3 Hz and 128 points/line. Both zones were totally polarized, but the injected charges during faster scans was less than that of the slower one.

negative voltages produce more charge injection than positive ones while positive polarization can produce reversal polarization do to charge effect), the process had to be optimized for both potentials.

### Optimization for negative potentials

Two arrays (each one with nine 1 $\mu$m x 1 $\mu$m squares) were polarized using a PPP-EFM tip with a different potential in each square (ranging from -8 V to -0.5 V as shown in figures 5.10 and 5.11). The experiment shown in figure 5.10 was acquired using a polarization speed of 1 Hz, while the experiment shown in figure 5.11 was acquired using a polarization speed of 0.25 Hz. The topography image was obtained in the AM-AFM mode and the PFM writing and reading were performed in the contact mode. Finally, a lift mode performing KPFM reading was used to obtain the CPD.

The first thing that must be noticed in these experiments (and also seen in figure 5.9) is that the negative charges injected to the sample diffuse out of the polarized

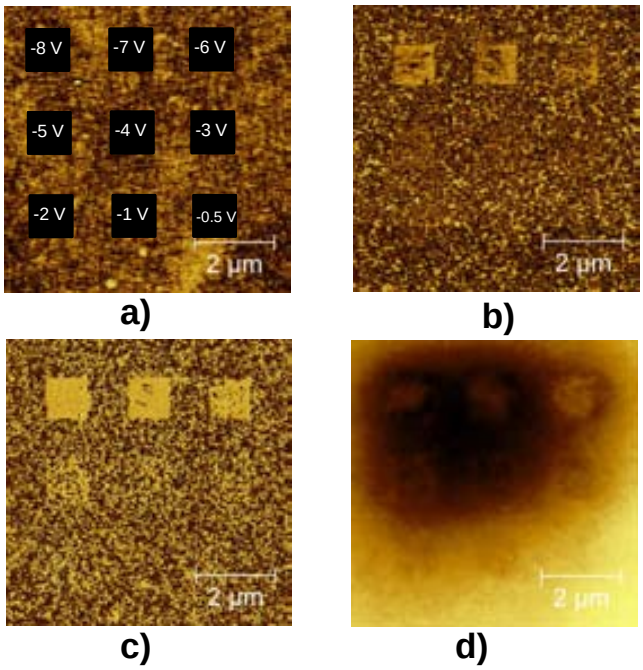


Figure 5.10: a) AM-AFM topography image displaying the nine polarized squares and the potential applied to each one. Each square was polarized at 1 Hz. b) PFM amplitude image obtained after the polarization process. c) PFM phase image obtained after the polarization process. d) KPFM image obtained using a lift mode.

zone. We will center our attention in this point latter. It can be also observed how the writings performed at 0.25 Hz speed produce KPFM images with a uniform negative CPD signal both inside and outside the polarized region, while the faster 1 Hz speed produces areas with positive CPD signals inside the polarized region with respect to the non polarized zone. If a closer look of the 1 Hz experiment is taken, it can be seen that the polarization at $-6$ V provides the best relation between oriented dipoles and injected charge (although if the polarized zone is compared with the region non$-$affected by the charge dissipaton, no large differences are observed between them in the KPFM signal, indicating that the trapped charges inside the polarized zone are near nulling the electrostatic effect of the oriented dipoles). It must taken into account that the KPFM image was acquired few seconds after the polarization process (using this time a second lift mode pass instead that to the SPFM mode used in the charge dissipation study), so while the dipoles will remain oriented the same, the trapped negative charges are expected to diffuse and decrease their influence up to $\sim$20% of their initial value in 2 hours (see fig. 5.8) and

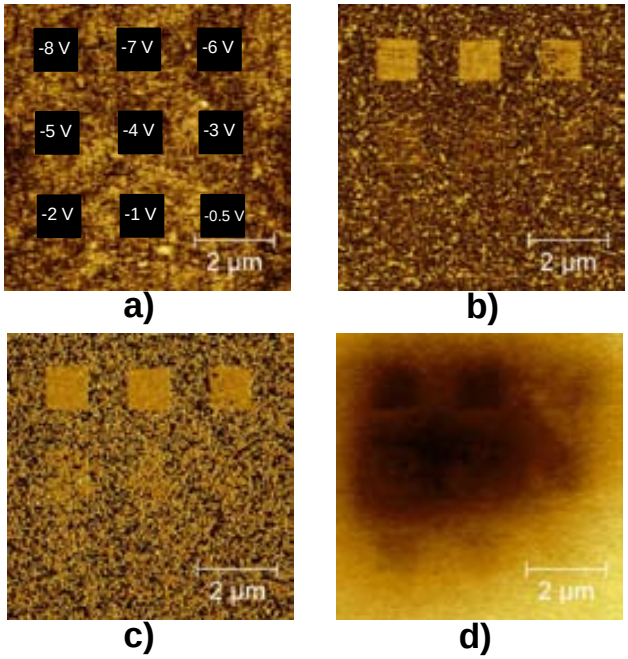


Figure 5.11: a) AM-AFM topography image displaying the nine polarized squares and the potential applied to each one. Each square was polarized at 0.25 Hz. b) PFM amplitude image obtained after the polarization process. c) PFM phase image obtained after the polarization process. d) KPFM image obtained using a lift mode.

thus making the influence of the dipoles more relevant. After several experiments, the best conditions to obtain an optimum electrostatic infuence of the polarization on the 100 nm thick PZT2080 sample, were found to be scanning at 1 Hz, a 1 $\mu$m x 1 $\mu$m square zone, with a single scan at $-6$ V. For negative potentials and a PZT2080 sample with a 100 nm thin film and a Nb-doped substracted, the optimum parameters for polarization are shown in table 5.2. Note (fig. 5.10b) that this refers only to the optimization of the injected charge, since the degree of polarization is far from 100% (the effectiveness of the polarization is measured using the PFM phase image, which shows the presence or not of the other domain inside the polarized region).

### Optimization for positive potentials

Taking as reference the results obtained in the previous section, the optimization of the parameters for positive potentials was studied. I decided to work with velocities of 1 Hz and scanned regions of 1 $\mu$m x 1 $\mu$m, the same that for negative potentials.

| | |
|---|---|
| Approaching speed | 6 $\mu$m/s |
| Stop setpoint | 0.3 V |
| Num. of lines | 256 |
| Points/line | 256 |
| Scanning speed | 1 lines/s |
| Setpoint while scanning | +0.7 V |
| Voltage | −6 V |
| Num. of sweeps | 1 |

Table 5.2: Optimum operational parameters for negative potentials polarization.

This time, I decided to avoid too large or small values and I centered this study at voltages of medium values. Figure 5.12 shows PFM images obtained after polarizing two different 1 $\mu$m x 1 $\mu$m square areas at 1 Hz, the image shows the change between a potential too low (+3 V) to align the dipoles in a satisfactory rate and a potential high enough (+4 V) to start obtaining a defined polarized zone.

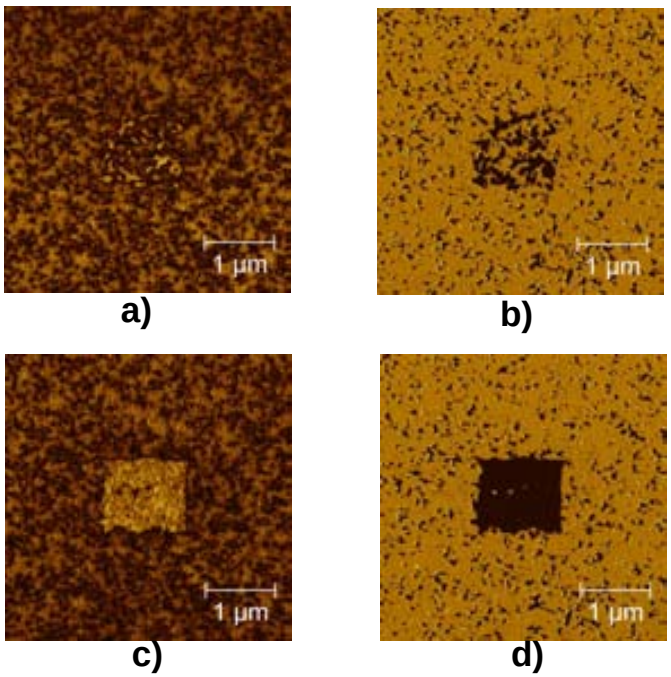


Figure 5.12: a) Amplitude and b) phase image of a 1 $\mu$m x 1 $\mu$m polarized square with a +3 V potential. The polarization takes place partially. c) Amplitude and d) phase image of a 1 $\mu$m x 1 $\mu$m polarized square with a +4 V potential. The polarization is majoritary, but still not 100%.

Once the minimum voltage able to satisfactorily polarize the sample was found, KPFM was acquired in the SPFM mode to study the possible screening that the injected charges would origin and to improve the removal of these residual charges. These were my observations:

(i) The trapped charges tend to remain inside the polarized zone, with low or no diffusion outside it.

(ii) If a previous contact image is adquiered (larger than those to come after), the trapped charges tend to diffuse outside the polarized zone all over the previously contact mode scanned area.

(iii) If contact images are acquired after the polarization, diffusion of the trapped charges outside the polarized zone is enhanced, as can be seen by KPFM in figure 5.13.

(iv) If low ac voltage (500 mV) scannings are performed over the polarized zone in contact mode, important quantities of trapped charge are removed with no erasing of the polarization (the voltage has not enough strength to re-orient the dipoles).

All these points are displayed in figure 5.13 where both a) and b) images show a 1 $\mu$m x 1 $\mu$m square polarized at +4 V with a scan speed of 1 Hz. The first image shows a KPFM image where the polarized area appears brighter than its surroundings, a clear indication that the trapped positive charges are masking the underlying aligned negative dipoles. After applying what is described in points (i), (ii), (iii) and (iv), the initial screened dipoles appear now in the KPFM images respect with the surrounding area.

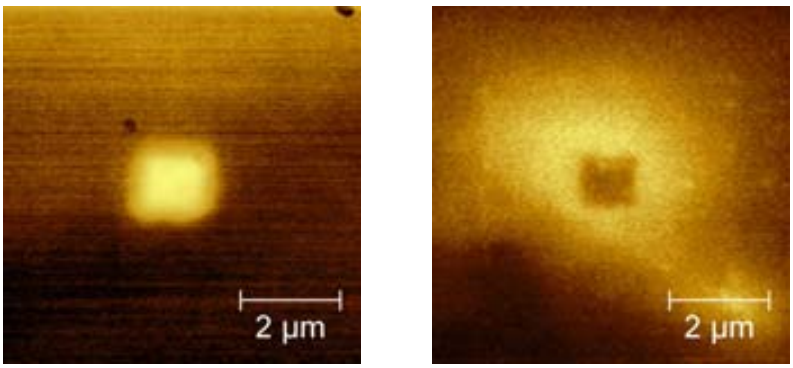


Figure 5.13: KPFM images of two +4 V polarized 1 $\mu$m x 1 $\mu$m areas. a) the aligned dipoles appear masked by the injected charge. b) If a previous and larger contact scan and two 500 mV ac contact scans are performed, the trapped charges are greatly dissipated, appearing now the polarized area.

Figure 5.13b can lead to incorrect interpretation because although now it is

possible to see the negative effect of the dipoles in the KPFM image they are detected only because the surrounding area contains some of the positive trapped charges, now diffused. If the difference between the polarized area and the most external region of the image, with no trapped charges is analyzed, it becomes clear that the difference between the two zones is minimal, concluding that the trapped positive charge inside the polarized area is, more or less, canceling the negative dipoles. Not being able to dissipate more of the trapped charge, the only solution to get a net signal of the dipoles was to use lower voltages, but that would imply an area with an incomplete polarization. In figure 5.14 a 1 $\mu$m x 1 $\mu$m region was polarized at +2 V. At this voltage only ∼70% of the scanned area becomes effectively polarized, but in the KPFM image the negative dipole can be clearly identified inside the negative polarized region. I ended up dealing with some kind of compromise between having a good polarized region and avoiding an excessive charge injection.

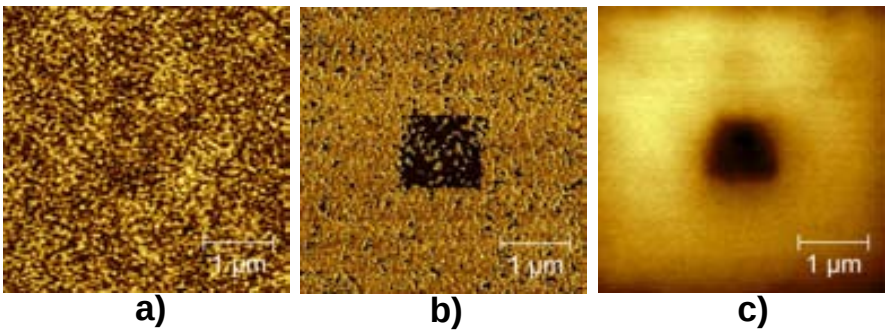


Figure 5.14: a) AFM topography image of a PZT2080. b) The polarization is not effective at 2 V, only ∼70% has been correctly aligned. c) The KPFM image shows the effect of the aligned dipoles respect to the sample.

After considering all the factors described above, I decided to continue this study with 100% polarized regions, to avoid any influence of opposite dipoles inside it. Of course this would implie a certain degree of charge injection (larger than that for polarizations at lower potentials), but if a previous contact image and an after PZT 500 mV ac reading are performed, most of the charge should diffused and eliminated.

| | |
|---|---|
| Approaching speed | 6 $\mu$m/s |
| Stop setpoint | 0.3 V |
| Num. of lines | 256 |
| Points/line | 256 |
| Scanning speed | 1 lines/s |
| Setpoint while scanning | +0.7 V |
| Voltage | +6 V |
| Num. of sweeps | 1 |

Table 5.3: Optimum operational parameters for positive potentials polarization.

## 5.3 Water ordering on PZT2080 polarized regions

### PZT2080 polarized with positive potentials

The described PZT2080 Nb-STO sample was polarized as follows:

Using a PPP-EFM tip, a 7 $\mu$m x 7 $\mu$m square region was scanned in the Contact Mode at 1 Hz, after that, a PFM image was taken in a 4 $\mu$m x 4 $\mu$m square region (inside this last one) using a 500 mV ac current. After these operations, a 1 $\mu$m x 1 $\mu$m square was polarized using the parameters shown in table 5.3, the RH during the process was 24% and the ambient T was 20°C. The 4 $\mu$m x 4 $\mu$m PFM images obtained after the polarization are shown in figure 5.15.

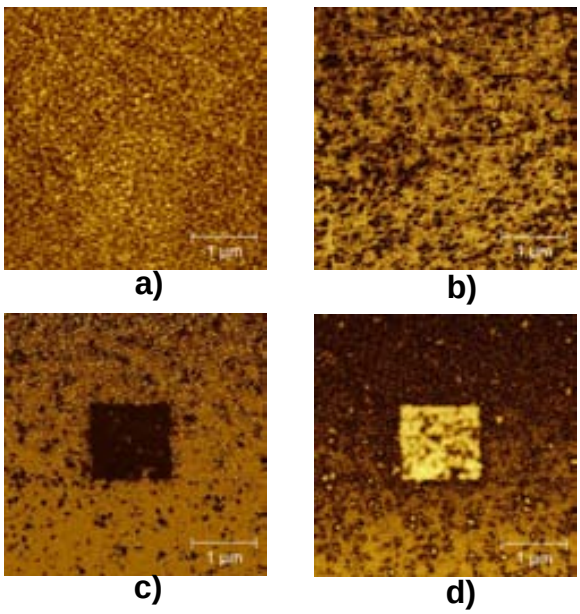


Figure 5.15: a) Contact topography and b) PFM phase AFM images previous to the polarization. c) PFM amplitude and d) phase after polarization.

KPFM images of this region were acquired using the lift mode KPFM, the CPD reading displayed positive values with respect to those of the surrounding area, a clear sign that the trapped charges were still masking the underlying dipoles. The study continued by lowering the sample stage temperature. Using the conversion described in the setup chapter (fig. 2.5) the RH on the sample is obtained from the sample s T and the ambient RH. The CPD difference between the polarized and the no-polarized zones has been plotted in figure 5.16.

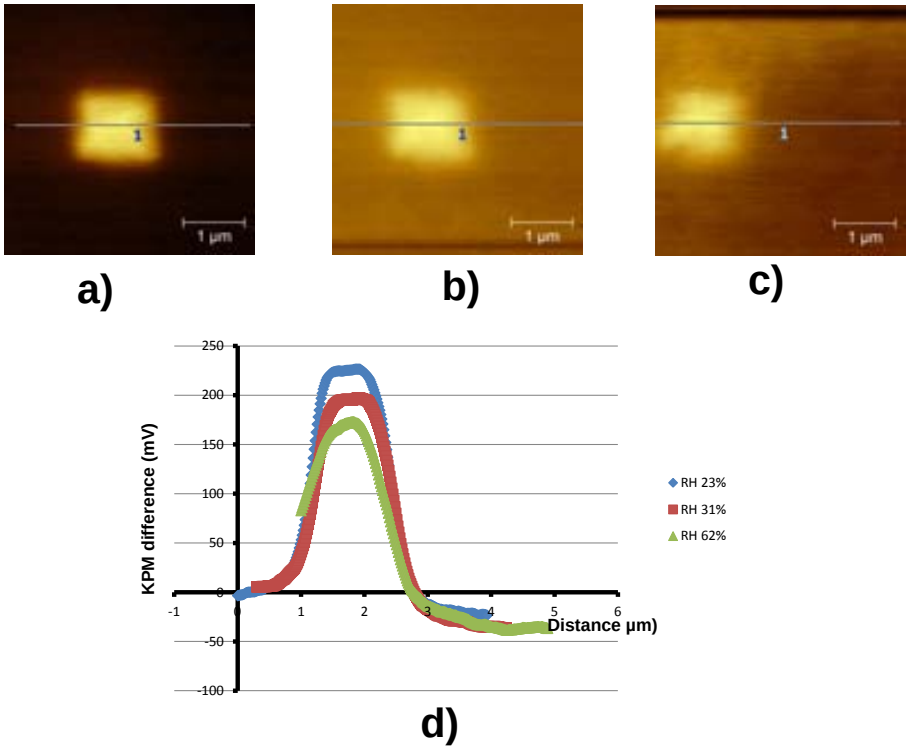


Figure 5.16: Evolution of the KPFM signal with humidity. KPFM images at RH a) 23% and blue line in graphic, b) 31% and red line in the graphic and c) 62% and green line in the graphic. d) Shows the profile lines shown in a), b) and c). The legend displays the RH on the surface

From figure 5.16 it can be seen that as humidity increases on the surface, the CPD difference between the polarized and the non−polarized regions reduces. This CPD decrease can be a result of (i) as water starts covering the polarized region, it screens the underlying electrostatic interactions or (ii) despite the injected charges, the water molecules orient themselves favorably with the sample s dipoles, and thus, they increase the dipolar moment of the surface. This would reduce the original

CPD signal caused by the injected charges (of opposite contribution than that of the dipoles).

In order to find which of these two possible reasons was causing this reduction of the CPD difference a similar experiment was performed, ensuring this time an initial polarized region with a corresponding KPFM signal showing a net contribution coming from the dipoles of the sample. The same parameters used in table 5.3 were used to polarize the sample, with an ambient T of 25°C and a RH of 28%. The KPFM signal showed negative CPD with respect to that of the non−polarized region, so the dipoles effect was dominating over the one of injected charges. The experiment consisted again in obtaining KPFM images of the sample at different T, ranging from 25°C to 5°C (close to 5°C the RH over the surface is around 100%, so no lower temperatures were reached to avoid water condensation). Several temperature cycles were performed, what was observed can be divided in two different behaviours, the first one takes the first temperature cycle, while the second counts all the temperature cycles to come after it.

What we observed during the first temperature cycle (fig. 5.17), was that as the T of the sample holder decreased (and RH over the sample increased), the CPD difference was reduced again. Just the same as in the previous case when charges were dominating the global KPFM signal. This result points to a screening of the KPFM signal due to water condensation.

However, when the sample stage was set again up to 25°C, the initial negative square in the KPFM image was almost nulled (fig. 5.18a). When a second T cycle was acquired, lowering the sample s T caused the polarized region to recover a negative CPD value with respect to the surrounding area. From this point on, this behaviour is totally reproducible, and several T cycles were adquiered showing always that for near ambient T the polarized zone is almost unnoticed from the surrounding area, while for low T (near 5°C, 100% RH) the polarized zone clearly appears in the KPFM signal as negative (fig. 5.18).

I repeated this experiment several times, performing for each experiment several T cycles, and the described behaviour was always observed. On the other hand, if RH variations are performed on the sample (using the glove box) while its T

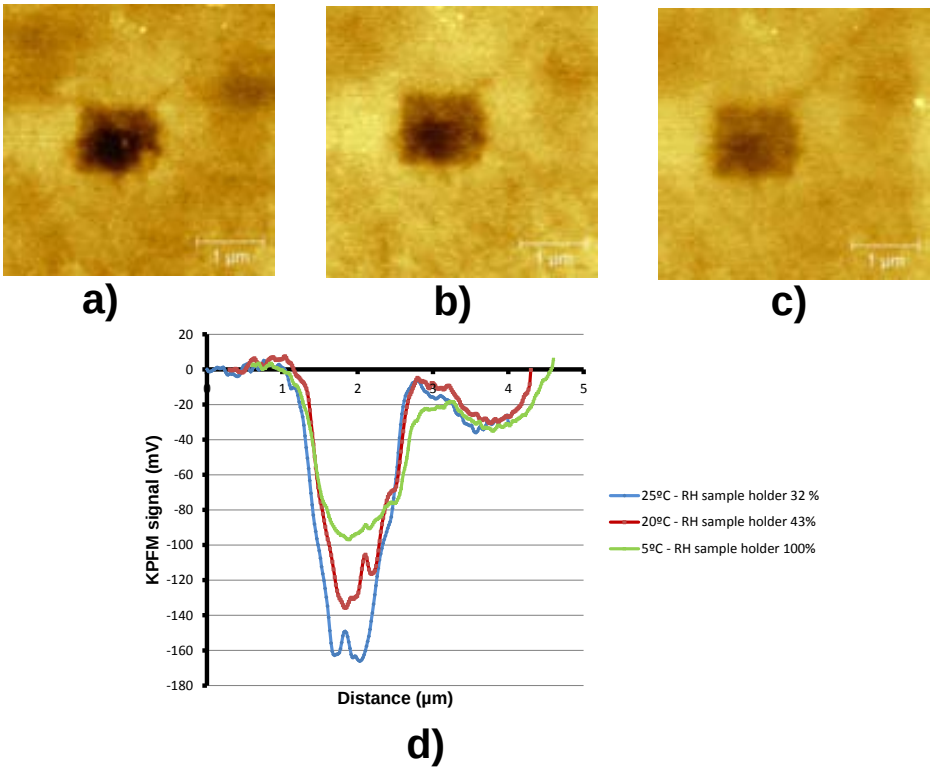


Figure 5.17: Evolution of the KPFM signal with temperature during the first cycle. KPFM images at T a) 25°C b) 15°C and c) 5°C. d) Shows their profile line for each T (RH over the sample is also included).

is maintained constant, the KPFM signal does not show this behaviour and the polarized region shows always a net difference with respect to its surrounding. I interpret these results as a sign of the importance of T rather than that of the RH, and as a tentative model, I propose the following processes occurring during the first cycle:

(i) During the first KPFM image at ambient T few water molecules are present on the sample (as mentioned in the introduction chapter, at RH=25%, no more than a monolayer is expected) and the KPFM signal comes basically from the PZT dipoles (although partially screened by the injected charges, fig. 5.19a).

(ii) As the T starts decreasing, RH over the sample increases, and this leads to an increasing of the presence of water molecules on the surface. These molecules are partially aligned with the PZT dipoles and also partially moving and exchanging with other water molecules, this originates a KPFM signal with the same sign than

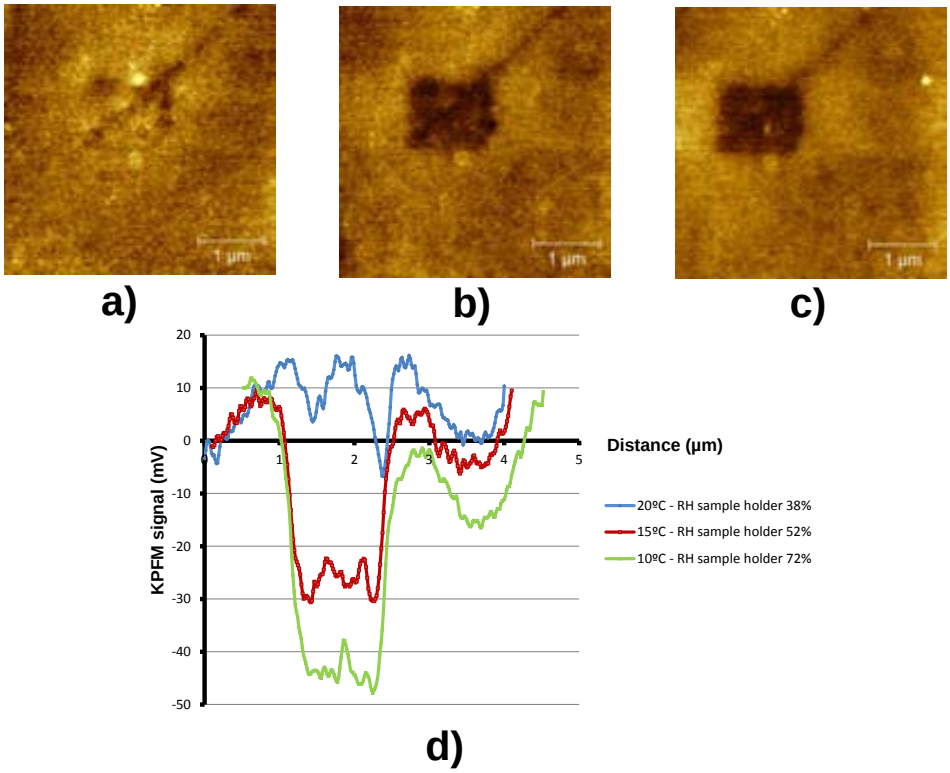


Figure 5.18: Evolution of KPFM signal with temperature during a second cycle. KPFM images at T a) 20°C b) 15°C and c) 10°C. d) Shows their profile line for each T (RH over the sample is also included).

that of the dipoles (i.e., negative in this case) but partially screened (fig. 5.19b).

(iii) The more the T decreases, the larger quantity of water molecules are on the surface, this should screen even more the KPFM signal, but since the temperature is low (i.e., near the freezing point), these molecules have more difficulty to move and exchange due to a loss of thermal energy, and they tend to stay aligned with the PZT dipoles more time than previously. This two factors competing one against the other give rise to small variations in the KPFM signal fig. 5.20a).

Also, for the second cycle, the proposed model is:

(iv) When T rises up again, the water molecules condensed over the sample gain thermal energy (i.e., mobility), so they can break the dipole-dipole interaction more easily and move more freely, thus, the KPFM signal decreases in intensity because water dipoles are now more random−like. At ambient T, water molecules can move freely over the polarized zone (and over the rest of the PZT surface), and KPFM

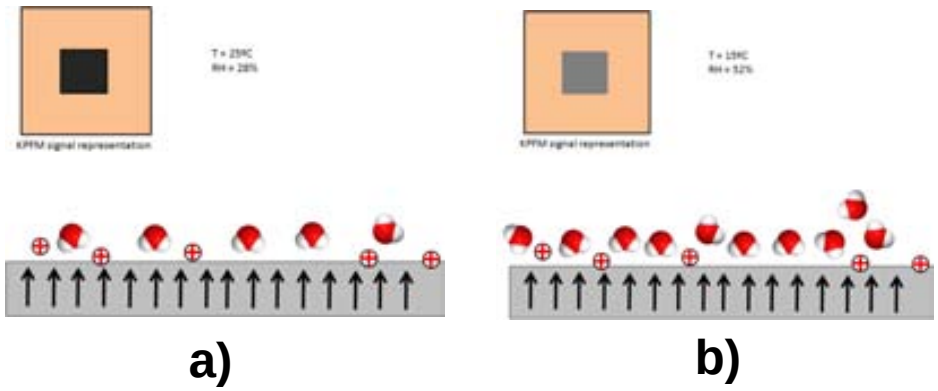


Figure 5.19: a) If low charge injection is achieved, the ambient conditions KPFM images show the influence of the PZT dipoles in the CPD. b) As the T goes to lower values, water molecules start to condense over the sample, screening the KPFM signal of the PZT, but since some of these molecules align themselves with the underlying dipoles, the screening effect is partially softened.

signal difference becomes almost 0 between them (fig. 5.20b).

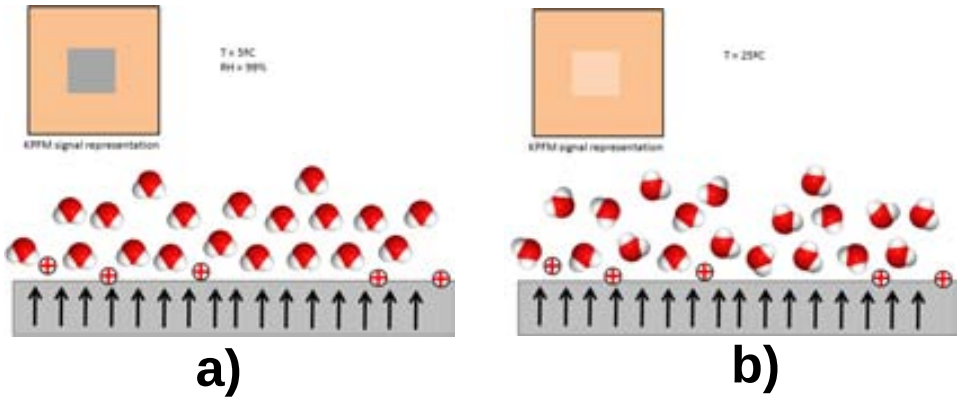


Figure 5.20: a) Just before the dew point, a large number of water molecules cover the sample, but the low temperature makes difficult for them to break the interaction of the underlying dipoles, so the KPFM signal still shows the underlying dipole effect. b) If T is raised again, all the condensed water molecules gain mobility, and thus, the dipole-dipole interaction are now easily overcome. Water moves freely now and the KPFM shows almost no difference between polarized and no polarized zones.

(v) If T is lowered again, water molecules lose mobility and gradually start to align again colinearly with the PZT dipoles, the KPFM signal of the polarized region appears again fig. 5.21).

If this interpretation is correct, the polarized zone would organize the water molecules at T slightly over the freezing point, and thus, it is expected to start the freezing processes before the rest of the unpolarized sample. Unfortunately, the

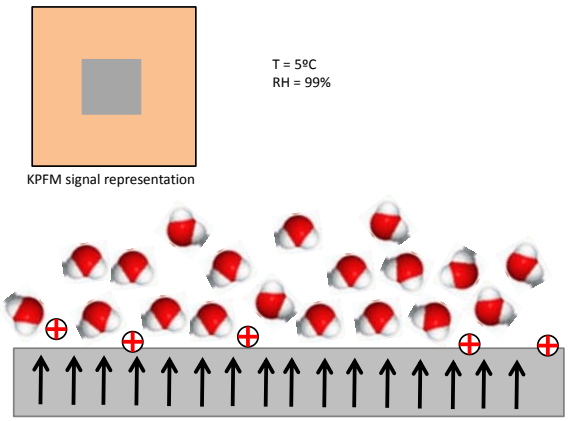


Figure 5.21: When T is again lowered, water molecules lose thermal energy and the dipole-dipole interactions becomes once again difficult to break, so water aligns again with the PZT dipoles, making the KPFM signal increase its CPD difference respect with the non-polarized zone.

Asylum Research AFM used to perform this polarizations could not control the humidity of the sample, and if T was lowered below 5°C, liquid water condenses all over the sample. It will be necessary to control the RH of the sample to allow KPFM measuring under 0°C, and thus, study if ice forms preferentially on the polarized zone.

### PZT2080 polarized with negative potentials

The experiments described for positive potentials were repeated for negative potentials. As previously mentioned, polarization does not present an equal response for opposite potentials. The amount of injected charge and the effectiveness of the polarization varies with the sign of the employed potential.

The first experiment with negative potentials was performed following the same conditions as for the positive one (see table 5.3), but using a $-6$ V potential instead of $+6$ V. Contrary to what happened for the positive value, the polarization was not 100% effective, and just $\sim$70% of the dipoles were effectively re-oriented (see fig. 5.22a), also in the KPFM image (see fig. 5.22b) the signal was dominated by the injected negative charges. Not being satisfied with an uncompleted polarization I only acquired the first T cycle, observing that (the same as for the previous case), the CPD difference between the polarized and the no$-$polarized regions was reduced when T was lowered (fig. 5.22c). A second T cycle was not acquired because the

large amount of trapped charges and the presence of dipoles oriented both up and down would lead to difficulties for interpreting the results.

Using a potential of −7 V (not shown) didn t reach either an acceptable polarization rate, instead −8 V reached it. Although the polarization was 100% effective (see fig. 5.22d) the injected charge was also important (fig. 5.22e). During the first T cycle the negative influence of the injected charge was still dominating the KPFM image (fig. 5.22f). Although the injected negative charges always dominate

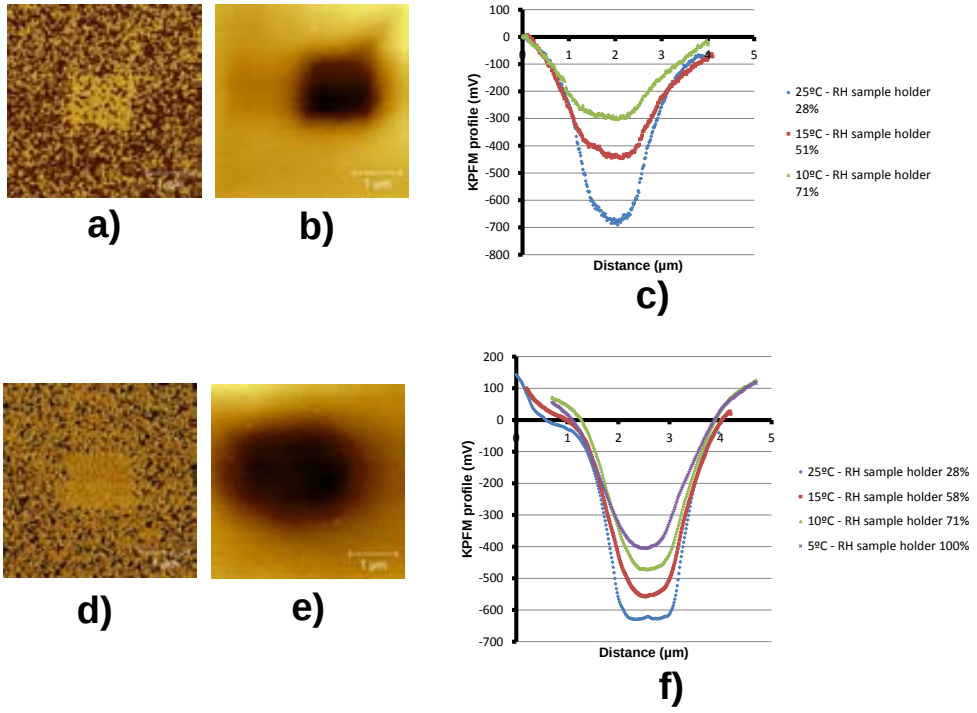


Figure 5.22: First T cycle of two different experiments. In the first experiment, partial polarization with −6 V was achieved (a) PFM phase) and the injected charge screened the KPFM signal (see b)). A Descending in the temperature leads to a reduction of CPD difference between the polarized region and its surrouding (see c)). In the second experiment, ∼100% polarization was achieved at −8 V, (see PFM phase signal at d)). The polarized region produced a KPFM signal screend by the injected negative charges, (see KPFM image at e)). f) again, a descending of the sample s T leads to the loss of KPFM difference between the polarized region and its surrounding.

the KPFM images, when T is lowered in a second T cycle, it can be observed (fig. 5.23) how the polarized region starts gaining positive a CPD with respect to its nearer area. If T is rised again, this small difference dissapears, appearing again during a new T descending. So it seems that the results with negative potentials are producing the same kind of response with water ant T than the positive ones,

but the injected charge is so important that it turns difficult to follow the process in these conditions.

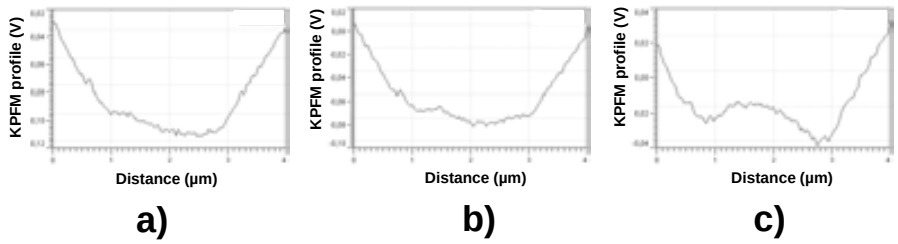


Figure 5.23: After the first T cycle the evolution of KPFM signal with T shows an enhancing of the dipole signal respect to its surrounding region at lower T. a) KPFM profile at 20°C. b) KPFM profile at 15°C. c) KPFM profile at 10°C.

### Interpretation

Several works study the dipole effect of the ordered water by quantifiying their CPD variations by means of KPFM imaging (Iedema et al., 1998; Bluhm, Inoue and Salmeron, 2000; Verdaguer, Cardellach and Fraxedas, 2008). In these works hydrophobic coatings on the cantilevers were used in order to ensure that water adsorbing on the tip did not influence the results, and CPD changes due to water ice−like layers ordering, ranging from tens of mV up to 400 mV, were measured. These values depend on the experimental conditions (RH, T) and on the imperfections of the water ice-like bilayer (solvated ions, disorder...), but MD simulations lead to a surface potential diference of -2.5 V if a perfect ice bilayer is formed over mica.

Prior to the interpretation of my results, I would like to discuss briefly the possibility of having secondary electrochemical reactions due to the presence of water (as well as other adsorbed molecules) on the PZT surface and the to voltage applied by the probe. With the voltages used during polarization, water undergoes different electrochemical reactions that can change the chemical nature of the scanned region ($-OH$ dangling groups covering surfaces is a well known phenomena involving water reactions on surfaces). Also, other molecules adsorbed on the surface when working at ambient air conditions can also react with the applied potentials and form a passivating layer over the scanned region. These processess are difficult to avoid

when you are not working in UHV conditoins, but it was not my intention to get rid of them since *this study is focused in the study of water interactions with surfaces in natural conditions*. However, the images obtained by PFM reading demonstrate that even if such passivating layer may exist on our surfaces, the apparent surface polarization is perfectly achieved (as PFM phase images show). Also, KPFM imaging shows that in spite of the water electrochemistry and the injected charge, the electrostatic effect of the PZT dipoles in the nearby water molecues is still detected. Once this point has been mentioned, I proceed to the interpretation of my results.

The KPFM measurement of water ordering as a function of T described in this chapter have been divided in two steps: (i) the first cycle and (ii) the second and following cycles. During the first cycle (figs. 5.17, 5.22c, 5.22f) for T changes ranging from 25°C down to 5°C CPD differences of hundreds of mV were recorded. But this variation cannot be assigned exclusively to water dipoles effect, because during this first cycle water molecules condense on the surface, some trapped charges are eliminated and water thermal energy decreases (making water more ice-like ), it becomes then difficult to assign each contribution to the final CPD change. On the other hand, during the second cycle, the trapped charges are supposed to have been driven away previously, and no extra water condensation will not take if T does not reach lower values than those of the first cycle. So during this second cycle changes on the CPD are expected to be mainly a function of the ordering of the water dipoles with the surface dipoles. Figure 5.18 shows the second T cycle of a positively polarized region, experimenting a variation of $\sim$ -55 mV when T is decreased from 20°C to 10°C.

Ice formation on the PZT sample is expected to be far from the ideal case due to bad lattice matching between PZT and Ih ice and to the trapped charges that will distort the PZT dipoles effect. However, this is a preliminar result that demonstrates that PZT thin films can be effectively used to study water adsorption on surfaces as a function of dipolar influence.

From this study we conclude that both positive and negative polarized PZT2080 regions can, despite the trapped charge, align the water molecules co−linearly with the sample dipoles when T is low enough to make the dipole-dipole energy larger

than the thermal energy of water molecules.

# Chapter 6

# CONCLUSIONS AND PERSPECTIVES

### Conclusions

In this thesis I have combined different AFM modes with surfaces of different nature to study the interaction with water molecules in controlled ambient conditions of humdity and temperature.

The conclusions derived from this thesis, related with the objectives described at the beginning, are:

(1) The underlying reason of the differentiated affinity of L−alanine (011) and (120) surfaces with water molecules is the distribution of their surface dipoles. While dipoles pointing perpendicularly to the surface plane induce the structuring of water molecules at short distances, dipoles parallel to the surface plane have little effect on water molecules, a text book example of electrostatic interaction between dipoles.

(2) Water molecules strongly interact with the initial hydrophilic L−alanine (011) surface, promoting the diffusion of L-alanine molecules and creating a two level landscape formed by terraces and islands . Although molecular resolution images shows no difference between these two featues, they exhibit the same nature and crystallographic structure with a 180° orientation, as revealed by Lateral Force Microscopy. A structural model based on energetic and geometric arguments is presented in which (011) surface self−passivates from water, its molecules lying now flat in a low density ordered arrangement with its dipoles parallel to the surface.

(3) Although being unaffected by water vapour, regular etch parallelepipeds with steps of one bilayer deep are obtained when etching the (001) surfaces of L−, D− and

DL−valine single crystals with liquid water. Elongated parallelepipeds are found for D− and L−valine crystals indicating a different dissolution rate, while DL−valine shows a similar length on the steps indicating a similar dissolution rate.

(4) L− and D−valine extend their molecular chirality to the obtained parallelepipeds, allowing chiral identification of the crystals by a single AFM topography image.

(5) The etching rate is dominated by the dipolar orientation of the valine molecules in the steps. Dipoles parallel (perpendicular) to a step are less (more) reactive. The hydrophobic character of the bilayer has an important effect on water etching, since the depletion layer (hydrophobic gap) on the (001) surface induces a major contribution from the upper part of the step, corresponding to the upper layer of the bilayer.

(6) Once water is present on the surface it interacts with the valine molecules solving some of them, so its almost impossible to assure that water adsorbed in the surface is free of an important amount of valine molecules. The presence of solvated valine molecules strongly affects the ice structures observed, appearing mainly as irregular flat structures.

(7) The experimental parameters to perform polarization processes on PZT thin films ensuring a complete polarization while minimizing the injected charge have been defined. Positive potentials and negative potentials do not produce an inverse polarization on PZT2080 100 nm thin film ferroelectrics. For equal values, the polarization is more effective using positive voltages. The operations to dissipate large quantities of trapped charge have been also defined.

(8) PZT2080 thin films have shown their ability to orient water molecules as a function of the sample s temperature. For small temperature variations, still far from the freezing point ($T_{initial} = 20°C$, $T_{final} = 10°C$), water molecules ordering has been demonstrated.

**Perspectives**

The observations and conclusions described here both for amino acids and ferroelectric PZT2080 thin films have left open several paths to follow related with this

study.

Although the findings apply to the particular cases of L−alanine, L−valine, D−valine and DL−valine, they should be of wider applicability to other dipolar molecular solids (they have shown valid to predict how L−leucine will etch with water) and may be of relevance for understanding the complex interplay of biomolecules, such as proteins, with water, that is, protein hydration, essential for their three-dimensional structure and activity. The rationalization of the physicochemical processes governing the interaction of water with molecules and extended surfaces should ultimately provide the basis for the future design of intelligent surfaces with desired response to water. The next logical step in the amino acids study should be start studying them with a little more complex molecules, like small peptides. If their inner dipoles shown to be more important than the orientation and nature of their side chains, these findings would be quickly incorpored into theoretical models describing protein−water interactions.

If water freezing can be locally controlled to occur on the polarized regions of PZT thin films (this step is now being studied in our group), the design of new surfaces able to be externally controlled in order to align their dipoles parallel or perpendicular to air will be an ambicious objective. This surface would act as hydrophobic or hydrophilic depending on how we orient its dipoles, and ultimately, it would be able to act as an ice nucleator only when it is told. The industrial interest of such a surface is out of question.

# REFERENCES.


[1] Abplanalp, M. Gunter, P. Influence of stress on the domain formation in barium-titanate films , *Ferroelectrics*, vol. 258, pp. 3, 2001.

[2] Al-Abadleh, H.A.; Grassian, V.H.; Oxide surfaces as environmental interfaces , *Surf. Sci. Rep.* vol. 52, pp. 63, 2003.

[3] Albrecht, T.R.; Grutter, P.; Horne, D.; Rugar, D. Frequency modulation detection using high-Q cantilevers for enhanced force microscope sensitivity , *J. Appl. Phys.* vol. 69, 1991.

[4] Amrein, M.; Muller, DJ. Sample preparation techniques in scanning probe microscopy , *Nanobiology* vol. 4, pp. 229, 1999.

[5] Ansari, A.; Jones, C. M.; Henry, E. R.; Hofrichter, J.; Eaton, W. A. The role of solvent viscosity in the dynamics of protein conformational−chages , *Science* vol. 256, pp. 1796, 1992.

[6] Arima, K.; Jiang, P.; Lin, D.S.; Verdaguer, A.; Salmeron, M. Ion Segregation and Deliquescence of Alkali Halide Nanocrystals on SiO(2) , *J. Phys. Chem. A* vol. 113, pp. 9715, 2009.

[7] Asay, D.B.; Kim, S.H. Evolution of the adsorbed water layer structure on silicon oxide at room temperature , *J. Phys. Chem. B* vol. 109, pp. 16760, 2005.

[8] Avouris, P.; Martel, R.; Hertel, T.; et al. AFM-tip-induced and current-induced local oxidation of silicon and metals , *Applied physics A − Materials science processing* vol. 66, pp. S659, 1998.

[9] Bai, C. Scanning tunneling microscopy and its applications , New York: Springer Verlag. ISBN 3540657150, 2000.

[10] Bandyopadhyay, S.; Chakraborty, S.; Bagchi, B. Secondary structure sensitivity of hydrogen bond lifetime dynamics in the protein hydration layer , *J. Am. Chem. Soc.* vol. 127, pp.1660, 2005.

[11] Ball, P. Water as an active constituent in cell biology , *Chem. Rev.* vol. 108, pp. 74, 2008.

[12] Bandyopadhyay, S.; Chakraborty, S.; Balasubramanian S.; Bagchi, B. Sensitivity of polar solvation dynamics to the secondary structures of aqueous proteins and the role of surface exposure of the probe , *J. Am. Chem. Soc.* vol. 127, pp. 4071, 2005.

[13] Barrena, E.; Ocal, C.; Salmeron, M. Molecular packing changes of alkanethiols monolayers on Au(111) under applied pressure , *J. Chem. Phys.* vol. 113, pp. 2413, 2000.

[14] Basagaoglu, H.; Green, C.T.; Meakin, P.; McCoy, B.J. Lattice-Boltzmann simulation of coalescence-driven island coarsening , *J. Chem. Phys.* vol. 121, pp. 7987, 2004.

[15] Beaglehole, D.; Christenson, H. K. Vapor adsorption on mica and silicon − entropy effects , *J. Phys. Chem.* vol. 96, pp. 3395, 1992.

[16] Becker, R.S.; Golovchenko, J.A.; Mc Rae, E.G.; Swartzentruber, B.S. Tunneling Images of Atomic Steps on the Si(111) 7x7 Surface , *App. Phys. Lett.* vol. 55, issue 19, pp. 2028, 1985.

[17] Beckman, W.; Lacmann, R.; Blerfreund, a. Growth rates and habits of ice crystals grown from the vapor phase , *J. Phys. Chem.* vol. 87, pp. 4142, 1983.

[18] Betzig, E.; Trautman, J.K.; Harris, T.D.; Weiner, J.S.; Kostelak, R.L. Breaking the Diffraction Barrier: Optical Microscopy on a Nanometric Scale , *Science* vol. 251 Issue 5000, pp. 1468, 1991.

[19] Bhushan, B.; Jung, Y.C. Micro- and nanoscale characterization of hydrophobic and hydrophilic leaf surfaces , *Nanotechnology* vol. 17, pp. 2758, 2006.

[20] Binnig, G.; Rohrer, H., Gerber, Ch.; Weibel, E. Tunneling through a controllable vacuum gap , *App. Phys. Lett.* vol. 40, issue 2, pp. 178, 1982.

[21] Binnig, G.; Rohrer, H., Gerber, Ch.; Weibel, E. Surface Studies by Scanning Tunneling Microscopy , *Phys. Rev. Lett.* vol. 49, issue 1, pp. 57, 1982.

[22] Binnig, G.; Quate, C.F.; Gerber, Ch. Atomic Force Microscope , *Physical Review Letters* vol. 56, issue 9, pp. 930, 1986.

[23] Binnig, G.; Rohrer, H. Scanning tunneling microscopy , *IBM Journal of Research and Development* vol. 30, issue 4, pp. 355, 1986.

[24] Bizarri, A.R.; Cannistraro, S. Molecular dynamics of water at the protein-solvent interface , *Journal of physical chemistry B* vol. 106, pp. 6617, 2002.

[25] Bluhm, H.; Schwarz, U.D.; Wiesendanger, R. Origin of the ferroelectric domain contrast observed in lateral force microscopy , *Phys. Rev. B* vol. 57, pp. 161, 1998.

[26] Bluhm, H.; Inoue, T.; Salmeron, M. Formation of dipole-oriented water films on mica substrates at ambient conditions , *Surface Science* vol. 462, pp. 599, 2000.

[27] Bluhm, H.; Ogletree, D.F.; Fadley, C.S.; Hussain, Z.; Salmeron, M. The premelting of ice studied with photoelectron spectroscopy , *J. Phys.: Condens. Matter* vol. 14, 2002.

[28] Bruchhaus, R.; Pitzer, D.; Schreiter, M.; Wersin, W. Sputtering of PZT Thin Films for Surface Micromachined IR-Detector Arrays , *lnregrared Ferroekcrrics* vol. 25, pp. 11, 1999.

[29] Buhlmann, S.; Colla, E.; Muralt, P. Polarization reversal due to charge injection in ferroelectric films , *Physical Review B* vol. 72, pp. 214120, 2005.

[30] Burton, Z.; Bhushan, B. Hydrophobicity, adhesion, and friction properties of nanopatterned polymers and scale dependence for micro- and nanoelectromechanical systems , *Nano Letters* vol. 5, pp. 1607, 2005.

[31] Cantrell, W.; Ewing, G. E. Thin film water on muscovite mica , *J. Phys. Chem. B* vol. 105, pp. 5434, 2001.

[32] Cao, P.; Xu, K.; Varghese, J.; Heath, J. The Microscopic Structure of Adsorbed Water on Hydrophobic Surfaces under Ambient Conditions , *Nano Letters* vol. 11, pp. 5581, 2011.

[33] Cardellach, M.; Verdaguer, A.; Fraxedas, J. Thin water films grown at ambient conditions on $BaF_2$ (111) studied by scanning polarization force microscopy , *The Journal of Chemical Physics* vol. 129, pp. 174705, 2008.

[34] Cardellach, M.; Verdaguer, A.; Santiso, J.; Fraxedas, J. Two−dimensional wetting: The role of atomic steps on the nucleation of thin water films on $BaF_2$(111) at ambient conditions , *J. Chem. Phys.* vol. 132, pp. 234708, 2010.

[35] Carpick, R.W. Controlling friction , *Science* vol. 313, pp. 184, 2006.

[36] Carpick, R.W; Salmeron, M. Scratching the surface: Fundamental investigations of tribology with atomic force microscopy , *Chem. Rev.* vol. 97, pp. 1163, 1997.

[37] Chakraborty, S.; Sinha, S.K.; Bandyopadhyay, S. Low−frequency vibrational spectrum of water in the hydrationlayer of a protein: a molecular dynamics simulation study , *J. Phys. Chem. B* vol. 111, pp. 13626, 2007.

[38] Chalikian, T.V.; Totrov, M.; Abagayan, R.; Breslauer, K.J. The hydration of globular proteins as derived from volume and compressibility measurements: cross correlating thermodynamic and structural data , *J. Mol. Biol.* vol. 260, pp.588, 1996.

[39] Chandler, D. Interfaces and the driving force of hydrophobic assembly , *Nature* vol. 437, pp. 640, 2005.

[40] Chaplin, M.F. Opinion: Do we underestimate the importance of water in cell biology? , *Nature Rev. Mol. Cell Biol.* vol. 7, pp. 861, 2006.

[41] Chattopadhyay, S.; Uysal, A.; Stripe, B.; Ha, Y.; Marks, T.J.; Karapetrova, e.A.; Dutta, P. How Water Meets a Very Hydrophobic Surface , *Phys. Rev. Lett.* vol. 105, 2010,

[42] Chen, J. Introduction to Scanning Tunneling Microscopy , Oxford University Press. ISBN 0195071506, 1993.

[43] Chowdhry, B.Z.; Dines, T.J.; Jabeen, S.; Withnall, R. Vibrational Spectra of alpha-Amino Acids in the Zwitterionic State in Aqueous Solution and the Solid State: DFT Calculations and the Influence of Hydrogen Bonding , *J. Phys. Chem. A* vol. 112, pp. 10333, 2008.

[44] Chung, K.H.; Lee, Y.H.; Kim, D.E. Characteristics of fracture during the approach process and wear mechanism of a silicon AFM tip , *Ultramicroscopy* vol. 102, issue 2, pp. 161, 2005.

[45] Cleaver, J.A.S.; Wong, P. Humidity-induced surface modification of boric acid , *Surf. Interface Anal.* vol. 36, pp. 1592, 2004.

[46] Colombo, M.F.; Rau, D.C.; Parsegian, V.A. Protein solvation in allosteric regulation − a water effect on hemoglobin , *Science* vol. 256, pp. 655, 1992.

[47] Dalhus, B.; Gorbitz, C.H. Triclinic form of DL-valine , *Acta Crystallogr., Sect. C: Cryst. Struct. Commun.*, vol. 52, pp. 1759, 1996.

[48] Danielewicz-Ferchmin, I.; Ferchmin, A.R. Lowering of the freezing temperature of water at the protein surface due to electric field , *J. Mol. Liq.* vol. 124, pp. 114, 2006.

[49] Darwich, S.; Mougin, K.; Rao, A.; Gnecco, E.; Jayaraman, S.; Haidara, H. Manipulation of gold colloidal nanoparticles with atomic force microscopy in dynamic mode: influence of particlesubstrate chemistry and morphology, and of operating conditions , *Beilstein J. Nanotechnol* vol. 2, pp. 85, 2011.

[50] Davies, M. *Some electrical and optical aspects of molecular behaviour*, Pergamon, Oxford, 1965

[51] Degtyarenko, I.; Jalkanen, K.J.; Gurtovenko, A.; Nieminen, R.M. The aqueous and crystalline forms of L-alanine zwitterion , *J. Comput. Theor. Nanosci.* vol. 5, pp. 277, 2008.

[52] Denisov, V.P.; Halle, B. Protein hydration dynamics in aqueous−solution − a comparison of bovine pancreatic trypsin−inhibitor and ubiquitin by O−17 spin relaxation dispersion , *J. Mol. Biol.* vol. 245, pp. 682, 1995.

[53] Devoto, P. *Gazz. Chim. Ital.* vol. 60, pp. 520, 1930.

[54] Devoto, P. *Gazz. Chim. Ital.* vol. 61, pp. 897, 1931.

[55] Devoto, P. *Gazz. Chim. Ital.* vol. 64, pp. 76, 1934.

[56] Dill, K.A. Dominant forces in protein folding , *Biochemistry* vol. 29, pp.7133, 1990.

[57] Doolittle, R.F. Redundancies in protein sequences , *Prediction of Protein Structures and the Principles of Protein Conformation*, Fasman, G.D., New York: Plenum, pp. 599623, ISBN 0-306-43131-9, 1989.

[58] Dove, P.M.; Platt, F.M. Compatible real-time rates of mineral dissolution by Atomic Force Microscopy (AFM) , *Chemical Geology* vol. 127, pp. 331, 1996.

[59] Durig, U.; Zulger, O.; Stalder, A. Interaction force detection in scanning probe microscopy: Methods and applications *J. Appl. Phys.* vol. 72, 1992.

[60] Eastman, T.; Zhu, D.M. Adhesion forces between surface-modified AFM tips and a mica surface , *Langmuir* vol. 12, issue 11, pp. 2859, 1996.

[61] Ebbinghaus, S.; Kim, J.; Heyden, M.; Yu, X.; Hengen, U.; Gruebele, M.; Leitner, D.M. An extended dynamical hydration shell around proteins , *Proc. Natl. Acad. Sci. USA* vol. 104, pp. 20749, 2007.

[62] Ebbinghaus, S.; Joong, K.S.; Matthias, H.; et al. An extended dynamical hydration shell around proteins , *PROCEEDINGS OF THE NATIONAL ACADEMY OF SCIENCES OF THE UNITED STATES OF AMERICA* vol. 104, issue 52, pp. 20749, 2007.

[63] Ekwinska, M.; Rymuza, Z. Normal Force Calibration Method Used for Calibration of Atomic Force Microscope , *Acta Physica Polonica A* vol. 116, 2009.

[64] Eng, L.M.; Bammerlin, M.; Loppacher, C.H.; Guggisberg, M.; Bennewitz, R.; Lthi, R.; Meyer, R.; Huser, T.H.; Heinzelmann, H.; Guntherodt, H.J. Ferroelectric domain characterisation and manipulation: a challenge for scanning probe microscopy , *Ferroelectrics* vol. 222, pp. 153, 1999.

[65] Engelhardt, J.B.; Dabringhaus, H.; Wandelt, K. Atomic force microscopy study of the $CaF_2(111)$ surface: from cleavage via island to evaporation topographies , *Surf. Sci.* vol. 448, pp. 187, 2000.

[66] Engkvist, O.; Stone, A.G. Adsorption of water on the NaCl(001) surface. III. Monte Carlo simulations at ambient temperatures , *J. Chem. Phys.* vol. 112, pp. 6827, 2000.

[67] Ehre, D.; Lavert, E.; Lahav, M.; et al. Water Freezes Differently on Positively and Negatively Charged Surfaces of Pyroelectric Materials , *Science* vol. 327, pp. 672, 2010.

[68] Ernst, J.A.; Clubb, R.T.; Zhou, H.X.; Gronenborn, A.M.; Clore, G.M. Demonstration of positionally disordered water within a protein hydrophobic cavity by NMR , *Science* vol. 267, pp. 1813, 1995.

[69] European Comission Homepage *http://cordis.europa.eu/nanotechnology/home.html*

[70] Ewing, G.E. Ambient thin film water on insulator surfaces , *Chem. Rev.* vol. 106, pp. 1511, 2006.

[71] Fanourgakis, G.S.; Sotiris, S.X. The bend angle of water in ice Ih and liquid water: The significance of implementing the nonlinear monomer dipole moment surface in classical interaction potentials *J. Chem. Phys.* vol. 124, 2006.

[72] Fecko, C.J.; Loparo, J.J.; Roberts, S.T.; et al. Local hydrogen bonding dynamics and collective reorganization in water: Ultrafast infrared spectroscopy of $HOD/D_2O$ *JOURNAL OF CHEMICAL PHYSICS* vol. 122, issue 5, pp. 355, 2005.

[73] Fenimore, P.W.; Frauenfelder, H.; McMahon, B.H.; Parak, F.G. Slaving: Solvent fluctuations dominate protein dynamics and functions , *Proc. Natl. Acad. Sci. USA* vol. 99, pp. 16047, 2002.

[74] Feynman, R. Speech There s Plenty of Room at the Bottom , 1959. http://lamp.tu-graz.ac.at *Chem. Rev.* vol. 103, pp. 4801, 2003.

[75] Foster, M.; Ewing, G.E. Adsorption of water on the NaCl(001) surface. II. An infrared study at ambient temperatures , *J. Chem. Phys.* vol. 112, pp. 6817, 2000.

[76] Foster, M.; DAgostino, M.; Passno, D. Water on MgO(100) − An infrared study at ambient temperatures , *Surf. Sci.* vol. 590, pp. 31, 2005.

[77] Franks, F. Protein stability: the value of old literature , *Biophysical Chemistry* vol. 96, pp. 117, 2002.

[78] Fukuma, T.; Ueda, Y.; Yoshioka, S.; Asakawa, H. Atomic-Scale Distribution of Water Molecules at the Mica-Water Interface Visualized by Three-Dimensional Scanning Force Microscopy , *Phys. Rev. Lett.* vol. 104, 2010.

[79] Gan, W.; Wu, D.; Zhang, Z.; Guo, Y.; Wan, H. Orientation and motion of water molecules at air/water interface , *Chinese J. Chem. Phys.* vol. 19, 2006.

[80] Ganpule, C.; Nagarajan, V.; Hill, B.K.; Roytburd, A.L.; Williams, E.D.; Alpay, S.P.; Roelofs, A.; Waser, R.; Eng, L. Imaging three-dimensional polarization in epitaxial polydomain ferroelectric thin films , *J. Appl. Phys.* vol. 91, pp. 1477, 2002.

[81] García, A.E.; Hummer, G. Water penetration and escape in proteins , *Proteins Struct. Funct. Genet.* vol. 38, pp. 261, 2000.

[82] García, R.; Perez, R. Dynamic atomic force microscopy methods , *Surface Science Reports* vol. 47, pp. 197, 2002.

[83] García-Manyes, S.; Verdaguer, A.; Gorostiza, P.; et al. Alkali halide nanocrystal growth and etching studied by AFM and modeled by MD simulations , *Journal of Physical Chemistry* vol. 120, pp. 2963, 2004.

[84] Garczarek, F.; Gerwert, K. Functional waters in intraprotein proton transfer monitored by FTIR difference spectroscopy , *Nature* vol. 439, pp. 109, 2006.

[85] Gavish, B.; Gratton, E.; Hardy, C.J. Adiabatic compressibility of globular proteins , *Proc. Natl. Acad. Sci. USA* vol. 80, pp. 750, 1983.

[86] Gavish, M.; Wang, J.L.; Eisenstein, M.; Lahav, M.; Leiserowitz, L. The role of crystal polarity in alpha-amino-acid crystals for induced nucleation of ice , *Science* vol. 256, pp. 815, 1992.

[87] Gekko, K.; Noguchi, H. Compressibility of proteins at 25$^o$C , *J. Phys. Chem.* vol. 83, pp. 2706, 1979.

[88] Geng, Y.L.; Xu, D.; Wang, X.Q.; Yu, G.W.; Zhang, G.H.; Zhang, H.B. AFM study of surface morphology of 100 cleavage planes of L-arginine acetate crystals `, *J. Cryst. Growth* vol. 282, pp. 208, 2005.

[89] Gil, A.; Colchero, J.; Luna, M.; Gmez-Herrero, J.; Bar, A.M. Adsorption of water on solid surfaces studied by scanning force microscopy , *Langmuir* vol. 16, pp. 5086, 2000.

[90] Goodman, A.L.; Bernadrand, E.T.; Grassian, V.H. Spectroscopic study of nitric acid and water adsorption on oxide particles: Enhanced nitric acid uptake kinetics in the presence of adsorbed water , *J. Phys. Chem. A* vol. 105, pp. 6443, 2001.

[91] Grayer Wolf, S.; Berkovitch-Yellin, Z.; Lahav M.; Leiserowitz, L. Use of tailor-made additives for the study of disorder in crystals - application to the racemic compound of valine , *Mol. Cryst. Liq. Cryst.*, vol. 186, pp. 3, 1990.

[92] Greef, R.; Frey, J. G.; The water-like film on water , *Physica Status Solidi 5* 4th International Conference on Spectroscopic Ellipsometry (ICSE4), pp. 1184, 2008.

[93] Greenstein, H.; Wyman, J. Further studies on dielectric constant and electrostriction of amino acids and peptides , *J. Am. Chem. Soc.* vol. 58, pp. 463, 1936.

[94] Guilemany, J.M.; Miguel, J.M.; Vizcaino, S.; Climent, F. Role of three-body abrasion wear in the sliding wear behaviour of WC-Co coatings obtained by thermal spraying *Surface and Coatings Technology* vol. 140, pp. 141, 2001.

[95] Guillot, B. A reappraisal of what we have learnt during three decades of computer simulations on water , *J. Mol. Liq.* vol. 101, 2002.

[96] Guo, H.M.; Liu, H.W.; Wang, Y.L.; Gao, H.J.; Gong, Y.; Jiang H.Y.; Wang, W.Q. Surface structures of DL-valine and L-alanine crystals observed by atomic force microscopy at a molecular resolution , *Surface Science* vol. 552, pp. 70, 2004.

[97] Haeni, J.H.; Irvin, P.; Chang, W.; Uecker, R. Room-temperature ferroelectricity in strained SrTiO3 , *Nature* vol. 430, pp. 758, 2004.

[98] Hartmann, U. Magnetic force microscopy: some remarks from the micromagnetic point of view , *Journal of Applied Physics.* vol. 64, issue 3, pp. 1561, 1988.

[99] Hartmann, U. Intermolecular and surface forces in noncontact scanning force microscopy , *Ultramicroscopy.* vol. 42, pp. 59, 1992.

[100] Hasted Liquid water: Dielectric properties in, *Water: A comprehensive treatise* vol. 1, Ed. F. Franks (Plenum Press, New York) pp. 255, 1972.

[101] Hemayet, U.M.; Ying, T.S.; Raymond, R.D. Characterization of Microdrops and Microbubbles in Emulsions and Foams Using Atomic Force Microscopy , *Langmuir* vol. 27, Isue 6, pp. 2536, 2011.

[102] Hamelberg, D.; Shen, T.; McCammon, J,A. Insight into the role of hydration on protein dynamics , *J. Chem. Phys.* vol. 125, 2006.

[103] Harnagea, C.; Alexe, M.; Hesse, D.; Pignolet, A. Contact resonances in voltage-modulated force microscopy , *Appl. Phys. Lett.* vol. 83, pp. 338, 2003.

[104] Henderson, M. A. The interaction of water with solid surfaces: fundamental aspects revisited , *Surf. Sci. Rep.* vol. 46, Issue: 1-8, pp. 5, 2002.

[105] Hidaka, T.; Maruyama, T.; Saitoh, M.; Mikoshiba, N.; Shimizu, M.; Shiosaki, T.; Wills, L.A.; Hiskes, R.; Discarolis, S.A.; Amano, J. Title: Formation and observation of 50 nm polarized domains in PbZr1-xTixO3 thin film using scanning probe microscope , *Appl. Phys. Lett.* vol. 68, pp. 2358, 1996.

[106] Higgins,M.J.; Christian, K. R.; Takayuki, U.; Sader, J.E.; Rachel, McK.; Suzanne P.J.; Frequency modulation atomic force microscopy: a dynamic measurement technique for biological systems *Nanotechnology* vol. 16, 2005.

[107] Hippel, A. von. Ferroelectricity, Domain Structure, and Phase Transitions of Barium Titanate , *Rev. Modern Phys.* vol. 22, pp. 221, 1950.

[108] Hisada, K.; Knobler, C.M. Microscopic friction anisotropy and asymmetry related to the molecular tilt azimuth in a monolayer of glycerol ester , *Colloids and Surfaces A: Physicochemical and Engineering Aspects* vol. 198, pp. 21, 2002.

[109] Hobbs, P.V., *Ice Physics*, Clarendon Press, Oxford, 1974.

[110] Hodgson, A.; Haq, S. Water adsorption and the wetting of metal surfaces Water adsorption and the wetting of metal surfaces , *Surf. Sci. Rep.* vol. 64, pp. 381, 2009.

[111] Hoper, R.; Gesang, T.; Possart, W.; Hennemann, O.D.; Bosecks, S. Imaging Elastic Sample Properties with An Atomic-Force Microscope Operating in the Tapping Mode. , *Ultramicroscopy* vol. 60, 1995.

[112] Hu, J.; Xiao, X.D.; Salmeron, M. Scanning polarization force microscopy - A technique for imaging liquids and weakly adsorbed layers , *Appl. Phys. Lett.* vol. 67, pp. 476, 1995.

[113] Hu, J.; Xiao, X.D.; Ogletree, D.F.; Salmeron, M. Imaging the condensation and evaporation of molecularly thin-films of water with nanometer resolution , *Science* vol. 268, issue 5208, pp. 267, 1995.

[114] Hu, J.; Carpick, R. W.; Salmeron, M.; Xiao, X. D. Imaging and manipulation of nanometer size liquid droplets by scanning polarization force microscopy , *J Vac Sci Technol B* vol. 14, pp. 1341, 1996.

[115] Ichikawa, K.; Kameda, Y.; Yamaguchi, T.; et al. Neutron-diffraction investigation of the intramolecular structure of a water molecule in the liquid-phase at high-temperatures , *Mol. Phys.* vol. 73, 1991.

[116] Israelachvili, J. N. *Intermolecular and Surface Forces* Academic, London, 1991.

[117] Itaya, K. In situ scanning tunneling microscopy in electrolyte solutions , *Progress in surface science* vol. 58, pp. 121, 1998.

[118] IUPAC-IUB Joint Commission on Biochemical Nomenclature (JCBN) Nomenclature and Symbolism for Amino, Acids and Peptides , *Biochem. J.* vol. 219, pp.345, 1984.

[119] Jalili N; Laxminarayana K A review of atomic force microscopy imaging systems: application to molecular metrology and biological sciences , *Mechatronics* vol. 14, pp. 907, 2004.

[120] Jensen, M.O.; Mouritsen, O.G.; Peters, G.H. The hydrophobic effect: Molecular dynamics simulations of water confined between extended hydrophobic and hydrophilic surfaces , *J. Chem. Phys.* vol. 120, pp. 9729, 2004.

[121] Johnson, C.A.; Lenhoff, A.M. Adsorption of Charged Latex Particles on Mica Studied by Atomic Force Microscopy , *Journal of colloid and interface science* vol. 179, pp. 587, 1996.

[122] Kalinin, S.V.; Bonnell, D.A. Local potential and polarization screening on ferroelectric surfaces , *Phys. Rev. B* vol. 63, pp. 125411, 2001.

[123] Kalinin, S.V.; Bonnell, D.A. Imaging mechanism of piezoresponse force microscopy of ferroelectric surfaces , *Phys. Rev. B* vol. 65, pp. 125408, 2002.

[124] Kanzig, W. Ferroelectrics and Antiferroelectrics , *Solid State Physics* Academic Press. pp. 5 ISBN: 0126077045, 1957.

[125] Karplus, P.A. Hydrophobicity regained , *Protein Sci.* vol. 6, pp. 1302, 1997.

[126] Kharakoz, D.P.; Sarvazyan, A.P. Hydrational and intrinsic compressibilities of globular proteins , *Biopolymers* vol. 13, pp. 11, 1993.

[127] Kijima, T. New low temperature preparation of ferroelectric $Bi_4Ti_3O_{12}$ thin films by MOCVD method , *Integrated Ferroelectrics* vol. 26, pp. 93, 1999.

[128] Krichevsky, O.; Stavans, J. Ostwald ripening in a 2-Dimensionial system - correlation effects , *Phys. Rev. B* vol. 52, pp. 1818, 1995.

[129] Kuo, I.W.; and Mundy, C.J. An ab initio molecular dynamics study of the aqueous liquid-vapor interface , *Science* vol. 303, pp. 658, 2004.

[130] Kyte, J.; Doolittle, R.F. A simple method for displaying the hydropathic character of a protein , *J. Mol. Biol.* vol. 157, pp. 105, 1982.

[131] Lambert, J.; Guthmann, C.; Saint-Jean, M. Relationship between charge distribution and its image by electrostatic force microscopy `, *J. Appl. Phys.* vol. 93, pp. 5369,, 2003.

[132] Landolt-Bornstein *Springer*, Heidelberg, 1982.

[133] Lauritsen, J.V.; Reichling, M. Atomic resolution non-contact atomic force microscopy of clean metal oxide surfaces , *Journal of physics−condensed matter* vol. 22, 2010.

[134] Lehmann, M.S.; Koetzle, T.F.; Hamilton, W.C. Precision neutron diffraction structure determination of protein and nucleic acid components. I. The crystal

and molecular structure of the amino acid L-alanine , *J. Am. Chem. Soc.* vol. 94, pp. 2657, 1972.

[135] Li, Z.; Lazaridis, T. Thermodynamics of buried water clusters at a protein-ligand binding interface , *Journal of physical chemistry B* vol. 110, pp.1464, 2006.

[136] Liang, M. No Rabbit ears on water - The structure of the water molecule - what should we tell the students *Journal of Chemical Education* vol. 64 Issue 2, pp. 124, 1987.

[137] Liaxing, M.; Feng, L. Explain the latent heat and specific heat of water, ammonia, and methanol with degrees of freedom *Lat. Am. J. Phys. Educ.* vol. 2, 2008.

[138] Libbrecht, K.G. Explaining the formation of thin ice crystal plates with structure-dependent attachment kinetics , *J. Cryst. Growth* vol. 258, pp. 168, 2003.

[139] Libbrecht, K.G. A Critical Look at Ice Crystal Growth Data , *Cornell University Library* 2004.

[140] Lienqueo, M.E.; Mahn, A.; Asenjo, J.A. Mathematical correlations for predicting protein retention times in hydrophobic interaction chromatography , *J. Chromatogr. A* vol. 978, pp. 71, 2002.

[141] Liley M; Gourdon D; Stamou D; et al. Friction anisotropy and asymmetry of a compliant monolayer induced by a small molecular tilt *Science* vol. 280, Num. 5361, pp. 273, 1998.

[142] Lin, J.; Balabin, I.A.; Beratan, D.N. The nature of aqueous tunneling pathways between electron-transfer proteins , *Science* vol. 310, pp. 1311, 2005.

[143] Lin, L.; Kim, D.; Kim, W.; et al. Friction and wear characteristics of multilayer graphene films investigated by atomic force microscopy *Surface & coatings technology* vol. 250, Issue 20, pp. 4864, 2011.

[144] Lines, M.; Glass, A. *Principles and applications of ferroelectrics and related materials* Clarendon Press, Oxford. ISBN: 0198512864, 1979.

[145] Lo Conte, L.; Cothia, C.; Janin, J. The atomic structure of protein-protein recognition sites , *J. Mol. Biol.* vol. 285, pp. 2177, 1999.

[146] Loparo, J.J.; Fecko, C.J.; Eaves, J.D.; et al. Reorientational and configurational fluctuations in water observed on molecular length scales *Phys. Rev. B* vol. 70 Issue 18, 2004.

[147] Lum, K., Chandler, D. and Weeks, J. D. Hydrophobicity at small and large length scales , *J. Phys. Chem. B* vol. 103, pp. 4570, 1999.

[148] Maccarini, M.; Steitz, R.; Himmelhaus, M.; Fick, J.; Tatur, S.; Wolff, M.; Grunze, M.; Janecek, J.; Netz, R.R. Density depletion at solid-liquid interfaces: A neutron reflectivity study , *Langmuir* vol. 23, pp. 598, 2007.

[149] MacKerell, A.D.; Bashford, D.; Bellott, M.; et al. All-atom empirical potential for molecular modeling and dynamics studies of proteins , *J. Phys. Chem. B* vol. 102, pp. 3586, 1998.

[150] Makarov, V.; Andrews, B.K.; Smith, P.E.; Pettitt, B.M. Residence times of water molecules in the hydration sites of myoglobin `, *Biophys. J.* vol. 79, pp. 2966, 2000.

[151] Makarov, V.; Pettitt, B.M.; Feig, M. Solvation and hydration of proteins and nucleic acids: A theoretical view of simulation and experiment , *Acc. Chem. Res.* vol. 35, pp. 376, 2002.

[152] Manne, S.; Cleveland, J.P.; Stucky, G.D.; Hansma, P.K. Lattice resolution and solution kinetics on surfaces of amino−acids crystals − an atomic force microscope study , *J. Cryst. Growth* vol. 130, pp. 333, 1993.

[153] Marchi, F.; Dianoux, R.; Smilde, H.J.H.; Murd, P.; Comin, F.; Chevrier, J. Characterisation of trapped electric charge carriers behaviour at nanometer scale by electrostatic force microscopy *Journal of electrostatics* vol. 66, pp. 538, 2008.

[154] Martin, R.B. Localized and spectroscopic orbitals: Squirrel ears on water *J. Chem. Educ.* vol. 65, pp. 668, 1988.

[155] Martin, R.B. Reorientational and configurational fluctuations in water observed on molecular length scales *Phys. Rev. B* vol. 70 Issue 18, 2004.

[156] Martin, Y.; Wickramasinghe, H.K.; Magnetic imaging by force microscopy with 1000 Å resolution `, *Appl. Phys. Lett.* vol. 50, pp. 1455, 1987.

[157] Matsumoto, M.; Tanaka, K.; Azumi, R.; Kondo, Y. Yoshino, N. Structure of phase-separated Langmuir-Blodgett films of hydrogenated and perfluorinated carboxylic acids investigated by IR spectroscopy, AFM, and FFM. *Langmuir* vol. 19, pp. 2802, 2003.

[158] Mezger, M.; Reichert, H.; Schoder, S.; Okasinski, J.; Schroder, H.; Dosch, H.; Palms, D.; Ralston, J.; Honkimaki, V. High-resolution in situ x-ray study of the hydrophobic gap at the water-octadecyl-trichlorosilane interface , *Proc. Natl. Acad. Sci. U.S.A.* vol. 103, pp. 18401, 2006.

[159] Mezger, M.; Sedlmeier, F.; Horinek, D.; Reichert, H.; Pontoni D.; Dosch, H. On the Origin of the Hydrophobic Water Gap: An X-ray Reflectivity and MD Simulation Study , *J. Am. Chem. Soc.* vol. 132, pp. 6735, 2010.

[160] Milhaud, J. New insights into water-phospholipid model membrane interactions , *Biochim. Biophys. Acta* vol. 19, pp. 1663, 2004.

[161] MIT Web page, chemistry section, nanoscience area. *http://www.mit.edu/*

[162] Mittal, J.; Hummer, G. Static and dynamic correlations in water at hydrophobic interfaces , *Proc. Natl. Acad. Sci. U.S.A.* vol. 105, pp. 20130, 2008.

[163] Molotskii, M. Generation of ferroelectric domains in atomic force microscope , *J. Appl. Phys.* vol. 93, pp. 6234, 2003.

[164] Moon, E. S.; Lee, C. W.; Kang, H. Proton mobility in thin ice films: a revisit , *Phys. Chem. Chem. Phys.* vol. 10, pp. 4814, 2008.

[165] Morita, T.; Cho, Y. Polarization reversal anti-parallel to the applied electric field observed using a scanning nonlinear dielectric microscopy , *Appl. Phys. Lett.* vol. 84, pp. 257, 2004.

[166] Munuera, C.; Ocal, C. Real time scanning force microscopy observation of a structural phase transition in self-assembled alkanethiols , *J. Chem. Phys.* vol. 124, pp. 206102, 2006.

[167] Munuera, C.; Barrena, E.; Ocal, C. Deciphering structural domains of alkanethiol self-assembled configurations by friction force microscopy *Journal of physical chemistry* vol. 111, Issue: 49, pp. 12721, 2007

[168] National Nanotechnology Initiative web page *http://www.nano.gov*

[169] Nelson, J.; Knight, C. Snow crystal habit changes explained by layer nucleation , *J. Atmos. Sci.* vol. 55, pp. 1452, 1998.

[170] Nettleton, R.E. Ferroelectric phase transitions: A review of theory and experiment , *Ferroelectrics* vol. 1, 1970.

[171] Neumeister, J.M.; Ducker, W.A. Lateral, normal and longitudinal spring constants of Atomic-Force Microscopy cantilevers , *Review of scientific instruments* vol. 65, Issue 8, pp. 2527, 1994.

[172] Ning, C.G.; Hajgat, B.; Huang, Y.R., et al. High resolution electron momentum spectroscopy of the valence orbitals of water , *Chem. Phys.* vol. 343, 2008.

[173] Nonnenmacher, M.; O Boyle, M.P.; Wickramasinghe, H.K. Kelvin probe force microscopy , *Applied Physics Letters* vol. 58 Issue 25, pp. 2921, 1991.

[174] NT MDT Web page, *http://www.ntmdt.com/spm-principles.*

[175] Oncins, G. *Nanomechanics of Organic Layers and Biomembranes*, Thesis (PhD), Universitat de Barcelona, 2007.

[176] Okita, S.; Miura, K. Molecular arrangement inC(60) andC(70) films on graphite and their nanotribological behavior , *Nano Letters* vol. 1 pp. 101, 2001.

[177] Olding, T.; Leclerc, B.; Sayer, M. Processing of multilayer PZT coating for device purposes , *Integrated ferroelectrics* vol. 26, pp. 225,1999

[178] Osted, A.; Kongsted, J.; Mikkelsen, K.V.; Christiansen, O. The electronic spectrum of the micro-solvated alanine zwitterion calculated using the combined coupled cluster/molecular mechanics method , *Chem. Phys. Lett.* vol. 429, pp. 430, 2006.

[179] Otting, G.; Liepinsh, E.; Wuthrich, K. Protein hydration in aqueous−solution , *Science* vol. 254, pp. 974, 1991.

[180] Paci, E.; Velikson, B. On the volume of macromolecules , *Biopolymers* vol. 41, pp. 785, 1997.

[181] Pal, S.K.; Peon, J.; Zewail, A.H. Biological water at the protein surface: Dynamical solvation probed directly with femtosecond resolution , *Proc. Natl. Acad. Sci. USA* vol. 99 , pp. 1763, 2002.

[182] Pan, D.; Liu, L.M.; Tribello, G. A.; Slater, B.; Michaelides, A.;Wang, E.; Surface energy and surface proton order of ice Ih , *Phys. Rev. Lett.* vol. 101, 2008.

[183] Panda, R.K.; Janas, V.F.; Safari, A. Ferroelectricity: Materials, characteristics & applications *Advanced ceramic materials: Applications of advanced materials in a high-tech society* vol. 122-1, pp. 35, 1996.

[184] Papoian, G.A.; Ulander, J.; Eastwood, M. P.; Luthey-Schulten, Z.; Wolynes, P.G. Water in protein structure prediction , *Proc. Natl. Acad. Sci. USA* vol. 101, pp. 3352, 2004.

[185] Park, S.; Ahn, D.; Lee, S. Dynamic paths between neutral alanine-water and zwitterionic alanine-water clusters: single, double and triple proton transfer , *Chem. Phys. Lett.* vol. 371, pp. 74, 2003.

[186] Park, J.Y.; Ogletree, D.F.; Salmeron, M.; Ribeiro, R.A.; Canfield, P.C.; Jenks, C.J.; Thiel, P.A. High frictional anisotropy of periodic and aperiodic directions on a quasicrystal surface , *Science* vol. 309, pp. 1354, 2005.

[187] Park, J.Y.; Ogletree, D.F.; Thiel, P.A.; Salmeron, M. Electronic control of friction in silicon pn junctions , *Science* vol. 313, pp. 207, 2006.

[188] Paruch, P.; Tybell, T.; Triscone, J.M. Nanoscale control of ferroelectric polarization and domain size in epitaxial $Pb(Zr_0\ 2Ti_0\ 8)O_3$ thin films , *Applied Physics Letters* vol. 79, pp. 530, 2001.

[189] Paruch, J. Atomic force microscopy studies of ferroelectric domains in epitaxial $PbZr_{0:2}Ti_{0:8}O_3$ thin films and the static and dynamic behavior of ferroelectric domain walls , *PhD Thesis* Université de Genève Faculté des Sciences Département de physique Professeur J.-M. Triscone de la matière condensée. 2003.

[190] Pauling, L. The Structure and Entropy of Ice and of Other Crystals with Some Randomness of Atomic Arrangement , *J. Am. Chem. Soc.* vol. 57, pp. 2680, 1935.

[191] Paz de Araujo, C.; Scott, J.F.; Taylor, G. W. *Ferroelectric thin films: synthesis and basic properties.* Gordon and Breach, Amsterdam. 1996.

[192] Petrenko, V. F.; Whitworth, R. W. Physics of ice , New York: Oxford University Press. 2002.

[193] Petrone, P.M.; Garcia, A.E. MHC-peptide binding is assisted by bound water molecules , *Journal of molecular biology* vol. 338, pp. 419, 2004.

[194] Poynor, A.; Hong, L.; Robinson, I.K.; Granick, S.; Zhang, Z.; Fenter, P.A. How water meets a hydrophobic surface , *Phys. Rev. Lett.* vol. 97, pp. 266101, 2006.

[195] Rao, A.; Gnecco, E.; Marchetto, D.; Mougin, K.; Schonenberger, M.; Valeri, S.; Meyer, E. Title: The analytical relations between particles and probe trajectories in atomic force microscope nanomanipulation , *Nanotechnology* vol. 20 2009.

[196] Rao, A.; Wille, M. L.; Gnecco, E.; Mougin, K.; Meyer, E. Title: Trajectory fluctuations accompanying the manipulation of spherical nanoparticles , *Phys Rev B*, vol. 80, 2009.

[197] Rashin, A.A.; Iofin, M.; Honig, B. Internal cavities and buried waters in globular proteins , *Biochemistry* vol. 23, pp. 3619, 1986.

[198] Richards, F.M. Areas, volumes, packing and protein structure , *Annu. Rev. Biophys. Bioengin.* vol. 6, pp. 151, 1977.

[199] Richards, F.M.; Lim, W.A. An analysis of packing in the protein folding problem , *Q. Rev. Biophys.* vol. 26, pp. 423, 1994.

[200] Rockefeller University Webpage hydrophobicity scales , *http://prowl.rockefeller.edu/aainfo/hydro.htm*

[201] Sacha, G.M.; Verdaguer, A.; Salmeron, M.J. Induced Water Condensation and Bridge Formation by Electric Fields in Atomic Force Microscopy , *Phys. Chem.* vol. 110, pp. 14870, 2006.

[202] Sacha, G. M.; Cardellach, M.; Segura, J. J.; Moser, J.; Bachtold, A.; Fraxedas, J.; Verdaguer, A. Influence of the macroscopic shape of the tip on the contrast in scanning polarization force microscopy images , *Nanotechnology* vol. 20, pp. 285704, 2009.

[203] Sader, J.E.; Larson, I.; Mulvaney, P.; White, L.R. Method for the calibration of atomic force microscope cantilevers , *Rev. Sci. Instrum.* vol. 66, pp. 3789, 1995.

[204] Sagarik, K.; Dokmaisrijan, S. A theoretical study on hydration of alanine zwitterions , *J. Mol. Struct.: THEOCHEM* vol. 718, pp. 31, 2005.

[205] Salmeron, M. Scanning polarization force microscopy - A technique for studies of wetting phenomena at the nanometer scale , *Oil gas science and technology* vol. 56 Issue 1, pp. 1294, 2001.

[206] Salmeron, M.; Kopta, S.; Barrena, E.; Ocal, C. Fundamentals of Tribology and Bridging the Gap Between the Macro- and Micro/Nanoscales, NATO Advanced Studies Institute , *Series E: Applied Sciences*, Vol. 10, pp. 41, edited by B. Bhushan, Kluwer Academic, Dordrecht, 2001.

[207] Samsonov, S.; Teyra, J.; Pisabarro, M.T. A molecular dynamics approach to study the importance of solvent in protein interactions , *Proteins−structure function and bioinformatics* Vol. 73, Issue 2, pp. 515, 2008.

[208] Santos, S.; Barcons, V.; Verdaguer, A.; et al. How localized are energy dissipation processes in nanoscale interactions? , *Nanotechnology* vol. 22, 2011.

[209] Schulson, E.M. The structure and mechanical behavior of ice , *Journal of the minerals metals & materials societey* vol. 51, pp. 21, 1999.

[210] Semin, D.J.; Lo, A.; Roark, S.E.; Skodje, R.T.; Rowlen, K.L. Time-dependent morphology changes in thin silver films on mica: A scaling analysis of atomic force microscopy results , *J. Chem. Phys.* vol. 105, pp. 5542, 1996.

[211] Schonherr, H., Chechik, V.; Stirling, C.J.M.; Vancso, G.J. Monitoring surface reactions at an AFM tip: An approach to follow reaction kinetics in self-assembled monolayers on the nanometer scale , *Journal of the American Chemical Society* vol. 122 Issue 15, pp. 3679, 2000.

[212] Segura J. J.; Verdaguer A.; Garzon L.; Barrena, E.; Ocal, C.; Fraxedas, J. Strong water-mediated friction asymmetry and surface dynamics of zwitterionic solids at ambient conditions: L-alanine as a case study , *Journal of Chemical Physics* vol. 134 Issue 12, 2011.

[213] Shaw, R.A.; Durant, A. J.; Mi, Y. Heterogeneous surface crystallization observed in undercooled water , *The journal of physical chemistry. B* vol. 109, pp. 9865, 2005.

[214] Shimon, L.J.W.; Lahav, M.; Leiserowitz, L. Design of stereoselective etchants for organic-crystals - application for the sorting of enantiomorphs and direct assignment of absolute-configuration of chiral molecules , *J. Am. Chem. Soc.* vol. 107, pp. 3375, 1985.

[215] Shindo, H.; Shitagami, K.; Sugai, T.; Kondo, S. Evidence of the contribution of molecular orientations on the surface force friction of alkaline earth sulfate crystals *Phys. Chem. Chem. Phys.* vol. 1, Issue 7, pp.1597, 1999.

[216] Shvebelman, M.; Urenski, P.; Shikler, R.; Rosenman, G.; Rosenwaks, Y.; Molotskii, M. Scanning probe microscopy of well-defined periodically poled ferroelectric domain structure , *Appl. Phys. Lett.* vol. 80, pp. 1806, 2002.

[217] Silvestrelli, P.L.; Parrinello, M.; Structural, electronic, and bonding properties of liquid water from first principles , *Journal of Chemical Physics* vol. 111 Issue 8, pp. 3572, 1999.

[218] Smith, J.C.; Merzel, F.; Verma, C.S.; Fischer, S. Protein hydration water: structure and thermodynamics , *J. Mol. Liq.* vol. 101, pp. 27, 2002.

[219] Smith, W.; Forester, T.J. DL_POLY_2.0: A general-purpose parallel molecular dynamics simulation package , *J.Mol.Graphics* vol. 14, pp. 136, 1996.

[220] Smyth, C.P. *Dielectric Behaviour and Structure*, McGraw-Hill, New York, 1955.

[221] Socoliuc, A.; Gnecco, E.; Maier, S. et al. Atomic-scale control of friction by actuation of nanometer-sized contacts , *Science* vol. 313, Issue 5784, 2006.

[222] Soper, A.K., Benmore, C.J. Quantum differences between heavy and light water , *Phys. Rev. Lett.* vol. 101, 2008.

[223] Stillinger, F.H. Structure in Aqueous Solutions of Nonpolar Solutes from the Standpoint of Scaled-Particle Theory , *J. Solution Chem.* vol. 2, pp. 141, 1973.

[224] Stokes, R.J.; Evans,D. F. *Fundamentals of interfacial engineering* Wiley VCH, pp. 21, 1997.

[225] Sugimoto, Y.; Pou, P.; Abe, M.; Jelinek, P.; Perez, R.; Morita, S.; Custance, O. Chemical identification of individual surface atoms by atomic force microscopy , *Nature* vol. 446, pp. 64, 2003.

[226] Summer, A.L.; Menke, E.J.; Dubowski, Y.; Newberg, J.T.; Penner, R.M.; Hemminger, J.C.; Wingen, L.M.; Brauers, T.; Finlayson-Pitts, B.J. The nature of water on surfaces of laboratory systems and implications for heterogeneous chemistry in the troposphere , *Phys. Chem. Chem Phys.* vol. 6, pp. 604, 2004.

[227] Sundararajan, S.; Bhushan, B. Development of a continuous microscratch technique in an atomic force microscope and its application to study scratch resistance of ultrathin hard amorphous carbon coatings , *Journal of materials research* vol. 16, Issue 2, pp. 437, 2001.

[228] Svergun, D.I.; Richard, S.; Koch, M.H.J.; Sayers, Z.; Kuprin, S.; Zaccai, G. Protein hydration in solution: Experimental observation by x-ray and neutron scattering , *Proc. Natl. Acad. Sci. USA* vol. 95, pp. 2267, 1998.

[229] Takano, K.; Funahashi, J.; Yamagata, Y.; Fujii, S.; Yutani, K. Contribution of water molecules in the interior of a protein to the conformational stability , *J. Mol. Biol.* vol. 274, pp. 132, 1997.

[230] Terabe, K.; Takekawa, s.; Nakamura, M.; Kitamura, K.; Higuchi, S.; Gotoh, Y.; Gruverman, A. Microscale to nanoscale ferroelectric domain and surface engineering of a near-stoichiometric LiNbO3 crystal , *Appl. Phys. Lett.* vol. 81, pp. 2044, 2003.

[231] Thiel, P. a.; Madey, T.E. The interaction of water with solid surfaces: Fundamental aspects , *Surf. Sci. Rep.* vol. 7, pp. 211, 1987.

[232] Toney, M.F.; Howard, J.N.; Richer, J. et al. Voltage-dependent ordering of water molecules at an electrodeelectrolyte interface , *Nature* vol. 368, pp. 444, 1994.

[233] Torii, K.; Iitaka, Y. Crystal structure of L-valine , *Acta Crystallogr., Sect. B: Struct. Crystallogr. Cryst. Chem.* vol. 26, pp. 1317, 1970.

[234] Tybell, T.; Ahn, C.H.; Triscone J.M. Control and imaging of ferroelectric domains over large areas with nanometer resolution in atomically smooth epitaxial $Pb(Zr_0\ 2Ti_0\ 8)O_3$ thin films , *Appl. Phys. Lett.* vol. 72, pp. 1454, 1998.

[235] University of Florida Webpage, Department of Chemistry, *http://www.chem.ufl.edu/*

[236] University of Leiden Webpage, Scanning-Probe-Microscopy section, *http://www.physics.leidenuniv.nl/.*

[237] Valdez, D.; Le Huerou, J−Y.; Gindre, M.; Urbach, W.; Waks, M. Hydration and protein folding in water and in reverse micelles: Compressibility and volume changes , *Biophysical Journal.* vol. 80, pp. 2751, 2001.

[238] Verdaguer, A.; Sacha, G. M.; Luna, M.; Frank Ogletree, D.; Salmeron, M. J. Initial stages of water adsorption on NaCl (100) studied by scanning polarization force microscopy , *Chem. Phys.* vol. 123, pp. 124703, 2005.

[239] Verdaguer, A.; Sacha, G. M.; Bluhm, H.; Salmeron, M. Molecular structure of water at interfaces: Wetting at the nanometer scale , *Chem. Rev.* vol. 106, pp. 1478, 2006.

[240] Verdaguer, A.; Weis, C.; Oncins, G.; Ketteler, G.; Bluhm, H.; Salmeron, M. Growth and structure of water on SiO2 films on Si investigated by Kelvin probe microscopy and in situ x−ray spectroscopies , *Langmuir* vol. 23, pp. 9699, 2007.

[241] Verdaguer, A.; Segura, J.J.; Fraxedas, J.; Bluhm, H.; Salmeron, M. Correlation between Charge State of Insulating NaCl Surfaces and Ionic Mobility Induced by Water Adsorption: A Combined Ambient Pressure X-ray Photoelectron Spectroscopy and Scanning Force Microscopy Study , *J. Phys. Chem. C* vol. 112, pp. 16898, 2008.

[242] Verdaguer, A.; Cardellach, M.; Fraxedas J. Thin water films grown at ambient conditions on BaF(2)(111) studied by scanning polarization force microscopy, *J. Chem. Phys.* vol. 129(17), pp. 174705, 2008.

[243] Verdaguer, A.; Cardellach, M.; Segura, J.J.; Sacha, G.M.; Moser, J.; Zdrojek, M.; Bachtold, A.; Fraxedas, J. Charging and discharging of graphene in ambient conditions studied with scanning probe microscopy , *Appl. Phys. Lett.* vol. 94, pp. 233105, 2009.

[244] Wang, W.Q.; Gong, Y.; Liang, Z.; Sun, F.L.; Shi, D.X.; Gao, H.J.; Lin, X.; Jiang, P.; Wang, Z.M. Direct observation of surface structure of D-alanine and D-/L-valine crystals by atomic force microscopy and comparison with X-ray diffraction analysis , *Surf. Sci.* vol. 512, pp. L379, 1993.

[245] Wang, W.Q.; Gong, Y.; Wang, Z.M.; Yan, C.H. Crystal structure of D-valine at the temperature of 293, 270, 223 and 173K , *Chin. J. Struct. Chem.* vol. 22, pp. 539 2003.

[246] Weaver, J.M.R.; Abraham, D.W. High resolution atomic force microscopy potentiometry , *Journal of Vacuum Science & Technology B: Microelectronics and Nanometer Structures* vol. 9 Issue 3, pp. 1559, 1991.

[247] Weissbuch, I.; Leiserowitz, L.; Lahav, M. Molecular recognition in chiral and non-chiral amphiphilic self-assemblies at interfaces , *Chirality* vol. 20, pp. 736, 2008.

[248] Welberry, T.R.; Goossens, D.J.; Withers, R.L.; et al. Monte Carlo Simulation Study of Diffuse Scattering in PZT, Pb(Zr,Ti)$O_3$ , *Metallurgical and materials transactions A* vol. 41A, pp.1110, 2010.

[249] Wesson, L.G. *Tables of electric dipole moments*, The Technology Press, MIT, Cambridge, MA. 1948.

[250] Wyman, J.; McMeekin, T.L. The dielectric constant of solutions of amino acids and peptides , *J. Am. Chem. Soc.* vol. 55, pp. 908, 1933.

[251] Xie, G.; Zheng, B.; Li, W.; Xue, W. Tribological behavior of diamond-like carbon film with different tribo-pairs: A size effect study , *Applied surface science* vol. 254, 2008.

[252] Xu, Y. Xu, Y. *Ferroelectric materials and their applications* North-Holland, Amsterdam, 1991.

[253] Xu, L.; Salmeron, M. An XPS and scanning polarization force microscopy study of the exchange and mobility of surface ions on mica , *Langmuir* vol. 14, pp. 5841, 1998.

[254] Xu, L.; Bluhm, H.; Salmeron, M. An AFM study of the tribological properties of NaCl (100) surfaces under moist air , *Surface Science* vol. 407, pp. 251, 1998.

[255] Xu, L.; Salmeron, M. The Topographiner: An Instrument for Measuring Surface Microtopography , *Nano-surface chemistry.* Long Island University, New York, Morton Rosoff, ISBN: 978-0-8247-0254-0, 2000.

[256] Xu, L.C.; Siedlecki, C.A. Effects of surface wettability and contact time on protein adhesion to biomaterial surfaces , *Biomaterials* vol. 28, pp. 3273, 2007.

[257] Xu, K.; Cao, P.; Heath, J.R. Graphene Visualizes the First Water Adlayers on Mica at Ambient Conditions , *Science* vol. 329, pp. 1188, 2010.

[258] Yokomizo, T.; Nakasako, M.; Yamazaki, T.; Shindo, H.; Higo, J. Hydrogen−bond patterns in the hydration structure of a protein , *Chem. Phys. Lett.* vol. 401, pp. 332, 2005.

[259] Yokomizo, T.; Higo, J.; Nakasako, M. Patterns and networks of hydrogen−bonds in the hydration structure of human lysozyme , *Chem. Phys. Lett.* vol. 410, pp. 31, 2005.

[260] Young, R.D. Surface Microtopography , *Physics Today* vol. 24 Issue 11, pp. 42, 1971.

[261] Young, R.D.; Ward, J.; Scire, F. Studies of wetting and capillary phenomena at nanometer scale with scanning polarization force microscopy , *Rev. Sci. Instrum.* vol. 43, pp. 999-1011, 1972.

[262] Yu, H.G.; Wolf, R.; Deng, K.; Zou, L.; Tadigadapa, S.; Trolier-McKinstry, S. Fabrication and performance of $d_{33}$-mode lead-zirconate-titanate (PZT) MEMS accelerometers , *Proceedings of SPIE* vol. 4559, pp. 131, 2001.

[263] Zhang, L.; Wang, L.; Kao, Y.T.; Qiu, W.; Yang, Y.; Okobiah, O.; Zhong, D. Mapping hydration dynamics around a protein surface , *Proc. Natl. Acad. Sci. USA* vol. 104, 18461, 2007.

[264] Zhang, L.; Tian, C.; Waychunas, G.A.; Shen, Y.R. Structures and charging of alpha-alumina (0001)/water interfaces studied by sum-frequency vibrational spectroscopy , *J.Am.Chem.Soc.* vol. 130, pp. 7686, 2008.

[265] Zheligovskaya, E.A.; Malenkov, G.G. Crystalline water ices , *Russian Chem. Rev.* vol. 75, pp. 57, 2006.

[266] Zhong, D.; Pal S. K.; Zewail a.H. Biological Water: A critique , *Chem. Phys. Lett.* vol. 503, pp. 1, 2010.

[267] Zobov, N.F.; Shirin, S.V.; Polyansky, O.L.; et al. Monodromy in the water molecule , *Chemical Physics Letters* vol. 414, pp. 193, 2005.

# Works by the author related with this thesis.

[1] Segura, J. J.; Verdaguer, A.; Cobin, M.; Hernndez, E. R. and Fraxedas, J. Amphiphillic Organic Crystals , *Journal of the American Chemical Society*, vol. 131, pp. 17853-17859, 2009.

[2] Segura, J. J.; Verdaguer, A.; Garzn, L; Barrena, E.; Ocal, C. and Fraxedas, J. Strong water-mediated friction asymmetry and surface dynamics of zwitterionic solids at ambient conditions: L-alanine as a case study , *Journal of Chemical Physics*, vol. 134(12), 2011.

[3] Segura, J. J.; Verdaguer, A.; Sacha, G. M.; Fraxedas, J. Dipolar origin of water etching of amino acid surfaces , *Physical Chemistry Chemical Physics*, vol. 13(48), pp. 21446-21450, 2011.

**Works in preparation directly related with this thesis contents.**

[4] Segura, J. J.; Verdaguer, A. and Fraxedas, J. Aminoacid dipoles determine water etching on valine crystals: water condensation and ice formation

[5] Segura, J. J.; Verdaguer, A.; Domingo, N. and Fraxedas, J. Dipole-dipole interactions between water and ferroelectric surfaces

**Other works published by the author during the thesis study.**

[6] Verdaguer, A.; Segura, J. J.; Fraxedas, J.; Bluhm, H. and Salmeron, M. Correlation between Charge State of Insulating NaCl Surfaces and Ionic Mobility

Induced by Water Adsorption: A Combined Ambient Pressure X-ray Photoelectron Spectroscopy and Scanning Force Microscopy Study , *J. Phys. Chem. C*, vol. 112(43), pp. 16898-16901, 2008.

[7] Sacha, G. M.; Cardellach, M.; Segura, J. J.; Moser, J.; Bachtold, A.; Fraxedas, J. and Verdaguer, A. Influence of the macroscopic shape of the tip on the contrast in scanning polarization force microscopy images , *Nanotechnology*, vol. 20(28), pp. 285704, 2009.

[8] Verdaguer, A.; Cardellach, M.; Segura, J. J.; Moser, J.; Bachtold, A. and Fraxedas, J. Charging of graphene by Scanning Probe Microscopy and the effect of water at environmental conditions , *Appl. Phys. Lett.*, vol. 94, pp. 233105, 2009.

[9] Murat Alanyalioglu, Juan José Segura, Judith Oro-Solé, Nieves Casan-Pastor The synthesis of graphene sheets with controlled thickness and order using surfactant-assisted electrochemical processes , *Carbon*, vol. 50, pp. 142, 2012.